Universidade de Lisboa

Faculdade de Ciências

Departamento de Física

Myocardial strain analysis with high temporal resolution MRI tagging: extended 3D motion tracking in normal and LBBB hearts

Sandra Raquel Ramos Tecelão

Doutoramento em Biofísica

2007

Universidade de Lisboa

Faculdade de Ciências

Departamento de Física

Myocardial strain analysis with high temporal resolution MRI tagging: extended 3D motion tracking in normal and LBBB hearts

Sandra Raquel Ramos Tecelão

Thesis supervised by Dr. J. Tim Marcus

Department of Physics and Medical Technology,

VU University Medical Center, Amsterdam, Netherlands

and by Prof. Doutor Alexandre Andrade

Instituto de Biofísica e Engenharia Biomédica,

Faculdade de Ciências, Universidade de Lisboa

Doutoramento em Biofísica

2007

To my boys/Aos meus rapazes:

Rui Potes

Pedro Tecelão Potes

CONTENTS

ACKNOWLEDGMENTS

Although a PhD is an individual project, it is only possible with the support of several persons.

Firstly I thank Prof. Doutor Eduardo Ducla-Soares, who imbued me with curiosity for the passionate area of medical physics. I am particularly grateful for all the professional and personal support given during this PhD.

To Dr. Tim Marcus, who supervised this thesis and provided me the knowledge in Cardiac Magnetic Resonance.

To Prof. Doutor Alexandre Andrade for his supervision and support.

To Prof. Heethaar for having accepted me in his research group.

To Joost Kuijer for all the help given and for the software essential for this thesis.

To Marieke Spreeuwenberg for the help in the statistical analysis of this thesis.

To the MEG group, Jan, Ilonka, Festje, Arent, Dennis, Geert, Jeroen, for the nice talks during lunch time and for showing me a little bit of the Dutch culture.

To Jaco Zwanenburg for the crucial support given during this thesis. I am grateful for all the suggestions and for always being available even when we were not sharing the same corridor. I specially thank the friendship which made me felt at home in a foreign country.

To Sónia and Iza for the excellent work environment we created in our office.

To Mia for the friendship and the trips to the gymnasium once a month.

To Teresa Montez for the friendship and for her contagious sense of humour.

To Patrik Andersson, for the strong friendship we built in six months; for the support to handle the distance from home, family and friends; for being the perfect neighbour; for the long talks and for always being there when I need it.

To the IBEBianos Mónica, Teresa, Nuno, Sofia, Ricardo, Susana, Luís, Patrícia for the excellent work environment.

To Prof. Doutor Pedro Almeida for always caring and for the help given during the most difficult periods of this PhD.

To Ana Sousa for the help with all bureaucratic issues and for the long and pleasant talks.

To Rita Nunes for the support and for the comments regarding the introduction of this thesis.

To my parents-in-law, for all the logistic and emotional support to manage this project.

To my sister, brother-in-law, and niece for the friendship and support.

To my grandparents, Laurinda and Manuel for always being there.

To my parents for providing me the conditions necessary to take a degree, for the encouragement to pursue with the PhD and for being my shelter.

My final and biggest thank goes to my husband Rui and to my son Pedro. To Rui for always believing me, for his unconditional love and support, for the words of encouragement in those moments when everything looked bad, for his happiness in the moments of success and for always remind me that we are a team and that I am never alone. To Pedro for all the smiles given during these months, for showing me the most intensive form of love and the real important things in life. Both of you make my life an exciting and happy journey. For these reasons and for those I am not able to put in words, I dedicate you this thesis.

I am grateful to the Fundação para a Ciência e Tecnologia (SFRH/BD/3005/2000) and Fundação Calouste Gulbenkian for the financial support of this thesis.

AGRADECIMENTOS

Apesar do doutoramento ser um projecto individual só é possível com o apoio de várias pessoas.

Em primeiro lugar agradeço ao Prof. Doutor Eduardo Ducla-Soares por me ter incutido o gosto pela Física Médica e por todo o apoio dado durante a realização desta tese, tanto a nível profissional como pessoal.

Ao Dr. Tim Marcus por ter aceite ser meu orientador e por todo o conhecimento que me deu na área da Ressonância Magnética Cardiovascular.

Ao Prof. Doutor Alexandre Andrade por me ter orientado e por todo o apoio dado.

Ao Prof. Heethaar por me ter aceite no seu grupo de investigação.

Ao Joost Kuijer pela ajuda dada e pelo *software* essencial para esta tese.

À Marieke Spreeuwenberg pela ajuda na análise estatística desta tese.

Ao grupo de MEG, Jan, Ilonka, Festje, Arent, Dennis, Geert, Jeroen, pelas agradáveis conversas de almoço e por me terem mostrado um pouco da cultura Holandesa.

Ao Jaco Zwanenburg pelo apoio fundamental para a realização desta tese. Por todas as sugestões e pela sua disponibilidade mesmo quando já não partilhávamos o mesmo corredor. Agradeço especialmente a sua amizade que me fez sentir em casa num país estrangeiro.

À Sónia e Iza pelo excelente ambiente de trabalho que criámos no nosso escritório.

À Mia pela amizade e pela companhia nas idas ao ginásio uma vez por mês.

À Teresa Montez pela amizade, pelo seu bom humor e boa disposição contagiantes.

Ao Patrik Andersson, pela forte amizade que construímos em 6 meses, pelo apoio para suportar a distância de casa, família e amigos, por ter sido o vizinho perfeito, pelas longas conversas e por estar sempre lá quando preciso.

Aos IBEBianos, Mónica, Teresa, Nuno, Sofia, Ricardo, Susana, Luís, Patrícia pelo excelente ambiente de trabalho.

Ao Prof. Pedro Almeida pela sua preocupação e pelo apoio dado nos períodos mais conturbados desta tese.

À Ana Sousa pela ajuda para tratar de toda a burocracia e pelas longas e agradáveis conversas.

À Rita Nunes pelo apoio e pelos seus comentários à Introdução desta tese.

Aos meus sogros por todo o apoio logístico e emocional para a realização deste projecto.

À minha irmã, cunhado e sobrinha pela amizade e por todo o apoio dado.

Aos meus avós, Laurinda e Manuel, por estarem sempre lá.

Aos meus pais, por me terem proporcionado as condições necessárias para tirar um curso superior, por me incentivarem em prosseguir com o doutoramento e por serem o meu porto de abrigo.

Em último, o meu maior agradecimento vai para o meu marido Rui Potes e para o meu filho Pedro Tecelão Potes. Ao Rui por sempre acreditar em mim, pelo seu amor e apoio incondicionais, pelas palavras de encorajamento nos momentos em que tudo parecia correr mal, pela sua alegria nos momentos de sucesso e por sempre me lembrar que somos uma equipa e que nunca estou só. Ao Pedro por todos os sorrisos que me tem dado nestes meses de vida em comum, por me mostrar uma forma tão intensa de amar e o lado realmente importante da vida. Com vocês a vida tem um sabor especial. Por estas razões e pelas muitas outras que não consigo passar para palavras dedico-vos esta tese.

Agradeço à Fundação para a Ciência e Tecnologia (SFRH/BD/3005/2000) e Fundação Calouste Gulbenkian o apoio financeiro para a realização desta tese.

ABSTRACT

Myocardial strain analysis has gained a significant clinical impact over the past few years, due to the relevant information that it provides regarding regional cardiac function. Cardiac magnetic resonance imaging (CMRI) is a unique technique to evaluate regional myocardial strain non-invasively and with high spatial and temporal resolutions. With tagged Magnetic Resonance Imaging (MRI), artificial magnetic markers are applied to the cardiac muscle, which allow the quantification of strain maps by tracking these markers. However, the introduction of this technique in clinical routine has been hampered by its time consuming post-processing.

The development of fully automatic and fast techniques to process tagged MR images is crucial to introduce this technique in clinical routine. With this in mind, this thesis has focussed on the development of an automatic technique to track 3D displacement of the myocardium, based on the Harmonic Phase (HARP) tracking technique. This technique enables to quantify regional strain maps of the cardiac muscle and its timing, by measuring the time to onset of shortening and time to peak of shortening.

Strain maps of healthy cardiac muscle can be used as a reference to correctly interpret strain maps of dysfunctional hearts. In this thesis the method developed to track cardiac muscle was applied to left bundle branch block (LBBB) patients and it was investigated which strain parameter better differentiates this group of patients from healthy controls. This analysis showed that the strain parameter most affected by the disease is the end-systolic circumferential shortening in the septum and the time to onset of the circumferential shortening in the septum.

Mechanical dyssynchrony of the cardiac muscle has been shown to be a better predictor of positive response to cardiac resynchronization therapy (CRT) in patients with heart failure (HF) than electrical dyssynchrony. Mechanical dyssynchrony can be measured from the time courses of the circumferential strain, which is the strain in the main direction of the cardiac fibres in the midwall of the heart. This strain component can be assessed using either 2D or 3D strain analysis. Although 2D circumferential strain does not take into account the longitudinal motion and deformation of the heart, its computation is less demanding than that of 3D circumferential strain analysis and easier to implement in clinical routine. The difference between these two strain analysis methods was investigated, as such a comparison is not yet reported in literature. This comparative study shows that the circumferential strain obtained with the fast and easy to implement 2D strain analysis method is not significantly different from that obtained with the much more complicated 3D strain analysis method.

From literature, it is known that the radial strain and the shear components related to the radial direction have a low accuracy. However, to understand why these low accuracies are obtained with HARP tracking several simulations were performed. These simulations have shown that the low accuracy in the radial direction can be explained by the inability of the filter used to compute the HARP angle to perfectly isolate the positive tag peak in *k*-space.

Keywords:

- Heart
- Magnetic Resonance Imaging (MRI)
- Myocardial tagging
- Harmonic Phase (HARP)
- Cardiac Resynchronization Therapy (CRT)

RESUMO

Desde há muitos séculos que o coração é alvo de curiosidade de filósofos e cientistas tendo-lhe sido atribuídas várias funções. Hoje em dia sabe-se que o coração é um músculo que bombeia o sangue através de uma rede de vasos sanguíneos com um comprimento total de cerca de 100.000 Km [1]. Esta pequena "bomba" começa a bater por volta do vigésimo dia de gestação e continua a bater durante toda a vida a um ritmo médio de sessenta batimentos por minuto. Aparentemente perfeita, esta "máquina" tornou-se na maior vítima das doenças causadas pelo estilo de vida moderno das civilizações ocidentais. As doenças cardiovasculares são a maior causa de morte e incapacidade na maioria dos países ocidentais. Cerca de metade das mortes na Europa (49%) são causadas por doenças cardiovasculares [2] e em Portugal um em cada três Portugueses é vítima destas doenças [3]. A melhor forma de reverter estes números é, para além de adoptar um estilo de vida saudável, conseguir diagnosticar estas doenças mais precocemente.

A quantificação da deformação do miocárdio fornece informação relativamente à função cardíaca que não pode ser obtida através dos parâmetros tradicionais, como o volume de sangue bombeado por ciclo cardíaco e a fracção de ejecção cardíaca. Imagens de Ressonância Magnética (RM) marcadas é uma técnica única para quantificar a deformação regional do miocárdio. Esta técnica consiste em aplicar marcadores magnéticos artificiais no músculo cardíaco que se deformam durante a sua contracção. Porém, o seu uso no meio clínico tem sido dificultado pelo demorado pós-processamento que estas imagens requerem. Actualmente, as imagens de RM marcadas são avaliadas visualmente, com os marcadores nas zonas afectadas a deformar menos do que os nas regiões normais. Nos últimos anos têm sido desenvolvidos vários métodos semi-automáticos para perseguir estes marcadores artificiais que, no entanto, continuam a ser demasiado demorados para serem utilizados no meio clínico.

O objectivo principal do projecto de investigação descrito nesta tese consiste em desenvolver um método automático para perseguir o movimento tridimensional do miocárdio. Posteriormente, este método é aplicado a sujeitos saudáveis e a doentes com bloqueio do ramo esquerdo do feixe de His, obtendo desta forma mapas de extensão do miocárdio do ventrículo esquerdo saudável e com esta perturbação da condução intraventricular.

Harmonic phase (HARP) tracking é uma técnica que persegue automaticamente os marcadores artificiais aplicados ao músculo cardíaco através da RM. Esta técnica baseia-se no facto de a fase dos pontos do miocárdio permanecer constante durante o ciclo cardíaco, e de o seu movimento reflectir o movimento do miocárdio. No entanto, devido ao movimento longitudinal do coração e à sua forma cónica, novo miocárdio aparece durante a sístole no plano

fixo da imagem que o *HARP tracking* não consegue perseguir. Para preencher esta lacuna, desenvolveu-se o método *extended 2D HARP tracking*, descrito no **Capítulo 2**. A precisão do método e das extensões obtidas foi determinada usando imagens simuladas. A precisão obtida para o *extended 2D HARP tracking* foi de 0.15 pixels, valor este equivalente ao de outros métodos existentes. A precisão da extensão na direcção circunferencial foi excelente, com um erro relativo máximo de 0.5%, o que mostra a eficiência do método em medir a deformação do miocárdio nesta direcção. Na direcção radial (extensão radial e distorção radial-circunferencial) a precisão da extensão foi baixa devido à reduzida espessura do músculo cardíaco, e consequentemente, à baixa resolução espacial nesta direcção. As vantagens do método *Extended 2D HARP tracking* relativamente à versão original foram avaliadas aplicando ambos os métodos a um grupo de seis voluntários saudáveis. Os resultados obtidos mostram que o novo método é capaz de perseguir todo o miocárdio durante todo o ciclo cardíaco, levando a uma diminuição significativa da extensão circunferencial ao nível médio e do ápice do ventrículo esquerdo. No entanto, esta técnica mede apenas o movimento bidimensional do miocárdio. Para medir o seu movimento tridimensional e determinar a deformação real do miocárdio, é necessário medir o seu movimento longitudinal. O método *Extended 3D HARP tracking*, descrito no **Capítulo 3**, persegue automaticamente o movimento 3D do miocárdio, combinando o movimento a 2D medido nas imagens do eixo-pequeno, com o movimento a 1D medido nas imagens do eixo-grande. Este método foi aplicado a seis sujeitos saudáveis e obteve-se um mapa da extensão 3D do ventrículo esquerdo normal. Este mapa mostra a existência de inhomogeneidade da extensão do ventrículo esquerdo saudável, realçando assim a importância de comparar regionalmente a extensão do miocárdio patológico com a extensão do miocárdio saudável. Com este método foi também possível medir o tempo de início da contracção circunferencial e longitudinal. Os resultados mostram que a contracção na direcção circunferencial inicia-se na parede livre do ventrículo esquerdo, propagando-se depois para o septo, como publicado em estudos anteriores [4]. No entanto, na direcção longitudinal a contracção inicia-se no septo propagando-se em seguida para a parede livre do ventrículo esquerdo, reflectindo a direcção de propagação do potencial de acção. Estes resultados levantam a hipótese de que a evolução temporal da contracção longitudinal reflecte melhor a activação eléctrica do ventrículo esquerdo do que a da contracção circunferencial.

O método *extended 3D HARP tracking* foi também aplicado a cinco sujeitos com bloqueio do ramo esquerdo de forma a investigar qual a componente da extensão tridimensional que melhor distingue este grupo de doentes dos saudáveis. Os resultados apresentados no **Capítulo 4** mostram que a componente da extensão mais afectada pela doença é a extensão circunferencial e o instante de início da contracção circunferencial no septo. Verifica-se também que os doentes estudados apresentam as extensões axiais da parede livre do miocárdio

inalteradas, enquanto que o septo contrai menos e começa a contrair antes do que nos saudáveis na direcção circunferencial e longitudinal.

Como as fibras cardíacas na parede média do ventrículo esquerdo estão orientadas na direcção circunferencial, esta componente de extensão é usualmente medida para avaliar a deformação do ventrículo esquerdo. Esta componente pode ser quantificada usando métodos 2D ou 3D de análise de extensão. Apesar dos métodos 3D terem em consideração o movimento longitudinal do coração, ainda não se sabe se esta componente do movimento afecta a extensão circunferencial. Para verificar se existe diferença entre a extensão circunferencial 2D e 3D, no **Capítulo 5** os métodos *extended 2D* e *3D HARP tracking* foram aplicados a um grupo de sujeitos saudáveis e de doentes com bloqueio do ramo esquerdo. Este estudo levou à conclusão de que não existe diferença significativa entre as extensões circunferenciais 2D e 3D nem entre a assincronia mecânica medida a partir destes parâmetros. Este resultado torna mais fácil a utilização das imagens de RM marcadas no meio clínico para medir a extensão circunferencial do miocárdio, uma vez que a análise a 2D da extensão é mais fácil de implementar e requer um pós-processamento mais rápido que a análise a 3D.

A razão para a baixa precisão do método *extended HARP tracking* na medição da extensão na direcção radial foi investigada usando um modelo 1D. Os resultados apresentados no **Capítulo 6** permitem concluir que a principal fonte de erro é a incapacidade do método para segmentar correctamente o pico das frequências positivas no espaço das frequências, aquando do cálculo do *HARP angle*. O erro na direcção radial é maior porque, nesta direcção, o número de marcadores é menor do que na direcção circunferencial, o que resulta em picos mais largos no espaço das frequências, e consequentemente, mais difíceis de segmentar.

Palavras-chave:

- Coração
- Imagem de Ressonância Magnética (IRM)
- *Myocardial tagging*
- *HARP*
- Terapia de Ressincronização Cardíaca (TRC)

ABBREVIATIONS AND SYMBOLS

ADP – Adenosine diphosphate

AL – Antero-lateral

ANT - Anterior

AS - Antero-septal

ATP – Adenosine triphosphate

AV – Atrioventricular

CAD – Coronary arteries disease

CANSEL - Cosine and sine modulation to eliminate

CCS – Coronary calcium scoring

CMRI – Cardiac magnetic resonance imaging

CRT - Cardiac resynchronization therapy

CSPAMM – Complementary spatial modulation of magnetization

CVD – Cardiovascular diseases

CT – Computed tomography

EBCT – Electron-beam computed tomography

ECG – Electrocardiogram

ED – End-diastole

EDV – End-diastolic volume

EF – Ejection fraction

EPI – Echo-planar imaging

ES – End-systole

ESV – end-systolic volume

FE – finite element

FFT – Fast Fourier transform

FID – Free induction decay

FISP – Fast imaging with steady precession

FLASH – Fast low-angle shot

FSE – Fast spin-echo

FT – Fourier transform

FOV – Field-of-view

GE – Gradient-echo

GRASS – Gradient recalled acquisition in the steady state

GSPECT – Gated single-photon emission computed tomography

HARM – Harmonic magnitude

HARP – Harmonic phase

HASTE - Half Fourier acquisition single shot turbo spin echo

HF – Heart failure

HR – Heart rate

IFFT – Inverse fast Fourier transform

IFT – Inverse Fourier transform

IL – Infero-lateral

INF - Inferior

IS – Infero-septal

LA – Long-axis

LBBB – Left bundle branch block

LISA – linearly increasing startup angle

LV – Left ventricle

LVEF – Left ventricle ejection fraction

LVF – Left ventricle function

MDCT – Multi-detector computed tomography

MR – Magnetic resonance

MRI – Magnetic resonance imaging

NMR – Nuclear magnetic resonance

NYHA – New York heart association

OS – Onset of shortening

PET – Positron emission tomography

RA – Right atrium

RARE - Rapid acquisition with refocused echoes

rc – Radial-circumferential

rcl – Radial-circumferential-longitudinal

RF – Radio-frequency

RV – Right ventricle

SA – Short-axis

SE – Spin-echo

SNR – Signal to noise ratio

SPAMM – Spatial modulation of magnetization

SPECT – Single photon emission computed tomography

SR – Strain rate

SRI – Strain rate imaging

SSFP – Steady state free precession

STI – Speckle tracking imaging

SV – Stroke volume

TagCNR – Tag contrast to noise ratio

TDI – Tissue Doppler imaging

TSE – Turbo spin-echo

T_1 – Longitudinal relaxation time

T_2 – Transverse relaxation time

TE – Echo time

TR – Repetition time

T_{avc} – Time of aortic valve closure

T_{avo} – Time of aortic valve opening

T_{mvo} – Time of mitral valve opening

T_{onset} – Time to onset

$T_{peak,first}$ – Time to peak first

$T_{peak,max}$ – Time to peak maximum

α_{cl} – Circumferential-longitudinal shear

α_{rc} – Radial-circumferential shear

α_{rl} – Radial-longitudinal shear

ε_c – Circumferential shortening

$\varepsilon_{c\ peak.max}$ – Maximum peak of circumferential shortening

$\varepsilon_{c\ peak.first}$ – First peak of circumferential shortening

ε_l – Longitudinal shortening

ε_r – Radial thickening

Chapter 1.

INTRODUCTION

1.1. AIM

Since ancient times the heart is the target of the curiosity of philosophers and scientists, and several functions have been attributed to it. Nowadays it is known that the heart is a muscle with the size of a closed fist that pumps the blood through a net of blood vessels with a total length of approximately 100.000 km [1]. This small pump of 12 cm and of approximately 300 g [1] starts beating around the 20th day of gestation and continues beating during all life at a mean rate of 60 beats per minute. Although apparently perfect, this engine turned into the main victim of the diseases of the modern lifestyle in western civilizations. Cardiovascular diseases (CVD) are the main cause of death and incapacity in most western countries. Nearly half of the deaths in Europe (49%) result from CVD [2] and in Portugal, one out of three Portuguese is victim of these diseases [3]. The best way to reverse this reality is, besides adopting a healthy lifestyle, to be able to perform an early and efficient diagnosis of the CVD.

CVD is the generic name for the diseases of the cardiovascular system, including disorders of the myocardium, of the coronary arteries and of the electrical system of the heart. These diseases lead to a decreased cardiac function, which is traditionally assessed with global parameters as the ejection fraction (EF) and stroke volume (SV). However, in the early stages of CVD these global parameters can not reflect dyssynchrony in contraction, as some regions with impaired contraction can be compensated by other regions with preserved function. For the early diagnosis of anomalous contraction, it is important to assess regional myocardial deformation. Up till recently, this could only be performed by invasively implanting markers in the cardiac muscle, which is not a procedure to be used in clinical routine.

In 1988, tagged Magnetic Resonance Imaging (MRI) allowed the non-invasive analysis of regional deformation of the myocardium with spatial and temporal resolutions that have been progressively improved during the following years. This technique is characterized by creating artificial magnetic markers in the cardiac muscle which deform with it. In this way, tracking the markers is equivalent to track the cardiac muscle, enabling the assessment of regional deformation of the myocardium. The use of this technique in clinical routine is still not possible, and even the use in scientific patient studies is challenging, due to the long post-processing times that it requires. The subject of this thesis is, therefore, to develop an automatic method to compute 3D myocardial deformation and apply it to healthy controls. These healthy strain maps can then be used as a reference to understand the abnormal deformation patterns of hearts with CVD like, for example, left bundle branch block (LBBB).

1.2. THESIS OUTLINE

This thesis comprises the following chapters.

Chapter 2 presents an extension of the 2D Harmonic Phase (HARP) tracking technique. This new method has the advantage of tracking new myocardium that appears in the image plane due to the longitudinal motion and the conical shape of the heart. This method is validated using a simulated data set and its accuracy is determined. A comparison between extended 2D HARP tracking and the original version is performed with a data set of six healthy controls.

In **Chapter 3** a 3D version of the extended HARP tracking is presented. With this method, it is possible to automatically quantify the 3D strain tensor of the myocardium. In this chapter, the method is applied to healthy subjects to obtain strain maps of the healthy left ventricle (LV). As the strain of the LV is inhomogeneous, it is important to completely characterize the healthy myocardium before studying hearts with cardiac diseases.

After characterizing the healthy LV myocardium, in **Chapter 4** the extended 3D HARP tracking method is applied to LBBB patients. In this study the 3D strain component that better differentiates patients with LBBB from healthy controls is investigated.

Recent studies have shown that the mechanical dyssynchrony in circumferential strain can be a good predictor of positive response for cardiac resynchronization therapy (CRT) in patients with heart failure (HF). As these results were mainly obtained using 2D strain analysis, which does not take into account the effect of longitudinal motion as 3D strain analysis does, it is important to verify if there is any difference between the results obtained with these two different strain analysis methods. Therefore, in **Chapter 5** the 2D and 3D circumferential strain obtained with the extended 2D and 3D HARP tracking techniques are compared.

From the accuracy assessment in **Chapter 2**, it was found that the accuracy of the radial strain component was low for the extended 2D HARP tracking method, which is in line with accuracies reported for other methods in literature. In **Chapter 6** this low accuracy for the radial direction is further explored. A model of the modulated tag pattern is simulated and the hypotheses for the sources of error in the HARP method formulated in **Chapter 2** are evaluated.

In **Chapter 7** a summary of the results obtained in this thesis and their importance for the widespread application of cardiac MRI in clinical routine is presented.

1.3. HUMAN HEART

1.3.1. Anatomy of the human heart

1.3.1.1. Macroscopic anatomy

The heart is located near the middle of the thoracic cavity, over the diaphragm, with two thirds of its mass on the left side of the body (Figure 1-1). It is surrounded by the pericardium, a triple-layered sac that, besides protecting the heart, also anchors it to the surrounding walls, prevents it from overfilling and reduces friction between the membranes with the pericardial fluid [1].

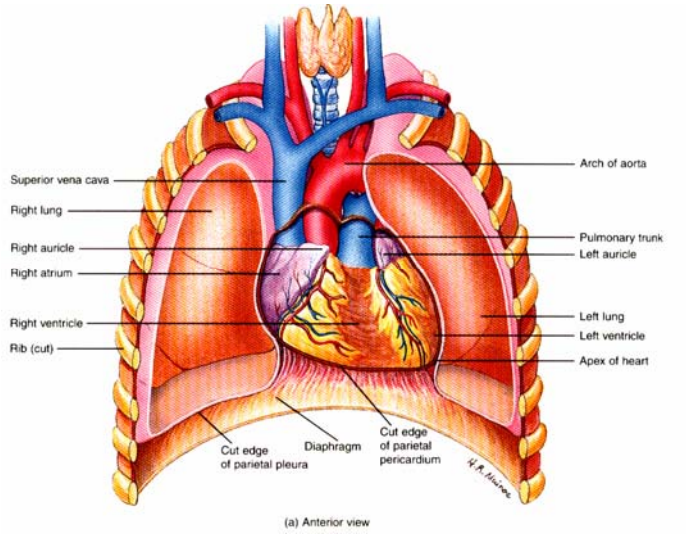

Figure 1-1 Illustration of the thoracic cavity.

Adapted from [1]

The heart wall is composed by three layers: the epicardium, the myocardium and the endocardium. The epicardium is the outermost layer of the cardiac wall. The endocardium covers the interior of the heart and the cardiac valves. The myocardium is in between these two layers and is formed by the cardiac muscle tissue responsible for cardiac contraction.

The interior of the heart is divided into four chambers: right atrium (RA), right ventricle (RV), left atrium and LV. The RA and RV are separated from the left atrium and LV by the interatrial and interventricular septum respectively, creating two independent pumps (see Figure 1-2).

The RA receives the venous blood from the superior and inferior vena cava and from the coronary sinus and pumps it to the RV. At the same time, the left atrium receives the arterial blood from the pulmonary veins and pumps it to the LV. Afterwards, the RV pumps the venous blood to the lungs through the pulmonary trunk and pulmonary arteries, while the LV pumps the arterial blood to whole body through the aorta and systemic arteries (see Figure 1-2).

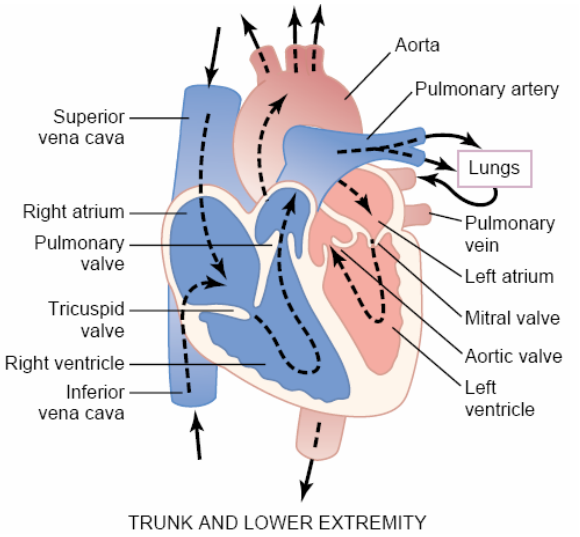

Figure 1-2 Schematic representation of heart anatomy and blood flow course through cardiac chambers and valves. Adapted from [5]

The unidirectional blood flow is ensured by the cardiac valves: the atrioventricular (AV) valves prevent the reflux of blood from the ventricles back to the atria and the semilunar valves prevent the reflux of blood from the main arterial trunks back to the ventricles. The right AV valve is designated by tricuspid valve and the left AV valve by bicuspid (or mitral) valve (see Figure 1-2). These valves are connected by the chordae tendineae to the papillary muscles existent on the inner surface of the ventricles, to prevent the valve cusps to enter the atria during ventricular contraction (see Figure 1-3). The right semilunar valve is designated by pulmonary valve and the left semilunar valve by aortic valve (see Figure 1-2). These valves are composed by three semilunar cusps, which obstruct the passage of blood when it starts flowing back to the ventricles during ventricular relaxation (see Figure 1-3).

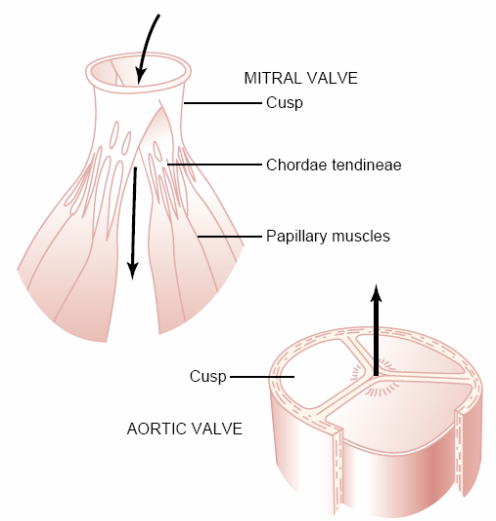

Figure 1-3 Sketch of the mitral valve and aortic valve. Adapted from [5]

As each cardiac chamber has different requirements during contraction, the cardiac muscle is not homogeneous. The ventricles have a thicker myocardium than the atria and LV myocardium is two to four times thicker than RV myocardium [1]. Additionally, the effectiveness of the LV contraction, which comprises wall thickening, circumferential shortening, longitudinal shortening and torsion, is highly dependent on the architecture of the muscle fibres that constitute the LV myocardium. This is clear in certain cardiomyopathies, where the rearrangement of the muscle fibres results in impairment of the LV function (LVF) [6]. However, the geometry of a healthy LV cardiac muscle is still the subject of research [7], since it is difficult to develop a theory that simultaneously explains its complex motion and its development from a single layered tube. Two main theories exist [6, 7]: one theory claims the existence of a ventricular myocardial band that can be untwisted [8, 9], and the other defends the importance of the supportive collagenous matrix and the existence of several intertwined helices which cannot be unwrapped like muscle bundles in a skeletal muscle [8, 10]. Nevertheless, both theories agree with a helical arrangement of the cardiac fibres, which changes gradually from a right-handed helix in the subendocardium to a left-handed helix in the subepicardium (see Figure 1-4).

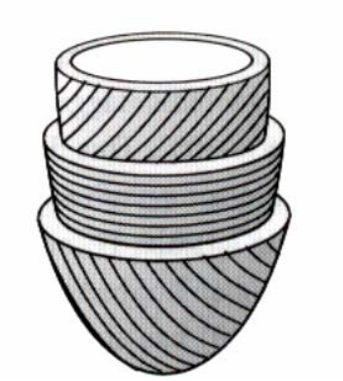

Figure 1-4 Schematic representation of the LV muscle fibres architecture.
At the subendocardium the right handed helix makes a 60º with the circumferential direction, while at the subepicardium the left handed helix makes a -60º with the circumferential direction. At the midwall the fibres are mainly oriented along the circumferential direction. Adapted from [11]

As any muscle, the heart needs a constant supply of oxygen and nutrients. This is assured by the right and left coronary arteries, which are branches of the ascending aorta, and by their ramifications. The carbon dioxide and wastes are collected by the coronary veins, which deliver it to the RA through the coronary sinus, located at the posterior surface of the heart (see Figure 1-5). This group of arteries and veins is designated by coronary circulation.

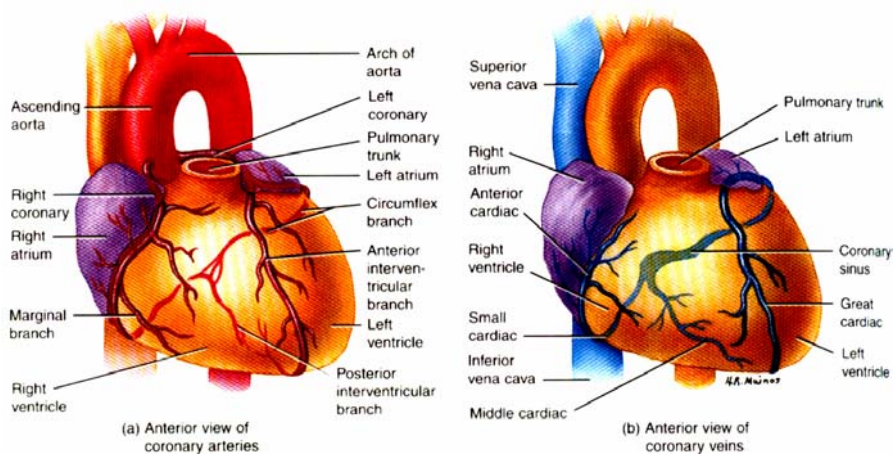

Figure 1-5 Schematic representation of the coronary circulation

Anterior view of the coronary arteries (a) and of the coronary veins (b). Adapted from [1]

1.3.1.2. Microscopic anatomy

Cardiac muscle constitutes by itself a category of muscle that has a striated appearance, like skeletal muscle, and is involuntary, like smooth muscle. The fibres that constitute the cardiac muscle, the cardiomyocytes, range between 50 to 100 µm in length, have about 14 µm in diameter and a Y shape with squarish transverse section (see Figure 1-6a).

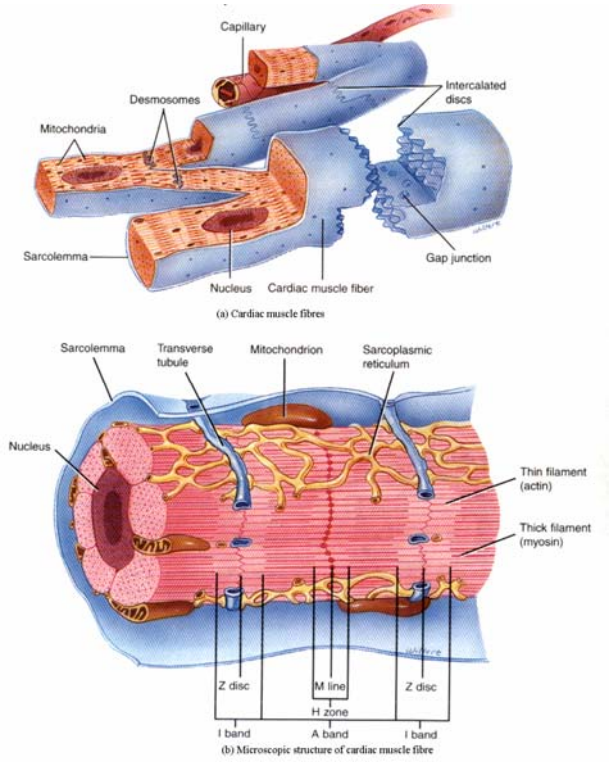

Figure 1-6 Histology of cardiac muscle tissue.

(a) Cardiac muscle fibre (b) Microscopic structure of cardiac muscle fibre. Adapted from [1]

These building blocks are connected to each other by intercalated discs, which contain desmosomes, to hold the cells together, and gap junctions, to spread the action potentials. The sarcolemma of the cardiomyocyte encircles a central nucleus (exceptionally two nuclei) and the sarcoplasm (cytoplasm of a muscle fibre). Like in other cells, the sarcoplasm is composed by several organelles with specific functions, namely: sarcoplasmic reticulum, thick, thin and elastic filaments, transverse tubules and mitochondria (see Figure 1-6b). The sarcoplasmic reticulum enables the storage of Ca^{2+} necessary for muscle contraction. The thick filaments are composed by myosin molecules; the thin filaments by actin, troponin and tropomyosin molecules and the elastic filaments by titin protein (see Figure 1-7).

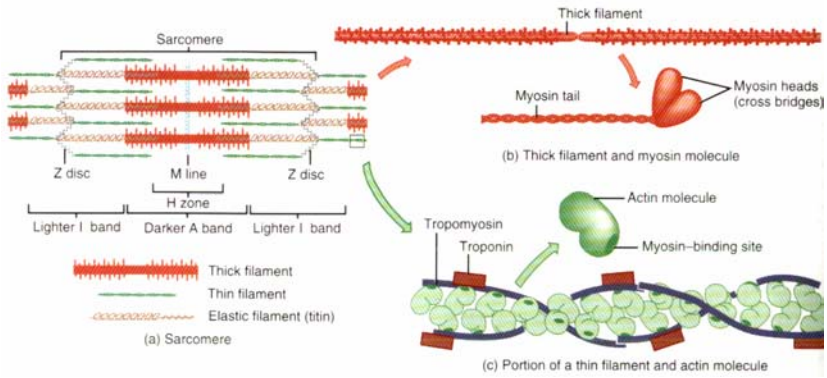

Figure 1-7 Microscopic structure of a muscle fibre
(a) Sarcomere (b) Thick filament (c) Thin filament. Adapted from [1]

These filaments are organized in functional units called sarcomeres. The sarcomeres are divided into several regions designated by bands. The dark A band includes the thick filaments and part of the thin filaments. The light I bands include only thin filaments. This pattern of dark and light bands gives the striated aspect of the cardiac muscle. Narrow plate-shaped regions of dense material located at the middle of the I bands [1] are designated by Z discs and separate neighbour sarcomeres. The H zone corresponds to the middle of the A band and contains only thick filaments. At the middle of the H zone, the M line formed by protein molecules connects adjacent thick filaments. The elastic filaments anchor the thick filaments to the Z discs. The transverse tubule consists of an infolding of the sarcolemma towards the centre of the cardiomyocyte filled with extracellular fluid and is located along the Z disks (see Figure 1-6b).

1.3.2. Physiology of the human heart

1.3.2.1. Cardiac cycle

During a cardiac cycle the volume and the pressure inside the cardiac chambers changes in a well defined pattern. The series of events occurring in the left side of the heart and corresponding changes are represented in Figure 1-8.

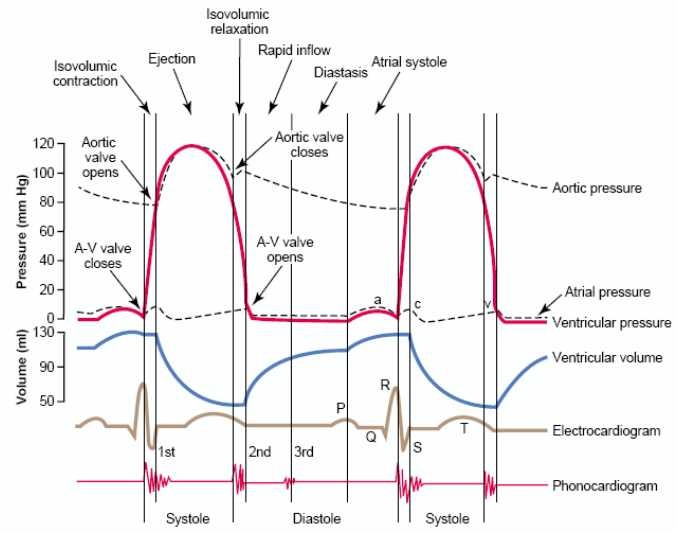

Figure 1-8 Description of the cardiac cycle.

Adapted from [5]

The cardiac cycle can be divided into four phases: atrial systole, ventricular systole, atrial diastole and ventricular diastole.

Atrial systole: When the myocardium of the atria depolarizes, the atria start to contract increasing the pressure in their interior (curve a in Figure 1-8). Due to atrial contraction, 25% more blood flows into the ventricles, which results in an increase of the pressure inside these chambers and of their volume (see Figure 1-8). At the end of this cardiac phase, the atrial and ventricular pressures return to their baseline values and the ventricular volume reaches its highest value. The atrial systole is represented in the electrocardiogram (ECG) by the P wave.

Ventricular systole: The ventricular systolic phase is divided into two different periods: the isovolumic contraction and the ejection. The isovolumic contraction begins immediately after atria contraction ceases and corresponds to the initial phase of the ventricular systole. This period starts with the closing of the AV valves due to the increased pressure felt inside the ventricles. As the semilunar valves are also closed, this phase of the cardiac cycle is characterized by a constant volume of the ventricles (isovolumic contraction). During this period, the atrial pressure also increases (curve c in Figure 1-8), as a result of slight backflow of blood and bulging of the AV valves backward towards the atria. The ejection period starts when the pressure built inside the ventricles is high enough to open the semilunar valves. This phase is characterized by an increase of the ventricular pressure and a decrease of the ventricular volume. In the ECG, the QRS complex reflects the depolarization of the ventricles, which triggers the cardiac muscle contraction, and consequently, the beginning of the systolic phase.

Atrial diastole: The atrial diastole starts with ventricular contraction and extends until two thirds of ventricular diastole. As mentioned before, the beginning of this phase is characterized by an increase of the atrial pressure due to slight backflow of blood and bulging of

the AV valves backward towards the atria. After this period, the pressure inside the atria decrease, increasing slowly close to the end of the ejection period of ventricular systole (curve v in Figure 1-8) due to accumulation of blood inside the atria that flows from the veins. When the pressure in the atria is higher than in the ventricles, the AV valves open. This allows the blood to pass directly from the veins into the ventricles, decreasing the pressure inside the atria.

Ventricular diastole: After the semilunar valves close, there is a small period, designated by isovolumic relaxation, where the pressure inside the ventricles drops rapidly at a constant volume. This period ends when the pressure inside the ventricles goes below the atria pressure and the AV valves open. In this instant the filling of the ventricles starts. At the first third of this phase there is a rapid filling of the ventricles with the volume of these chambers increasing. At the second third the ventricular pressure and volume do not change significantly, and the last third corresponds to the atrial systole, where the last portion of blood is pumped into the ventricles. The ventricular diastole is represented in the ECG by the T wave.

1.3.2.2. Electric conduction system

Cardiac contraction is preceded by the propagation of an action potential through the cardiac muscle. The electric conduction system that transmits this action potential to all cardiac fibres comprises the following elements: sinoatrial node, internodal pathways, AV node, AV bundle, left and right bundle branches and Purkinje fibres. These elements and the respective propagation times (in seconds) are represented in Figure 1-9.

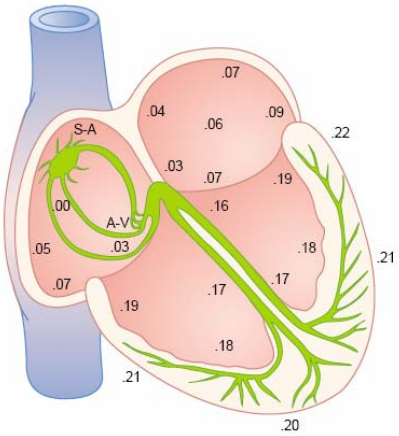

Figure 1-9 Electric conduction system of the heart.
The numbers denote the propagation times in seconds. S-A – sinoatrial node. A-V – atrioventricular node. Adapted from [5].

The sinoatrial node, also known as sinus node, is the natural pacemaker of the heart responsible for triggering the action potential that causes its rhythmical contraction. This node, located at the right atrial wall below the opening of the superior vena cava (see Figure 1-9), is

formed by several cardiomyocytes that have the ability of self-excitation. Self-excitable cardiomyocytes can be found in other regions of the cardiac muscle; however these located at the sinoatrial node have a higher frequency of triggering, which prevents other self-excitable cardiomyocytes to trigger other action potentials in different regions of the heart. The fibres of the sinoatrial node are directly connected to the atrial cardiomyocytes, allowing the action potential to spread through the atrial myocardium, and the atria to contract.

The internodal pathways are small bundles of atrial cardiomyocytes that have a higher velocity of conduction and are responsible for transmitting the action potential from the sinoatrial node to the AV node.

The AV node is located in the posterior wall of the RA immediately behind the tricuspid valve [5] (see Figure 1-9). This group of fibres delays the action potential, in order to allow the atria to contract prior to the ventricles, and conducts it to the AV bundle.

The AV bundle, also known as bundle of His, is the bridge between the atria and the ventricles. This bundle of fibres only allows the action potential to propagate in this direction and is the only connection existent between upper and lower chambers. Outside this region, a continuous fibrous barrier separate them [5].

The AV bundle splits into the left and right bundle branches. These branches are located underneath the endocardium on the two respective sides of the interventricular septum and transmit the action potential to the apex.

The Purkinje fibres located in the ventricular myocardium transmit, at a high velocity, the action potential from the left and right bundle branches to the other ventricular cardiomyocytes. The propagation of the action potential through these fibres leads to ventricular contraction.

1.3.2.3. Action potential

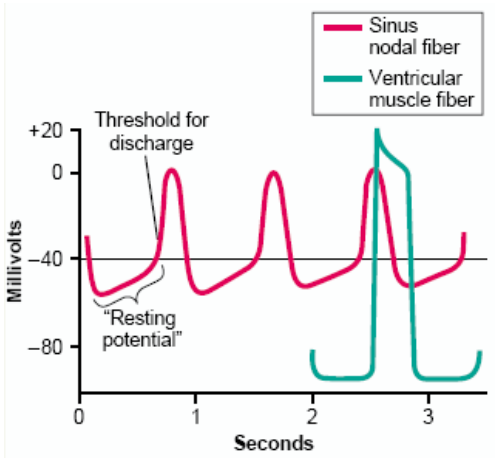

Figure 1-10 Diagram of an action potential of a LV muscle fibre and a sinoatrial node muscle fibre. Adapted from [5]

Cardiac muscles fibres have a resting membrane potential close to –90 mV (see Figure 1-10) [1]. When an impulse arrives from a neighbouring fibre, a sequence of events is triggered. First, the voltage-gated fast Na^+ channels in the sarcolemma open. This results in a rapid inflow of Na^+ to the sarcoplasm, as the fibre cytoplasm is more negative than the extra-cellular fluid and the concentration of Na^+ is higher outside the fibre than inside. The inflow of high quantities of Na^+ increases the membrane potential from –90 mV to 20 mV, and corresponds to the rapid depolarization period. After that the voltage-gated fast Na^+ channels start closing, decreasing the permeability of the sarcolemma to this type of ions. Then, the voltage-gated slow Ca^{2+} channels (also called Ca^{2+}-Na^+ channels) [5], existent in the sarcolemma and in the sarcoplasmic reticulum membrane, start to open allowing an inflow of Ca^{2+} and Na^+ to the sarcoplasm. This type of channels is slower to become active but remains in this state for longer time. Concomitantly, the permeability of the sarcolemma to K^+ decreases, preventing the outflow of this type of ions to the extra-cellular fluid. The combination of these two factors allows cardiac contraction to last fifteen times more than that of skeletal muscles, as the membrane potential is kept positive for tenths of a second (plateau in Figure 1-10). This plateau, observed during the depolarization period, is characteristic of the cardiomyocytes action potential. The repolarization period begins when the voltage-gated Ca^{2+}-Na^+ channels start to become inactive and the voltage-gated K^+ channels active. The result is the rapid outflow of positive charges to the extra-cellular fluid and the ceasing of inflow of positive charges to the sarcoplasm, leading the membrane potential back to its resting value.

After an action potential, any muscular fibre goes through a period during which it is not possible to trigger a new action potential. This period, designated by refractory period, is longer for cardiomyocytes than for skeletal fibres (0.15 sec for the atria and 0.25-0.30 sec for the ventricles [5]), starting before and ending after cardiac contraction. This particularity renders impossible the occurrence of a maintained contraction of the cardiac muscle [1].

The capacity of self-excitation of some cardiomyocytes is possible due to a special action potential (represented in Figure 1-10 by the red curve). The resting membrane potential of this type of cardiac muscle fibres is less negative than that of other cardiomyocytes, reaching a minimum value between –55 mV and –60 mV. At this value, the voltage-gated fast Na^+ channels are inactivated, which disables the rapid depolarization period that characterizes the cardiac muscle fibres. Instead, the membrane potential slowly increases due to the natural likeness of the sarcolemma of the self-excitable fibres to Na^+, which allows an inflow of positive charges to the sarcoplasm. This natural likeness is responsible for the self-excitation ability of these muscle fibres. After this period, designated by resting potential (see Figure 1-10), the membrane potential reaches a value that triggers the voltage-gated slow Ca^{2+}-Na^+ channels and the action potential starts. After some tenths of a second, these channels become

inactive, the voltage-gated K^+ channels open and a rapid outflow of positive charges to the extra-cellular fluid begins. These channels remain open for another few tenths of a second leading the membrane potential to a resting membrane potential of –55 to –60 mV. This phenomenon is designated by hyperpolarization. The closing of this type of channels and the natural leakiness of the membrane fibres to Na^+ increases the resting membrane to –40 mV, triggering a new action potential.

1.3.2.4. Muscular contraction

Muscular contraction occurs as a mechanical response to the propagation of an action potential in a muscle fibre. The theory that is presently used to explain this phenomenon is the sliding mechanism of contraction. This theory states that the size of the filaments that constitute the muscle do not change during contraction. Instead, the thin filaments slide over the thick filaments towards the centre of the sarcomere, thereby decreasing its size.

The triggering of muscle contraction depends on the existence of Ca^{2+} and Adenosine Triphosphate (ATP) in the sarcoplasm. The Ca^{2+} is necessary to trigger the chemical reactions that promote the sliding of the filaments over each other and the ATP provides the energy necessary for these reactions.

In the relaxed state, the thick and thin filaments are detached from each other due to the troponin-tropomyosin complex that blocks the myosin-binding site in the actin molecule (Figure 1-11d). In this state an ATP molecule is attached to the head of the thick filaments that cleavage it resulting in a molecule of Adenosine Diphosphate (ADP) plus phosphorus (P). This reaction occurs thanks to the action of a part of the myosin head which acts as an ATPase enzyme. After this chemical reaction, the head of the myosin is said to be in an energized state.

When an action potential reaches the sarcolemma of a cardiomyocyte, it propagates into its sarcoplasm through the membranes of the transverse tubules, which in turn transmit it to the sarcoplasmic reticulum. This opens the Ca^{2+} release channels existent in the membrane of the transverse tubules and in the membrane of the sarcoplasmic reticulum, enabling the inflow of high quantities of Ca^{2+} to the sarcoplasm. In turn, these ions bind to the troponin protein, making the troponin-tropomyosin complex uncover the myosin binding site on the actin molecule. The activated myosin heads are then able to bind to the actin (Figure 1-11a) and swivel toward the centre of the sarcomere (Figure 1-11b), releasing the ADP molecule. An ATP molecule attaches then to the myosin head, causing the separation between this and the actin molecule (Figure 1-11c). At this stage the myosin head once again proceeds to break the ATP molecule, preparing the filaments to a new step towards the centre of the sarcomere. This process continues until there is ATP and Ca^{2+} in the sarcoplasm, or until the Z discs reach the end of the thick filaments.

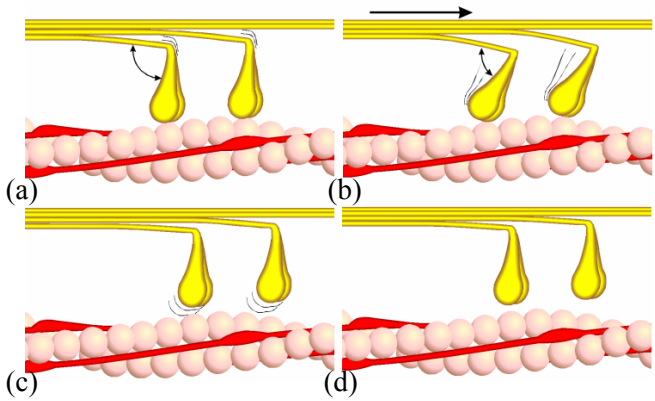

Figure 1-11 Phases of the power stroke that leads to fibre muscle contraction.
The myosin heads are represented in yellow, the actin molecules in pink and the tropomyosin in red. Adapted from [12]

1.4. CARDIAC IMAGING

1.4.1. Echocardiography

Echocardiography is one of the cardiac imaging modalities most used in clinical routine. It is a non-invasive technique that generates cardiac images from ultrasound echoes that are reflected at tissue interfaces with different acoustic impedances.

Ultrasound consists of a sound wave with a frequency that goes beyond the human audible range (16Hz - 20KHz). For echocardiography, the frequency usually used is around 2 - 3 MHz. These ultrasounds are produced and detected by transducers. The main element of a transducer is the piezoelectric. This element, usually a synthetic ceramic, has the ability to transform electrical signals into mechanical signals and vice-versa [13]. When a voltage is applied to this material, its shape changes and it vibrates at its natural resonance frequency, creating an ultrasonic wave. On the other hand, when an ultrasonic echo reaches the surface of the piezoelectric element, it creates a voltage that can be measured and processed.

Echocardiography comprehends several methods that allow the assessment of different parameters of cardiac function, like valvular and ventricular hemodynamics, global or regional systolic and diastolic functions [14].

The main advantages of echocardiography are its non-invasiveness, low cost, high temporal and spatial resolutions and portability. These characteristics make this imaging modality the most widely used for the assessment of LVF [15]. However, it does not enable imaging of gases or bones, the acoustic window is limited, and the technique has a low reproducibility with the results being highly dependent on operator expertise.

The presently available echocardiographic techniques are described in this section.

1.4.1.1. M-mode echocardiography

The simplest echocardiographic technique is the 1D M-mode, with M for motion. With this technique, the densities of the cardiac structures that originate the ultrasonic echoes are depicted using a grey-scale, with the spatial and temporal information drawn on the *y*-axis and *x*-axis, respectively (see Figure 1-12).

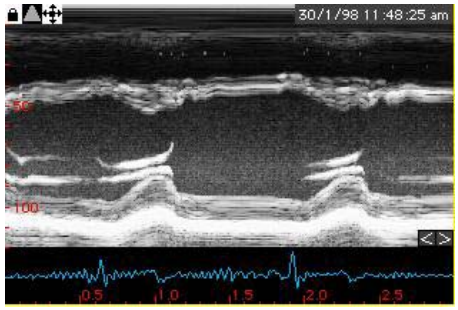

Figure 1-12 M-mode image of a LV.
Adapted from [16]

The spatial localizations of the reflectors are computed using the echoes detection times and the propagation velocity of the sound in soft tissue (1540 ms^{-1}). This mode of echocardiography allows qualitative and semi-quantitative evaluation of the cardiac function, by observing and/or measuring myocardial thickening [17], longitudinal shortening and dyssynchrony between septum and posterior wall [18, 19]. The main advantages of this technique is, besides its simplicity and widespread availability, high temporal and spatial resolutions. However there are several drawbacks, namely the inability to quantify cardiac function, the constraint to measure deformation only along the radial direction and in a limited number of segments [17, 20].

1.4.1.2. 2D echocardiography

2D echocardiography provides static or dynamic 2D anatomical images of the heart. These images are acquired with transducers that have an array of piezoelectric elements. Each of these elements sends an ultrasonic beam and detects the respective ultrasonic echo.

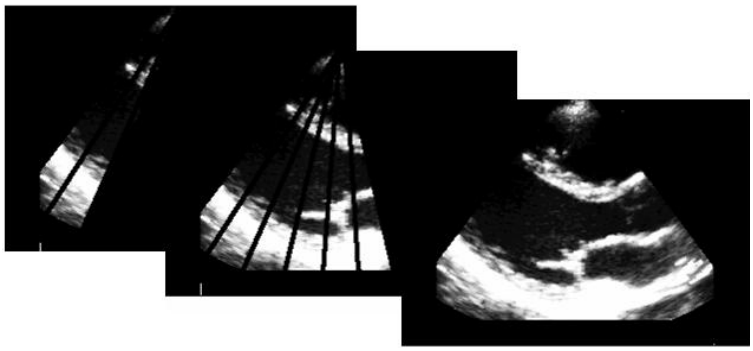

Figure 1-13 Schematic representation of a 2D echocardiographic image generation
Adapted from [16]

The several detected echoes are displayed side by side giving origin to a cone-shaped grey-scale image (see Figure 1-13). With these images it is possible to evaluate qualitatively and semi-quantitatively the cardiac structure and global function [20], and diagnose coronary arteries disease (CAD) non-invasively. The main limitations are the inability to quantify myocardial function [21], and the fact that the computation of both EF and LV volume is highly dependent on the endocardium delineation and is based on geometric assumptions regarding the LV [14], which do not necessarily hold true.

1.4.1.3. Doppler echocardiography

When a sound wave reaches a moving object, its perceived frequency changes. The frequency increases if the object moves towards the receptor, and decreases if it moves away from it. This effect, known as Doppler effect, is used in echocardiography to measure the blood flow through the heart's chambers and valves. Blood cells velocity is computed by comparing the incident ultrasound frequency with the reflected ultrasound frequency using the relation:

$$v\cos\theta = \frac{f_R c}{2 f_0} \qquad \text{Equation 1-1}$$

where f_R is the reflected ultrasound frequency, f_0 the incident ultrasound frequency, c the sound velocity and θ the angle between blood cells and the ultrasound beam. As the blood velocity is around $1 ms^{-1}$, the detected Doppler frequency falls inside the audible range.

Colour coding is usually used to show blood flow directions, with red representing blood moving towards the transducer and blue representing blood moving away from it [13]. With autocorrelation methods, this colour code can be matched with 2D grey-scale echocardiographic images or M-mode images (see Figure 1-14).

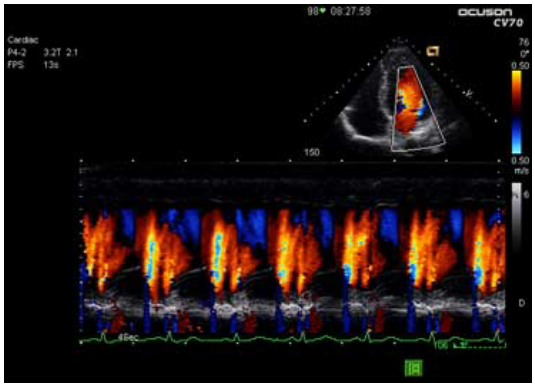

Figure 1-14 Example of a normal LV inflow (Top: 2D image Bottom: M-mode image)
Adapted from [22]

Doppler echocardiography is presently widely used in clinical routine to assess blood flow patterns and detect regurgitation, obstructive or shunt lesions [23]. Yet, this technique has the drawback of only measuring the velocity component parallel to the ultrasound beam, since it is not possible to know the angle θ (see Equation 1-1) [24].

1.4.1.4. Tissue Doppler Imaging

The Doppler principle can also be applied to assess cardiac muscle motion [23, 24]. As blood moves at higher velocities than muscle, the spectrum of frequencies detected by the transducer is composed by two distinguishable peaks: one at low frequency with high amplitude, resultant from the myocardium, and one at high frequency with low amplitude, resultant from the blood cells. The velocity of the myocardium is then computed by applying a low-pass filter or gain adjustment to the frequency spectrum [23].

Tissue Doppler imaging (TDI) is used to compute the left ventricle ejection fraction (LVEF) [23], to quantify systolic and diastolic functions [23, 24], to assess right ventricular function [24] and to compute LV dyssynchrony [18, 23]. Like Doppler echocardiography, TDI also uses parametric images to provide a visual representation of tissue velocities. In this case, myocardial velocity can be displayed as a colour Doppler signal superimposed to a 2D grey-scale image or to an arbitrarily oriented M-mode tracing [14, 21, 23, 24]. The main advantage of this echocardiographic technique is its ability to quantify LVF. However, being based on the Doppler principle, again it can only measure tissue velocity parallel to the ultrasound beam [14, 17, 24], with the velocity error increasing with θ (see Equation 1-1) [23]. Additionally, this method cannot differentiate velocities caused by active movement (shortening or lengthening of cardiac muscle fibre) from velocities caused by passive movement (translation and tethering) [14, 17, 21, 23-26].

1.4.1.5. Strain Rate Imaging

To overcome the impossibility of TDI to distinguish between active and passive myocardial motion [21, 23, 25], a new echocardiographic technique has been developed. The Strain Rate Imaging (SRI), instead of computing myocardial velocity, computes its deformation (strain) or its deformation rate (strain rate). The strain rate (SR) can be computed using the relation:

$$SR = \frac{v_a - v_b}{d} \qquad \text{Equation 1-2}$$

where v_a and v_b represent the instantaneous velocity of the myocardial points a and b and d the distance between these two points [27]. The temporal integral of SR gives myocardial strain. As the distance d is measured in the deformed state, this echocardiographic technique measures Eulerian strain.

The SR results can be represented in an M-mode image or matched with a 2D echocardiographic image. With the M-mode representation, a curve of the SR and strain during a cardiac cycle can be obtained (see Figure 1-15).

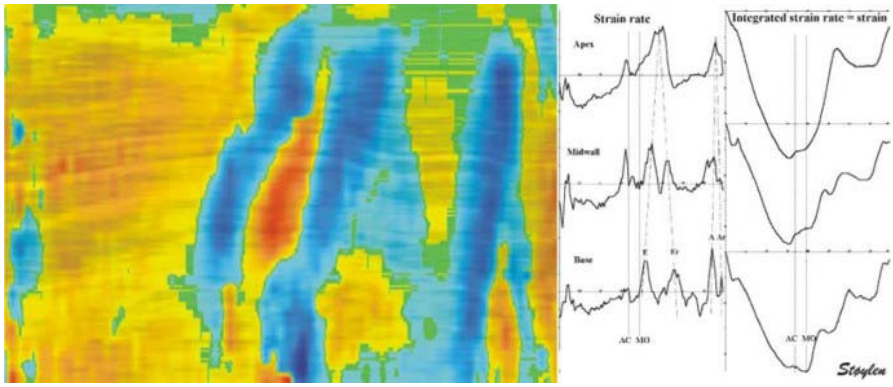

Figure 1-15 Example of a SRI of an healthy interventricular septum

On the left: M-mode SRI of an healthy interventricular septum (apex on the top and base on the bottom). On the right: plots of the SR and strain at the apical, mid and basal septum during a cardiac cycle. Yellow to red represents shortening during systole and cyan to blue represents lengthening during diastole. Adapted from [16].

This echocardiographic technique allows the quantification of regional systolic and diastolic functions with a high temporal resolution. However, as velocities v_a and v_b are computed using Doppler principle, SRI still has the disadvantage of not being able to compute myocardial deformation in all segments, because the velocity can only be measured in the direction of the ultrasound beam. Consequently, only the longitudinal strain can be computed in all segments using the apical 2, 3 and 4 chamber views [27], the radial strain can only be computed in the posterior wall and the circumferential strain only in the lateral wall [17].

Additionally, out-of-plane motion of the heart is not taken into account in SR computation, which can lead to errors in the strain results [20].

1.4.1.6. Speckle tracking imaging

The most recent echocardiographic technique, Speckle Tracking Imaging (STI), aims to automatically quantify regional deformation of the myocardium without using Doppler principle and consequently, to be independent of the insonation angle.

Interference of ultrasound beams in the myocardium creates speckle patterns. These patterns are characterized by having a random nature, which ensures their exclusivity and stability during myocardial motion [14, 28]. The tracking of these speckles is performed by minimizing the sum of absolute differences between a region of interest at two successive time frames (see Figure 1-16) [28].

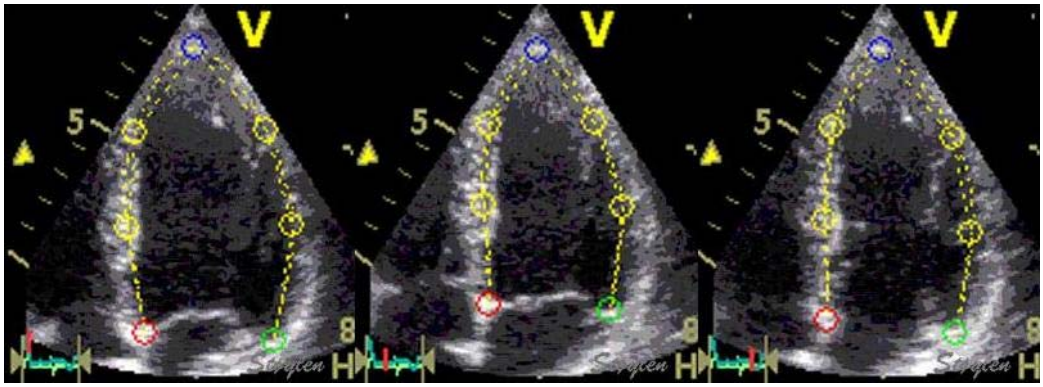

Figure 1-16 Result of the application of Speckle Tracking technique to a LV (LA view).
In this figure three phases of the cardiac cycles are represented with the positions of the tracked region of interest represented by coloured circles. Adapted from [16]

STI can automatically assess strain, SR, velocities and displacement of the cardiac wall. The most promising clinical applications of STI are quantitative assessment of LVF, diagnosis of myocardial infarction, estimation of LV torsion, quantification of dyssynchrony and prediction of response to cardiac resynchronization therapy (CRT) [29]. This technique has the advantage of being direction independent, allowing the tracking in longitudinal and transversal directions, and of being automatic and, consequently, independent of technicians expertise, which decreases interobserver variability. The main limitations of STI are that the out-of-plane motion of the heart is not taken into account, and that large displacements between two successive time frames are not accurately tracked. This technique is still in development, but published results show a good agreement with sonomicrometry values and MRI tagging [28, 29].

1.4.1.7. 3D echocardiography

In the beginning, 3D echocardiograms were obtained by combining several 2D images. These 3D anatomical images of the heart allowed the assessment of LVF, however, the inherent technical difficulties in the acquisition of all the data and the time consuming post-processing hindered its clinical application. Presently, it is possible to acquire real time 3D echocardiograms, using transducers with a grid of ultrasound elements (see Figure 1-17) [30].

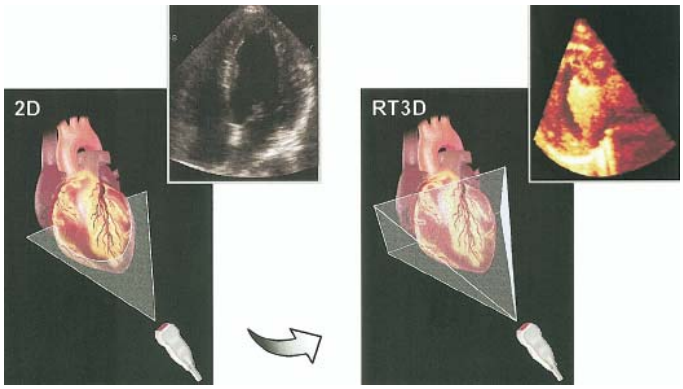

Figure 1-17 Example of a 2D and real time 3D (RT3D) echocardiogram. Adapted from [31]

With real time 3D echocardiography it is possible to assess LVF with a higher accuracy than with 2D echocardiography, as no geometric assumptions are made to compute LV volumes [15, 31]. The real time 3D modality also gives the possibility to evaluate RV function, left atrium volume, RA volume and cardiac valves [30].

1.4.2. Cardiac Computed Tomography

Computed Tomography (CT) is a non-invasive imaging modality that acquires several X-ray images around an axis of rotation. With appropriate reconstruction algorithms, filtered back projection or iterative reconstruction algorithms, 2D and 3D attenuation maps of the bones, muscles, fat and organs inside the field-of-view (FOV) are obtained. The application of CT to cardiac imaging has been hampered by the mechanical inertia of the scanner systems. Originally, CT scanners were composed by an x-ray tube with pencil beam geometry and a single detector that translated and rotated all over the FOV. For example, with this type of scanner, to acquire a FOV with 24 cm it was necessary to collect 28.800 rays [13], which resulted in a minimum temporal resolution of about 2.5 minutes, a value too high for cardiac imaging.

Specifically thinking about cardiac applications, a new type of scanner was developed: the electron-beam scanner or cine-CT. With this scanner, the X-rays are not produced in a traditional X-ray tube. Instead, the electron beam is electro-magnetically deflected towards

fixed tungsten anode targets located around the patient, and the emitted X-rays are then detected by detector rings located on the opposite side (see Figure 1-18). With this scanner, there are no moving parts, which results in scan times of about 50-100 ms [32].

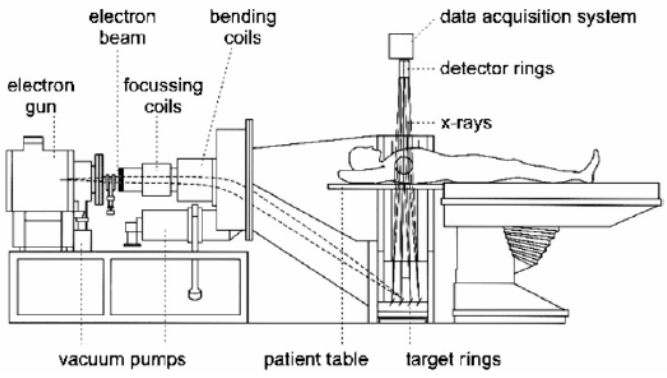

Figure 1-18 Schematic representation of an Electron-beam CT scanner. Adapted from [33].

Electron-beam CT (EBCT) is typically used to detect calcium in the walls of the coronary arteries. Coronary calcium scoring (CCS) is currently the most accurate method for the early detection of coronary atherosclerosis, as it has the ability to detect atherosclerotic lesions even before hemodynamic impairment emerges [34]. The quantification of calcium in the walls of the coronary arteries is possible without use of intravascular contrast, since calcium has a high x-ray attenuation value [32].

The state-of-art of the mechanical CT scanner is a scanner with multi-detector rings. These multi-detector CT (MDCT) scanners combine a lower rotation time of the x-ray tube (0.37 seconds per rotation) with simultaneous acquisition of several slices per rotation (up to 64 slices) [22]. With a 64-slice CT scanner it is possible to achieve in-plane spatial resolutions up to 0.4×0.4 mm^2 [32], through plane spatial resolutions of 0.6-0.8 mm [35] and temporal resolutions up to 165 ms [36].

Cardiac CT is mainly used to assess coronary arteries using coronary CT angiography, and more recently, to assess global and regional LVF. A new possible clinical application is to assess myocardial viability, through the detection of myocardial infarctions using the first pass or the delayed enhancement methods [37].

The main advantages of this cardiac imaging technique are the ability to provide coronary CT angiography images of the wall vessels in addition to the lumen, which allows the detection of noncalcified coronary plaques [34, 36]; to be non-invasive, which makes coronary CT angiography a good alternative to the traditional coronary angiography; to be able to assess LVF of patients with pacemakers and other metal implants, who cannot undergo cardiac MR exams (the gold standard to evaluate LVF [15, 36, 38]); to combine LVF assessment with

coronary CT angiography, without additional contrast or prolonged data acquisition [15, 38-40]; and to have a higher spatial resolution and thinner slice thickness than MR images, which can reduce partial volume effects [38]. Despite all these advantages, cardiac CT is usually not the first choice in clinical practice. This is due to the exposure to high doses of radiation during an exam, which can go from 1 mSv for the CCS with EBCT [32, 35] (equivalent to 0.4 years of exposure to background radiation of 2.5 mSv per year) to 10 mSv [41] for the assessment of myocardial viability (equivalent to 4 years of exposure to background radiation of 2.5 mSv per year). Additionally, coronary CT angiography is limited to regular heart rhythms and low heart rates in order to minimize cardiac motion artefacts [34, 36].

An example of an anatomical image of the heart acquired with a MDCT is presented in Figure 1-19. This image shows the detail that is possible to obtain with the high spatial resolution that characterizes this imaging technique.

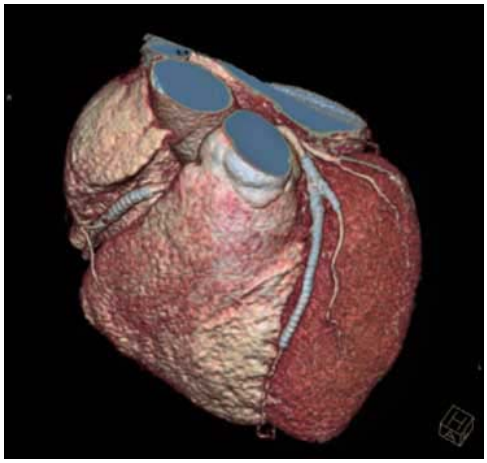

Figure 1-19 Anatomical image obtained with a MDCT.
The spatial resolution is equal to 0.4 mm. Adapted from [22]

Cardiac CT is presently a topic of intensive research, with the development of faster scanners, as the 256-slices MDCT and the dual source CT scanners, which will decrease the acquisition time and, consequently, reduce motion artefacts at high heart rates and allow shorter breath hold periods.

1.4.3. Nuclear cardiac imaging

Nuclear cardiac imaging is the branch of cardiac imaging that uses radioactive tracers to perform functional images of the heart. Single-Photon Emission Computed Tomography (SPECT) and Positron Emission Tomography (PET) are nuclear tomographic imaging techniques, which differ in the type of radioisotope used to label the tracer.

SPECT uses gamma-emitting radioisotopes, with ^{201}Tl, ^{99m}Tc being the most common for cardiac applications [42]. SPECT images depict the distribution of gamma radiation detected

by one or more gamma cameras that rotate around the patient. In clinical routine, cardiac SPECT is often used to image myocardial perfusion [42, 43]. With this type of exam, ischemic regions resultant from coronary arteries stenosis are detected with high accuracy, allowing the early diagnosis and evaluation of CAD [44, 45]. The acquisition of perfusion SPECT images can be synchronized with the R-wave of the ECG. This modality, designated by gated-SPECT, acquires several perfusion images in one cardiac cycle. With the systolic and diastolic images, it is possible to evaluate LVF, LVEF and regional wall thickening. By combining this functional information with myocardial perfusion information, gated-SPECT can also assess myocardial viability, by differentiating scarred tissue (low perfusion associated with absent wall motion) from attenuation artefacts (low perfusion associated with preserved wall motion) [42, 46-48]. The main disadvantages of cardiac SPECT are the use of gamma radiation, the relatively long scanning time, the low spatial resolution (around 15 mm [49]) and the attenuation artefacts, mainly in the inferior wall [50].

The principle of PET is to use radiotracers that closely resemble natural substances used by the body to obtain functional images of the processes where these substances participate. The radiotracers used are labelled with positron-emitting radioisotopes, with $^{13}NH_3$, ^{82}Rb and ^{18}F-FDG being the most common in cardiac applications [45]. PET images are constructed from the spatial information provided by the detected coincidence photons resultant from the annihilation reactions between the emitted positrons and electrons. The most common cardiac applications of PET are quantification of myocardial perfusion (with $^{13}NH_3$ and ^{82}Rb); assessment of myocardial viability (with ^{18}F-FDG), by identifying flow-metabolism mismatch; and prediction of improvement of regional function after revascularization intervention, by identifying hibernating myocardium. However, besides having a higher spatial resolution than SPECT and allowing the quantification of physiologic parameters [45], PET is still not widespread in clinical routine. The main reasons to restrict PET mostly to research issues are its high cost and the necessity of having an on-site cyclotron to prepare the short living radiotracers [47, 49].

1.4.4. Multimodal cardiac imaging

Recently, CT scans have been combined with SPECT and PET systems. These new multimodal imaging techniques, designated by SPECT/CT and PET/CT, allow the fusion in a single image of the anatomical information provided by the CT with the functional information provided by the SPECT or PET. Although these techniques have been mostly used in oncology, their application in cardiac imaging offers several advantages, namely, the use of CT scan to perform attenuation correction and to perform CCS together with functional PET image [47, 49].

1.5. FUNDAMENTS OF MAGNETIC RESONANCE IMAGING

1.5.1. Nuclear Magnetic Resonance

Nuclear Magnetic Resonance (NMR) is the basis of MRI and is explained in this section. NMR was discovered independently in 1946 by Bloch and Purcell [51]. This physical phenomenon can be observed in nucleus with a spin angular momentum ($\vec{J}$) different from zero, which results from an odd number of protons and/or neutrons. Associated with this angular momentum is a dipolar magnetic momentum $\vec{\mu}$, given by:

$$\vec{\mu} = \gamma \vec{J} \qquad \text{Equation 1-3}$$

with γ the gyromagnetic ratio.

There are several elements that have an angular momentum different from zero. However, not all are suitable for MRI. Besides a magnetic moment, the candidates for MRI must have a high natural and biological abundance. The natural abundance of an isotope is its fraction relative to all the isotopes of the considered chemical element. The biological abundance corresponds to the fraction of this element in the human body. A list of possible candidates for MRI is presented in Table 1-1:

Nuclei	Net Spin	γ (MHz/T)	Natural abundance (%)	Biological abundance (%)
^{1}H	1/2	42.58	99.99	63.00
^{31}P	1/2	17.25	100.00	0.24
^{23}Na	3/2	11.27	100.00	0.041
^{14}N	1	3.08	99.63	1.50
^{13}C	1/2	10.71	1.11	9.40

Table 1-1 Elements candidates for MRI.
γ - gyromagnetic ratio. Adapted from [52]

From these candidates, the element/isotope most used in MRI is the hydrogen proton, ^{1}H, since it has the highest biological abundance. This value is explained by the presence of this proton in the water molecules, which constitute 60% of the human body, and in fat tissue ($-CH_2-$).

For MRI, the human body can be seen as a pool of protons of ^{1}H spinning around their axes, usually designated by spins. As these axes are randomly distributed in space, the sum of all $\vec{\mu}$, known as the net magnetization $\vec{M}$, is zero. In order to obtain an image with MR, a non-zero net magnetization is necessary, which is achieved by applying a magnetic field to these spins (see Figure 1-20).

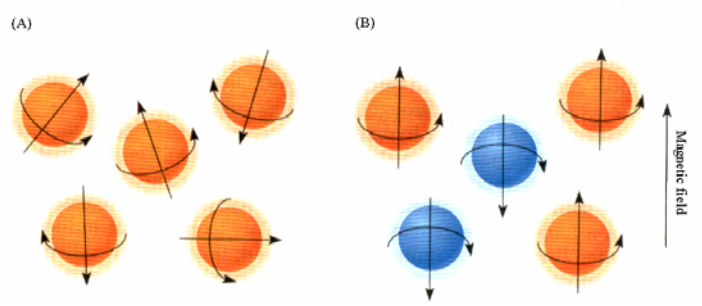

Figure 1-20 (A) ^{1}H spinning randomly around their axes. (B) ^{1}H aligned with magnetic field axis. Adapted from [53]

1.5.1.1. Static Magnetic Field $\vec{B}_0$

When a constant magnetic field $\vec{B}_0$ is applied to a group of spins, two phenomena occur (Figure 1-21):

- spin axes align with $\vec{B}_0$
- spins precess around $\vec{B}_0$ axis at a well defined frequency.

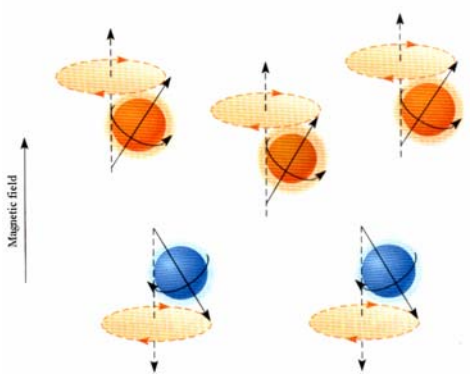

Figure 1-21 Spins aligned with the magnetic field axis and precessing around it. Adapted from [53]

The alignment of all spins with $\vec{B}_0$ originates a net magnetization $\vec{M}$ different from zero. This phenomenon can be explained under the light of quantum mechanics. From quantum mechanics, it is known that the proton can take two spin values ($\vec{S}$): +1/2 (parallel state) and –1/2 (anti-parallel state). The difference between these two energy levels is given by:

$$\Delta E = h\nu = h\frac{\gamma}{2\pi}B_0 \qquad \text{Equation 1-4}$$

with the parallel state corresponding to the lower energy level and the anti-parallel state to the higher energy level (see Figure 1-22). In this equation *h* is Plank constant.

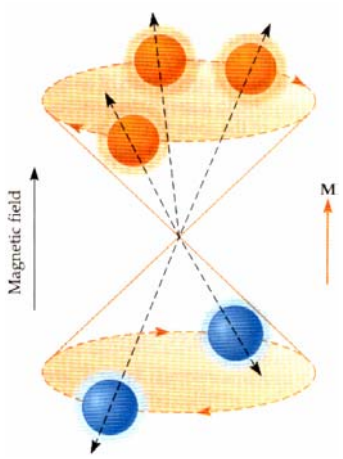

Figure 1-22 Possible energy levels of the spins.
The lower energy level corresponds to the parallel state and the higher energy level to the anti-parallel state. Adapted from [53]

This equation shows that the electromagnetic wave necessary to transfer a spin from the lower energy level to the higher energy level has to have a frequency proportional to the gyromagnetic ratio and to the magnetic field amplitude. This frequency in angular terms is designated by Larmor frequency and is given by:

$$\omega = \gamma B_0 \,(\text{rad/s}) \qquad \text{Equation 1-5}$$

This equation is known as the Larmor equation, and underpins the whole NMR phenomenon.

The non-zero net magnetization $\vec{M}$ is the result of more spins being in the parallel state than in the anti-parallel state. The ratio of the number of spins in both states is given by the Boltzmann distribution:

$$\frac{n_-}{n_+} = e^{-\Delta E / KT} \qquad \text{Equation 1-6}$$

with n_- and n_+ the number of spins in the anti-parallel and parallel state respectively, T the absolute temperature and K the Boltzmann constant (1.3806×10^{-23} J/K^{-1}).

The precession of the spins around the $\vec{B}_0$ axis is better explained using an analogy with the gravitational field. As it is well known, a spinning top does not align with the earth's gravitational field axis. Instead, its axis of rotation describes a circle perpendicular to the axis of the gravitational field, performing a gyroscopic motion. This motion is analogous to the precession of the net magnetization vector around $\vec{B}_0$. The equation that describes this motion is:

$$\frac{d\vec{M}}{dt} = \gamma \vec{M} \times \vec{B}_0 \qquad \text{Equation 1-7}$$

The solution of this differential equation in Cartesian coordinates is:

$$\vec{M}(t) = (M_x \cos\omega t + M_y \sin\omega t)\vec{e}_x + (M_y \cos\omega t - M_x \sin\omega t)\vec{e}_y + M_z\vec{e}_z \qquad \text{Equation 1-8}$$

with ω the Larmor frequency (Equation 1-5) and $\vec{e}_x, \vec{e}_y, \vec{e}_z$ the unit vectors of the Cartesian coordinate system. This equation represents the circular motion of $\vec{M}$ around the $\vec{B}_0$ axis. It also shows that $\vec{M}$ precesses around the external magnetic field $\vec{B}_0$ at the frequency of the electromagnetic pulse necessary to transfer the spins from the parallel to the anti-parallel energy state.

1.5.1.2. Radiofrequency Magnetic Field B_1

To measure the net magnetization resultant from the application of a constant magnetic field $\vec{B}_0$ to a group of spins, it is necessary to disturb the system. Such perturbation is achieved by applying a magnetic field in the transverse plane (perpendicular to $\vec{B}_0$).

The simultaneous application of $\vec{B}_1$ and $\vec{B}_0$ results in a combined precessional motion of the net magnetization, which in the laboratory reference frame consists in a spiral motion, known as nutation (Figure 1-23b).

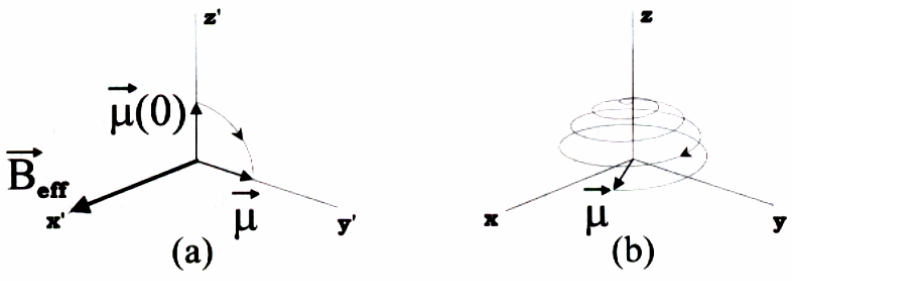

Figure 1-23 Motion of the magnetization vector after application of a 90º radio-frequency pulse (a) in the rotating reference frame and (b) in the laboratory reference frame. Adapted from [51]

This motion can be simplified if observed from a reference frame rotating about $\vec{B}_0$ at frequency ω_0 (Figure 1-23a). In this reference frame, the total field felt by the spins is designated by $\vec{B}_{eff}$ and is given by:

$$\vec{B}_{eff} = \left(B_0 - \frac{\omega}{\gamma}\right)\vec{e}_z + B_1\vec{e}_{x'} \qquad \text{Equation 1-9}$$

with the unprimed unit vectors corresponding to the laboratory reference frame and the primed unit vectors to the rotating reference frame. The net magnetization vector on the rotating reference frame rotates around $\vec{B}_{eff}$ with a frequency ω_{eff} given by:

$$\omega_{eff} = \sqrt{(\omega_0 - \omega)^2 + \omega_1^2} \qquad \text{Equation 1-10}$$

Equation 1-9 and Equation 1-10 show that when ω is equal to the Larmor frequency ω_0, the *z*-component of $\vec{B}_{eff}$ is null, $\vec{B}_{eff} = \vec{B}_1$ and $\omega_{eff} = \omega_1$. So, the most efficient way to tip the magnetization vector to the transverse plane is to apply a magnetic field perpendicular to $\vec{B}_0$ in resonance with the spins precession motion around the *z*-axis. Therefore, the frequency of the $\vec{B}_1$ field must be equal to the Larmor frequency of the ^{1}H protons at the field $\vec{B}_0$. This magnetic field $\vec{B}_1$ is designated by radio-frequency (RF) pulse. The tip angle resultant from the application of an RF pulse is given by:

$$\theta = \gamma B_1 T \qquad \text{Equation 1-11}$$

with *T* the time during which $\vec{B}_1$ is applied and θ the tip angle.

1.5.1.3. Signal measurement

After the application of an RF pulse to the net magnetization vector, the net magnetization vector is at an angle θ with the *z*-axis, and precesses with frequency ω_0 around it. This results in a signal that can be measured by a receiver coil placed in the transverse plane, because the precessional motion of this magnetization vector on this plane causes a magnetic flux in the receiver coil that varies with time. By Faraday's law of induction, this change of flux induces an electromotive force (emf) in the receiver coil given by:

$$emf = -\frac{d\Phi}{dt} \qquad \text{Equation 1-12}$$

with Φ the magnetic flux through the coil.

The time varying signal detected by the receiver coil is designated by Free Induction Decay (FID), and is the basic signal measured in a NMR experiment.

It is important to realize that only the transverse component of the net magnetization vector induces an emf in the receiver coil, which explains why RF pulses have to be applied to create an MR signal.

Often, the RF pulse is generated with the built-in body coil, while the MR signal is measured by dedicated coils that more closely fit the area of interest (cardiac, extremities, etc).

1.5.1.4. Spin relaxation

The application of the RF pulse to the net magnetization vector $\vec{M}$, flips this vector by an angle θ towards the transverse plane. Once the RF pulse is turned off, the signal decays quickly as the result of two phenomena: longitudinal relaxation and transverse relaxation.

Longitudinal relaxation also designated by spin-lattice relaxation, results from the transfer of the energy absorbed during the application of the RF pulse to the surrounding lattice. By emitting this electromagnetic energy, the spins that are in the high energy state (anti-parallel) decay to the low energy state (parallel), and increase the longitudinal component of the net magnetization vector. The longitudinal relaxation is mathematically described by:

$$M_z(t) = M_0\left(1 - e^{-t/T_1}\right) \qquad \text{Equation 1-13}$$

with T_1 the longitudinal relaxation time and M_0 the original magnetization. As the longitudinal relaxation is related with the transition of spins from population n_+ to population n_-, the time necessary to recover M_0 increases with $\vec{B}_0$ strength (see Equation 1-4 and Equation 1-6). Additionally, the transfer of energy to the surrounding lattice necessary for this transition is more efficient when the natural frequency of the spins is closer to the Larmor frequency. Consequently, T_1 also depends on the atoms to which the ^{1}H protons are attached to or close to.

The transverse relaxation also designated by spin-spin relaxation, results from the interaction of the spins with their neighbours and from the inhomogeneity of the magnetic field. These effects are in addiction to the fact that the longitudinal relaxation automatically reduces the transverse component of the magnetization. In the case of spin-spin interaction, each ^{1}H proton in the tissue "feels" a slightly different magnetic field, due to the influence of the magnetic field of its neighbours. Consequently, different spins precess with different Larmor frequencies, leading to dephasing of the transverse component of the individual spins. In this process the transverse component of the resultant macroscopic magnetization decays to zero. This situation is mathematically described by the formula:

$$M_{xy}(t) = M_0 e^{-t/T_2} \qquad \text{Equation 1-14}$$

with M_0 the original magnetization and T_2 the transverse relaxation time. T_2 is an intrinsic characteristic of the tissue, and is longer for tissues for which the ^{1}H protons dephase more slowly. A similar process occurs in the presence of main field inhomogeneities. The time constant that describes both causes of spin dephasing is T_2*.

1.5.1.5. Bloch equation

The MR phenomenon can be mathematically described by the equation:

$$\frac{d\vec{M}}{dt} = \gamma\vec{M} \times \vec{B} + \frac{1}{T_1}\left(M_0 - M_z\right)\vec{e}_z - \frac{1}{T_2}\left(M_x\vec{e}_x + M_y\vec{e}_y\right) \qquad \text{Equation 1-15}$$

with $\vec{B}$ the magnetic field applied to the spins, M_0 the original magnetization of the spins, M_i the components of the magnetization vector in the Cartesian coordinate system, and $\vec{e}_x, \vec{e}_y, \vec{e}_z$ the unit vectors of this coordinate system.

This equation, known as the Bloch equation, summarizes the effect of the application of a magnetic field to a group of spins. The net magnetization vector precesses around the axis of the magnetic field at the Larmor frequency, with the relaxation processes of its longitudinal component governed by T_1 and of its transverse component by T_2. This equation constitutes the theoretical foundation for all MRI experiments.

1.5.2. Magnetic Resonance Imaging

Although the NMR phenomenon was known since 1946, only in 1972 was acquired the first MR image. The bridge between NMR and its potential biological and physical applications was established by the American physicist Paul Lauterbur, and consisted in spatial encoding the magnetic field using spatial gradients. In 1976 the physicist Peter Mansfield made another fundamental contribution to the development of MRI by developing the echo-planar imaging (EPI) technique. EPI considerably reduced the acquisition time and opened the doors to the clinical application of MRI. The importance of the work developed by these two physicists was recognized in 2003, with the attribution of the Nobel Prize in Physiology or Medicine. Following their seminal, numerous developments have been made and nowadays MRI is a non-invasive imaging technique widely used in clinical routine. The main advantage of this imaging technique is the use of non-ionizing radiation (see Figure 1-24), since MR images result from the spatial variation in phase and frequency of the RF energy absorbed and emitted by the patient.

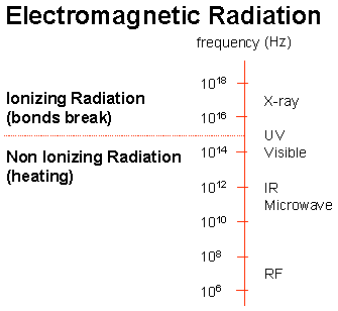

Figure 1-24 Range of frequencies of ionizing and non-ionizing radiation.
The electromagnetic radiation used in MRI is on the radio-frequency domain, which is a non-ionizing radiation. Adapted from [52]

In the next section the physics behind this imaging technique are presented.

1.5.2.1. Gradient magnetic field

Up to now the effect of two types of magnetic fields on spins was described:

- the main constant magnetic field $\vec{B}_0$ created by the magnet, which aligns the spins with its axis creating a net magnetization vector M_0

- the RF pulse $\vec{B}_1$ created by the transmitter-receiver coil, which tips M_0 to the transverse plane allowing its measurement

The signal measured after application of $\vec{B}_1$ results from the entire sample of spins. To create a medical image, it is necessary to have a spatial correspondence between the measured signal and the region of the body being imaged. This is achieved by applying a gradient magnetic field $\vec{G}$ with a gradient coil in addition to the main magnetic field $\vec{B}_0$. As a result, the effective $\vec{\mathrm{B}}$ depends on the position inside the magnet and the spins at different positions precess with different Larmor frequencies.

The total magnetic field experienced by the spins is given by:

$$\vec{B}(\vec{r},t) = \left(B_0 + \vec{G}(t)\cdot\vec{r}\right)\vec{e}_z \qquad \text{Equation 1-16}$$

and the Larmor frequency by:

$$\omega(\vec{r}) = \omega_0 + \gamma\vec{G}(t)\cdot\vec{r} \qquad \text{Equation 1-17}$$

In this case, the equation for the transverse magnetization (Equation 1-14) takes the form:

$$M_{xy}(\vec{r},t) = M_{xy0}(\vec{r})e^{-t/T_2}e^{-i\omega_0 t}e^{-i\gamma\int_0^t \vec{G}(\tau).\vec{r}\,d\tau} \qquad \text{Equation 1-18}$$

This equation shows that the transverse magnetization at a given point in space and time $M_{xy}(\vec{r},t)$ depends on the original transverse magnetization in this position, on the signal loss due to spin-spin interactions, on the accumulated phase due to the main magnetic field and on the accumulated phase due to gradient field.

1.5.2.2. The MR signal

The MR signal measured by the receiver coil corresponds to the sum of all transverse magnetization vectors inside the imaged volume, and it is described by the formula:

$$S(t) = \int_{vol} M_{xy}(\vec{r},t)dV = \iiint M_{xy0}(\vec{r})e^{-t/T_2}e^{-i\omega_0 t}e^{-i\gamma\int_0^t \vec{G}(\tau).\vec{r}\,d\tau}\,dxdydz \qquad \text{Equation 1-19}$$

This equation can be simplified if the following considerations are taken into account. First the term $e^{-i\omega_0 t}$ can be dropped out as the scanners demodulate the signal with the Larmor frequency. Secondly, in this thesis only 2D images will be considered. The resultant equation has then the simpler form:

$$S(t) = \iint M_{xy0}(x,y)e^{-t/T_2}e^{-i\gamma\int_0^t (G_x(t)x+G_y(t)y)dt}\,dxdy \qquad \text{Equation 1-20}$$

This equation describes the measured MR signal from most of the imaging methods.

1.5.2.3. Slice selection and spatial encoding

To build an MR image, three different types of magnetic field gradients are applied:

- slice select gradient
- phase-encoding gradient
- read-out or frequency-encoding gradient

The goal of the slice select gradient is to excite the spins of a thin slice of the imaged 3D sample. The slice selection is achieved by applying a linear gradient field perpendicular to the plane of the slice to be acquired, simultaneously with the RF pulse $\vec{B}_1$. Consequently, only the spins with a Larmor frequency that falls within the bandwidth of the RF pulse are excited (see Figure 1-25).

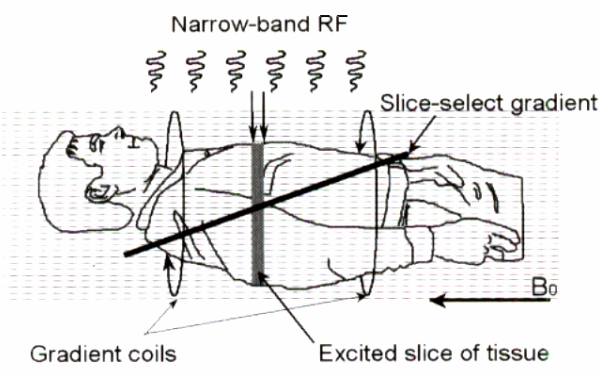

Figure 1-25 Principle of the slice select gradient.
Adapted from [51]

The thickness of the excited slice depends on the bandwidth of the RF pulse and on the magnitude of the slice select gradient. This gradient can be applied in the *z*-direction, leading to a slice parallel to the *x*-*y* plane (transverse slice), in the *x*-direction resulting in a slice parallel to the *y*-*z* plane (sagittal slice), and in the *y*-direction which results in a slice parallel to the *x*-*z* plane (coronal slice) (see Figure 1-26). By combining the three gradients, a slice in any arbitrary orientation can be selected.

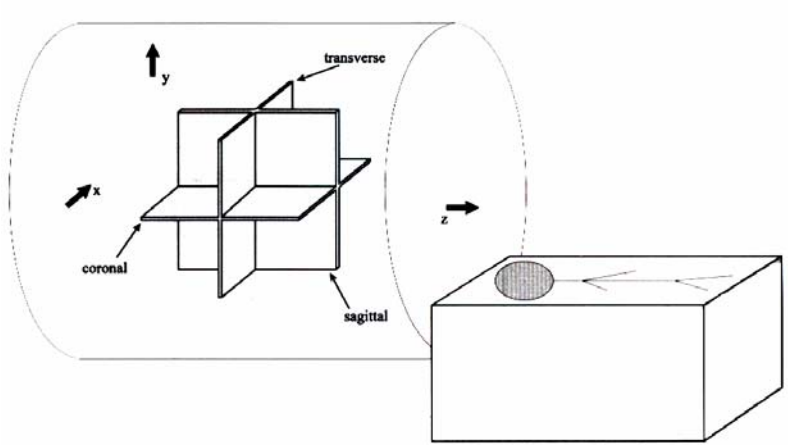

Figure 1-26 Orientation of the transverse, coronal and sagittal image planes. Adapted from [51]

The signal obtained from this slice corresponds to the sum of the transverse magnetization of all the voxels inside this slice. However, it is still necessary to differentiate the different voxels. This spatial encoding is performed by the phase encoding and frequency encoding gradients. The phase encoding gradient is applied before data acquisition and its effect is to make the main magnetic field vary along this axis. After the gradient is turned off, the voxels at different positions in this direction have different phases, turning them distinct from each other. During data acquisition a gradient in the read direction is turned on and the voxels at different positions in this direction precess around the magnetic field with a different frequency. At the end, each voxel inside the slice is characterized by a different Larmor frequency and phase.

1.5.2.4. K-space

Equation 1-20 for the transverse magnetization can be rewritten in the simpler form:

$$S(t) = \int_x \int_y M_{xy0}(x,y) e^{-i2\pi k_x(t)x} e^{-i2\pi k_y(t)y} dxdy \qquad \text{Equation 1-21}$$

using the following notation:

$$k_x(t) = \frac{\gamma}{2\pi} \int_0^t G_x(\tau) d\tau$$
$$k_y(t) = \frac{\gamma}{2\pi} \int_0^t G_y(\tau) d\tau \qquad \text{Equation 1-22}$$

With the equation in this form it is easy to recognize that the MR signal is the Fourier transform of the transverse magnetization. $k_x(t)$ and $k_y(t)$ are the spatial frequency space units. This frequency space is designated by *k*-space.

A schematic representation of the relation between *k*-space and image space is presented in Figure 1-27.

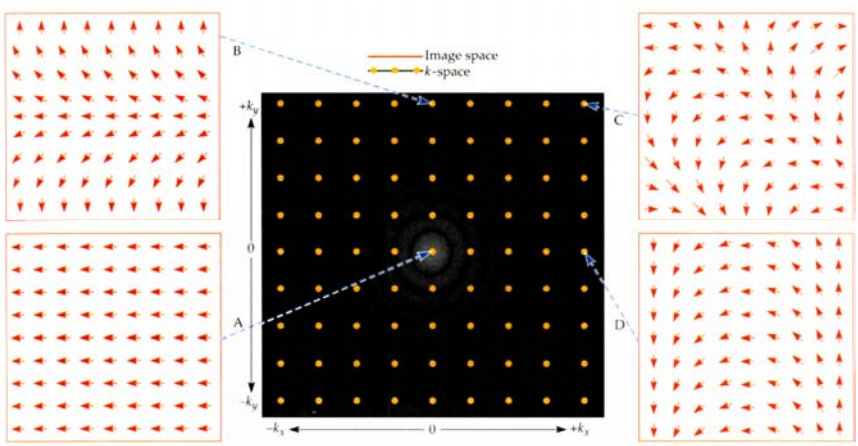

Figure 1-27 Relation between image space and frequency space (*k*-space). Adapted from [1]

This scheme shows that there is no direct correspondence between a point in *k*-space and a voxel in image space and that each point in *k*-space corresponds to a different acquisition instant and has a contribution from all voxels inside the slice.

An example of how the *k*-space is filled in for a gradient echo RF pulse (see Section 1.5.3.2.) is presented in Figure 1-28.

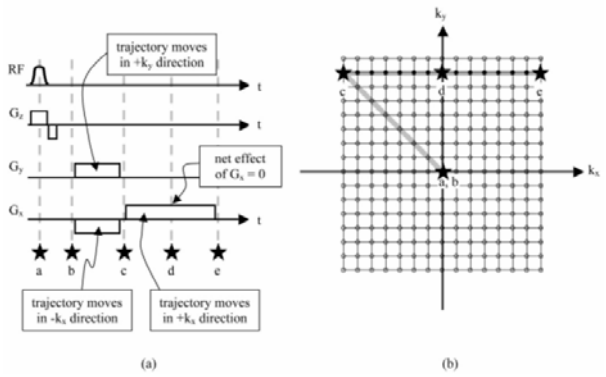

Figure 1-28 (a) Timing diagram of the gradient echo pulse sequence. (b) Corresponding *k*-space trajectory. Adapted from [54]

The central point in the *k*-space *(a,b)* is always the starting point of the *k*-space trajectory and corresponds to the instant when both phase and frequency gradients are turned off. As in this instant all the spins are spinning in phase, this point has the maximum amplitude. When a positive phase encoding gradient G_y is applied (in the *y*-direction for example), the point moves along the $+k_y$ direction of *k*-space, with the row position dependent on the strength of G_y. When a negative frequency encoding gradient is applied (G_x), the point moves to the $-k_x$ direction in *k*-space. The simultaneous application of these two gradients results in the movement of the point *b* to point *c* in Figure 1-28b. To go from point *c* to point *e*, a positive G_x

is applied. This example shows that the position of each point in *k*-space is determined by the strength and/or duration of the phase and frequency encoding gradients. Stronger and/or longer gradients correspond to points further away from the central point in *k*-space. The points in the middle of *k*-space contain most of the signal and are responsible for the image shape and contrast. The points in the periphery contain the fine details of the image, determining its spatial resolution.

Relations between parameters that describe *k*-space and image space can be established. The relation between the sampling intervals in *k*-space (Δk_x and Δk_y where k_x runs from $-k_{x\,max}$ to $+k_{x\,max}$, and k_y runs from $-k_{y\,max}$ to $+k_{y\,max}$), sampling time Δt, and the size of the image in image space (FOV) is given by:

$$FOV_x = \frac{1}{\Delta k_x} = \frac{1}{\frac{\gamma}{2\pi} G_x \Delta t}$$
$$FOV_y = \frac{1}{\Delta k_y} = \frac{1}{\frac{\gamma}{2\pi} \Delta G_y t_y}$$

Equation 1-23

This means that a finer sampling in *k*-space results in a larger image. Voxel sizes δ_x and δ_y can be expressed as:

$$\delta_x = \frac{1}{2k_{x\,max}} = \frac{1}{\frac{\gamma}{2\pi} G_x T}$$
$$\delta_y = \frac{1}{2k_{y\,max}} = \frac{1}{\frac{\gamma}{2\pi} 2G_{y\,max} t_y}$$

Equation 1-24

In the above equation, T is the total sampling time, and t_y is the time that the G_y gradient is on, (assuming square gradient shapes).

1.5.3. Pulse sequences

The optimal use of MRI in clinical practice is highly dependent on the correct choice of the pulse sequence, which in turn is dependent on the tissues to be enhanced for the diagnosis of a pathologic process. A pulse sequence consists on a set of RF pulses and gradients applied to a sample of spins to produce a specific form of NMR signal. By changing the sequence parameters it is possible to change image contrast, Signal to Noise Ratio (SNR) and acquisition time. In this way, images weighted in T_1, T_2, T_2* or proton density can be obtained. There are numerous types of pulse sequences which have different names, depending on the scanner manufacturer (see Figure 1-29).

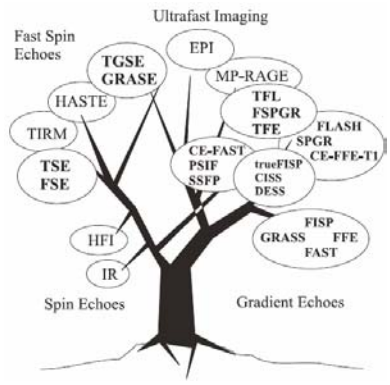

Figure 1-29 Schematic representation of pulse sequences denominations.
Inside each balloon it is shown the name given by each manufacturer to each pulse sequence. Adapted from [55]

All pulse sequences are usually organized in two groups: the spin-echo (SE) and the gradient-echo (GE) sequences. The main goal of sequence development is to obtain images with a good contrast and SNR in the shortest time possible. This is particularly important for cardiac imaging where long acquisition times lead to increased motion and breathing artefacts.

A survey of the existent sequences is beyond the aim of this chapter. This section describes the basic sequences SE and GE and their variants used for cardiac imaging, with special attention to the fast sequences used for cine cardiac imaging and cine cardiac imaging with myocardial tagging, the research topic of this thesis.

1.5.3.1. SE sequences

SE sequence is composed by a 90º RF pulse and a 180º RF pulse separated by TE/2, with TE the echo time. The timing diagram of this sequence is presented in Figure 1-30.

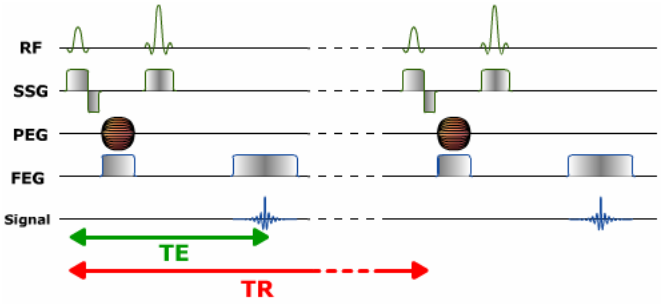

Figure 1-30 Timing diagram of the SE pulse sequence.
RF – Radio Frequency. SSG – Slice Select Gradient. PEG – Phase Encode Gradient. FEG – Frequency Encode Gradient. TE – Echo time. TR – Repetition time. Adapted from [56]

The effect of each of these RF pulses in the magnetization vector is represented in Figure 1-31.

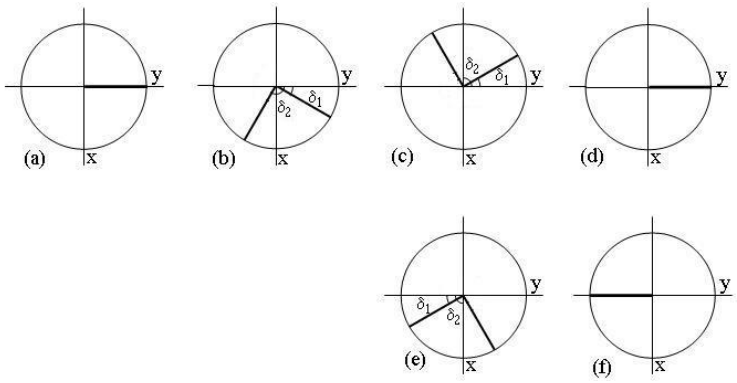

Figure 1-31 Effect of the 90º and 180º RF pulses of the SE sequence in the magnetization vector.

The 90º RF pulse is applied along the *x*-axis and tilts the magnetization vector to the transverse plane (Figure 1-31a). Due to T_2 and T_2* relaxation, the transverse magnetization starts to dephase (Figure 1-31b). The application of the 180º RF pulse refocuses the spins creating an echo at t = TE. This RF pulse can be applied either along the *y*-axis (Figure 1-31c) or along the *x*-axis (Figure 1-31e). In the first case the resultant echo aligns with the *y* direction (Figure 1-31d) and in the second case with the -*y* direction (Figure 1-31f). The application of the refocusing RF pulse, cancels out the field inhomogeneity effects, which means that the amplitude of the echo only depends on the spin-spin interactions (T_2), and true T_2 weighted images can be obtained.

The intensity of the echo measured at t = TE is given by:

$$S = N(H)\left[1 - e^{-TR/T_1}\right]e^{-TE/T_2} \qquad \text{Equation 1-25}$$

with *N(H)* the spin density.

This equation shows that the contrast of the image acquired with SE depends on TR and TE. In Table 1-2 the relations between TR and TE to obtain T_1, T_2 or proton density weighted images are shown.

Image contrast	TR (ms)	TE (ms)	Signal (Theoretical)
T_1W	Short (250-700)	Short (10-25)	$N(H)(1-e^{-TR/T_1})$
T_2W	Long (>2000)	Long (>60)	$N(H)(e^{-TE/T_2})$
PDW	Long (>2000)	Short (10-25)	N(H)

Table 1-2 Range of values of the pulse sequence parameters to obtain T_1, T_2, and proton density weighted images.

TR – Repetition time. TE – Echo time. T_1W – T_1-weighted. T_2W – T_2-weighted. PDW – Proton density weighted. N(H) – spin density. [57, 58]

The main disadvantage of this sequence is the long acquisition time required. For example, to acquire an image with 256 × 256 pixels with a TR = 600 ms (T_1 weighted image) it takes 2.56 minutes. If the acquired image is T_2 or proton density weighted this time is even higher. As these acquisition times are too long for cardiac imaging, SE sequences are not usually used in cardiac MRI. However, this acquisition time can be considerably reduced if the dead time between the echo acquisition (at t = TE) and the application of a new cycle of 90º and 180º RF pulses (at t = TR) is used. This is the basis of the fast SE sequences here presented.

1.5.3.1.1. Fast SE sequences

One of the fast SE sequences acquires several slices during the same TR by applying a train of 90º and 180º pulses. As these pulses select different regions of the patient, the image contrast should be preserved.

Another approach to reduce SE acquisition time is to acquire several lines of *k*-space during a single TR (see Figure 1-32).

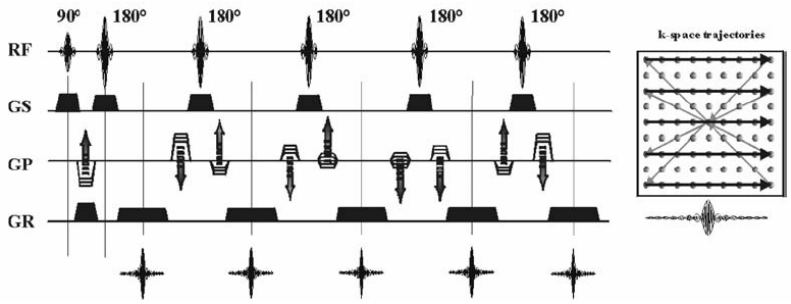

Figure 1-32 Timing diagram of a fast SE or turbo SE sequence with an example of *k*-space trajectories. Adapted from [59]

This sequence, designated by fast SE (FSE) or turbo SE (TSE) applies, after the 90º RF pulse, a train of 180º RF pulses with different amounts of phase encoding. Due to T_2 relaxation the amplitude of later echoes is smaller, which results in an image contrast lower than the image contrast obtained with conventional SE sequence. A possible solution to optimize image contrast is to acquire the bulk of the image information (central lines in *k*-space) with one of the first echoes (echoes with higher amplitude). The "effective" TE of this sequence is defined as the TE corresponding to the acquisition of the central area in *k*-space.

HASTE (Half Fourier Acquisition Single Shot Turbo Spin Echo) sequence is another fast SE sequence. In this case all the images are acquired in a single TR and the train of 180º refocusing RF pulses applied after the 90º RF pulse only fills in half of the *k*-space (see Figure 1-33). The remaining *k*-space is filled in using the symmetry properties of *k*-space. Assuming that the image is real (no imaginary components), *k*-space displays Hermitian conjugate symmetry. However, this is not strictly valid and a few additional lines of *k*-space have to be

acquired to account for symmetry imperfections [59]. In this case the acquisition time can be reduced by almost 50%. This sequence can be used to acquire cardiac images without gating. However, the resultant spatial resolution and SNR are low.

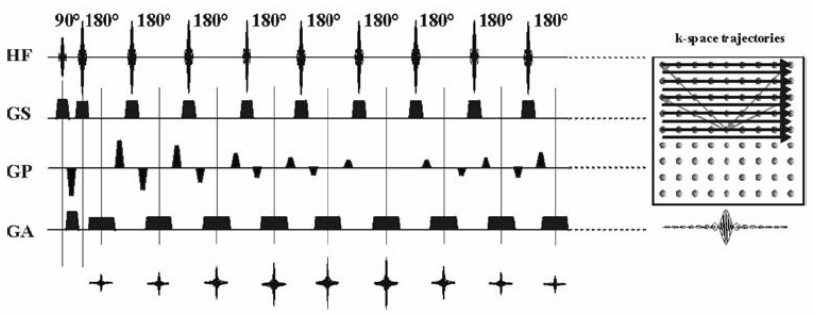

Figure 1-33 Timing diagram and *k*-space filling of the HASTE pulse sequence. Adapted from [59]

1.5.3.2. GE sequences

The main goal of the GE sequence is to speed up image acquisition. This is achieved by applying a partial flip angle. The diagram of a GE sequence is shown in Figure 1-34.

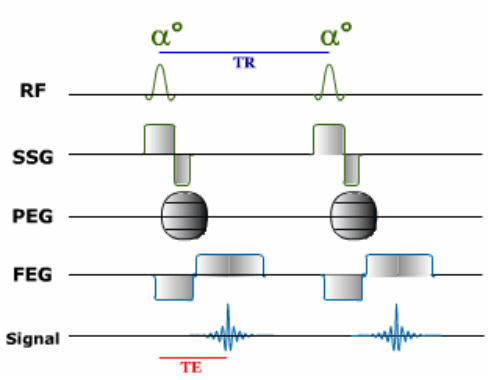

Figure 1-34 Timing diagram of a GE pulse sequence. RF – Radio Frequency. SSG – Slice Select Gradient. PEG – Phase Encode Gradient. FEG – Frequency Encode Gradient. TE – Echo time. TR – Repetition time. α - Flip angle. Adapted from [56]

As the magnetization vector is only partially flipped to the transverse plane the amplitude of the measured echo is smaller. On the other hand, the time required to fully recover the longitudinal magnetization is also smaller, allowing a shorter TR. With the GE sequence the dephasing and refocusing of the transverse magnetization vector are achieved by applying a gradient in the frequency encoding direction. This gradient has a negative lobe that dephases the spins in the transverse plane. After that, the spins are refocused with a positive lobe with the same duration. At the end of the positive lobe, an echo is obtained at TE. Contrarily to the 180º RF pulse in the SE pulse sequence, the refocusing gradient does not compensate for $\vec{B}_0$ inhomogeneities, which results in images that are dependent of T_2* decay.

The amplitude of the echo measured at TE is given by:

$$S = N(H)\left[1 - e^{-TR/T_1}\right] \cdot \sin\alpha \cdot \frac{e^{-TE/T_2^*}}{1 - \cos\alpha . e^{-TR/T_1}} \qquad \text{Equation 1-26}$$

with α the flip angle that ranges between 10º and 90º.

From this equation it is observed that the contrast of the images acquired with GE sequence depends on the flip angle and on TR and TE. For higher flip angles the images are more T_1 weighted while short TE leads to less T_2* weighting. Another difference between SE and GE sequence is the transverse magnetization at TR. With a SE sequence as TR is usually long enough to allow for complete longitudinal recovering and T_2 is smaller than T_1, the transverse magnetization vector has time to completely dephase and at TR is usually equal to zero. However, the GE sequence uses smaller TR to speed up image acquisition. Although the initial transverse magnetization is smaller due to the use of a flip angle smaller than 90º, the TR is often not long enough for the transverse magnetization to completely dephase. Consequently, at t = TR M_{xy} is different from zero, and accumulates over time until reaching a steady state after some cycles (~5T_1/TR) [60].

The standard GE sequence can be optimized to allow faster image acquisitions. Examples of rapid GE sequences are the Fast Imaging with Steady Precession (FISP), fast low-angle shot (FLASH) and balanced steady state free precession (SSFP). These rapid GE sequences are specially indicated for cine cardiac imaging.

1.5.3.2.1. Fast GE sequences

The fast GE sequences can be classified into three categories: spoiled GE, partially refocused GE and fully refocused GE.

The spoiled gradient recalled acquisition in the steady state (spoiled GRASS), or FLASH is a spoiled GE sequence that destroys the transverse magnetization vector after each echo using a spoiler RF and/or gradient. A diagram of this sequence is presented in Figure 1-35.

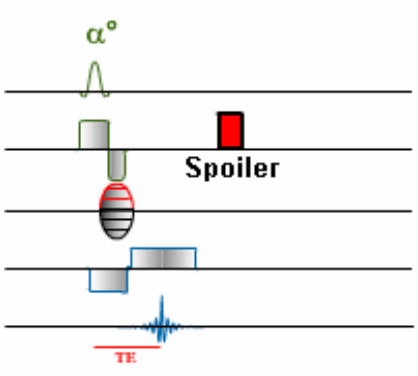

Figure 1-35 Timing diagram of a spoiled GE pulse sequence.
TE – Echo time. α - Flip angle. Adapted from [59]

With this sequence it is possible to obtain T_1 weighted images using short TR, short TE and a moderate to large flip angle. The image contrast obtained with spoiled GRASS/FLASH and its short acquisition time turn this sequence appropriate for MR angiography.

An example of a partially refocused GE is the FISP or GRASS. A diagram of this sequence is presented in Figure 1-36:

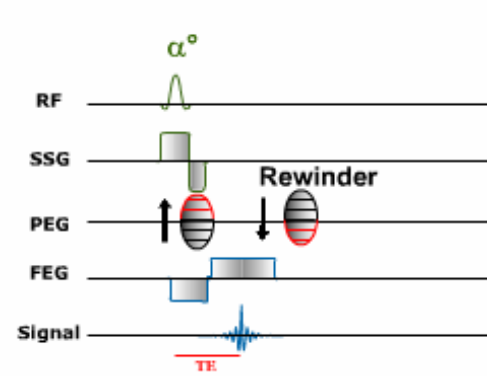

Figure 1-36 Timing diagram of a partially refocused GE pulse sequence.
RF – Radio Frequency. SSG – Slice Select Gradient. PEG – Phase Encode Gradient. FEG – Frequency Encode Gradient. TE – Echo time. α - Flip angle. Adapted from [59]

With GRASS/FISP, the steady state of the transverse magnetization is preserved by applying after the echo a gradient in the phase-encoding direction that cancels out the phase encoding gradient.

For a fully refocused GE sequence, which is the case of the balanced-SSFP or True-FISP, all gradients applied to the spins (slice selection, phase and frequency encoding) are refocused. This means that the initial and final magnetizations are almost the same, with some differences due to T_1 and T_2 relaxations (see Figure 1-37).

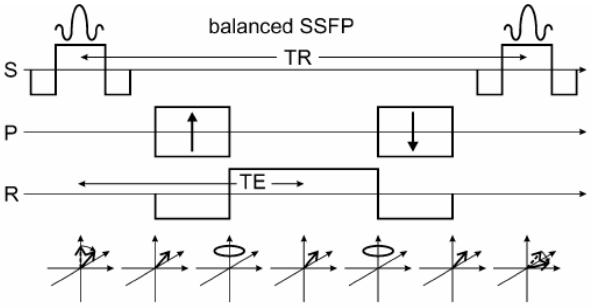

Figure 1-37 Effect of the RF pulses applied in a balanced-SSFP sequence on the transverse magnetization vector.
S- slice select gradient. P - Phase encode gradient. R – read encode gradient. TE – Echo time. Adapted from [60]

The diagram of a balanced-SSFP/True-FISP sequence is presented in Figure 1-38

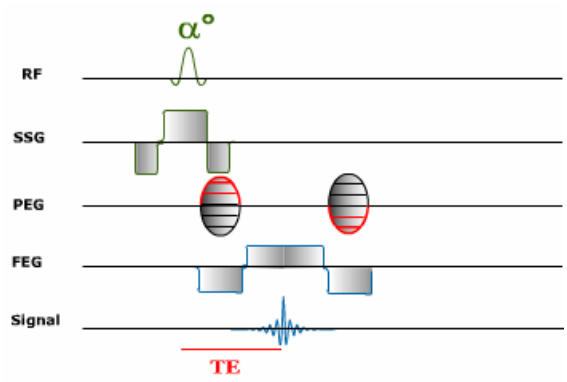

Figure 1-38 Timing diagram of a balanced-SSFP pulse sequence.
RF – Radio Frequency. SSG – Slice Select Gradient. PEG – Phase Encode Gradient. FEG – Frequency Encode Gradient. TE – Echo time. α - Flip angle. Adapted from [59]

The amplitude of the acquired signal is given by:

$$S = N(H)\frac{\sin\alpha}{1+\cos\alpha+(1-\cos\alpha).(T_1/T_2)} \qquad \text{Equation 1-27}$$

where it is assumed that TR << T_1 and T_2. This equation shows that the contrast of an image obtained with a balanced-SSFP/True-FISP sequence depends on the T_1/T_2 ratio, which turns this pulse sequence a good choice for cine cardiac imaging due to the excellent contrast that is obtained between blood and myocardium [60, 61]. In practice, the balanced-SSFP/True-FISP sequence requires a preparation of the magnetization vector. One possibility is to apply a preparation α/2 pulse prior to the ±α RF pulses. The ±α pulses are separated by TR and the α/2 is applied TR/2 before the first α RF pulse [60]. This decreases the acquisition time by bringing the magnetization vector close to its steady state [60, 61].

1.5.3.3. Fast imaging acquisition

Other fast scanning approaches used in cardiac imaging are EPI and parallel imaging.

A diagram of the EPI sequence is presented in Figure 1-39.

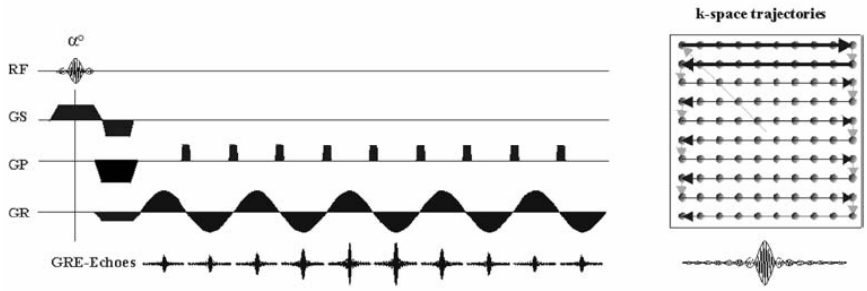

Figure 1-39 Timing diagram of an EPI sequence with a schematic representation of *k*-space filling. Adapted from [59]

The short acquisition time that is required by this pulse sequence results from the fast switching on and off of the phase encoding and frequency encoding gradients, which enables a fast filling of the *k*-space. EPI sequences are classified as single shot EPI, if all *k*-space is filled in during a TR, and as multi-shot EPI, if several TR's are required to acquire the entire *k*-space. Image contrast obtained with EPI is defined by the pulse sequence used to create the transverse magnetization. If it is a SE, the contrast is mainly T_2 weighted, if it is a GE the contrast is mainly defined by T_2*. In cardiac imaging, EPI sequences are usually combined with segmented acquisition. In this case, multiple segments of the *k*-space are covered per heart beat.

Parallel imaging is a relatively new technique that accelerates the acquisition time of already existing pulse sequences. With this technique, the image is acquired with an array of coils and the inherent spatial sensitivity of the different coils provides some of the spatial information required to reconstruct the image. This imaging technique has several advantages in cardiac imaging, namely, the reduction of acquisition time by a factor of typically 2 to 3, a reduction of the number of electrocardiographic triggers, which is important in case of patients with abnormal heart rhythm, a reduction in the breath-hold times and the possibility to acquire ungated real-time cine images [62, 63]. However, the increase in speed acquisition leads to a decrease in SNR and to potential reconstruction artefacts.

1.5.3.4. LISA-SSFP

Steady state free precision with linearly increasing startup angles (LISA-SSFP) [64] is the pulse sequence used in this thesis to image the myocardial tagging pattern (see Section 1.6.2.1.) applied to the cardiac muscle. Pulse sequences to image myocardial tagging have to fulfil certain conditions, namely, fast imaging, a long tag persistence, to image the entire cardiac cycle and a good tag contrast. Traditionally myocardial tagging is imaged using spoiled gradient echo (SGRE) imaging.

LISA-SSFP is based on the SSFP pulse sequence (see Section 1.5.3.2.), that is traditionally used for cine imaging. A timing diagram of LISA-SSFP sequence is presented in Figure 1-40

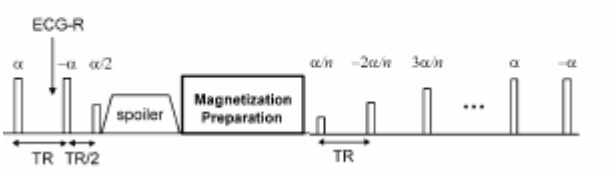

Figure 1-40 Timing diagram of LISA-SSFP pulse sequence.
TR - Repetition time. α - Flip angle. Adapted from [64]

This pulse sequence comprises three main phases: the interruption of the steady state, the magnetization preparation and the restoration of the steady state.

The interruption of the magnetization steady state and its storage is performed using the approach described in [65]. In this case, the steady state magnetization is stored as longitudinal magnetization by applying a $\alpha/2$ flip-back pulse at time TR/2 after the $\pm\alpha$ pulse. To destroy the remaining transverse magnetization, a spoiler is applied as represented in Figure 1-40.

The magnetization preparation consists of applying a magnetization saturation pattern to the cardiac muscle. A sinusoidal tag pattern is obtained using the spatial modulation of magnetization (SPAMM) technique [66]. This technique is described in detail in Section 1.6.2.1.

Cine image acquisition needs to start immediately after the magnetization preparation, which requires an efficient restoration of the steady state after magnetization preparation, to avoid ghost artefacts resultant from the transient period in the approach to the steady state. A quick restoration of the steady state is obtained by using the LISA approach. This consists in a train of pulse sequences, where the first n pulses have a flip angle that increases linearly from α/n to $(-1)^{n-1}\alpha$, with n a positive integer, and the remaining pulses have a flip angle equal to $\pm\alpha$. In this thesis n is equal to 5. This value was determined empirically and corresponds to the minimum amount of pulses necessary to obtain artefact free images in vivo [64, 67].

In this thesis, cine imaging with myocardial tagging was performed using the following parameters: TE/TR = 2.3/4.7 ms, readout bandwidth = 369 Hz/pixel, matrix size = 256 × 78 (readout × phase encoding), FOV = 300 × 300 mm^2, slice thickness = 6 mm. Flip angle α was set equal to 20º. This value was determined empirically and corresponds to the flip angle value that provides better tag persistence without reduction of tag contrast to noise ratio (tagCNR is defined as the contrast between tagged and non-tagged myocardium, relative to the standard deviation of the background noise).

The main advantages of this pulse sequence relatively to the usually used SGRE pulse sequence are a higher tagCNR and longer tag persistence (more than 100 ms [64]), as shown in Figure 1-41. With this pulse sequence it is possible to acquire complementary spatial modulation of magnetization (CSPAMM) images with a temporal resolution of 51 ms in a single breath hold, which prevents mismatch errors during subtraction of the SPAMM images (for a detailed description of CSPAMM images computation see Chapter 2). In this thesis, a high temporal resolution was obtained by acquiring three k_y lines per cardiac cycle, yielding a temporal resolution equal to 14 ms. Because the acquisition requires 4 cines (horizontal and vertical tag lines with both inverted and non-inverted patterns) of 26 heartbeats each (78 k_y-lines, 3 k_y-lines acquired per beat), the acquisition was performed in a multiple brief expiration breath-hold scheme. In this breath-hold scheme, acquisition was performed in periods of 4 heart

beats each, which were interleaved by a single inhalation and exhalation cycle of approximately 6 seconds.

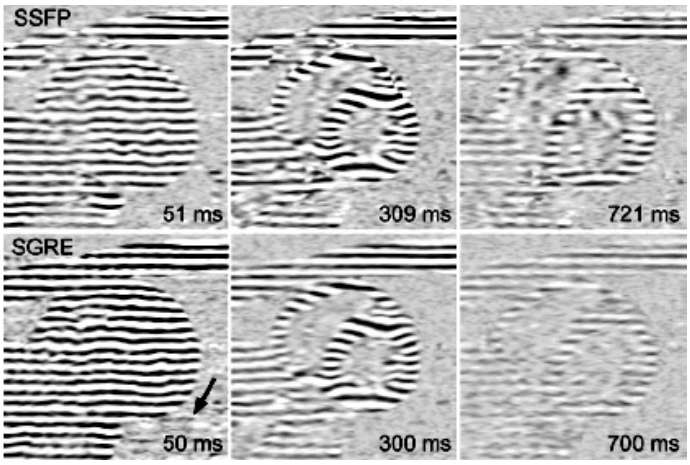

Figure 1-41 CSPAMM images at three phases of the cardiac cycle, obtained with LISA-SSFP (top row) and SGRE (bottom row) pulse sequence.
The arrow indicates a ghost artefact observed in the first SGRE image. These images were acquired with a temporal resolution equal to 51 ms (LISA-SSFP) and 50 ms (SGRE). Adapted from [64]

The main drawback of the LISA-SSFP pulse sequence is the limited tagCNR of the first images, due to the small flip angles during the LISA interval. Since the tag pattern has maximum amplitude (no significant decay) at the beginning of the cardiac cycle, and since the ramp-up is short (only 5 RF pulses), this is not a serious limitation for the purpose of this thesis.

1.6. CARDIAC MAGNETIC RESONANCE IMAGING

The aim of this section is to present a brief description of the cardiac MRI (CMRI) state-of-art.

The physical principles of CMRI are the same as those presented in the previous section. However, imaging the heart brings in additional challenges due to artefacts resultant from heart motion, breathing motion and blood flow. These difficulties have hindered the introduction of this imaging technique into clinical routine.

To reduce artefacts resultant from cardiac motion, cardiac image acquisition can be synchronized with the ECG. This synchronization can be performed with prospective triggering or with retrospective gating (see Figure 1-42). With prospective triggering, the image acquisition starts after detection of the R wave in the ECG. With retrospective gating the image is continuously acquired and a time label is given to each line in *k*-space. Afterwards *k*-space lines are sorted within a cardiac cycle. In this thesis, the images were acquired using the

prospective triggering synchronization. However, this approach has the limitation of not covering the end of the cardiac cycle as can be observed in Figure 1-42.

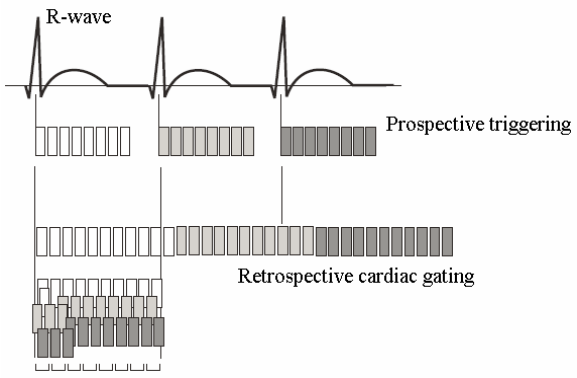

Figure 1-42 Schematic representation of prospective triggering and retrospective cardiac gating. Each box represents an acquisition and the grey scale represents different regions in *k*-space. Adapted from [55]

Regarding breathing motion, during quiet breathing it is known that the diaphragm can move 2-3 cm, which causes substantial heart displacement [68]. To avoid breathing artefacts, several approaches can be taken, namely, respiratory gating, breath-hold acquisitions and free-breathing navigator-echo acquisitions. The respiratory gating is equivalent to the cardiac triggering and synchronizes the image acquisition with the respiratory cycle. However, this approach is rarely used in clinical routine as it increases the acquisition time due to the long period of the respiratory cycle. The breath-holding acquisition is the simplest approach and consists of acquiring the image during breath-hold. Taking into account that a patient can breath-holding during 10-15 s, this solution requires the use of fast pulse sequences to acquire the image during this period. The main disadvantage of this technique is that for some patients it is impossible to sustain breath-holding. When the acquisition time is too long for one breath-hold, the breathing artefacts are avoided using a free-breathing navigator-echo acquisition. In this case, the position of the diaphragm is tracked using a 1D navigator image, and the images are only acquired during a particular period of the breathing cycle like end expiration. This approach requires regular breathing.

In CMRI, the most useful imaging planes are those parallel and perpendicular to cardiac axes. Short-axis (SA) image planes are acquired perpendicularly to the long-axis (LA) of the heart and between base and apex. These image planes allow the visualization of the cardiac chambers and of the heart wall (see Figure 1-43).

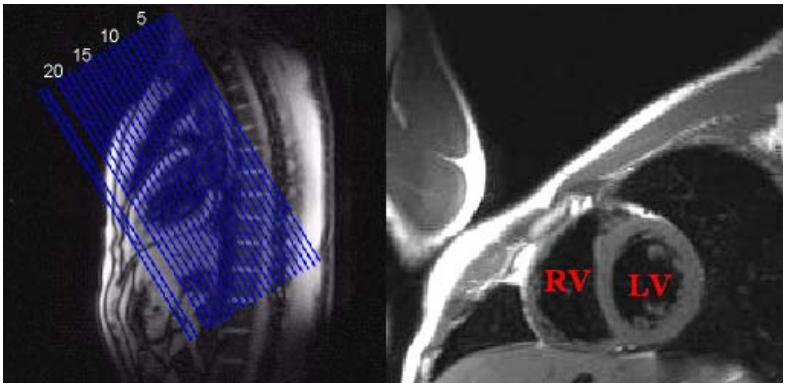

Figure 1-43 Left image: orientation of the SA image planes. Right image: SA image (slice 14). RV - Right ventricle. LV - Left ventricle. Adapted from [69]

LA image planes are acquired around the LV perpendicular to the SA. Traditionally three LA views are used: the 2 chamber view, which includes the left atrium and LV; the 3 chamber view, which includes the left atrium, RV and LV and the 4 chamber view which image all cardiac chambers (see Figure 1-44).

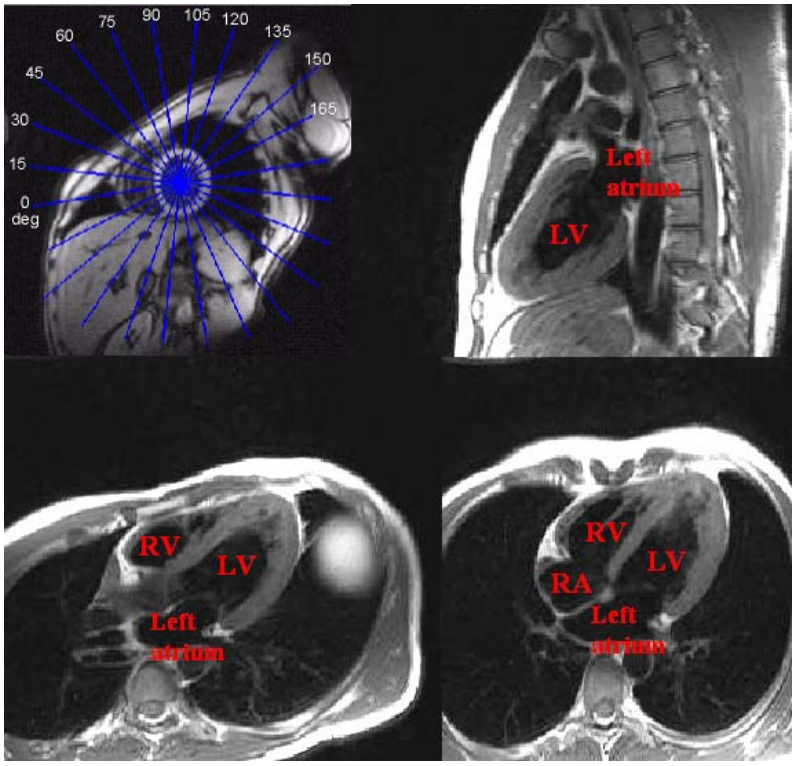

Figure 1-44 From left top to right bottom: Orientation of the LA image planes, 2 chamber LA image plane (slice at 90º), 3 chamber LA image plane (slice at 30º), 4 chamber LA image plane (slice at 0º). RA – Right atrium. RV – Right ventricle. LV – Left ventricle. Adapted from [69]

Some clinical applications of CMRI are described hereafter.

1.6.1. Cardiac morphology

One of the several clinical applications of CMRI is the visualization of cardiac morphology. For this purpose, FSE sequence with breath-hold and prospective triggering is usually used. With FSE it is possible to obtain images of the cardiac chambers and great vessels with a high contrast between blood pool (which appears dark) and cardiac muscle [70].

Cardiac morphology is usually evaluated using the widely spread and non-invasive echocardiography. However, as CMRI is a tomographic technique, it has the advantage to be able to acquire images in any direction.

1.6.2. Cardiac function

Cardiac global function is usually characterized by parameters computed from the chamber volumes at end-diastole (ED) and end-systole (ES). Such parameters are the stroke volume (SV), which is the difference between end diastolic volume (EDV) and end systolic volume (ESV), the EF, which is the ratio between SV and EDV, and the cardiac output, which is the product between SV and heart rate (HR).

Cardiac regional function is described by myocardial wall thickness, systolic wall thickening, and circumferential and longitudinal wall motion or shortening.

Although echocardiography is the first choice for clinical cardiac function quantification [15, 71], it has several limitations as explained in section 1.4.1. These limitations together with the technological progresses during the past years in the development of fast pulse sequences in MRI have made CMRI the gold standard for this type of exams [15, 38, 72]. One of the advantages of cardiac magnetic resonance is that no geometric assumptions have to be made to compute the volume of the cardiac chambers, which is important in case of pathologic hearts and in case of RV function assessment, which shape does not resemble any simple geometric form [71].

Cine CMRI is the technique of choice to quantify global and regional cardiac function [73]. In this case, the ideal pulse sequence has to be fast and provide a high contrast between blood pool and cardiac wall, in order to allow automatic segmentation of the myocardium. Pulse sequences that fulfil these conditions are the fast GE sequences, such as, FLASH with segmented *k*-space cine acquisition. Currently, balanced SSFP pulse sequences are the first choice due to the higher contrast between blood pool and myocardium and better signal to noise efficiency (obtained SNR per unit acquisition time).

To completely evaluate cardiac function it is also important to quantify myocardial deformation. The computation of myocardial strain gives information about the regional deformation of the myocardium and has the advantage of not being sensitive to rigid cardiac motion. To compute myocardial deformation it is essential to define markers in the cardiac

muscle. This has been possible since the introduction of the myocardial tagging technique. Since the first techniques presented by Zerhouni et al [74], several new approaches have been developed. All these techniques have the same goal: to be able to provide 2D and 3D myocardial strain. As this is the technique used in this thesis, a detailed description of myocardial tagging is given in the next section.

1.6.2.1. Myocardial tagging

Myocardial tagging is a technique that allows the tracking of myocardial motion and quantification of myocardial strain. It consists on applying RF pulses prior to image acquisition that saturate the magnetization in specific regions of the cardiac muscle, creating a pattern of dark and bright bands. These tags deform with cardiac muscle and allow the quantification of regional myocardial deformation.

This technique, originally applied to assess blood velocity [75], was first applied to assess myocardial function in 1988 by Zerhouni et al [74]. This technique consists on applying a selective RF pulse before image acquisition. Simultaneously, a linear gradient field is applied to saturate spins magnetization only in certain regions. Tagged regions can be altered by changing RF pulse angle, and the strength and direction of the magnetic field gradient. MR images are then obtained in a plane orthogonal to the tag planes using a standard pulse sequence. The main limitation of this technique is the use of selective RF pulses to create the tag pattern, which limits the number of tag planes that can be created [76].

After the introduction of this technique, several other myocardial tagging schemes were developed. One of them was proposed by Axel et al in 1989 [75] and consists on applying a periodic spatial modulation of magnetization (SPAMM). This technique uses two non-selective RF pulses that are separated by a magnetic field gradient. A schematic representation of this modulation technique is presented in Figure 1-45.

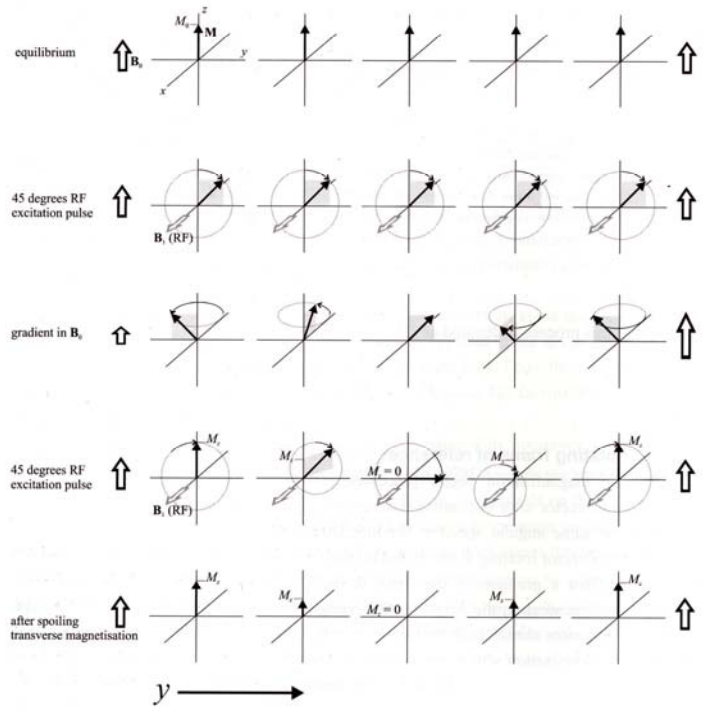

Figure 1-45 Schematic representation of the SPAMM technique. Adapted from [11]

The first RF pulse flips the magnetization vector to the transverse plane by an angle θ (Figure 1-45, second row). After this, a gradient is applied causing dephasing of the magnetization vectors (Figure 1-45, third row). A second RF pulse with the same flip angle θ is then applied leading to a modulated longitudinal magnetization (Figure 1-45, forth row). The remaining transverse magnetization is removed by a spoiler, as represented in the fifth row of Figure 1-45. The resultant longitudinal magnetization has a sinusoidal modulation, with the period determined by the strength and duration of the magnetic field gradient and the direction determined by the direction of the magnetic field gradient. The amplitude of the sinusoidal modulation is determined by the flip angles of the RF pulses. The weak point of the SPAMM technique is that the sinusoidal intensity profile of the tag pattern turns more difficult the tracking of the tag line with image-contrast based analysis techniques.

After the introduction of the SPAMM technique, several other approaches have been proposed for myocardial tagging. A summary of some of the tagging pulses, their advantages and disadvantages has been given by Axel et al in their survey study [75] and are summarized in Table 1-3.

	Description	Advantages	Disadvantages
Selective tags [74]	Selective saturation bands	Flexible	Inefficient
1-1 SPAMM [66]	Gradient between RF pulses	Fast, efficient	Sinusoidal tags
Higher order SPAMM [76]	Longer pulse trains with different strengths	Sharper tags	Slightly longer to play out
DANTE	Train of RF pulses during gradient	Faster than pulsing gradient	Sinc-shaped tags if same RFs; requires hard RF
Sinc-DANTE	Sinc modulation of RF pulses	Sharper tags	Requires hard RF
SPAMM/DANTE	Reduced gradient during RF	Less demanding on RF than full DANTE and on gradients than fully pulsing them	Less benefits than either alone, too
Radial	Selective tags in radial pattern	Better suitable for assessing circumferential deformation	Inefficient to create

Table 1-3 Summary of some tagging pulses.
Adapted from [75]

Cine CMRI with myocardial tagging is a unique technique to asses cardiac function non-invasively. Traditionally this technique is applied to the LV. Its application to the RV is limited by the thinness of the myocardium of this cardiac chamber, which leads to a sparse number of tag lines across the myocardial wall [73].

1.6.3. Myocardial perfusion

A relatively recent application of CMRI is the assessment of myocardial perfusion to diagnose and evaluate CAD.

Myocardial perfusion with MRI consists on evaluating the variation of myocardial signal intensity that is caused by an endogenous tracer (spin labelling) or by an exogenous tracer (Gadolinium-based compounds). From these techniques the one that is more available for clinical studies is the first-pass technique with an exogenous contrast agent; usually the Gd-DTPA (Gadolinium-Diethylene Triamine Penta-acetic Acid). This technique consists on imaging the first passage of a contrast bolus that is administered intravenously into the patient.

As Gd-DTPA enhances T_1 contrast, an ischemic region is characterized in a T_1-weighted image as a region with low signal intensity (as the agent does not reach this region). However, when the administered contrast is a magnetic susceptibility agent, the ischemic region appears in a T_2-weighted image as an enhanced area.

In order to visualize the first pass of bolus, it is necessary to use fast pulse sequences like the turbo-FLASH, EPI/hybrid EPI, SSFP or parallel imaging sequences [77].

With CMRI it is possible to evaluate myocardial perfusion qualitatively and/or quantitatively [77]. The visual interpretation of the results is the easiest approach, and consequently, the most used in clinical practice [70]. However it has the limitation of being highly dependent on the observer. A quantitative analysis can be performed by measuring parameters related to the perfusion or by measuring the absolute perfusion. The last approach brings several challenges and is still a research topic [78]. The first approach uses several parameters obtained from the signal intensity-time curve, namely, the upslope of the curve during first pass [77, 78], the maximum signal during first pass, the time to peak, the mean transit time and the area under the signal curve [78]. Despite the fact that SPECT is the first choice to assess myocardial perfusion, the first steps of the CMRI in this area show that myocardial perfusion with CMRI has several advantages, namely, a higher spatial resolution, lack of attenuation in the inferior wall and lack of ionizing radiation. However, to include myocardial perfusion with CMRI in clinical routine, and additionally, to turn this technique the first choice in this type of exam, it is still necessary to standardize the protocol to be used. Namely, it is necessary to define the best pulse sequence and parameters, the contrast and dose to employ, as well as how to perform the analysis.

1.6.4. Myocardial viability

Assessment of myocardial viability is an essential tool to select patients who will benefit from revascularisation surgery. The aim of this type of exam is to distinguish ischemic regions of the myocardium that are viable, and likely to recover after revascularisation, from non-viable scars.

Myocardial viability is usually assessed with PET. However, the high cost of this technique, together with its sparse availability and the use of ionizing radiation hampers its use in clinical routine, and turns CMRI a good alternative. Late enhancement or delayed enhancement is the CMRI technique that allows the assessment of myocardial viability. This technique consists on injecting a contrast agent intravenously and after waiting a period of 10 minutes or more, an image is acquired [79]. The pulse sequences that can be used are T_1 weighted SE and TSE, IR TSE (Inversion Recovery TSE) and IR GE. The IR is performed in order to increase the contrast between enhanced and non-enhanced tissue by nulling the

intensity of normal myocardium [80]. In this case, viable tissue corresponds to regions with minimal intensity [77] and scar tissue to bright areas [78, 79]. The advantages of CMRI, as its high spatial resolution, the availability in cardiology units and the absence of ionizing radiation, turn this technique the first choice for myocardial viability studies in the near future. However, some limitations still have to be overcome, namely, the high cost of the technique and the impossibility to image patients with pacemakers.

1.7. MYOCARDIAL TRACKING

The main advantage of MRI tagging is to create artificial magnetic markers in the myocardium which can be tracked. The post-processing of these images can go from the simple visual inspection to the full quantification of the myocardial strain. A summary of some techniques existent to track the tag pattern of the tagged images is presented in this section.

1.7.1. Snakes

One of the proposed approaches to quantify the kinematics of the myocardium is the Active Contour Model [81]. This technique, also designated by snakes, consists of deforming the contour model in order to match a certain image feature. Each snake is assigned to an energy function, and the matching with the tag pattern is achieved when the energy minimum is found. The snakes deform by internal and external forces. The image forces push the snakes to a certain image feature, which in the cardiac tagged images is usually a dark stripe. The internal forces result from the snakes's resistance to stretch and bend. Since the snakes can sometimes fall in a wrong local minimum, the user can correct their position by applying external forces. The main drawback of this method is that a user interface is required in order to avoid incorrect solutions. Due to the amount of data that comprises a cardiac tagged MR study, the post-processing using this technique appears to be too time-consuming.

1.7.2. Optical flow

Optical flow methods have been developed to determine the velocity maps from the tag pattern applied to the myocardium. These methods rely on the assumption that the brightness of the tracked material points remains constant over time, which is not valid for the cardiac tagged images. To address this problem, some improvements have been made to the standard optical flow technique, namely, the Variable Brightness Optical Flow method [82]. This method accounts for the fact that the intensity of the tag point changes in time; nevertheless, to estimate its brightness variation pattern *a priori* knowledge of image parameters and tissue parameters, such as proton density, T_1 and T_2 is required. Since these values are not always precisely known,

this technique is not applied in the clinical routine. Recently, progress has been made in order to reduce the dependence on the knowledge of image parameters to determine the brightness pattern over time. The method developed by Gupta and Prince [83] only requires the T_1 value to determine the brightness transformation field. Despite showing better results than the previous version, the dependence on the T_1 parameter still makes the method not as robust as desired.

1.7.3. Find tags

An automatic method to analyse cardiac tagged MR images was proposed by Guttman et al [84]. The goal of Find Tags is to track the tag pattern by using a template matching approach. In this case, the position of a tag line is tracked by fitting its brightness profile to a Gaussian template. The drawback of this technique is that it only provides correct results when applied to myocardial regions that are far from the contours.

1.7.4. 2D HARP Tracking

HARP tracking is a phase sensitive method to analyse tagged cardiac MR images. This image processing technique is based on the fact that SPAMM cardiac MR images correspond to an array of spectral peaks in the Fourier domain and that each spectral peak provides information regarding a component of myocardial motion.

The amplitude of an image acquired immediately after tagging with SPAMM technique (see Section 1.6.2.1.) is given by [11]:

$$I(x,y) = I_0(x,y)m(y) \qquad \text{Equation 1-28}$$

with $I_0(x,y)$ the magnitude of the non-tagged myocardium and $m(y)$ a tag modulation function which provides a tag pattern with horizontal tag lines. When the flip angle of the two RF tag pulses is equal to 45º, the modulation function is mathematically described by:

$$m(y) = \frac{1}{2} + \frac{1}{2}\cos\phi(y) \qquad \text{Equation 1-29}$$

with the harmonic phase (HARP) $\phi(y)$ given by:

$$\phi(y) = k_0 y + \phi_i \qquad \text{Equation 1-30}$$

where k_0 is the spatial frequency of the tag lines in the y-direction at the undeformed state and ϕ_i the phase at y = 0.

Using the complex notation for the modulation function $m(y)$ and assuming a homogeneous piece of myocardium with constant magnitude I_0 throughout the image, the amplitude of the tagged image I is given by:

$$I(y) = \frac{1}{2} I_0 \left[1 + \frac{1}{2}\left(e^{jk_{0i}y} e^{j\phi_i} + e^{-jk_{0i}y} e^{-j\phi_i} \right) \right] \qquad \text{Equation 1-31}$$

The Fourier transform (FT) of this equation is equal to:

$$I(k) = \pi I_0 \left[\delta(k) + \frac{1}{2} e^{j\phi_i} \delta(k - k_0) + \frac{1}{2} e^{-j\phi_i} \delta(k + k_0) \right] \qquad \text{Equation 1-32}$$

This equation shows that the tagged MR image consists of three peaks in *k*-space: one at $k = 0$, corresponding to the non-tagged myocardium, and two peaks at $\pm k_0$, corresponding to the tag modulation function. The HARP method consists on the isolation of the positive tag peak using a band-pass filter. After application of the filter, the inverse Fourier transform (IFT) is computed and the following complex signal is obtained:

$$g(y) = \frac{1}{4} I_0 \left[cos\, \phi(y) + i\, sin\, \phi(y) \right] \qquad \text{Equation 1-33}$$

The group of steps described above, Fourier transformation, band-pass filtering of positive frequencies and inverse Fourier transformation is known as the Hilbert transformation. This complex signal is composed by a real part equal to the original tagged signal but without offset, and by an imaginary part which is the original tagged signal shifted by 90º. The harmonic magnitude (HARM) of this complex signal is proportional to the amplitude of the non-tagged myocardium, and the harmonic phase (HARP) is obtained with the formula:

$$a(y) = tan^{-1} \left(\frac{Im(g(y))}{Re(g(y))} \right) \qquad \text{Equation 1-34}$$

where *Im* is the imaginary part of *g(y)* and *Re* its real part.

From Equation 1-33 and Equation 1-34 it is verified that the HARP angle *a(y)* corresponds to the phase of the modulation function $\phi(y)$ wrapped between $[-\pi,\pi)$.

The principle that underpins the HARP tracking technique is that both $\phi(y)$ and *a(y)* are material properties of the tagged myocardium and consequently, their values remain constant during cardiac deformation. This allows to track a tag point by tracking its HARP value. Applying the HARP tracking algorithm to the complete cardiac cycle gives the displacement of the tracked point on the direction perpendicular to the tag lines. For real tagged MR images, the 2D myocardial motion is determined from two sets of images with perpendicular tag patterns. The mathematical description of the HARP tracking principle applied to this case, is given by:

$$\vec{\phi}(\vec{r}, t_{m+1}) - \vec{\phi}(\vec{r}_m, t_m) = 0 \qquad \text{Equation 1-35}$$

where $\vec{\phi}(\vec{r}, t_{m+1})$ and $\vec{\phi}(\vec{r}_m, t_m)$ represent the following 2×1 vectors. The first element of the vector $\vec{\phi}(\vec{r}, t_{m+1})$ is the HARP value at position $\vec{r}$ = *(x,y)* in the image with horizontal tag pattern at time frame t_{m+1} and the second element is the HARP value at position $\vec{r}$ = *(x,y)* in the image with vertical tag pattern at time frame t_{m+1}. Similarly, the elements of the vector $\vec{\phi}(\vec{r}_m, t_m)$

are the HARP values at $\vec{r}_m = (x_m, y_m)$, in the images with horizontal and vertical tagging, respectively, at time frame t_m.

The numerical solution of this equation is determined using the Newton-Raphson technique and is given by:

$$\vec{r}^{(n+1)} = \vec{r}^{(n)} - \left[\vec{\nabla}\vec{\phi}\left(\vec{r}^{(n)}, t_{m+1}\right)\right]^{-1} . \left[\vec{\phi}\left(\vec{r}^{(n)}, t_{m+1}\right) - \vec{\phi}\left(\vec{r}_m, t_m\right)\right] \qquad \text{Equation 1-36}$$

with n the iteration number.

As the HARP image ($\vec{\phi}$) is unknown, the previous result must be written as a function of the (wrapped) HARP angle image ($\vec{a}$), obtained from the Hilbert transform of the tagged images. To perform this change of variables, a relation between the gradient of both variables has to be established. First, as $\vec{a}$ is wrapped, the gradient cannot be defined in the traditional way. To avoid the 2π jumps, $\vec{\nabla}\ \vec{a}$ is defined has being equal to the smaller of two gradients: the HARP angle gradient ($\vec{\nabla}\ \vec{a}$) and the gradient of the rewrapped HARP angle plus π ($\vec{\nabla}\ (W(\vec{a} + \pi))$). *W* is the wrapping function defined as [85]:

$$W(b) = \mathrm{mod}(b+\pi, 2\pi) - \pi \qquad \text{Equation 1-37}$$

The function *mod* is defined as:

$$mod(c,d) = c - f.d \qquad \text{Equation 1-38}$$

with *f* the nearest integer towards minus infinity of the quotient between *c* and *d*.
Figure 1-46 and Figure 1-47 show how this method avoids the wrapping effect.

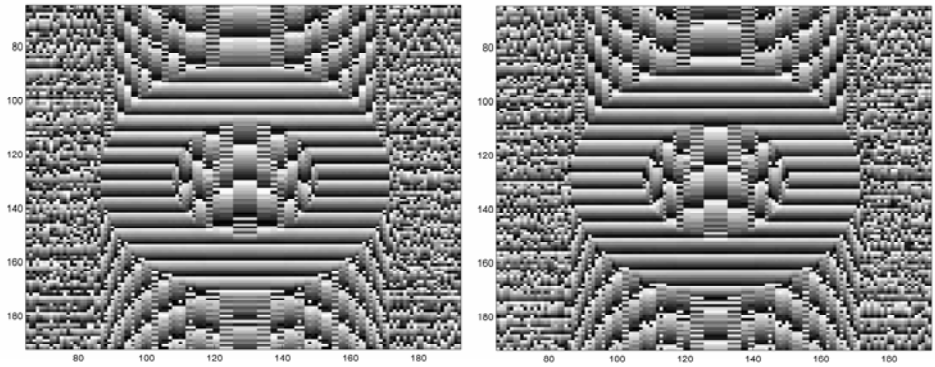

Figure 1-46 Left image: HARP angle of a simulated tagged image with horizontal tag lines. Right image: HARP angle image on the left after adding π and rewrapping.

Figure 1-46 shows the HARP angle of a simulated tagged image with horizontal tag lines and the same HARP angle image after adding π and rewrapping. These images show that adding π to the HARP angle image and rewrapping it, causes the wrapping effect to shift half a tag period. This phase difference is shown in Figure 1-47 (a) where the HARP angle *a* is

represented by the blue curve and $W(a + \pi)$ by the red curve for $x = 100$. The $\frac{\partial a}{\partial y}$ (blue curve), the $\frac{\partial}{\partial y}\left(W\left(a+\pi\right)\right)$ (red curve) and their minimum (black curve) are represented in Figure 1-47b for x = 100. The *x*-component of the gradient is not represented because it is close to zero for tagged images with horizontal tag lines.

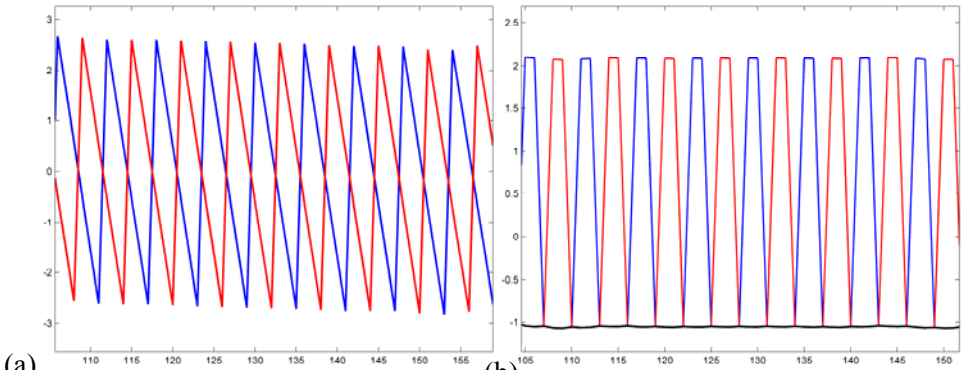

(a) (b)

Figure 1-47 (a) Profiles at x = 100 of the images in Figure 1-46. (b) Derivative relative to *y* of the HARP angle (blue curve), of the wrapped HARP angle plus pi (red curve) and the gradient star of HARP angle (black curve).

This plot shows that, the minimum of both gradients (black curve), avoids the wrapping effect, and is representative of $\vec{\nabla}\vec{\phi}$. In summary, $\vec{\nabla}\vec{\phi}$ and $\vec{\nabla}\vec{a}$ are related by the formula:

$$\vec{\nabla}\vec{\phi} = \vec{\nabla}^{*}\vec{a} = \begin{cases} \vec{\nabla}a_k & \left\|\vec{\nabla}a_k\right\| \le \left\|\vec{\nabla}W\left(a_k+\pi\right)\right\| \\ \vec{\nabla}W\left(a_k+\pi\right) & otherwise \end{cases} \qquad \text{Equation 1-39}$$

The change of variables in the difference term in Equation 1-36 cannot be performed directly, due to the wrapping effects on the computed HARP angle $\vec{a}$. To avoid erroneous values due to the 2π jumps, the result of the difference $\vec{a}\left(\vec{r}^{\,(n)},t_{m+1}\right)-\vec{a}\left(\vec{r}_m,t_m\right)$ has to be wrapped between [-π,π). The relation

$$\vec{\phi}\left(\vec{r}^{\,(n)},t_{m+1}\right)-\vec{\phi}\left(\vec{r}_m,t_m\right)=W\left(\vec{a}\left(\vec{r}^{\,(n)},t_{m+1}\right)-\vec{a}\left(\vec{r}_m,t_m\right)\right) \qquad \text{Equation 1-40}$$

is only valid when this difference is smaller than π, which is equivalent to assume small displacements. As the expected motion between successive time frames is small, this approximation does not constitute a problem.

After changing variables, the resulting iterative equation is given by:

$$\vec{r}^{\,(n+1)} = \vec{r}^{\,(n)} - \left[\nabla^{*}a\left(\vec{r}^{\,n},t_{m+1}\right)\right]^{-1}.W\left(a\left(\vec{r}^{\,(n)},t_{m+1}\right)-a\left(\vec{r}_m,t_m\right)\right) \qquad \text{Equation 1-41}$$

To develop the HARP tracking algorithm from this equation, several issues have to be addressed. Firstly, the solution of this equation is not unique due to the periodicity of the tag

pattern. In reality, there is one solution in each tag line. To avoid that the tracking point jumps to an incorrect tag line, it is crucial to correctly choose the starting point and to limit the displacement of the tracked point. As the cardiac muscle does not move significantly between two successive time frames, a good initialization is to consider that the point in the time frame t_{m+1} has the same position as in the time frame t_m. To avoid large displacements, the step is limited to one pixel. Moreover, as the HARP angle is a tissue property, the reference HARP angle $a(\vec{r}_m, t_m)$ in Equation 1-41 can be replaced by a single angle that does not depend on the time. This angle is called the HARP target angle, and denoted by a^*. Taking into account all these considerations, the HARP tracking algorithm is defined in the following way.

To find the position at the time frame t_{m+1} of the point that at the time frame t_m is on the position $\vec{r}_m$, it is considered $\vec{r}_m$ as the initial guess for the tracked position, which means that the tag point did not move between these two time frames. The first step is to verify if this position is correct. The stopping criteria of the iterative Equation 1-41 are that the HARP angle value of the new position is close enough to the target HARP angle value or that the maximum of allowed iterations is reached. If these criteria are not fulfilled, the step direction is computed using the following equation:

$$\vec{v}^{(n)} = -\left[\nabla^* \vec{a}(\vec{r}^{(n)}, t)\right]^{-1} . W\left(\vec{a}(\vec{r}^{(n)}, t) - a^*\right) \qquad \text{Equation 1-42}$$

with $\vec{a}(\vec{r}^{(n)}, t)$ the HARP angle value of the estimated position at time frame t_{m+1} and iteration n and a^* the respective target HARP angle. To compute the difference between the HARP angle at the estimated position $\vec{a}(\vec{r}^{(n)}, t)$ and the target HARP angle a^*, it is necessary to interpolate the HARP angle to the estimated position. Due to the wrapping effects the HARP angle values have to be locally unwrapped prior to interpolation, then interpolated and then wrapped again. The gradient of the HARP angle is also interpolated for the estimated position $\vec{r}^{(n)}$. After computing the vector direction, it is necessary to verify if the step is smaller than 1 pixel, using the formula:

$$\alpha(n) = min\left\{\frac{1}{\left\|\vec{v}^{(n)}\right\|}, 1\right\} \qquad \text{Equation 1-43}$$

Next, the estimated position is updated:

$$\vec{r}^{(n+1)} = \vec{r}^{(n)} + \alpha^{(n)}\vec{v}^{(n)} \qquad \text{Equation 1-44}$$

If this new position does not fulfill the stopping criteria, a new step direction is computed and the previous steps are repeated.

Osman et al [85] compared this processing image technique with Find Tags (see section 1.7.3.) and verified that the automated HARP tracking has an accuracy comparable to that of Find Tags, which is of 0.1 to 0.2 pixels.

The main advantage of the HARP tracking is the fact that it is not limited to the intersections of tag lines, and can be used to automatically track any myocardial point [85]. Additionally, this method works better with a sinusoidal pattern (relative simple acquisition), since this pattern yields only one peak in *k*-space, which makes it easy to filter this peak out and to compute the HARP angle image.

1.8. STRAIN ANALYSIS

Myocardial strain measures the deformation of a piece of cardiac muscle caused by stress action. This change in size and shape of the cardiac muscle is quantified relatively to an undeformed state. As there is no real undeformed state in the heart, by definition ED is considered the reference state with zero strain. The advantage of assessing myocardial strain, instead of myocardial displacement is that the first is independent of rigid body rotation and translation.

Myocardial strain can be expressed in different coordinate systems. For 3D strain, the most popular are: principal strains, radial/circumferential/longitudinal (rcl) system and radial/fibre/cross-fibre system. 2D strain can be expressed as principal strains and radial/circumferential (rc) strains. In this thesis the coordinate system used was the radial/circumferential/longitudinal and the radial/circumferential for the 3D and 2D strain respectively, because it is well suited to the cardiac geometry. Radial direction is defined as perpendicular to the epicardial surface, directed outward. Circumferential direction lies in the SA plane and is tangent to the heart surface, directed anticlockwise as viewed from the base. Longitudinal direction is perpendicular to the first directions, pointing from the apex towards the base [86].

1.8.1. Two-dimensional strain

2D strain is described by two linearly independent vectors. For myocardial strain analysis, these vectors are defined at the ED along radial and circumferential directions (Figure 1-48a). A schematic representation of the 2D strain components in a SA image plane is presented in Figure 1-48.

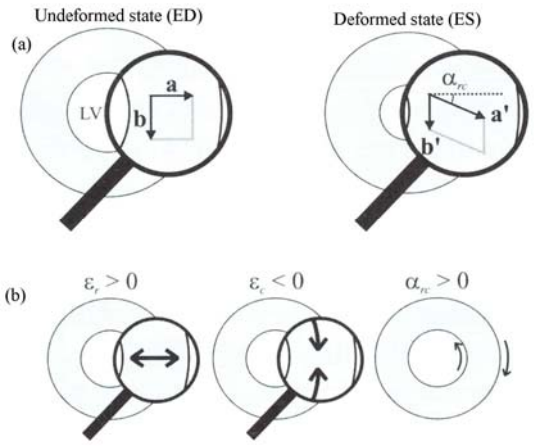

Figure 1-48 Illustration of 2D strain parameters in a SA slice.
The grey circle indicates the LV heart wall, viewed from the apex. (a) Left figure shows the undeformed state with the vectors a and b aligned with the radial and circumferential directions respectively. and right figure the deformed state. (b) Motion associated with normal values of 2D rc-strain in a SA slice. From left to right: radial thickening, circumferential shortening, and radial-circumferential shear. Adapted from [11]

Radial strain measures the relative change in length of a line segment aligned at ED with the radial direction. For myocardial strain, a positive value of radial strain corresponds to wall thickening of the LV, as represented in Figure 1-48b. A negative value corresponds to wall thinning and is associated with scar tissue after infarction [11].

Circumferential strain measures the relative change in length of a line segment aligned at ED with the circumferential direction. For myocardial strain, a negative value of this component represents circumferential shortening of the LV wall, as shown in Figure 1-48b. A positive value of circumferential strain corresponds to an increase of the myocardium in the circumferential direction and is associated with bulging.

Radial-circumferential shear strain measures the relative change of the angle between the segments aligned at ED with the radial and circumferential directions. For myocardial strain, a positive value of this strain component means that the subepicardium rotates clockwise, while the subendocardium rotates anticlockwise (viewed from the apex), as shown in Figure 1-48b. In this case a shear strain of 8º means that the angle between the undeformed line segments along the radial and circumferential directions decreased from 90º to 82º [11].

1.8.2. Three-dimensional strain

3D strain is described by three non-planar vectors, as represented in Figure 1-49. The three additional strain components assessed with 3D strain analysis are longitudinal strain, radial-longitudinal shear strain and circumferential-longitudinal shear strain (see Figure 1-49b).

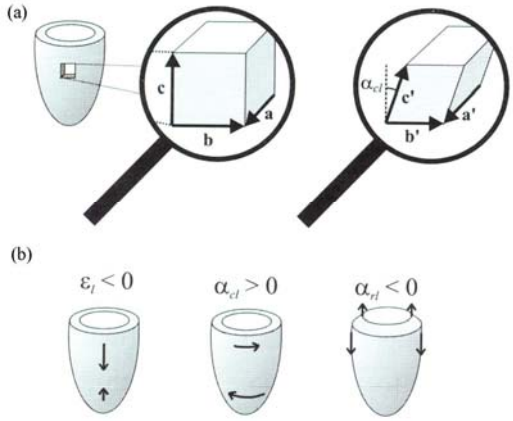

Figure 1-49 Illustration of 3D strain parameters with respect to the rcl-directions.
(a) Magnification of a small cube taken out of the LV heart wall. The vectors a, b and c in the left figure are aligned with the radial, circumferential and longitudinal directions. The right figure shows the deformed state.
(b) Motion associated with the 3D strains. From left to right: longitudinal shortening, circumferential – longitudinal shear (global LV torsion) and radial-longitudinal shear. Adapted from [11]

Longitudinal strain measures the relative change in length of a line segment aligned at ED with the longitudinal direction. For myocardial strain, a negative value of longitudinal strain corresponds to longitudinal contraction, as represented in Figure 1-49b.

Radial-longitudinal shear strain measures the relative change of the angle between the segments aligned at ED with the radial and longitudinal directions. A negative radial-longitudinal shear means that the subendocardium moves towards the base, while the subepicardium moves towards the apex, as presented in Figure 1-49b.

Radial-circumferential shear strain, commonly designated by torsion, represents the rotation of the base relative to the apex. A positive torsion means that the base moves anticlockwise, while the apex moves clockwise (see Figure 1-49b).

1.8.3. Homogeneous strain analysis

To compute 2D myocardial strain a homogeneous strain analysis is performed. With this approach a mesh of triangular elements is defined with the myocardial points and the deformation of each of these elements is measured [11, 87]. The strain inside each triangle is assumed to be homogeneous. As the sizes of the triangles used in this thesis are small, it is possible to detect strain inhomogeneity in regions of the myocardium covered by more than one triangular element.

A deduction of the mathematical formulation of the 2D strain components is given assuming that the myocardium is a continuum and that the myocardial deformation is locally homogeneous. Consider the deformation of a line element from ds_0 to ds, as represented in Figure 1-50.

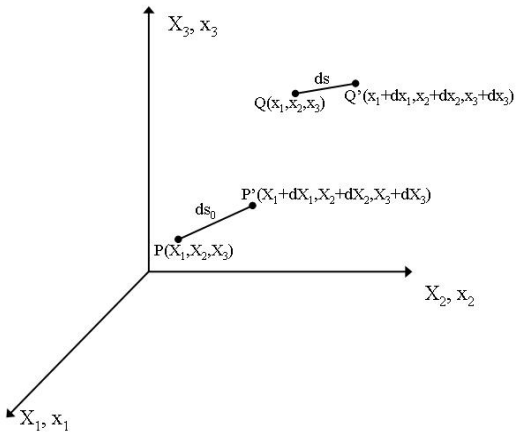

Figure 1-50 Deformation of a material line element.
X_i correspond to the coordinates of the undeformed line element and x_i to the coordinates of the deformed line element.

In this figure the X_i coordinates represent the coordinates of the undeformed line element and the x_i the coordinates of the deformed line element. The relation between these two sets of coordinates is given by the deformation gradient tensor, denoted by:

$$F_{ij} = \frac{\partial x_i}{\partial X_j} \qquad \text{Equation 1-45}$$

However, the deformation strain tensor is not appropriate to measure deformation because, although it is independent of rigid translation, it changes with rigid-body rotation. To overcome this limitation a new deformation measure is defined and is given by:

$$\vec{E} = \frac{1}{2}\left(\vec{F}^T \vec{F} - \vec{I}\right) \qquad \text{Equation 1-46}$$

with $\vec{I}$ the identity tensor and $\vec{F}^T$ the transpose of the deformation gradient tensor. This tensor $\vec{E}$ is the Green's strain tensor, also designated by Lagrangian strain tensor, and is a suitable deformation measure as it takes the value zero when there is no deformation even when there is rigid-body translation and/or rotation [88]. The elements of this tensor provide the change in squared length of the vectors in the undeformed state. In some studies, myocardial strains are expressed with these elements [86, 89, 90]. However, axial strains can be expressed as fractional or percent length changes, which often are easier to understand than true Lagrangian strain [86]. In this case, the 2D strain components are related to the Lagrangian strain tensor in the following way [91]:

$$\varepsilon_r = \left(\sqrt{1+2E_{rr}} - 1\right) \quad \text{Equation 1-47}$$

$$\varepsilon_c = \left(\sqrt{1+2E_{cc}} - 1\right) \quad \text{Equation 1-48}$$

$$sin\,\alpha_{rc} = \frac{2E_{rc}}{(\varepsilon_r + 1)(\varepsilon_c + 1)} \quad \text{Equation 1-49}$$

The 3D myocardial strain is computed in a similar way however, the myocardium is divided in several tetrahedrons instead of triangles. In this case the 3D myocardial strain components are defined as:

$$\varepsilon_i = \left(\sqrt{1+2E_{ii}} - 1\right) \quad \text{Equation 1-50}$$

$$sin\,\alpha_{ij} = \frac{2E_{ij}}{(\varepsilon_i + 1)(\varepsilon_j + 1)} \quad (i \neq j) \quad \text{Equation 1-51}$$

where E_{ij} are elements of the strain tensor $\vec{E}$ and i and j are equal to r (radial direction), c (circumferential direction) or l (longitudinal direction). The axial strains ε_i correspond to the percent change in length of a segment initially oriented in the i direction [91]. The shear strain components α_{ij} correspond to the change in angle between segments initially oriented in the perpendicular i and j directions [91].

The 2D or 3D myocardial strain of the LV can be presented as a global mean strain, where the strain is averaged for the entire myocardium, or as regional strain. In this case, the regions used in this thesis were: three longitudinal slices, six circumferential segments and three transmural segments. A schematic representation of these regions is given in Figure 1-51.

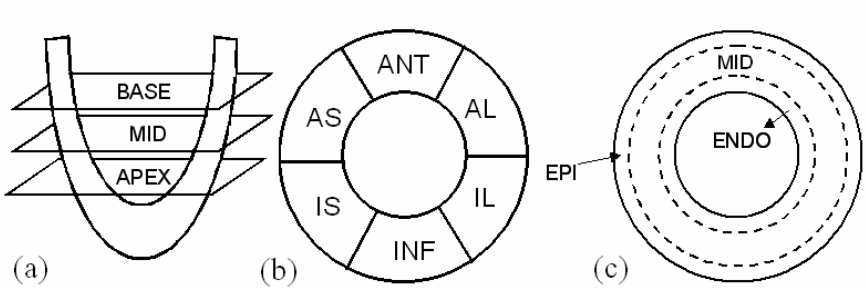

Figure 1-51 Schematic representation of longitudinal slices (a) and of circumferential (b) and transmural (c) segments.

IS - infero-septal. AS - antero-septal. ANT – anterior. AL - antero-lateral. IL - infero-lateral. INF - inferior. EPI – subepicardium. MID – Midwall. ENDO - Subendocardium

Regarding the longitudinal slices, the basal slice was defined just below the outflow tract at ES, and the apical slice at about 1 cm above the apex at ES. The mid slice was defined half way in between base and apex. The circumferential segments were defined with the IS

segment starting in the inferior insertion of the RV. Transmural segments were defined in the following way: midwall corresponds to the middle 50% of myocardium, subendocardium to the interior 25% of myocardium and subepicardium to the outermost 25% of myocardium.

Chapter 2.

EXTENDED 2D HARP TRACKING

The extended 2D Harmonic Phase (HARP) tracking method aims to track the myocardial tissue that appears near the epicardial contour during systole, and the myocardial tissue that reappears near the endocardial contour during diastole, due to the longitudinal motion and conical shape of the heart.

A mathematical model of myocardial deformation was used to quantify the accuracy of the extended HARP tracking and of the strain computation. For 6 healthy volunteers, the number of tracked points and the 2D strain components were computed with the extended and with the original HARP tracking version.

A high accuracy was obtained for the circumferential strain (maximum error of 0.5% relative to analytical strain). The extended version tracked 22±7%, 51±19% and 67±20% more points than the original version on the basal, mid and apical slices respectively ($P \leq 0.001$ for each slice), and yielded a decreased circumferential shortening (relative decrease: 2±4%, 9±4%, 12±5% for the basal, mid and apical slices respectively ($P < 0.005$ for mid and apex)), at end-systole (ES). These differences in circumferential strain were related to the more complete coverage of the myocardial wall with tracked points.

In this chapter it is shown that the extended HARP tracking provides strain values also from myocardial regions that were not covered by the original HARP tracking method.

Published in:
JMRI 2006; 23:682-690

2.1. INTRODUCTION

Since the first publication on Magnetic Resonance imaging (MRI) and myocardial tagging [66, 74], myocardial strain analysis with Magnetic Resonance (MR) has become a more common procedure. The post-processing performed on tagged images can go from the simple visual inspection of the tag pattern deformation, to the exhaustive computation of strain maps. Important efforts have been made during the past few years in the latter field. The published methods include active contour models [81], optical flow methods [82, 83], template matching methods [84] and HARP tracking (see Chapter 1 and reference [85]). Due to its automatic nature, HARP tracking is a promising tool for clinical application. HARP tracking is a phase sensitive method to determine tag line displacement by tracking its angle value over the cardiac cycle, normally starting at the time frame with undeformed tag pattern.

Due to the combination of the conical shape of the heart and its longitudinal motion, new tag lines appear during the systolic phase near the epicardial contour, and other tag lines disappear near the endocardial contour. As these new tag lines are not present at the time frame with undeformed tag pattern, their angle values are not known and, consequently, these tag lines are not tracked. However, disregarding these tag lines can lead to systematic errors in the strain results, due to the transmural gradient in the strain [90].

This chapter aims to present a new method designated by extended 2D HARP tracking, which tracks the new tag lines that enter into the image plane during the systolic phase, and recovers the tag lines that reappear near the endocardial contour during the diastolic phase. With this extended method, all parts of the myocardium are completely tracked during all phases of the cardiac cycle. In this chapter, the accuracy of the extended 2D HARP tracking method is reported. Next, the extended and original HARP tracking versions are applied to six healthy volunteers. To illustrate the improved coverage achieved with the extended 2D HARP tracking, the number of tracked points using both versions is compared and the influence of these new tracked points on the strain results is quantified.

2.2. MATERIALS AND METHODS

2.2.1. Original HARP Tracking

The HARP Tracking method developed by Osman et al [85] is explained in detail in Chapter 1. In summary, HARP tracking is an automatic phase sensitive method that tracks the magnetization saturation pattern applied to the myocardium. Spatial modulation of magnetization (SPAMM) technique (see Chapter 1 and reference [66]) is applied in order to

obtain this sinusoidal tag pattern. The image with horizontal tag lines, obtained with a 1-1 RF tagging pulse with a total tagging angle of 90º, has an intensity profile given by:

$$I(x,y) = I_0(x,y)\left[\frac{1}{2} + \frac{1}{2}cos(\phi(y))\right] \qquad \text{Equation 2-1}$$

where $I_o(x,y)$ is the intensity of the underlying MR image and $\phi(y)$ the harmonic phase (HARP). On this equation the longitudinal relaxation is not taken into account. Immediately after the application of the tag pattern, the harmonic phase is given by:

$$\phi(y) = k_0 y + \phi_i \qquad \text{Equation 2-2}$$

where k_0 is the spatial frequency of the tag lines in the y-direction at the undeformed state, and ϕ_i is the initial phase. In the frequency domain, this tag pattern consists of three peaks: one in the centre, which contains information referent to the non-tagged tissue and two at $+k$ and $-k$ that contain the information referent to the tag signal. To extract the tagging information from the underlying MR image, a band-pass filter is applied to select the positive frequencies in the Fourier domain. After applying the filtering, the inverse Fourier transform is computed and a complex image is obtained. The phase of this image is referred to as the HARP angle, and the magnitude as the harmonic magnitude (HARM). Representing the complex image *by g(x,y)*, the HARP angle can be obtained from:

$$a(x,y) = tan^{-1}\left(\frac{Im(g(x,y))}{Re(g(x,y))}\right) \qquad \text{Equation 2-3}$$

The HARP angle a is an estimate of ϕ, wrapped between the values $[-\pi,\pi)$. The HARM image gives an estimation of the amplitude of the non-tagged myocardium. An example of these two images is given in Figure 2-1.

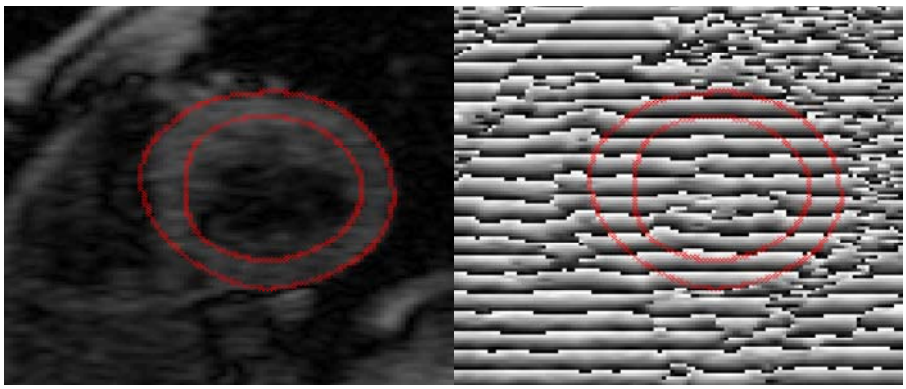

Figure 2-1 Example of an HARM image (on the left) and of an HARP image (on the right) obtained from a tagged image with horizontal tag lines.
Red lines represent the myocardial contours of the left ventricle.

HARP tracking relies on the principle that the HARP angle of a point in the myocardium remains constant through the entire cardiac cycle [85]**.** The HARP angle of the

image with undeformed tag pattern is used to determine the initial position of each point as well as its target HARP angle, which is the value that will be tracked on the following time frames. Thus, tracking a point that is on the position $\vec{r}_m\ (x_m,y_m)$ at the time frame t_m, consists of finding the position $\vec{r}\ (x,y)$ on the next time frame that has the same HARP angle value. Applying the HARP tracking algorithm to the complete cardiac cycle gives the displacement of the tracked points on the direction perpendicular to the tag lines. In order to obtain 2D displacement, two sets of tagged images with orthogonal tag line directions have to be acquired.

A refinement of the HARP tracking was proposed by Osman et al. to deal with tracked points lost due to noise and image artefacts [85]. This method consists of using the displacement of a point that is correctly tracked, usually located at the septum where the displacement is smaller, to correct the displacement of the remaining points. In this implementation of the original HARP tracking algorithm, an equivalent to HARP refinement is applied.

2.2.2. Extended 2D HARP Tracking

The goal of the algorithm here presented is to extend the HARP tracking in order to track the myocardial tissue that appears near the epicardial contour during systole, and the myocardial tissue that reappears near the endocardial contour during diastole, due to the combination of the longitudinal motion and conical shape of the heart. A flow chart of the extended HARP tracking algorithm is presented in Appendix I. The main steps of this algorithm are described in detail hereafter.

2.2.2.1. Input

The input of the extended HARP tracking algorithm is:

- Complementary SPAMM (CSPAMM) MR images with horizontal and vertical tag lines
- contours of the left ventricle (LV) myocardium
- image parameters
- tracking parameters

CSPAMM images [92] are obtained from the subtraction of two SPAMM images with inverted tag patterns. Using Equation 2-1 and considering that the underlying intensity of the SPAMM images with inverted tag patterns is equal, it can be deduced that the intensity profile of a CSPAMM image with horizontal tag lines is given by:

$$I(x,y) = I_0(x,y)\cos(\phi(y)) \qquad \text{Equation 2-4}$$

This equation is characterized by having only two peaks in k-space: one at $+k$ and one at $-k$. This means that the computation of the CSPAMM image results in the cancellation of the

non-tagged signal and consequently, in the removal of the central peak in *k*-space (see Figure 2-2).

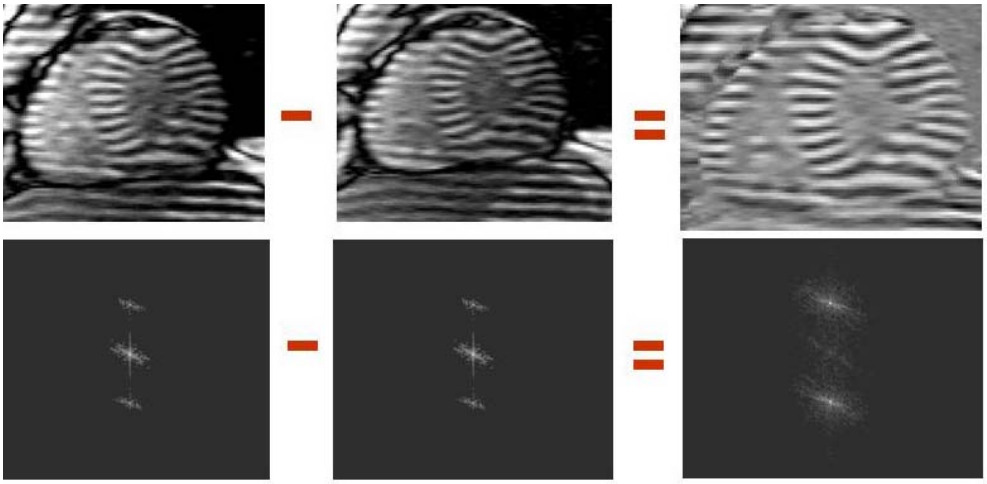

Figure 2-2 Top: Computation of a CSPAMM image with horizontal tag lines is performed by subtraction of a SPAMM image with inverted tag pattern from a SPAMM image with non-inverted tag pattern. Bottom: Spectrum in *k*-space of the SPAMM images and of the resultant CSPAMM image. In the SPAMM images the central peak is brighter than the other two peaks, while in the CSPAMM image the central peak has almost disappeared.

Having only two peaks in *k*-space, CSPAMM images are less sensitive to the choice of the cut-off filter frequency and lead to more accurate strain results [93].

The myocardial contours of the LV are drawn manually for all time frames on the HARM images, using the MASS software package (version 5.1b, MEDIS, Leiden, The Netherlands).

The image parameters provided by the user are: field-of-view (FOV) in mm, FOV in pixels, tag period in mm.

The tracking parameters are: maximum of iterations allowed for a successful tracking, the fraction of myocardial wall to be tracked, the image used to compute target HARP angle and the minimum distance allowed between tracked points. These tracking parameters are discussed below.

2.2.2.2. HARM and HARP images computation

After providing the input, the algorithm proceeds with the computation of the HARM and HARP images. These images correspond to the magnitude and phase of the complex image resultant from the Hilbert transformation of the CSPAMM images, as described in Chapter 1. In this step, the only difference to the original version is that in the algorithm here presented a high-pass filter is applied instead of a band-pass filter. This decision was taken based on preliminary studies that showed better results with this type of filter. The cut-off frequency of

the filter was set equal to $\frac{20k_0}{43}$ [93]. 43 is the applied spatial tag frequency reported in terms of $\nu = \frac{k_0}{2\pi} FOV$ and corresponds to the number of tag cycles in the FOV for a FOV of 300 mm and a tag spacing of 7 mm, which are the standard values used in this thesis. 20 is the value of the cut-off spatial frequency ν_c. The ratio $\frac{20}{43}$ roughly indicates $\frac{1}{'cut-offstrain'}$. This means that, for these values a tissue stretching above 215% is filtered out, limiting in this way, the maximum stretch that can be detected. Since this value is far away from the strain measured in the human LV, a slight difference in this ratio has not much influence on the strain results.

2.2.2.3. Target HARP Angle Computation

In the next step the target HARP angle is computed for each pixel. The target HARP angle consists on the HARP angle value that will be tracked on the following time frames (see Chapter 1).

In the original version, the target HARP angle is measured from the HARP angle of the first time frame. In the extended version this value is computed because of two reasons. Firstly, the images analysed in this study are acquired with the steady state free precession (SSFP) sequence using the linearly increasing startup angle approach (LISA) (see Chapter 1 and reference [64]), which yield a limited tag contrast to noise ratio (tagCNR) for the first time frame (see Figure 2-3a), and on later images the myocardium is already deformed. Secondly, since the tag lines that enter into the image plane due to through plane motion and conical shape of the heart are not present on the first time frame, their target HARP angle cannot be measured from this image.

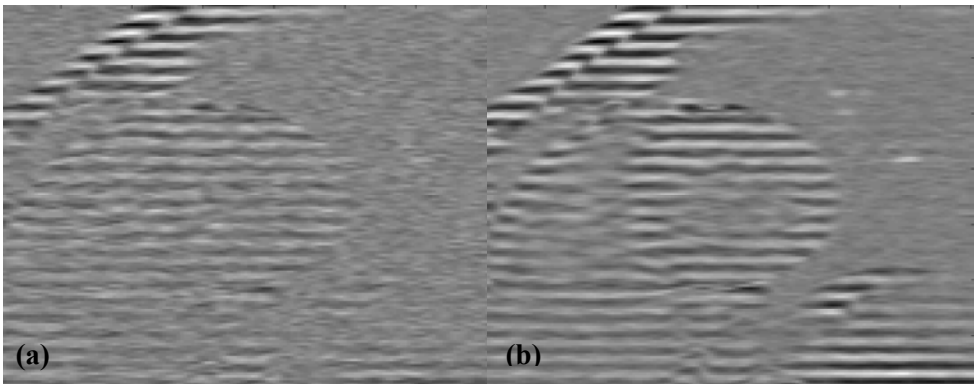

Figure 2-3 Example of the first (a) and second (b) time frames acquired with LISA-SSFP sequence at the basal level of the LV.

The first acquired time frame shows a reduced tagCNR. The second acquired time frame shows an acceptable tagCNR and a tag pattern still undeformed. Due to these characteristics this image is used to compute the target HARP angle.

Assuming that the second time frame is still undeformed, which is a reasonable assumption thanks to the high temporal resolution of the analysed images (14 ms), as it can be observed in Figure 2-3b, all tag lines within the contours can be used to estimate the target HARP angle. The target HARP angle is computed using Equation 2-2, taking $k_0 = \frac{2\pi}{\lambda}$. The initial phase ϕ_i of the HARP angle image with horizontal tag pattern is estimated using the following equation:

$$\phi_i = \frac{1}{M}\sum_m W\left(\frac{1}{N_m}\sum_n a(x_n, y_m) - k_0 y_m\right) \qquad \text{Equation 2-5}$$

where $a(x_n , y_m)$ is the locally unwrapped HARP angle at the second time frame, with (x_n , y_m) inside the myocardial contours. N_m is the number of points inside the myocardial contours in row m and M is the number of rows inside the myocardial contours. The rows y_m and y_{m+1} are separated by λ. W is the wrapping function defined as [85]:

$$W(b) = \text{mod}(b+\pi, 2\pi) - \pi \qquad \text{Equation 2-6}$$

The function *mod* is defined as:

$$mod(c,d) = c - f.d \qquad \text{Equation 2-7}$$

with f the nearest integer towards minus infinity of the quotient between c and d.

The target HARP angle is computed for every pixel within a rectangular region of tracking which encompasses the LV epicardial contour, with an additional margin of two tag distances to account for the tag lines that appear during systole. Since the HARP tracking method is not limited to tag line intersections, the tracking is applied to each pixel inside this rectangular region of tracking. After computing the target HARP angle, a label is given to each pixel inside the region of tracking of the second time frame HARP angle. The points inside the myocardial contours are labelled as “active” and those outside are labelled as “inactive”. During the tracking process, this label is used as the trigger to track or not to track a point.

2.2.2.4. Tracking “Active” Points

After rejecting the first acquired image and computing the target HARP angle using the HARP angle of the second acquired image, the algorithm owns all the information necessary to track the first image (which corresponds to the reference image). A tracking algorithm, based on that described by Osman et al. (see Chapter 1 and reference [85]) is then applied to all “active” points. The differences between this new algorithm and the original version are the following:

- tracking error, which corresponds to the maximum difference between target HARP angle and the HARP angle at the tracked position
- computation of the HARP angle gradient
- successful tracking stop criteria.

In the original algorithm, the tracking error ε is a constant defined by the user. In the extended HARP tracking ε is not constant. Instead, ε increases for later time frames to overcome the decreased tagCNR of these images due to tag fading, and is given by the formula:

$$\varepsilon = 0.0005 + 0.00125 \times \frac{n - n_{ref}}{Nframes - n_{ref}} \text{ (pixels)} \qquad \text{Equation 2-8}$$

with N_{frames} the total number of time frames to be tracked, n_{ref} the number of the image used to compute the target HARP angle and n the number of the image being tracked. So, as the first image to be tracked corresponds to the reference image (n_{ref}), in this case the minimum tracking error is equal to 0.0005 pixels, and as the number of the last image to be tracked corresponds to N_{frames}, the maximum tracking error is 0.00175 pixels.

In the original algorithm, the gradient of the HARP angle is computed as described in Chapter 1. In the algorithm here presented the gradient is given by the formula:

$$\vec{\nabla}\vec{a} = \frac{\vec{a}(\vec{r}+1) - \vec{a}(\vec{r}-1)}{2} \qquad \text{Equation 2-9}$$

with $\vec{\nabla}\vec{a}(\vec{r})$ a 2×2 matrix, which first row includes the gradient of the HARP angle of the image with horizontal tag lines and the second row the gradient of the HARP angle of the image with vertical tag lines.

In the original algorithm the successful tracking stop criteria are (see Chapter 1 and reference [85]):

- tracking error smaller than a constant defined by the user
- maximum of iterations not exceeded

In the algorithm here presented the criteria are:

- tracking error smaller than the value given by Equation 2-8
- maximum of iterations not exceeded
- tracked position falls inside the myocardial contours of the current time frame
- displacement of the tracked point smaller than c.λ/2 (with c a scaling constant equal to 0.8 in this study)
- topology of the set of "active" points remains unchanged during tracking process
- number of "active" near neighbours is larger than 2, in order to check the topology
- relative distance between "active" near neighbours remains larger than a minimum value defined by the user

The two first conditions are equivalent to the conditions of the original version. The maximum of iterations were set equal to 30, as it was verified that usually the algorithm required less than 10 iterations to converge to the correct solution. The third condition ensures that the tracked point belongs to the myocardium. However, as the subendocardium is difficult to distinguish from the papillary muscle existent in the inner surface of the LV, a fuzzy

endocardial contour is defined. This means that if the tracked point falls inside the LV less than two pixels away from the endocardial contour is still considered active. The remaining conditions are related to the fact that the solution for the tracking algorithm is not unique. Since the HARP angle is wrapped, tracked points can converge to neighbouring tag lines if a large motion occurs between two time frames. In order to address this problem, the fourth condition does not allow displacements higher than c.λ/2, since half tag distance is the theoretical maximum distance that can be tracked with HARP. The fifth and sixth conditions check the topology of the set of "active" points, to prevent them from jumping over each other due to noise or errors in the HARP angle. The user can choose the kernel size of the window that defines the set of neighbours. In this study this parameter is set equal to 5. However, the topology of the set of "active" points can be correct but, due to noise, some neighbours of the set can nearly overlap. To avoid such an incorrect result, the last condition checks the distance between neighbours relative to their undeformed distance. Only if this value is larger than 0.05 pixels the point is considered "active". If all these conditions are fulfilled the point is set as "active", otherwise it is labelled as "inactive".

2.2.2.5. Tracking new tag lines and recover lost tag lines

After tracking all "active" points, the absolute displacement field is computed and used to estimate the displacement of the "inactive" neighbours. If a point is currently "inactive" but two or more of its near neighbours are "active", the displacement of this "inactive" point is set equal to the averaged displacement of its "active" neighbours. The resulting estimated displacement is then applied to the "inactive" point (see Figure 2-4). If the estimated position falls inside the current myocardial contours, the point is tracked using the procedure described above; otherwise it remains "inactive" on its original position in the undeformed grid.

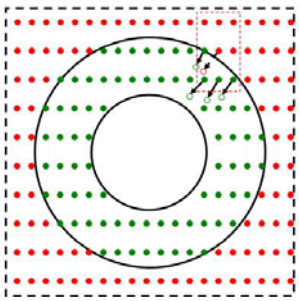

Figure 2-4 Schematic representation of the method used to track new tag lines and to recover tag lines lost during the cardiac cycle.

Solid lines represent myocardial contours and the dashed line delimit the tracking region. Full green dots correspond to the "active" points and the full red dots to the "inactive" points on the first time frame. The empty green dots correspond to the tracked position of the "active" points on the second time frame and the empty red dot the estimated position of an "inactive" point. The arrows represent the displacement of the points between first and second time frames

2.2.2.6. 2D displacement

After tracking all "active" points, tracking the new myocardium that enters the image plane in the first time frame, and if is the case, recovering the myocardium than have been lost due to through plane motion or noise, the same procedure is applied to the remaining time frames of the cardiac cycle. At the end an absolute displacement field is obtained for each time frame. These displacement fields are then filtered using a moving average with a kernel size of 5 pixels. This filter is applied in order to obtain smoother strain values.

2.2.2.7. Output

The algorithm output is a text file with the filtered positions for all time frames of all the points that are initially inside the tracking region. When the point is inactive its filtered position is set negative. This nomenclature is given in order to not include these points on the definition of the triangular mesh for strain computation. After all the positions are listed the coordinates of the contours of the LV myocardium are written for all time frames. With this information the 2D strain components of the myocardium are computed.

2.2.3. Strain Computation

A detailed description of the strain computation method is given in Chapter 1. In summary, 2D strain components are computed applying a homogeneous strain analysis to triangular finite elements connecting the "active" points on each time frame [87]. In order to obtain the undeformed shape for each element, the mesh on the undeformed grid is defined using the same points. From the deformation of each element, the deformation gradient tensor $\vec{F}$ is determined. The Lagrangian strain tensor $\vec{E}$ is related to $\vec{F}$ by the following equation:

$$\vec{E} = \frac{1}{2}\vec{F}^T\vec{F} - 1 \qquad \text{Equation 2-10}$$

Using the radial-circumferential coordinate system, the radial and circumferential strains and the radial-circumferential shear are given by:

$$\varepsilon_r = \left(\sqrt{1+2E_{rr}} - 1\right)\times 100\% \qquad \text{Equation 2-11}$$

$$\varepsilon_c = \left(\sqrt{1+2E_{cc}} - 1\right)\times 100\% \qquad \text{Equation 2-12}$$

$$sin\,\alpha_{rc} = \frac{2E_{rc}}{(\varepsilon_r + 1)(\varepsilon_c + 1)} \qquad \text{Equation 2-13}$$

where E_{ij} are elements of the strain tensor $\vec{E}$.

The strain results for each time frame were obtained by averaging the strain of all the triangles inside the current myocardial contours.

2.2.4. Simulations

The extended 2D HARP tracking was validated using simulated tagged images of an incompressible cylinder [94] with and without noise. An example of the undeformed and deformed cylinder with and without noise is presented in Figure 2-5.

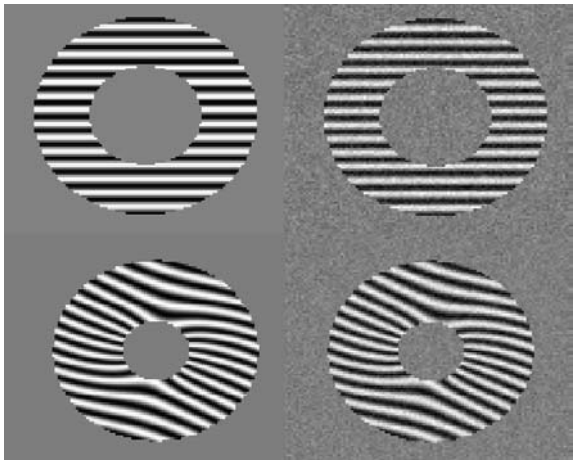

Figure 2-5 Tagged images of the cylinder simulating end-diastole and ES.
From top left to right bottom: end-diastole without noise, end-diastole with noise, ES without noise, ES with noise.

The set is composed by 21 images and the maximum deformation occurs at time frame 10 (500 ms). In the simulation the temporal resolution is 50 ms.

In the undeformed state, at time frame 0, the cylinder has an inner radius R_i = 25 mm, an outer radius of 50 mm and a length of 100 mm. The inner radius decreases linearly from R_i = 25 mm to r_i = 15 mm at t = 500 ms. From t = 550 ms to t = 1000 ms, the inner radius increases back to its initial value, and the deformation returns to the undeformed state again.

The deformed position (r, θ, z), corresponding to the undeformed tag point position (R, Θ, Z), is given by the following equations:

$$r = \sqrt{r_i^2 + \frac{\left(R^2 - R_i^2\right)}{\lambda}} \qquad \text{Equation 2-14}$$

$$\theta = \phi R + \Theta + \gamma Z + \varepsilon \qquad \text{Equation 2-15}$$

$$z = \omega R + \lambda Z + \delta \qquad \text{Equation 2-16}$$

The model parameters were chosen in order to exaggerate the human heart motion and, simultaneously, allow the appearance of new tag lines inside the contours:
longitudinal contraction λ = 1, R-Θ shear ϕ = 0.556°/mm, axial torsion γ = 0.6°/mm, rigid body rotation ε = 18.334°, R-Z shear ω = 0.278, rigid body displacement δ = 4.167 mm. Equation 2-14 represents the incompressibility of the cylinder.

Inaccuracy in the HARP angle computation by means of the Hilbert transform leads to errors in tracking. To quantify this effect on the tracking error, the model without noise was used as input of the extended 2D HARP tracking. Another error source is noise in the tagged images. This effect was quantified using the model with noise. The tagCNR of the synthetic images with noise was computed using the equation:

$$tagCNR(t) = \begin{cases} 10 & t = 0ms \\ 28.e^{-t/\tau} & t \geq 50ms \end{cases} \qquad \text{Equation 2-17}$$

with the time constant τ set equal to 670 ms. This equation simulates the tagCNR of the real MR images acquired with the LISA - SSFP sequence [64].

Using this model the tracking accuracy and the strain accuracy were computed. The tracking accuracy was defined as the distance between the positions tracked with the extended 2D HARP version and the analytical positions obtained with Equation 2-14, Equation 2-15 and Equation 2-16. The strain accuracy was quantified by comparing the strain results obtained from the tracked positions with the strain results obtained from the corresponding analytical positions.

2.2.5. Subjects

Two compare the extended 2D HARP tracking with the original HARP tracking version, both methods were applied to real tagged MR images. Images were acquired in 6 healthy volunteers (6 male; mean age: 38±11), with no history of cardiac diseases. Each subject provided informed consent before data acquisition.

Subject	**1**	**2**	**3**	**4**	**5**	**6**
Age	28	53	31	48	43	26
T_{avc} **(ms)**	345	347	358	375	366	317
T_{mvo} **(ms)**	441	462	450	500	475	414
RR (ms)	1180-1220	990-1020	880-950	1200-1330	880-1010	700-900
$N_{\text{time frames}}$	63	49	56	49	56	46

Table 2-1 Characterization of the analysed healthy population.
$N_{timeframes}$ – Number of tracked time frames. T_{avc} – Time of aortic valve closure. T_{mvo}- Time of mitral valve opening. RR – Range of intervals between two R-waves

2.2.6. Image acquisition

Imaging was performed with a 1.5T system (Sonata, Siemens Medical Solutions, Erlangen, Germany), using a phased-array receiver coil. The cine imaging with myocardial tagging was acquired with LISA - SSFP sequence (see Chapter 1 and reference [64]). Tissue

tagging was applied with two non-selective 45° RF pulses separated by a field gradient in the readout direction, yielding a sinusoidal modulation of the magnetization (see Chapter 1 and reference [66]). Images were acquired in three short-axis (SA) planes for each volunteer at basal, mid and apical level. The basal slice was defined just below the outflow tract at ES, and the apical slice at about 1 cm above the apex at ES. The mid slice was defined half way in between base and apex. Four sets of images were acquired for each SA plane: vertically and horizontally tagged images with sinusoidal and inverted sinusoidal tagging. The tag distance λ was 7 mm and the readout direction perpendicular to the tag lines. Other imaging parameters were: FOV 300×300mm^2, excitation flip angle 20°, repetition time TR = 4.7 ms, echo time TE = 2.3 ms, receiver bandwidth BW = 369 Hz/pixel, imaging matrix size = 256×78 acquired with 3 k_y lines per beat, yielding a temporal resolution of 14ms.

To avoid mismatching between the four sets of images acquired per SA plane, a multiple brief expiration breath hold scheme was performed. Data was acquired during each breath hold of 4 heart beats, and at the end the subject was given 6 seconds to inhale and exhale. The resultant acquisition time for each image plane was approximately 4.5 minutes.

To determine the instant of aortic valve closure (T_{avc}) and the instant of mitral valve opening (T_{mvo}) LA cine images in the 3-chamber view were acquired with SSFP imaging with a temporal resolution of 14 ms. The image parameters were: excitation flip angle 60°, repetition time TR = 3.4 ms, echo time TE = 1.7 ms, receiver bandwidth BW = 1085 Hz/pixel, imaging matrix size = 256×160.

2.2.7. Statistics

The results are presented as mean ± standard deviation. The methods were compared using paired t-test. The difference between methods was considered statistically significant if $P < 0.05$.

2.3. RESULTS

2.3.1. Simulations

2.3.1.1. Simulation Without Noise

Inaccuracy in the HARP angle computation by means of the Hilbert transform leads to tracking errors. To quantify this effect, the model without noise was used as input of the extended HARP tracking version.

Figure 2-6 shows that the tracking error increases with increasing tag pattern deformation. At maximum deformation (t = 500 ms), the tracking error reaches a maximum of 0.14 ± 0.15 pixels.

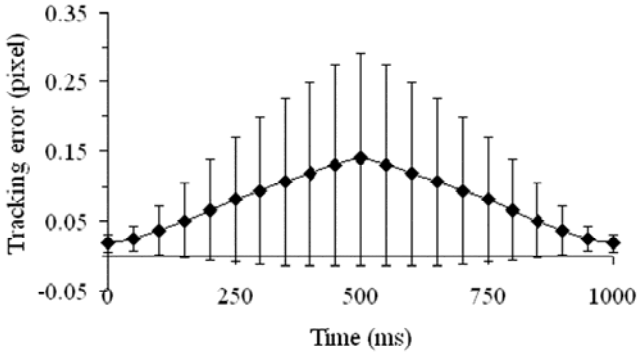

Figure 2-6 Plot of the tracking error over time.

The tracking error was defined as the mean distance between tracked and analytical positions. Each point represents the mean distance over all "active" points. The error bar represents the standard deviation. This simulation was performed using the model without noise. ES occurs at t = 500 ms.

2.3.1.2. Simulation With Noise

Another source of error in the tracking is the noise in the tagged images. To quantify this effect on the tracking error, the model with noise was used as input of the extended 2D HARP tracking version.

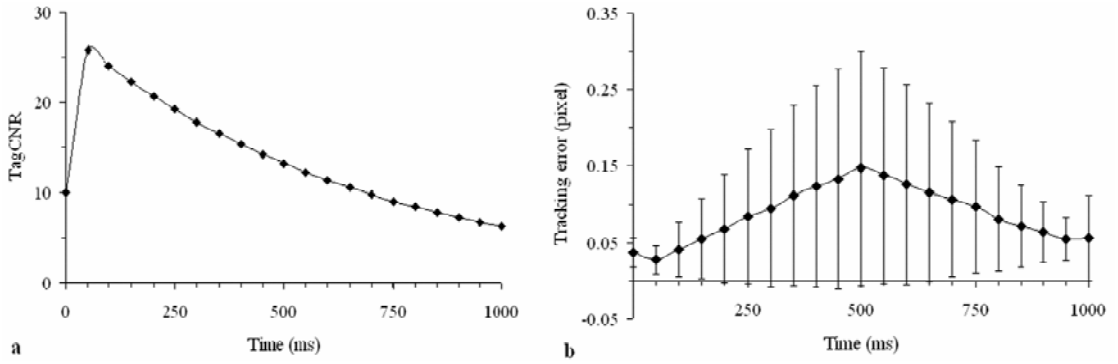

Figure 2-7 (a) TagCNR plotted over time simulated for the LISA – SSFP sequence and (b) plot of the tracking error over time.

In the first time frame, the tagCNR is limited due to the initially small flip angles. In the second time frame, the tagCNR has increased due to larger flip angles; after the second time frame tagCNR decays over time due to T_1 relaxation. Tracking error was defined as the mean distance between tracked and analytical positions. This simulation was performed using the model with noise. Each point represents the mean distance over all "active" points. The error bar represents the standard deviation.

The tagCNR curve of the simulated tagged images is shown in Figure 2-7a, and the tracking error over time is presented in Figure 2-7b. Due to the noise, the tracking error at the first time frame is larger than in Figure 2-6. However, from t = 50 ms till t = 600 ms the difference between simulations with and without noise is within 0.01 pixels. The maximum

tracking error occurs at t = 500 ms and is equal to 0.15 ± 0.15 pixels, which is close to the error obtained for the simulation without noise. Thus up to ES, the error due to the Hilbert transform (Figure 2-6) dominates over the additional error due to noise (Figure 2-7b). At t = 1000 ms, the effect of noise has increased: the error with noise is 0.06 pixels, while without noise it is 0.02 pixels.

2.3.1.3. Strain Accuracy

Similarly to the tracking accuracy, the error in strain increases with the tag pattern deformation (Figure 2-8). The circumferential strain component is an exception, since no difference is observed for any time frame. The measured radial strain is 26% smaller at t = 500 ms than expected and the measured radial-circumferential shear angle at this instant remains 75% below the analytical shear angle. The measured circumferential strain is only 0.5% larger than the analytical strain for t = 500 ms.

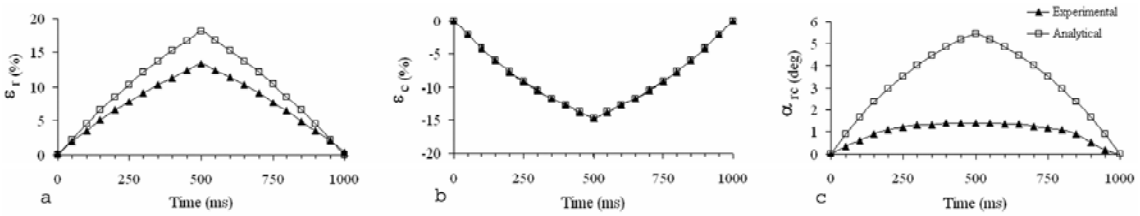

Figure 2-8 Plot of the 2D experimental and analytical strain components over time.

The simulations were performed using the model with noise with the tagCNR of Figure 2-7a. The analytical strain was computed from the analytical positions and the experimental strain from the positions obtained with the extended 2D HARP version. (a) Radial strain (b) Circumferential strain (c) Radial-circumferential shear

2.3.2. Healthy Volunteers

2.3.2.1. Number of Tracked Points

Figure 2-9 shows the points tracked by the original HARP version (Figure 2-9a) and by the extended 2D HARP version (Figure 2-9b), for a mid ventricular slice at ES of a volunteer. With the original version, there is a lack of information near the subepicardium due to the fact that the new tissue entering the image plane is not tracked. With the extended version, this region is successfully tracked.

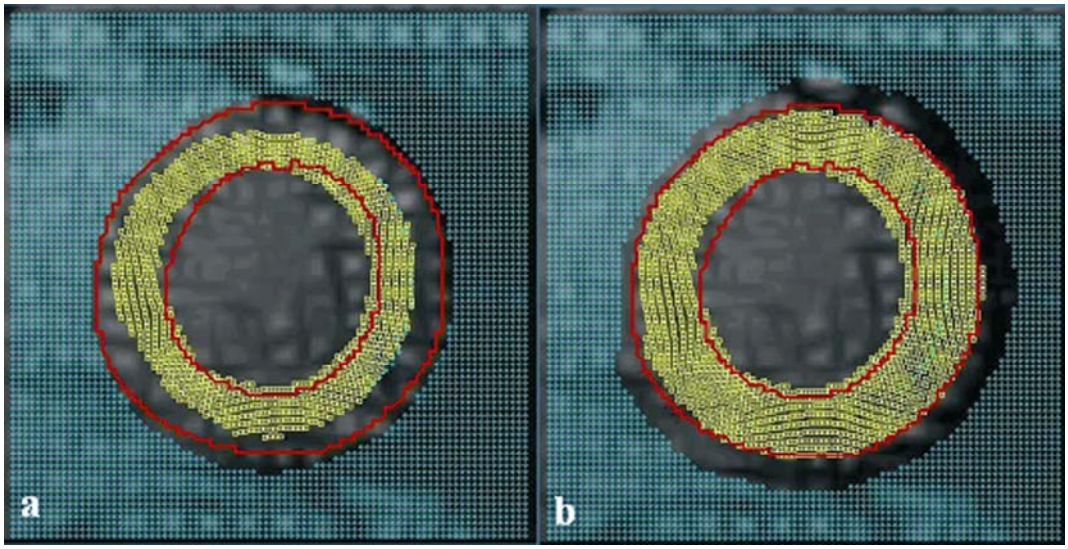

Figure 2-9 Visualization of the rectangular region of tracking encompassing the left ventricular SA image at ES.

The red curves represent the myocardial contours, the blue marks the "inactive" points and the yellow marks the "active" points. Since the endocardial contour is difficult to delineate, a point that is successfully tracked and falls in the blood pool within two pixels distance from the endocardial contour, is labelled as "active". (a) Original HARP tracking version (b) Extended 2D HARP tracking version. Visualization was performed using SPAMMVU software, (University of Pennsylvania, PA).

For a quantitative comparison, the difference in the number of tracked points between both HARP versions relative to the original version is measured over time for each slice.

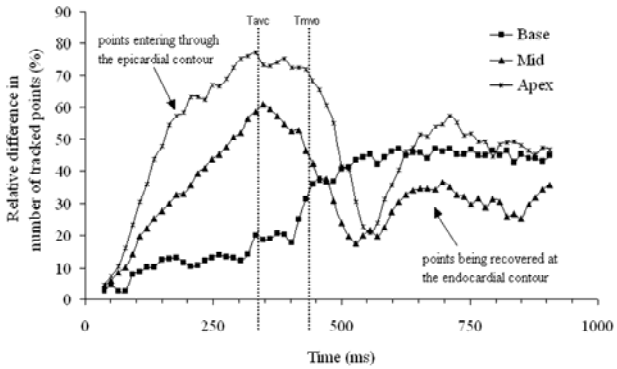

Figure 2-10 Example curves of the amount of extra points tracked with the extended version relative to the original version in one healthy subject, for basal, mid and apical slices.

The number of points tracked with the original HARP version consists of all the "active" points inside the present myocardial contours and the points recovered after they had been lost due to noise. The number of points tracked with the extended HARP version consists of all the points tracked with the original version and also the points that enter near the epicardial contour and the points that reappear near the endocardial contour. T_{avc} – Time of aortic valve closure T_{mvo} – Time of mitral valve opening.

Figure 2-10 shows an example of the obtained curves. In this case, the basal slice shows a continuous increase in the amount of extra points tracked with the extended version, with a

maximum of 47 %. For the mid and apical slices the number of extra tracked points have two maxima, one around the time of aortic valve closure and one after mitral valve opening. For this example, the extended HARP tracking version is able to track at maximum 61% (mid slice) and 77 % (apex slice) more points than the original HARP tracking version.

The relative differences in the number of tracked points, at the time of aortic valve closure, and the minimum relative differences after this instant are presented in Table 2.2 for all six subjects.

Volunteer	Relative difference in number of tracked points (%) at T_{avc}			Minimum relative difference in number of tracked points (%) after T_{avc}		
	BASE	MID	APEX	BASE	MID	APEX
1	18.6	60.9	73.4	17.7	17.5	20.8
2	28.5	73.9	80.5	28.5	73.9	38.2
3	27.1	51.6	50.9	24.8	41.8	35.3
4	24.0	59.3	96.7	22.6	38.2	49.6
5	22.6	41.8	42.7	22.6	28.4	20.3
6	9.4	19.5	57.0	5.9	12.6	23.9
Mean	21.7 ± 7.0♣	51.2 ± 18.8♣	66.8 ± 20.3♣	20.4 ± 7.9*	35.4 ± 22.0*	31.3 ± 11.7♣

Table 2-2 Differences in number of tracked points between extended and original HARP tracking versions relative to original version.

T_{avc} – Time of aortic valve closure, in ms from the ECG R-wave. (♣ P ≤ 0.001 * P ≤ 0.003)

At the T_{avc} (ES), the extended HARP version tracks 22 ± 7 %, 51 ± 19 % and 67 ± 20 % more points on the basal, mid and apical slice than the original version (P ≤ 0.001 for each slice). The minimum relative differences after the T_{avc} shows that the extended HARP version tracks at least 20 ± 8 %, 35 ± 22 % and 31 ± 12 % more points on the basal, mid and apical slice than the original version, during the diastolic phase (P ≤ 0.003).

2.3.2.2. 2D Strain

The curves for the radial and circumferential strain components and radial-circumferential shear component were obtained for each volunteer with the extended and with the original HARP tracking versions. An example is presented in Figure 2-11.

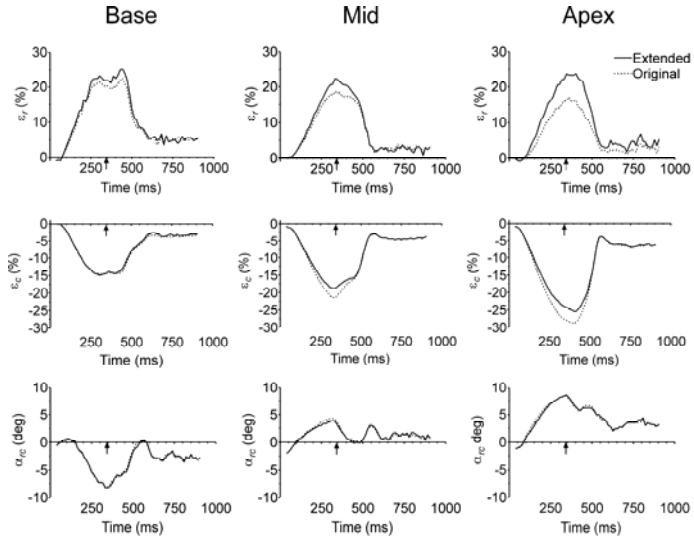

Figure 2-11 Plots of the 2D strain components of a healthy volunteer for basal, mid and apical slices. The two curves represent the strain results obtained from the points tracked with the extended 2D HARP tracking version (solid line) and with the original HARP tracking version (dashed line). The arrow at the time-axis indicates the time of aortic valve closure (ES).

In this example, the difference in strain components increases from the basal to the apical slice. This result was observed for almost all volunteers. The relative differences in strain at ES are presented in Table 2-3. It is observed that the extended version leads in most of the cases to higher radial thickening, ε_r, and less circumferential shortening, ε_c. The differences were significant for the circumferential strain at mid and apical slices ($P < 0.005$).

Subject	Relative $\Delta\varepsilon_r$ (%)			Relative $\Delta\varepsilon_c$ (%)			Relative $\Delta\alpha_{rc}$ (%)		
	BASE	MID	APEX	BASE	MID	APEX	BASE	MID	APEX
1	7.0	20.4	45.6	-0.3	-12.6	-13.4	1.5	-11.8	3.5
2	16.1	35.3	37.5	0.2	-5.6	-16.6	1.6	25.2	0.3
3	16.2	23.7	19.1	0.7	-5.4	-6.8	10.4	85.8	8.3
4	14.7	33.6	76.1	-4.9	-12.1	-18.6	32.8	8.3	-1.1
5	-7.8	-8.0	-13.1	-8.9	-11.3	-10.3	5.1	0.7	0.9
6	1.7	-1.7	-6.3	-1.4	-4.8	-6.5	3.2	13.1	-6.8
Mean	8.0	17.2	26.5	-2.4	-8.6	-12.0	9.1	20.2	0.8
SD	9.7	18.1	33.6	3.7	3.7	5.0	12.1	34.4	5.0
	p=0.14	P=0.07	p=0.06	P=0.18	p=0.005	p=0.005	p=0.07	p=0.17	p=0.72

Table 2-3 Relative differences in two-dimensional strain components between extended and original tracking versions, at time of aortic valve closure.

In case of decrease in circumferential shortening, the difference in ε_c is positive. However because this difference is divided by the value of ε_c obtained with the original version (which is negative), the relative difference in ε_c will be negative. $\Delta\varepsilon_r$ – Difference in ε_r between extended and original version, relative to original version, $\Delta\varepsilon_c$ – Difference in ε_c between extended and original version, relative to original version, $\Delta\alpha_{rc}$ – Difference in α_{rc} between extended and original version, relative to original version.

2.3.2.3. Correlation Between Difference in Circumferential Strain and Difference in Radial Positions

The difference between extended and original HARP tracking was further explored. The question is whether the difference in ε_c is related to the newly tracked points, which are mainly at the subepicardial region during systole. To answer this question, the difference in mean ε_c was plotted against the difference in mean radial position, for each time frame. A positive difference in ε_c means less circumferential shortening. A higher difference in mean radial position means that more subepicardial points are tracked with the extended HARP version. On Figure 2-12 an example plot from one volunteer for basal, mid and apical slices is presented.

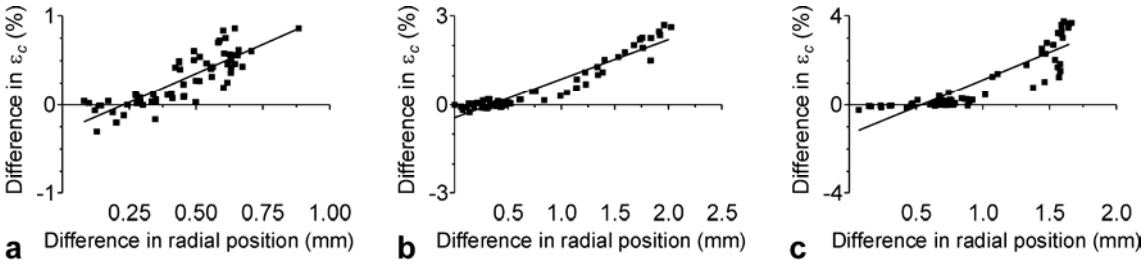

Figure 2-12 Plot of the difference in mean circumferential strain between extended and original versions versus the corresponding difference in mean radial position.

Each point represents the average over all "active" points for each time frame. A trend line was fitted and the correlation coefficient was obtained. (a) – basal slice (b) – mid slice (c) – apical slice.

In this case, a positive correlation is obtained for the three slices, with correlation coefficients of 0.84, 0.95 and 0.88 for basal, mid and apical slice respectively ($P < 0.001$). The correlation coefficients obtained for all volunteers are presented in Table 2-4 and are significant for all volunteers at all locations, except for the basal slice of one volunteer.

Volunteer	Base	Mid	Apex
1	0.84 *	0.95 *	0.88 *
2	0.83 *	0.48 *	0.93 *
3	0.51 *	0.83 *	0.72 *
4	0.64 *	0.94 *	0.96 *
5	0.64 *	0.90 *	0.92 *
6	- 0.24 ♣	0.82 *	0.81 *

Table 2-4 Correlation coefficients between the difference in mean circumferential strain and the difference in mean radial positions of the tracked points

(extended versus original tracking). *P < 0.001. ♣P = 0.10

2.4. DISCUSSION

The accuracy obtained for the extended HARP tracking, 0.15 ± 0.15 pixels, is in agreement with the value reported for the original HARP tracking version and for the find tags method (0.1-0.2 pixel) [85].

From the simulations without noise, it was observed that the tracking error increases with tag deformation. This implies that there is a small systematic error in the HARP angle calculated by means of the Hilbert transform, which depends on the actual state of the tagging pattern. This error in the HARP angle may result from the non-linearity of the tag spatial frequency, or from the truncation of the tag signal at the epicardial and endocardial contours. However, more simulations are needed to evaluate both possibilities (see Chapter 6).

At the first and last time frames of the simulations with noise, the obtained tracking error is higher than the tracking error obtained from the simulations without noise. The difference at the first time frame represents the difference between the computed and the measured target HARP angle. The difference on later time frames is the result of the limited tagCNR of these images. Given the good tagCNR obtained with SSFP imaging, these simulations make clear that the error in the HARP angle, which depends on the tag pattern deformation, is currently the main source for the tracking errors during systole. Image noise only influences the latest time frames when the tag pattern is considerably faded.

With respect to the strain computation, the accuracy obtained for the circumferential strain is high, however for the radial strain and radial-circumferential shear the accuracy decreases noticeably when tag deformation increases. Apparently, the effect of the error in the HARP angle computation on the strain is more severe in the radial direction, as in this direction both the non-linearity and the truncation of the tag pattern are most pronounced. From the values obtained for the strain accuracy it can be concluded that the extended 2D HARP tracking version is appropriate to compute strain on the circumferential direction.

The variation, during the cardiac cycle, of the amount of extra points tracked with the extended version can be explained by the through plane motion and conical shape of the heart. The new tissue that appears near the subepicardium, induces an increase in the relative difference in the number of tracked points between the extended and the original versions. After ES this difference starts to decrease, since the new tag lines included during systole, start to disappear at the subepicardium. However, during diastole, the amount of recovered tissue near the subendocardium increases and the relative difference in number of tracked points increases again. For the mid and apical slices this pattern was obtained for almost all the volunteers. The basal slice shows for all volunteers a constant increase in the relative difference which levels off during diastole. From the mean difference in the number of tracked points at the time of aortic

valve closure and from the minimum mean difference after this instant, it can be concluded that the pattern described for the three slices was verified for all subjects.

In this study the most improvement in the number of tracked points was obtained on the apical level. However, the opposite result could be expected since, during systole the base moves towards the apex, leading to more through plane motion at the basal level than at the apical. For example, Marcus et al used tagging MR in the 2-chamber LA view to quantify the displacement of the LV on the LA direction. For a population of 8 healthy volunteers, the mean amount of systolic LA translation at the posterior wall was 15 mm, 10 mm and 6 mm at the basal, mid and apical levels respectively [95]. Nevertheless, as it was remarked before, the appearance of new tag lines on the image plane is not only due to the through plane motion but also due to the conical shape of the heart. These results can then be explained by the fact that the myocardial wall is more oblique at the apical level than at the basal.

Comparing the strain results obtained with both HARP tracking versions it is observed that, on average, the extended version leads to less circumferential shortening, ε_c, and more radial thickening, ε_r. The decrease in ε_c is expected since the myocardial points near the subendocardium have higher circumferential shortening and the original HARP tracking version is biased toward this region. For the ε_r an increase is observed, while a decrease would be expected. However, since the radial strain error obtained from the simulations is higher than the difference observed between the extended and the original HARP versions, it is not possible to draw any conclusion. Knowing that the accuracy of the radial strain is lower near the myocardial contours [93], a possible solution is to restrict the computation of the strain on the radial direction to the middle 50% of the myocardium. Even then it could be useful to use the extended 2D HARP tracking version, since new tissue is still appearing in this region.

The correlation obtained between the circumferential strain difference and the radial position difference shows that when the mean position of the points tracked with the extended HARP version is more subepicardial (higher difference in radial position), the circumferential strain difference is also larger. This result supports the assumption that the difference obtained on the circumferential strain is a consequence of tracking the new tissue appearing on the image plane near the subepicardium.

Because the extended 2D HARP tracking version is able to track more points than the original one, this version opens the prospect for an extended 3D strain analysis, since in 3D strain analysis, a high amount of data per slice is desirable due to the methods used to compute the strain components (i.e. field fitting or finite element analysis). Besides, higher differences in strain may be observed when the extended 2D HARP tracking version is applied to patients with regional cardiac diseases.

On this study, the extended HARP tracking was only applied to SA view of the left ventricle, however, this method could also be expanded to LA tagged images (see Chapter 3), and right ventricular tagged images when the right ventricular wall is thick enough to detect the tag pattern.

2.5. CONCLUSION

The extended 2D HARP tracking is able to track all myocardial points at all time frames. In comparison with the original HARP tracking version, this extended version leads to strain results that represent more myocardium.

Chapter 3.

EXTENDED 3D HARP TRACKING

The extended 3D Harmonic Phase (HARP) tracking method presented in this chapter aims to automatically track the 3D myocardial motion during a cardiac cycle. This method was applied to 6 healthy volunteers and the 3D myocardial strain of the healthy left ventricle (LV) was characterized.

The obtained 3D myocardial strains were comparable with previous published results. These results show that circumferential strain increases 3% from base towards apex ($P < 0.001$) and 10% from subepicardium towards subendocardium ($P < 0.001$). For longitudinal strain a transmural gradient was also observed from subepicardium towards subendocardium, with a higher longitudinal shortening at apex and a lower longitudinal shortening at mid level. The radial dependent strain components showed a high variability between subjects and between regions of the same subject, indicative of a low accuracy of the myocardial tagging in the assessment of strain in this direction. It was also verified that during diastolic phase, the LV first untwist and then relaxes on the radial, longitudinal and circumferential directions. Differences on the time to onset of shortening in the circumferential and longitudinal directions were observed between septum and lateral wall, with the circumferential shortening starting 13 ms earlier in the lateral wall than in the septum ($P < 0.001$) and the longitudinal shortening 9 ms earlier in the septum than in the lateral wall ($P = 0.045$).

These results show that 3D myocardial strain of the healthy LV is inhomogeneous, and consequently, the comparison between myocardial strain of healthy controls and patients should be performed regionally instead of globally.

3.1. INTRODUCTION

On the previous chapter the extended 2D HARP tracking method was described. This method has relatively to the original version (see Chapter 1 and ref [85]) the advantage of being able to track the myocardial tissue that enters the image plane near the epicardial contour during systole, and to recover the myocardial tissue that reappears near the endocardial contour during diastole. Nevertheless, 2D tracking is only able to quantify the apparent motion of the myocardium and, consequently, the radial, circumferential and radial-circumferential components of the strain tensor. To assess the real motion of the LV and the remaining strain components it is necessary to acquire images of the long-axis (LA) of the heart, in addition to the short-axis (SA) image planes, track the myocardium in these image planes and reconstruct the 3D motion of the myocardium.

Although there are already several methods to track the cardiac muscle [84, 96, 97], the HARP method has the advantage of being automatic and relatively fast, which enables its use in clinical environment.

As it was referred in Chapter 1, the LV cardiac muscle is not homogeneous. Consequently, there are differences in strain between different regions of the LV myocardium which are physiologic and not pathologic. This shows the importance of mapping the healthy LV myocardial strain before study the dysfunctional myocardium.

This chapter aims to present the extended 3D HARP tracking method, and apply it to healthy subjects to obtain strain maps of the healthy LV muscle. In order to compare the different regions of the LV myocardium this was divided in three longitudinal slices, six radial segments and three transmural segments. In this chapter, a detailed description of the developed method is given. Next, the 3D myocardial strain components are computed for the six healthy volunteers. The obtained 3D myocardial strains at end-systole (ES) are then compared for the different regions of the LV. Additionally, the existence of a strain gradient in the transmural direction is investigated for all strain components. At the end the time to onset of circumferential and longitudinal shortening are measured at the septum and lateral wall and the existence of temporal differences between these two regions is investigated.

3.2. MATERIALS AND METHODS

3.2.1. Extended 3D HARP Tracking

Extended 3D HARP tracking consists on the combination of the extended 2D HARP tracking algorithm (for a detailed description see Chapter 2) with the 1D HARP tracking algorithm (Figure 3-1).

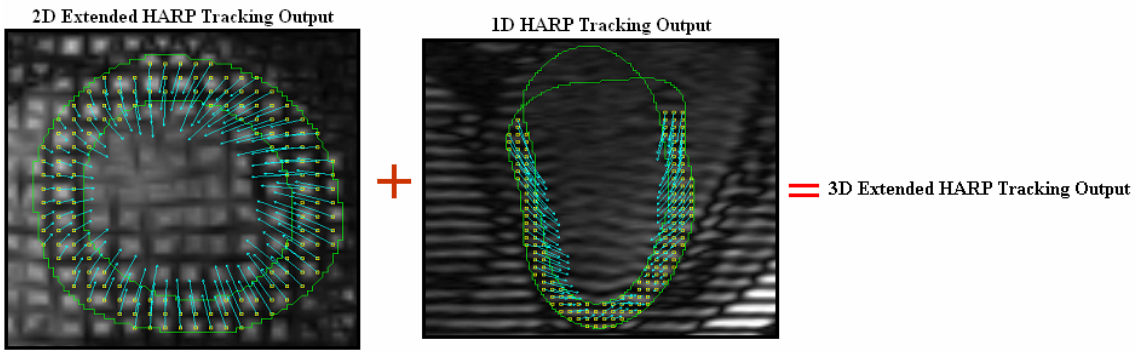

Figure 3-1 Schematic representation of the extended 3D HARP tracking algorithm. Blue arrows represent the displacement of the tag points between end-diastole and ES. Green lines correspond to the endocardial and epicardial contours of the LV myocardium. Yellow points represent the tracked tag points. On the left – SA image plane at end-diastole. On the right – LA image plane at end-diastole.

The 2D algorithm tracks the tag points on the SA image planes, giving the projection of their motion on these planes. The 1D HARP tracking algorithm tracks the tag points on the LA image planes, determining the longitudinal component of their motion. In this chapter a detailed description of the 1D HARP tracking algorithm is given.

3.2.2. 1D HARP Tracking

The principle of 1D HARP tracking is the same as that of 2D HARP tracking (see Chapter 1 and ref [85, 98]). However, due to differences in the inputs, some changes have to be applied. A flow chart of the 1D HARP tracking algorithm is presented in Appendix II. The main steps of this algorithm are described in detail hereafter.

3.2.2.1. Input

The input of the 1D HARP tracking algorithm is:

- Complementary spatial modulation of magnetization (CSPAMM) MR images of the LA image planes with tag lines perpendicular to the LA
- contours of the LV myocardium
- image parameters
- tracking parameters

CSPAMM images [92] are computed as explained in Chapter 2. Contrarily to the 2D algorithm that requires two sets of CSPAMM images as input (one with horizontal tag lines and one with vertical tag lines), the 1D algorithm only requires one set of CSPAMM images with the tag lines perpendicular to the LA. An additional set of images with tag lines parallel to the LA could also be acquired, however, that would increase the acquisition time and no new information would be added, since the 2D algorithm already tracks this component of the myocardial motion.

Myocardial contours of the LV are drawn manually for all time frames on the HARM images, using the MASS software package (version 5.1b, MEDIS, Leiden, The Netherlands).

The image parameters provided by the user are: field-of-view (FOV) in mm, FOV in pixels, tag period in mm, direction of the tag lines in the LA image planes.

The tracking parameters provided by the user are: maximum of iterations allowed for a successful tracking, the image used to compute target HARP angle and the minimum distance allowed between tracked points. These tracking parameters are discussed below.

3.2.2.2. HARM and HARP images computation

The harmonic magnitude (HARM) and HARP angle images are obtained from the CSPAMM images after applying the Hilbert transform as explained in Chapter 2.

The HARM images are used to define the epicardial and endocardial contours that delineate the LV myocardium. The HARP angle images are used to track the tag points inside these myocardial contours at each time frame.

3.2.2.3. Target HARP angle computation

As for the extended 2D HARP tracking, the target HARP angle is computed as explained in Chapter 2. As no new tag lines were observed on the LA image planes processed in this thesis, the target HARP angle is only computed for the pixels inside the myocardial contours of the undeformed image. However, an extended version of the 1D HARP tracking is also possible.

After computing the target HARP angle, an activity label is given to each tag point as in the extended 2D version. The points inside the myocardial contours are labeled as “active” and those outside are labeled as “inactive”. During the tracking process, this activity label is used as a trigger to track or not to track a tag point.

Besides the activity label, the 1D HARP tracking algorithm also requires a localization label for each tag point. This label is necessary to estimate the displacement of the tag points on the direction of the tag lines (y-direction in Figure 3-2). As this algorithm has only one set of

images with the tag lines perpendicular to the LA, only the component in the LA direction can be tracked (*z*-direction in Figure 3-2). However, during myocardial contraction, it is necessary to update the *y*-component of the tag points position, otherwise these tag points end up falling outside the myocardial contours due to the conical shape of the heart, and become inactive (see Figure 3-2).

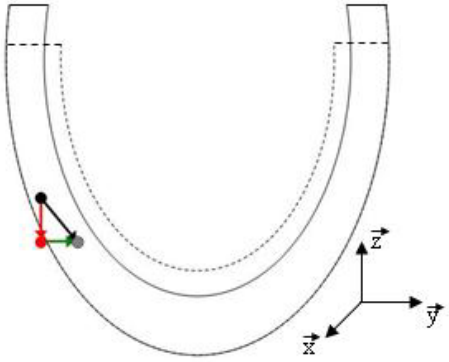

Figure 3-2 Schematic representation of a tag point displacement in a LA image plane. Solid line represents the myocardial contours of the LV at end-diastole and dashed line the myocardial contours of the LV at the next time frame. For a better visualization, the displacement of the tag point between these two successive time frames was exaggerated. The black point represents the tag point at end-diastole and the grey point the tag point at the next time frame. The displacement performed by the tag point is depicted by the black arrow. However, the 1D algorithm only tracks the tag point along *z*-direction (red arrow), as the tag lines are parallel to the *y*-axis (not visualized). The displacement in the *y*-direction (perpendicular to the LA) has to be estimated (green arrow). If this component of the motion is not updated, the point ends up outside the myocardial contours and is set as inactive (red point). This component of the motion is estimated by assuming that the relative distance in the *y*-direction between the point and the myocardial contours does not change during deformation.

Such situation can be overcome using the myocardial contours to estimate this component of the tag point position. For a LA image plane with the tag lines in the *y*-direction, this estimation is done in the following way:

first the LV is divided into three regions: region A, region B and apex (see Figure 3-3). This is performed automatically, based on the coordinates of the myocardial contours and taking into account that at the apex there is no endocardial contour.

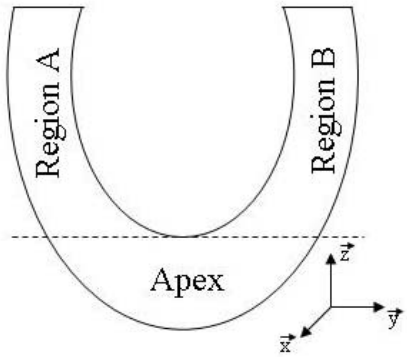

Figure 3-3 Definition of the LV regions.
In the apical region there is only epicardial contour of the LV myocardium

Secondly, the relative distance in the *y*-direction between each tag point and the myocardial contours is computed in the undeformed state, using the formula (see Figure 3-4):

$$\begin{cases} \dfrac{y - Epi_{y\,min}}{Endo_{y\,min} - Epi_{y\,min}} & if \ \ (y,z) \in regionA \\ \dfrac{y - Endo_{y\,max}}{Epi_{y\,max} - Endo_{y\,max}} & if \ \ (y,z) \in regionB \\ \dfrac{y - Apex_{y\,min}}{Apex_{y\,max} - Apex_{y\,min}} & if \ \ (y,z) \in apex \end{cases} \qquad \text{Equation 3-1}$$

with *(y,z)* the undeformed position of the tag point, Epi_{ymin}, Epi_{ymax}, $Endo_{ymin}$, $Endo_{ymax}$, $Apex_{ymin}$, $Apex_{ymax}$ the *y*-coordinates of the intersection of an horizontal line through the tag point, with the epicardial and endocardial contours in the regions A, B and apex respectively (see Figure 3-4).

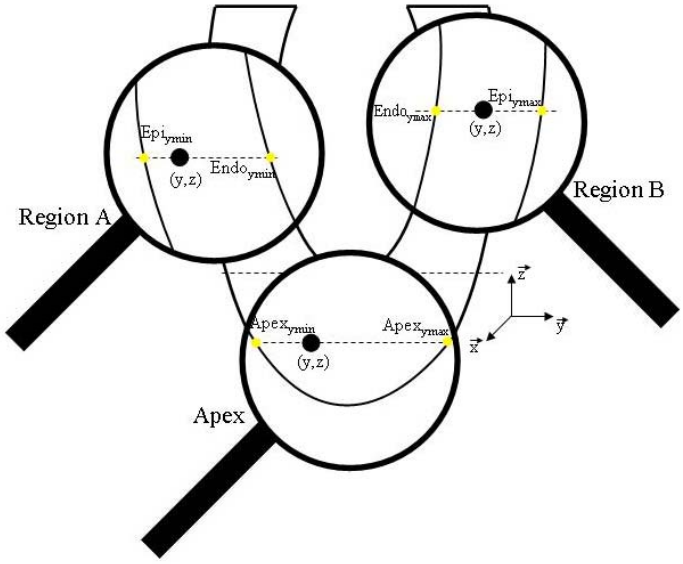

Figure 3-4 Definition of the LV myocardial contour coordinates.
These coordinates are used to compute the position of the tag point (black point) relative to the myocardial contours. Yellow points represent the projection of the tag point position into the myocardial contours. The *z*-position of the intersections points (in yellow) is the same as the tag point (in black).

Assuming that the relative distance to the myocardial contours is constant during all the cardiac cycle, the position of a tag point in the tag line direction in the deformed state is given by (see Figure 3-4):

$$\begin{cases} y_d = \dfrac{(y - Epi_{y\,min}) * (Endo_{yd\,min} - Epi_{yd\,min})}{Endo_{y\,min} - Epi_{y\,min}} + Epi_{yd\,min} & if \ \ (y,z) \in regionA \\ y_d = \dfrac{(y - Endo_{y\,max}) * (Epi_{yd\,max} - Endo_{yd\,max})}{Epi_{y\,max} - Endo_{y\,max}} + Endo_{yd\,max} & if \ \ (y,z) \in regionB \\ y_d = \dfrac{(y - Apex_{y\,min}) * (Apex_{yd\,max} - Apex_{yd\,min})}{Apex_{y\,max} - Apex_{y\,min}} + Apex_{yd\,min} & if \ \ (y,z) \in apex \end{cases}$$

Equation 3-2

where y_d is the deformed position of the tag point, and Epi_{ydmin}, Epi_{ydmax}, $Endo_{ydmin}$, $Endo_{ydmax}$, $Apex_{ydmin}$, $Apex_{ydmax}$ the y-coordinates of the epicardial and endocardial contours in the deformed state in regions A, B and apex respectively. However, during the cardiac cycle a tag point that is initially in region A or B can migrate to the apex, and vice-versa. For this reason, it is necessary at each time frame to verify the region where the tag point is, and in case of changes automatically update the localization label. In this case, the reference relative position will not be the relative position at the undeformed state but the relative position at the time frame the tag point enters the new region.

3.2.2.4. Tracking "Active" points

The 1D HARP tracking algorithm is based on the following equation:

$$\phi(\vec{r}, t_{m+1}) - \phi(\vec{r}_m, t_m) = 0 \qquad \text{Equation 3-3}$$

with $\phi(\vec{r}_m, t_m)$ the harmonic phase on position $\vec{r}_m = (y_m, z_m)$ at time t_m. y-direction corresponds to the tag line direction and z-direction to the LA direction. As the phase value of a tag point remains constant through all the cardiac cycle, tracking a point that is on the position $\vec{r}_m = (y_m, z_m)$ at the time frame t_m, consists of finding the position $\vec{r} = (y_d, z)$ on the next time frame for which the phase difference is null, with y_d given by Equation 3-2. With an iterative process, this position can be estimated using the equation:

$$\vec{r}^{(n+1)} = \vec{r}^{(n)} - \left[\frac{\partial}{\partial z}\phi(\vec{r}^{(n)}, t_{m+1})\right]^{-1} \cdot \left[\phi(\vec{r}^{(n)}, t_{m+1}) - \phi(\vec{r}_m, t_m)\right] \qquad \text{Equation 3-4}$$

with $\partial / \partial z$ the derivative on the LA direction and n the iteration step counter. For each iteration, the position in the tag line direction is updated by computing y_d from Equation 3-2.

As in the original version, the HARP image, $\phi(\vec{r}_m, t_m)$, is unknown and the computed HARP angle image, $a(\vec{r}_m, t_m)$, has to be used instead. To replace the unknown $\phi(\vec{r}_m, t_m)$ in the previous equation by the known $a(\vec{r}_m, t_m)$ some modifications have to be made (see Chapter 2), and the resulting equation is:

$$\vec{r}^{(n+1)} = \vec{r}^{(n)} - \left[\frac{\partial^*}{\partial z}a(\vec{r}^{(n)}, t_{m+1})\right]^{-1} \cdot W\left(a(\vec{r}^{(n)}, t_{m+1}) - a(\vec{r}_m, t_m)\right) \qquad \text{Equation 3-5}$$

On the original HARP tracking version the successful tracking stop criteria for this iterative equation are (see Chapter 1 and reference [85]):

- tracking error smaller than a constant defined by the user
- maximum of iterations not exceeded

For 1D HARP tracking the criteria are the same as for the extended 2D HARP tracking, which are:

- tracking error smaller than a value given by Equation 2-8
- maximum of iterations not exceeded
- tracked position falls inside the myocardial contours of the current time frame
- displacement of the tracked point smaller than c.λ/2 (with c a scaling constant equal to 0.8 in this study)
- topology of the set of "active" points remains unchanged during tracking process
- number of "active" near neighbours is larger than 2, in order to check the topology

- relative distance between “active” near neighbours remains larger than a minimum value defined by the user

The reason for each of these conditions is explained in detail in Chapter 2. In summary, they restrict the tracking to the tag points inside the myocardial contours and prevent the tracked position to converge to an incorrect tag line.

The first step to track a tag point that is on position $\vec{r}_m$ at time frame t_m is to define its starting position $\vec{r}^{(0)}$ at time frame t_{m+1}. Since the motion between successive time frames is small, a good estimation is $\vec{r}^{(0)} = \vec{r}_m$, which means that the point has the same position as on the previous time frame. Secondly, the stop criteria are checked for this new position on the time frame t_{m+1}. If all conditions are fulfilled, the point is considered successfully tracked and the algorithm proceeds tracking another point inside the myocardial contours. Otherwise, the following steps are followed. The step size is computed using the formula:

$$v^{(n)} = -\left[\frac{\partial^*}{\partial z} a(\vec{r}^{(n)}, t)\right]^{-1} . W\left(a(\vec{r}^{(n)}, t) - a^*\right) \qquad \text{Equation 3-6}$$

with $a(\vec{r}^{(n)}, t)$ the HARP angle value of the estimated position at time frame *t* and iteration *n* and a^* the respective target HARP angle. As the HARP angle is wrapped between [-π,π), it is necessary to locally unwrap it before interpolating $a(\vec{r}^{(n)}, t)$ to the position $\vec{r}^{(n)}$. After that, the interpolated HARP angle is wrapped between [-π,π) and the target HARP angle is subtracted from it. The resultant difference is again wrapped between [-π,π), as is represented in Equation 3-6 by the operator *W*. The derivative of the HARP angle is also interpolated for the tracked position $\vec{r}^{(n)}$. Both interpolations are performed using a window with 4 near neighbors. Since the solution for this iterative equation is not unique due to the wrap effect of the HARP angle, it is necessary to restrict the step size in order to avoid jumps between different tag lines. The step size is then limited to 1 pixel using the formula:

$$\alpha(n) = min\left\{\frac{1}{\left|v^{(n)}\right|}, 1\right\} \qquad \text{Equation 3-7}$$

Next, the estimated position is updated:

$$\vec{r}^{(n+1)} = \vec{r}^{(n)} + \alpha^{(n)} v^{(n)} \cdot e_z \qquad \text{Equation 3-8}$$

with $\vec{e}_z$ the unit vector in the *z*-direction. If this new position does not fulfill the stop criteria, a new step size is computed and the previous steps are repeated.

This algorithm is applied to all active points at all time frames.

3.2.2.5. Recover tag points lost due to noise

During the cardiac cycle, some tag points can be lost due to artefacts in the image. However, it is important that the tracking algorithm is able to recover these points in subsequent time frames. To do so, a procedure equivalent to that described in Chapter 2 to track new tag lines that appear in the image plane and recover tag lines that disappear is applied. In summary, the information of the successfully tracked points is used in the following way: after tracking all "active" points, the absolute displacement field is computed. If a point is currently "inactive" due to noise in the image, but two or more of its near neighbours are "active", the displacement of this "inactive" point is set equal to the averaged displacement of its "active" neighbours. The resulting extrapolated displacement is then applied to the "inactive" point which will be tracked.

3.2.2.6. 1D displacement

After tracking all active points and recovering possible "inactive" tag points for the first time frame, the same procedure is applied to the remaining time frames of the cardiac cycle. At the end an absolute displacement field is obtained for each instant. These 1D displacement fields are then filtered using a moving average with a kernel size of 5 pixels. This filter is applied in order to obtain smoother strain values.

3.2.2.7. Output

The algorithm output is a text file with the filtered positions of all the points that are initially inside the tracking region for all time frames. When the point is inactive its filtered position is set negative. This nomenclature is given in order to avoid the inclusion of these points on the definition of the tetrahedrons mesh for strain computation. After the positions are listed the coordinates of the contours of the LV myocardium are written for all time frames. This information is then used to compute the 3D myocardial strain.

3.2.3. 3D displacement of the LV myocardium

Due to through plane motion of the heart, a myocardial point is not imaged during the full cardiac cycle. Consequently, when tracking a tag point on a SA image plane, the measured displacement corresponds to the projection of the true 3D displacement of the myocardial point on this image plane.

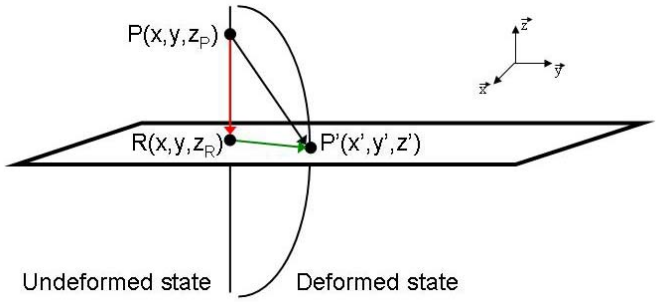

Figure 3-5 Comparison between displacement assessed with extended 2D and 3D HARP tracking. R(x,y,z_R) and P'(x',y',z') correspond to the tag points imaged in the undeformed and deformed state, respectively. P(x,y,z_p) is the material point corresponding to the point P' imaged in the deformed state. The green arrow represents the projection of the displacement of the material point P in the SA image plane, assessed with the extended 2D HARP tracking. The red arrow depicts the longitudinal motion of the material point P. The black arrow represents the 3D displacement of the material point, assessed with extended 3D HARP tracking

In Figure 3-5, a diagram with the displacements assessed by the extended 2D (green arrow) and 3D (black arrow) HARP tracking methods are presented. In the undeformed state the tag lines are perpendicular to the SA image plane. In Figure 3-5, two points are represented: the material point P which is located at the intersection line of two orthogonal tag planes and the R tag point which is located at the intersection line of two orthogonal tag planes inside the SA image plane. When an image is acquired at this time frame, the point that is imaged is the R point. When the deformed state is imaged, it is verified that the tag point R is not anymore in the SA image plane. Instead, the imaged tag point P' corresponds to the material point P in the undeformed state. However, as the tag planes are perpendicular to the SA image plane in the undeformed state, the x- and y-coordinates in the image plane of the material point P and of the imaged tag point R are the same. This means that when the tag pattern is tracked in the SA image plane, the result is the 2D projection in the SA image plane (represented in Figure 3-5 by the green arrow) of the 3D displacement of the material point P (represented in Figure 3-5 by the black arrow). To measure the 3D displacement of the material point P (black arrow in Figure 3-5), the only coordinate that is unknown is the z-coordinate of P, as its (x,y) coordinates in the undeformed state correspond to the coordinates of the imaged tag point R and the deformed coordinates (x',y',z') of P' are know from the tracking and from the z position of the SA image plane. The longitudinal displacement (from the z_p position in the undeformed state to z' in the deformed state) is obtained with the 1D HARP tracking algorithm applied to the tagged images of the LA LV (which have the tag lines perpendicular to the LA).

The 3D displacement of the tag pattern is obtained by combining the 2D displacement computed with the extended 2D HARP tracking (green arrow in Figure 3-5) with the 1D displacement computed with the 1D HARP tracking (red arrow in Figure 3-5). This is

performed by interpolating the *z*-component of the displacement between the LA image planes, in order to estimate the *z*-component of the tracked points in the SA image planes. The interpolation along the curved geometry of the LV is done using a finite element (FE) model as is described below.

3.2.3.1. Geometric fit

To obtain a geometric model of the LV, inner and outer surfaces are fitted to the LA and SA myocardial contours of this cardiac chamber, using a FE model [11, 94]. As is shown in Figure 3-6**,** the most appropriate coordinate system to build a LV model is the prolate spheroidal.

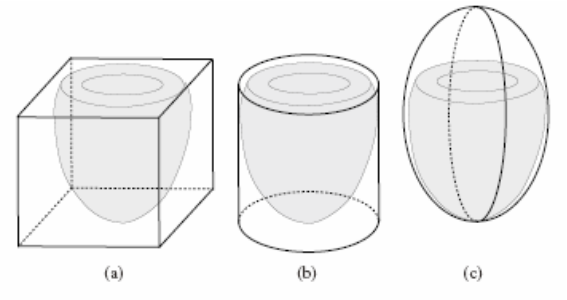

Figure 3-6 Coordinate systems typically used to model the LV.
(a) Cartesian domain, (b) cylindrical domain and (c) prolate spheroid domain. The LV model is represented in grey ([99])

This coordinate system is defined by (λ,ϕ,θ) with λ the radial coordinate, ϕ the longitudinal coordinate and θ the circumferential coordinate (see Figure 3-7).

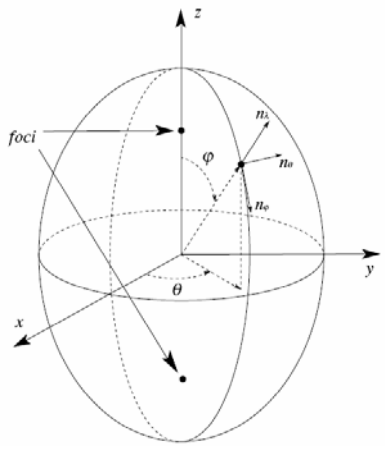

Figure 3-7 Prolate spheroidal coordinate system [99]

The Cartesian coordinate system (x,y,z) is related to this coordinate system by the formula:

$$\begin{aligned} x &= f \sinh\lambda \sin\phi \cos\theta \\ y &= f \sinh\lambda \sin\phi \sin\theta \\ z &= f \cosh\lambda \cos\phi \end{aligned} \qquad \text{Equation 3-9}$$

with f the distance between the origin and the focus in the z-axis. The origin of this coordinate system is set at one third from the base of the distance between the projections onto the z-axis of the basal and apical markers. The markers are manually defined by the user on an end systolic LA image (see Figure 3-8), with the basal marker in the mitral valve plane and the apical marker at the point on the endocardial contour closest to the apex. The focus of the coordinate system is computed by setting the radial position λ of the projected apical marker equal to 0.35. This value was determined empirically in order to obtain the model that better resembles a contracted LV [11].

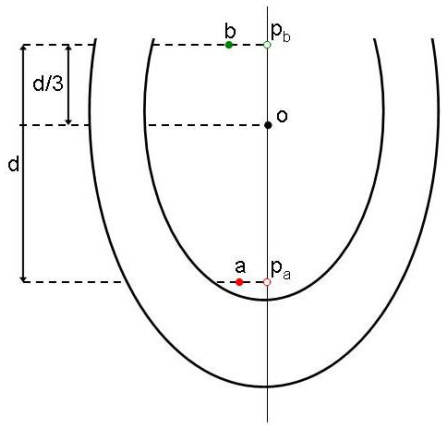

Figure 3-8 Definition of the origin of the prolate spheroidal coordinate system.
Solid lines represent the myocardial contours of the LV in a LA image plane. d – distance between the projection onto the z-axis of the apical and basal markers. O – origin of the prolate spheroidal coordinate system. a – apical marker. p_a – projection of the apical marker onto the z-axis. b – basal marker. p_b – projection of the basal marker onto the z-axis.

The Cartesian coordinate system of the LV is defined in the following way: z-axis is set perpendicular to the SA image planes and along the intersection line of the LA image planes, x-axis is set parallel to the septum, in the first LA image plane, pointing to the anterior region of the LV, and the y-axis is set perpendicular to the x-axis pointing to the free wall of the LV (see Figure 3-9)

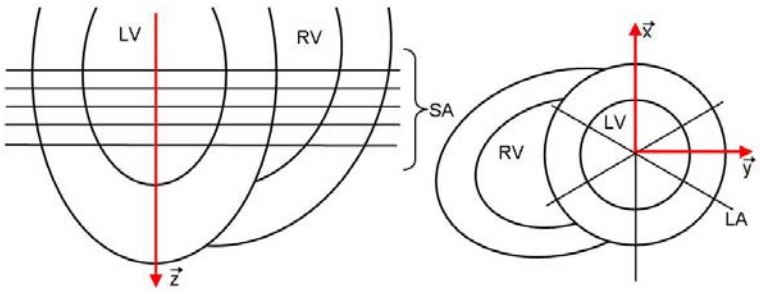

Figure 3-9 Definition of the Cartesian coordinate system of the LV.
Solid lines represent the myocardial contours of the LV in a LA image plane (left image) and in a SA image plane (right image). LV - left ventricle. RV- right ventricle.

The FE model fitted to the LV myocardial contours comprises 16 elements equally distributed in the circumferential and longitudinal directions. The LV geometry is defined by fitting the radial coordinate λ of the FE nodes to the LV myocardial contours of the LA and SA, using a least-square fit. By using the SA contours a better estimate of the LV curvature between LA image planes is achieved [11].

3.2.3.2. *z*-displacement field fit

After obtain the LV geometry, a 1D displacement field is fitted to the longitudinal motion measured in the LA image planes by the 1D HARP tracking algorithm [11]. A new mesh of FE is defined with the nodal points located at the intersections of the fitted surfaces of the LV model and the LA image planes. The nodal values are then fitted to the measured *z*-displacement data again using a least-squares fit. An example of the resulting FE geometry for three LA image planes is shown in Figure 3-10 [11].

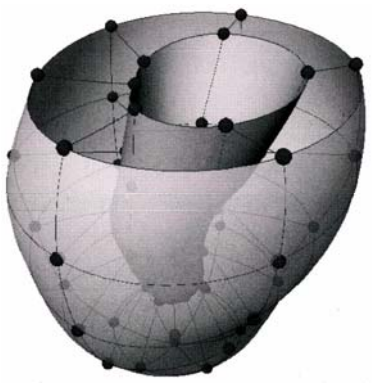

Figure 3-10 Example of the FE geometry for three LA image planes.
Black points represent the nodal points placed in the intersection of the LA image planes with the fitted surfaces of the LV model. Adapted from [11].

An estimation of the *z*-displacement in any point of the LV can then be obtained by interpolation between the fitted nodal values.

Finally, the 3D displacement of the LV myocardial points is determined by combining the *x*- and *y*-displacements measured directly from the SA image planes with the *z*-displacement at the same point estimated from the fitted displacement field.

3.2.4. 3D myocardial strain

The 3D strain computation is explained in detail in Chapter 1. In summary, a homogeneous strain analysis was applied to a mesh of tetrahedrons defined with the points tracked in the 5 SA image planes [100]. For each tetrahedron the deformation gradient tensor $\vec{F}$ was computed and the Lagrangian strain tensor $\vec{E}$ was given by:

$$\vec{E} = \frac{1}{2}\left(\vec{F}^T\vec{F} - 1\right) \qquad \text{Equation 3-10}$$

Using the radial-circumferential-longitudinal (rcl) coordinate system, the strain components were given by:

$$\varepsilon_i = \left(\sqrt{1+2E_{ii}} - 1\right)\times 100\% \qquad \text{Equation 3-11}$$

$$sin\,\alpha_{ij} = \frac{2E_{ij}}{(\varepsilon_i + 1)(\varepsilon_j + 1)} \quad (i \neq j) \qquad \text{Equation 3-12}$$

where E_{ij} are elements of the strain tensor $\vec{E}$ and *i* and *j* are equal to *r* (radial direction), *c* (circumferential direction) or *l* (longitudinal direction). The axial strains ε_i correspond to the percent change in length of a segment initially oriented in the *i* direction [91]. The shear strain components α_{ij} correspond to the change in angle between segments initially oriented in the perpendicular *i* and *j* directions [91].

To compare the 3D strain at different regions of the LV myocardium, the mean of the strain components was computed for three longitudinal slices, six circumferential segments and three transmural segments. A schematic representation of these regions is given in Figure 1-51.

3.2.5. Timing analysis

To investigate the existence of differences in the time to onset (T_{onset}) of circumferential and longitudinal shortening at different regions of the cardiac muscle, the T_{onset} of these strain components were computed for the septum and lateral wall. The septum comprises the segments infero-septal (IS) and antero-septal (AS) and the lateral wall the segments antero-lateral (AL) and infero-lateral (IL).

T_{onset} is defined as the instant when the down slope of the ε_c or ε_l curve starts. The definition of this timing parameter is given in Figure 3-11, for the circumferential strain curve of a healthy subject [67].

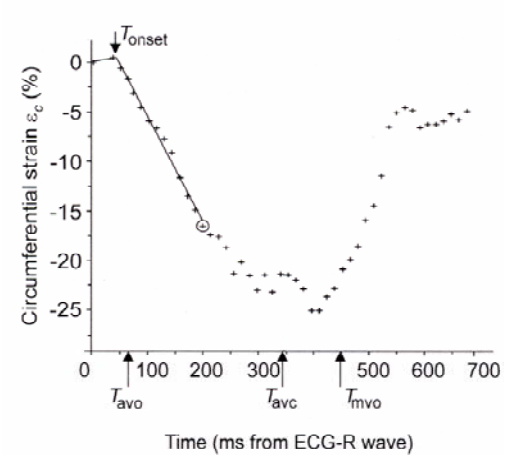

Figure 3-11 Definition of the time to onset (T_{onset}) of the circumferential shortening.
Solid line shows the model fitted to the data for estimating T_{onset}, and the encircled point marks the end point of the data used in the fit. T_{avo} – time of aortic valve opening. T_{avc} – time of aortic valve closure. T_{mvo} – time of mitral valve opening. Adapted from [67].

This timing parameter is automatically determined as described before [4]. Values of T_{onset} where automatically discarded for segments in which the goodness of fit, R, was less than 0.9 [4]. When the observer did not agree with the obtained values, he/she could discard them, but not adjust to prevent subjective changes of the results.

3.2.6. Subjects

Images were acquired in six healthy volunteers (6 male; mean age: 43 ± 13), who provided informed consent. No history of cardiac diseases was referred by any of these subjects.

Subject	1	2	3	4	5	6
Age	56	28	53	48	46	26
RR (ms)	1330	1200	1000	1270	1050	800
T_{avc} (ms)	412	345	347	375	358	317
$N_{time\ frames}$	49	63	49	49	56	46

Table 3-1 Characterization of the analysed healthy population.
RR – mean time interval between two R-waves. $N_{timeframes}$ – Number of tracked images during a cardiac cycle. T_{avc} – time of aortic valve closure.

3.2.7. Image acquisition

Images were acquired with a 1.5T whole body scanner (Magnetom Sonata, Siemens Medical Solutions, Erlangen, Germany), using a 4 element phased-array receiver coil.

Cine imaging with myocardial tagging was acquired with the steady state free precession (SSFP) sequence using the linearly increasing startup angle (LISA) approach (see Chapter 1 and reference [64]), with the parameters described in Chapter 2. Tissue tagging was applied with two non-selective 45° radio-frequency (RF) pulses separated by a field gradient in the readout direction, yielding a sinusoidal modulation of the magnetization [66]. The period of the tag lines was equal to 7 mm and the readout direction perpendicular to the tag lines.

Five equidistant SA planes were imaged between base and apex, with a distance between image planes equal to 10 mm to 15 mm. Three LA planes uniformly distributed around the LV and perpendicular to the SA were imaged, with an angular spacing equal to 60º [100] and the first LA image plane set parallel to the interventricular septum. Previous studies [100] have shown that this number of LA image planes suffices to detect abnormal contraction of the LV, as each territory of the coronary arteries (left-anterior descending artery, circumflex branch and right coronary artery) is (partly) present in at least one of these LA image planes.

To improve myocardial tagging contrast, CSPAMM was used on the SA and LA image planes [92]. Four sets of images were acquired for each SA image plane: vertically and horizontally tagged images with sinusoidal and inverted sinusoidal tagging (Figure 3-12). Two sets of images were acquired for each LA image plane: tagged images with sinusoidal and inverted sinusoidal tagging with the tagging direction perpendicular to the LA (Figure 3-12). The multiple brief expiration breath hold scheme described in Chapter 2 was performed in order to avoid mismatching between the several images per set.

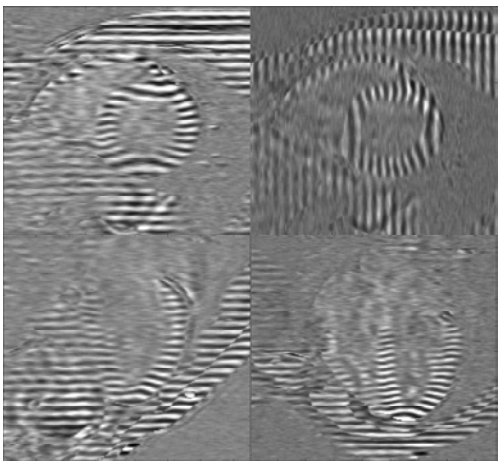

Figure 3-12 Example CSPAMM images of SA and LA image planes of a healthy volunteer. These images represent ES. From top to bottom and left to right: SA CSPAMM image with horizontal tag lines, SA CSPAMM image with vertical tag lines, LA 2 chamber view, LA 4 chamber view

To determine T_{avc} LA cine images in the 3-chamber view were acquired with SSFP imaging with a temporal resolution of 14 ms and with the image parameters described in Chapter 2.

3.2.8. Statistics

Results are presented as mean ± SD. P-values < 0.05 are considered statistically significant.

To compare the strain components at different regions of the LV, a multilevel regression analysis was performed (MLwiN, version 1.02.0002, Centre for Multilevel Modelling, London, United Kingdom [101, 102]). This analysis was used because the data is structured in a hierarchy with three levels (segments are clustered within slices and slices within subjects).

To compare the different regions of the LV myocardium, for each strain component a regression coefficient is computed, where the outcome variable is the strain component and the independent variable is the LV myocardial region (dichotomous variable that takes the value 0 for the region taken as the reference and 1 for the region to be compared). In this case, the obtained regression coefficients reflect the differences between strains in the two regions of the myocardium. The multilevel analysis corrects these regression coefficients between strain components and the myocardial region for dependency in the data due to the hierarchy.

To compare the T_{onset} of the circumferential and longitudinal shortening at the septum with the T_{onset} of the circumferential and longitudinal shortening at the free wall, a regression coefficient is computed. In this case the outcome variable corresponds to the timing variable and the independent variable to the LV myocardial region (dichotomous variable that takes the value 0 for the septum and 1 for the lateral wall). The obtained regression coefficient gives the timing difference between the lateral wall and the septum.

3.3. RESULTS

The LV myocardial strain curves at each slice and segment are presented for two healthy volunteers, one with the images with best quality (Subject 5, Figure 3-13) and the other with the images with least quality (Subject 1, Figure 3-14). For Subject 1, it was not possible to define tetrahedrons at the apical slice during ES due to some artefacts in the inferior wall.

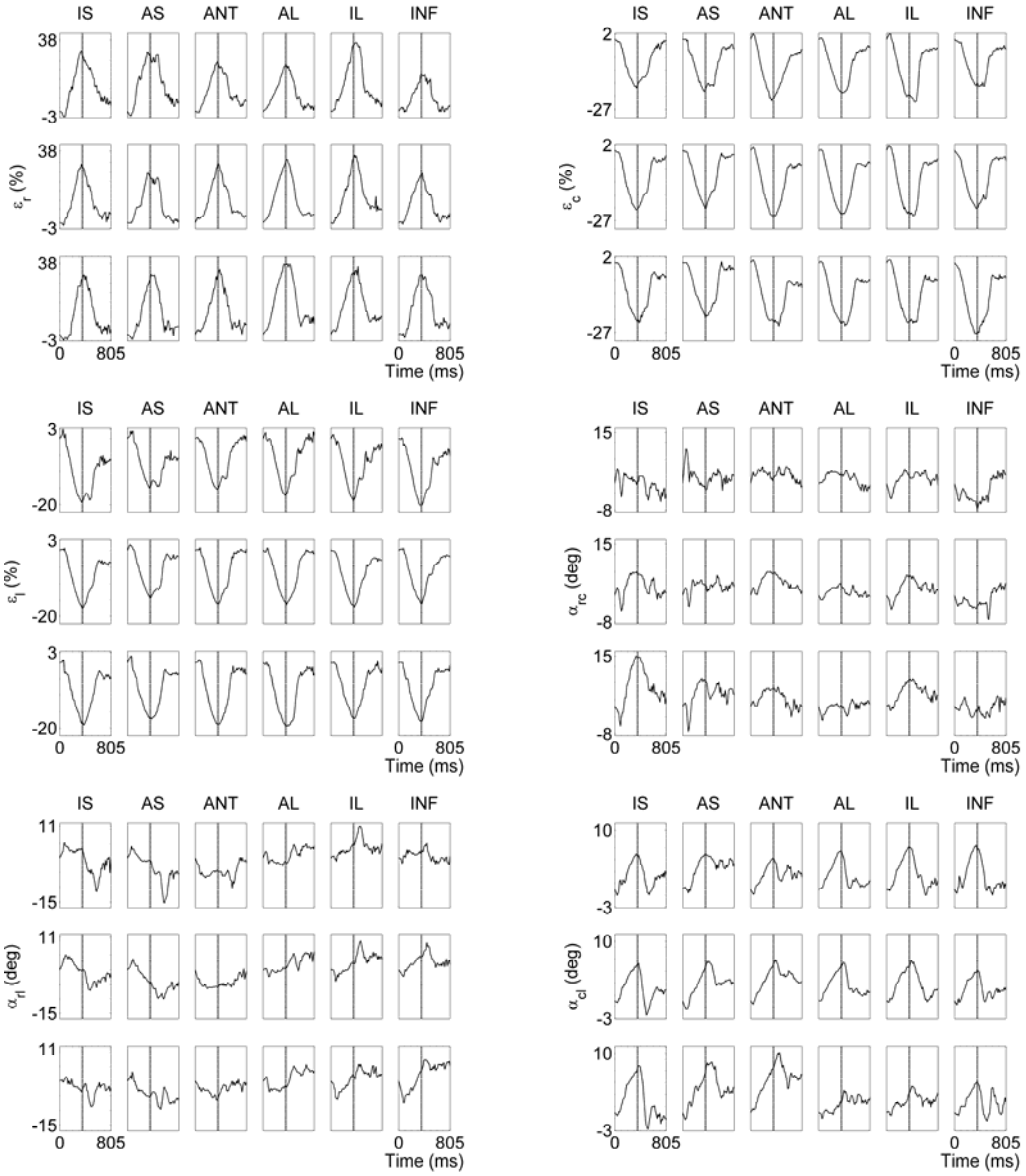

Figure 3-13 Temporal evolution of the LV myocardial strain components in each slice and circumferential segment (Subject 5).

Each group of 18 plots represents a component of the strain tensor. Inside each group, the top row corresponds to the basal slice, the mid row to the mid slice and the bottom row to the apical slice. The vertical line denotes the time of aortic valve closure (T_{ave}). ε_r – radial thickening; ε_c – circumferential shortening; ε_l – longitudinal shortening; α_{rc} – radial-circumferential shear; α_{rl} – radial-longitudinal shear; α_{cl} – circumferential-longitudinal shear. IS - infero-septal; AS - antero-septal; ANT - anterior; AL - antero-lateral; IL - infero-lateral; INF - inferior.

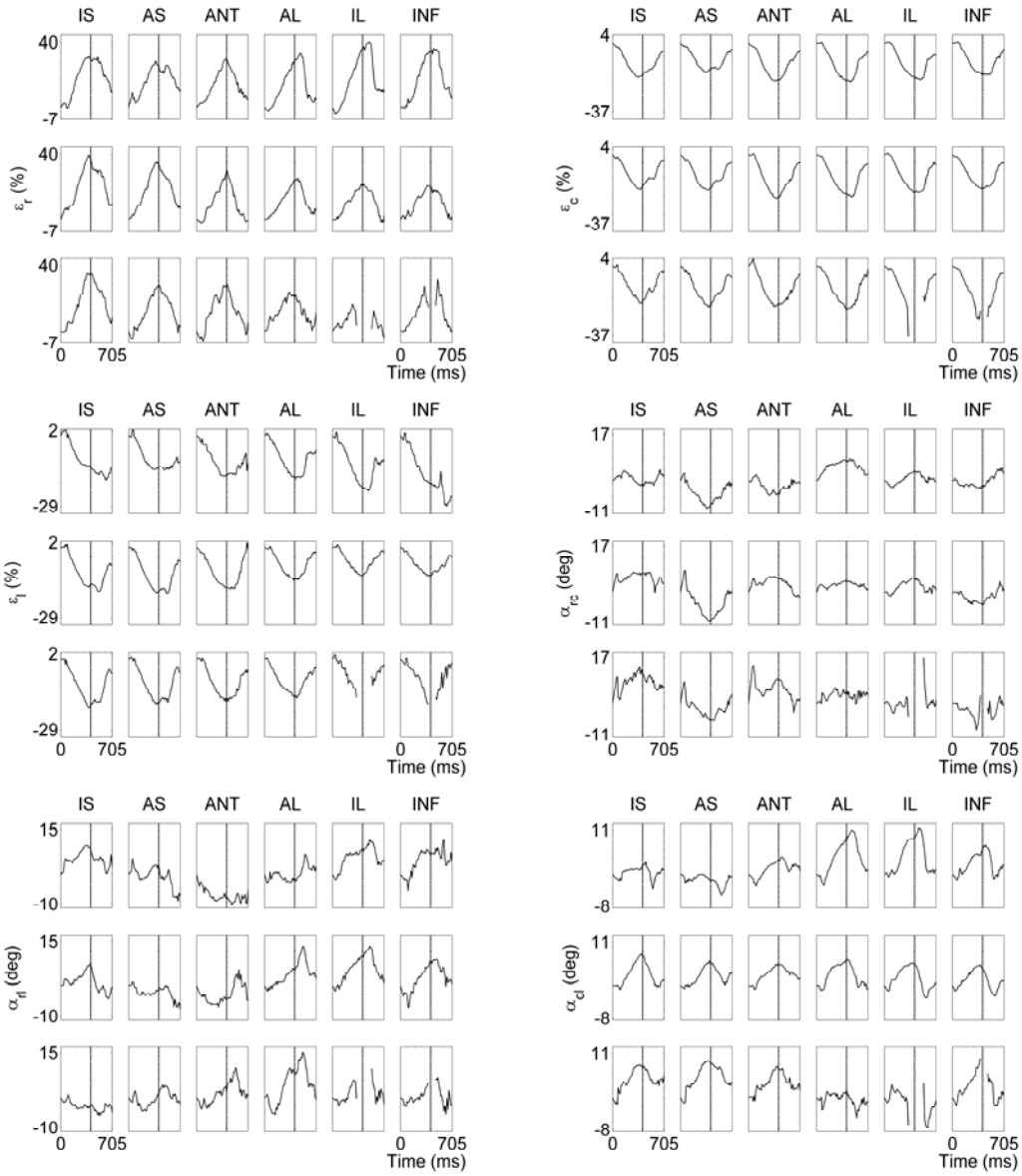

Figure 3-14 Temporal evolution of the LV myocardial strain components in each slice and circumferential segment (Subject 1).

Each group of 18 plots represents a component of the strain tensor. Inside each group, the top row of plots corresponds to the basal slice, the mid row to the mid slice and the bottom row to the apical slice. The vertical line denotes the time of aortic valve closure (T_{ave}). ε_r – radial thickening; ε_c – circumferential shortening; ε_l – longitudinal shortening; α_{rc} – radial-circumferential shear; α_{rl} – radial-longitudinal shear; α_{cl} – circumferential-longitudinal shear. IS - infero-septal; AS - antero-septal; ANT - anterior; AL - antero-lateral; IL - infero-lateral; INF - inferior.

The following plots show the temporal evolution of the mean strain components at each circumferential segment, for the same two subjects (Figure 3-15 and Figure 3-16).

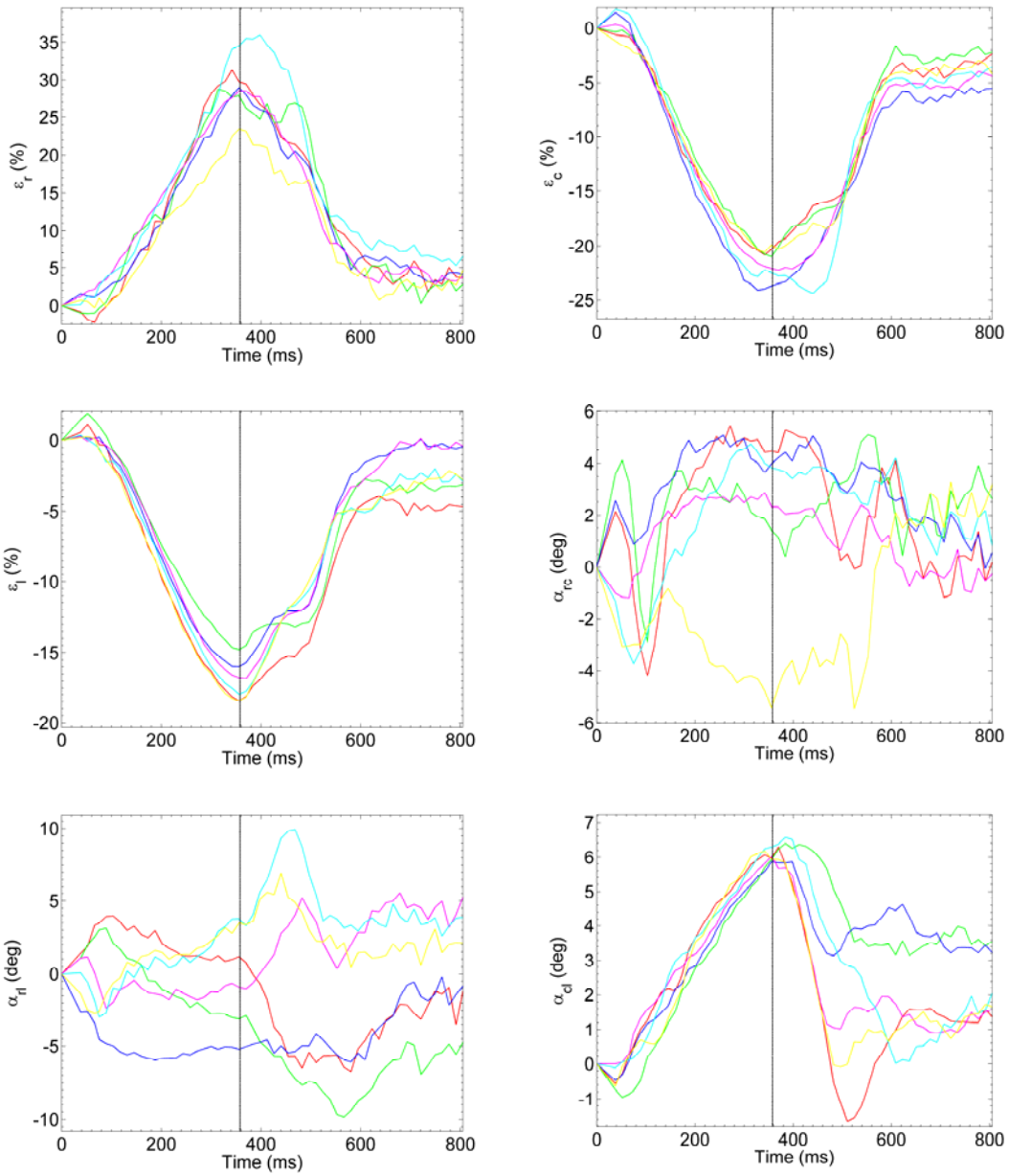

Figure 3-15 Temporal evolution per circumferential segment of the LV myocardial strain components during a cardiac cycle (Subject 5). The vertical line denotes the time of aortic valve closure (T_{avc}). ε_r – radial thickening; ε_c – circumferential shortening; ε_l – longitudinal shortening; α_{rc} – radial-circumferential shear; α_{rl} – radial-longitudinal shear; α_{cl} –circumferential-longitudinal shear. Red curve - IS (infero-septal); Green curve – AS (antero-septal); Blue curve - ANT (anterior); Pink curve - AL (antero-lateral); Light blue curve - IL (infero-lateral); Yellow curve - INF (inferior).

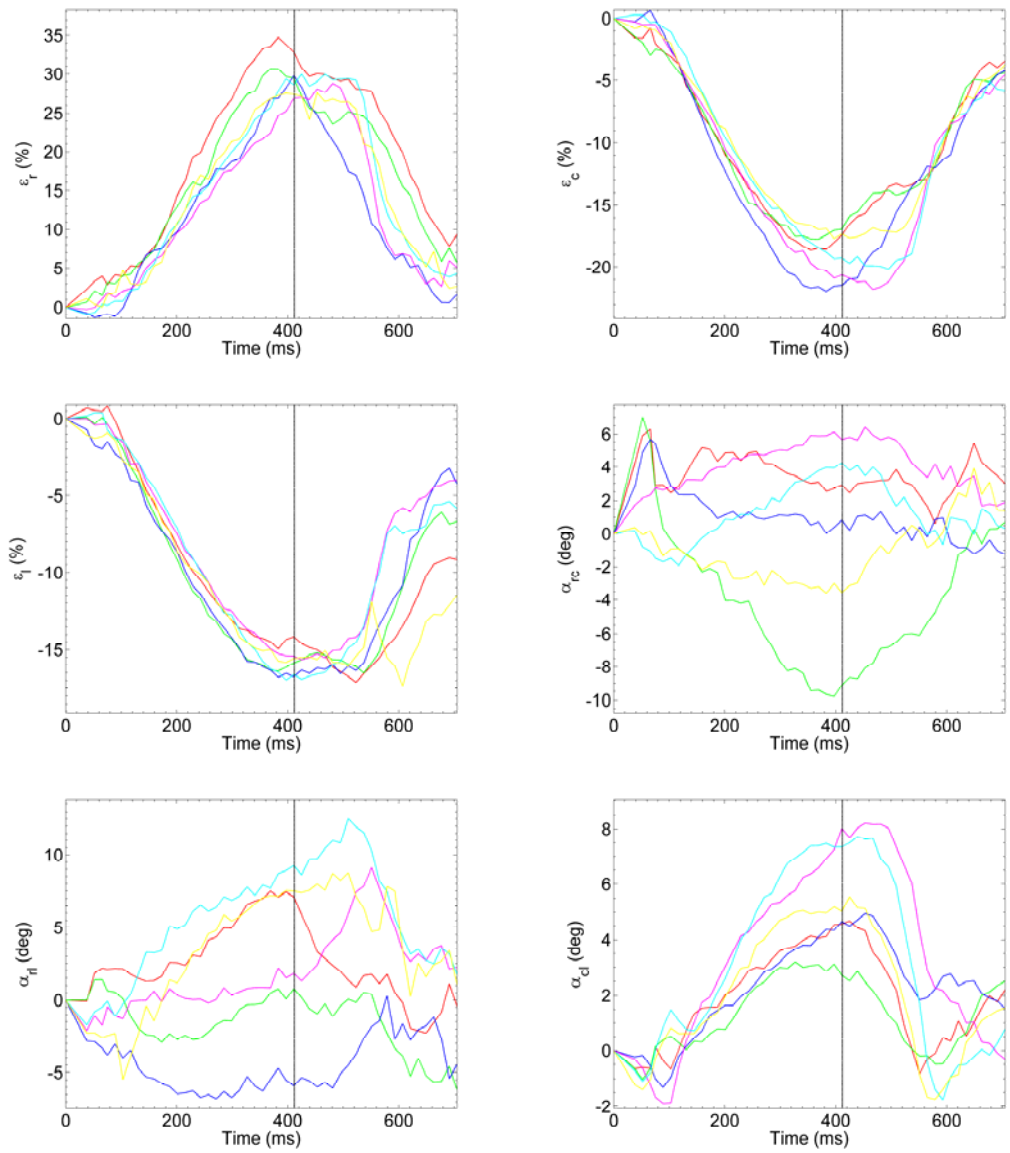

Figure 3-16 Temporal evolution per circumferential segment of the LV myocardial strain components during a cardiac cycle (Subject 1). The vertical line denotes the time of aortic valve closure (T_{avc}). ε_r – radial thickening; ε_c – circumferential shortening; ε_l – longitudinal shortening; α_{rc} – radial-circumferential shear; α_{rl} – radial-longitudinal shear; α_{cl} –circumferential-longitudinal shear. Red curve - IS (infero-septal); Green curve – AS (antero-septal); Blue curve - ANT (anterior); Pink curve - AL (antero-lateral); Light blue curve - IL (infero-lateral); Yellow curve - INF (inferior).

The temporal evolution of the LV myocardial strain components per slice is also represented in the following plots (Figure 3-17 and Figure 3-18).

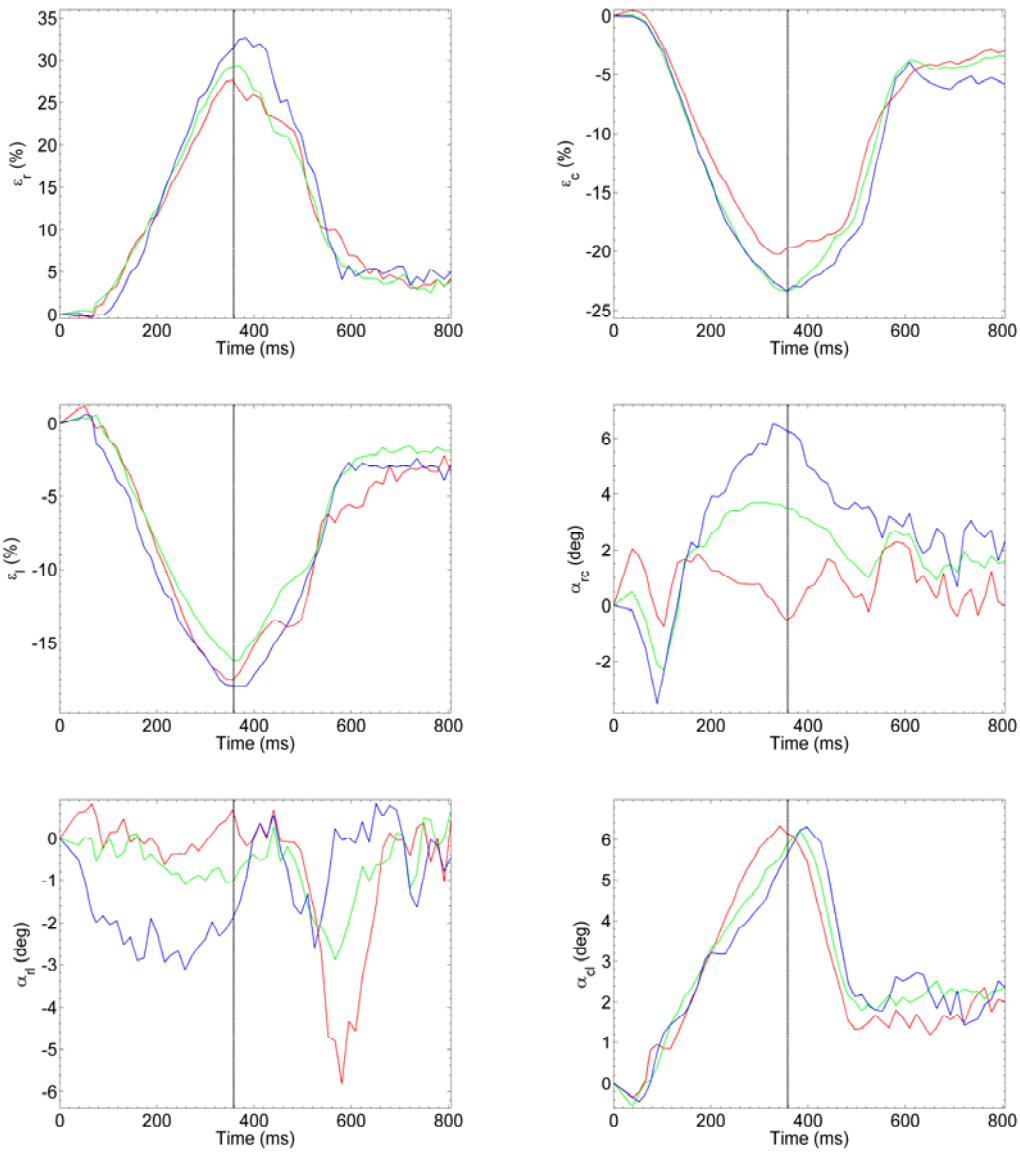

Figure 3-17 Temporal evolution per slice of the LV myocardial strain components (Subject 5). **The vertical line denotes the time of aortic valve closure (T_{avc}). ε_r – radial thickening; ε_c – circumferential shortening; ε_l – longitudinal shortening; α_{rc} – radial-circumferential shear; α_{rl} – radial-longitudinal shear; α_{cl} – circumferential-longitudinal shear. Red curve – Basal slice. Green curve – Mid slice. Blue curve – Apical slice.**

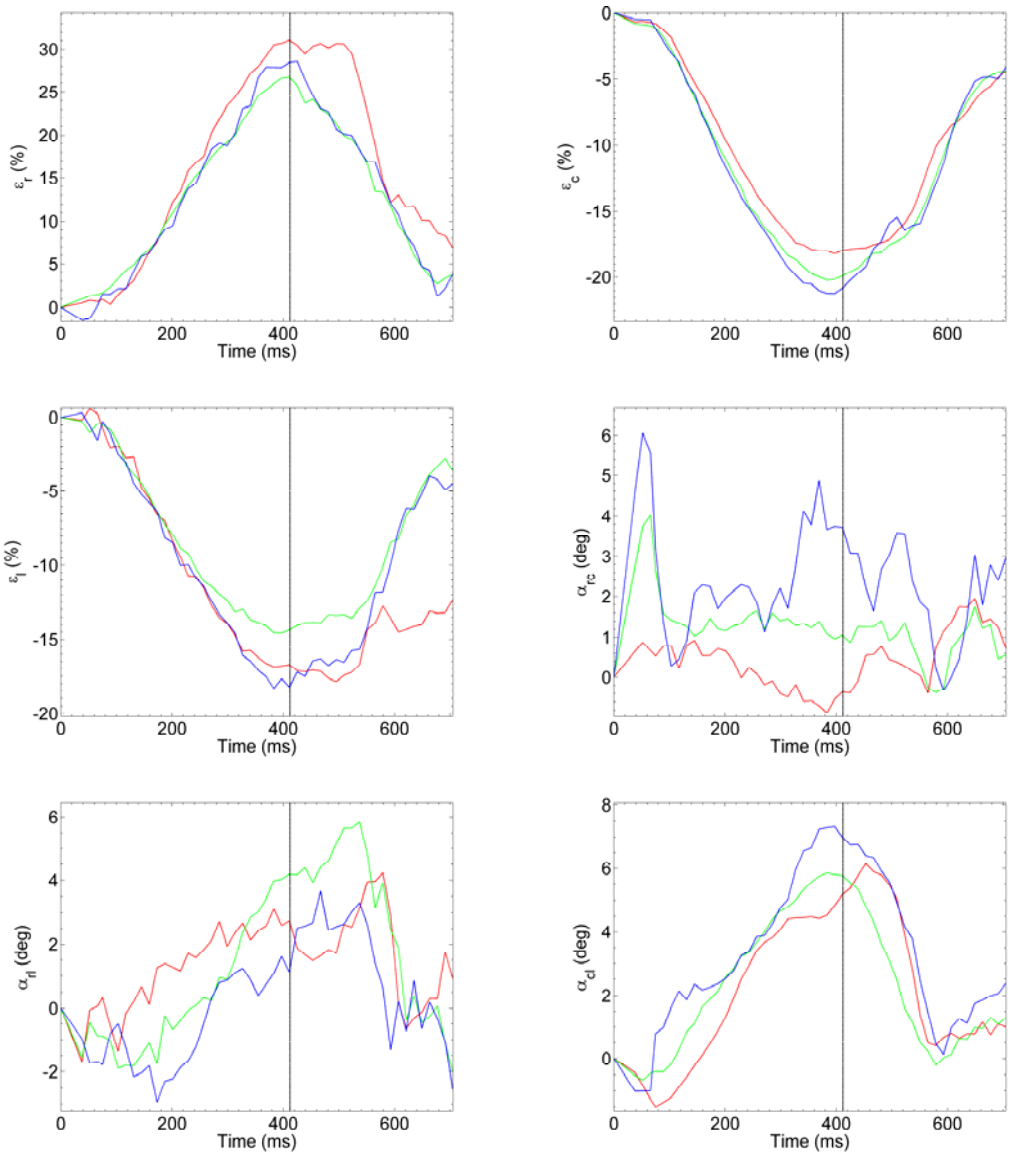

Figure 3-18 Temporal evolution per slice of the LV myocardial strain components (Subject 1). The vertical line denotes the time of aortic valve closure (T_{avc}). ε_r – radial thickening; ε_c – circumferential shortening; ε_l – longitudinal shortening; α_{rc} – radial-circumferential shear; α_{rl} – radial-longitudinal shear; α_{cl} – circumferential-longitudinal shear. Red curve – Basal slice. Green curve – Mid slice. Blue curve – Apical slice.

These plots show that the temporal evolution of ε_r, ε_c, ε_l and α_{cl} during a cardiac cycle describe well defined patterns in the different LV regions. The maximum of these strain components are reached around the T_{avc} and usually the strain value do not return to zero at the end of the covered period of the cardiac cycle (80 – 90% of the RR interval for all subjects). Instead it reaches a positive plateau, for ε_r and α_{cl}, and a negative plateau for ε_c and ε_l.

For α_{rc} and α_{rl} the curves are less smooth and a high variability is observed between subjects.

3.3.1. LV myocardial strain at ES

The mean strains of the 6 subjects at ES are presented in Table 3-2. In average ES occurred at 355 ± 33 ms.

	Mean	IS	AS	ANT	AL	IL	INF
ε_r (%)							
BASE	27.22 ± 6.61	27.33 ± 4.26	25.06 ± 7.41	25.83 ± 6.02	27.46 ± 8.18	34.26 ± 7.78	23.51 ± 9.08
MID	23.11 ± 5.74	28.55 ± 7.02	26.09 ± 4.74	21.78 ± 8.54	22.05 ± 8.03	22.52 ± 10.02	19.51 ± 4.91
APEX	25.92 ± 6.05	25.15 ± 8.26	27.34 ± 5.16	25.77 ± 5.09	24.54 ± 8.95	26.87 ± 11.11	28.02 ± 7.52
	25.58 ± 5.84	**27.45 ± 5.44**	**25.77 ± 4.90**	**24.56 ± 6.10**	**25.24 ± 7.15**	**28.99 ± 7.12**	**22.42 ± 6.52**
ε_c (%)							
BASE	-19.02 ± 2.12	-18.08 ± 3.48	-18.34 ± 3.59	-20.79 ± 2.10	-19.92 ± 1.25	-19.81 ± 1.57	-16.77 ± 2.82
MID	-21.50 ± 2.85	-20.29 ± 4.16	-21.07 ± 4.37	-24.25 ± 2.74	-21.90 ± 3.34	-22.39 ± 1.53	-18.90 ± 3.28
APEX	-22.46 ± 2.27	-20.83 ± 3.97	-22.42 ± 3.03	-23.18 ± 2.15	-22.34 ± 1.81	-22.71 ± 1.49	-23.37 ± 4.77
	-20.30 ± 2.32	**-19.28 ± 3.66**	**-19.99 ± 3.70**	**-22.33 ± 1.91**	**-20.77 ± 1.90**	**-21.01 ± 1.39**	**-18.09 ± 2.91**
ε_l (%)							
BASE	-16.20 ± 2.98	-15.18 ± 3.23	-12.23 ± 2.60	-15.29 ± 2.63	-16.99 ± 2.90	-18.70 ± 4.08	-18.32 ± 3.72
MID	-14.80 ± 1.63	-15.44 ± 1.61	-15.59 ± 2.07	-15.92 ± 1.66	-13.60 ± 1.34	-13.90 ± 2.98	-14.47 ± 2.60
APEX	-17.40 ± 1.36	-18.21 ± 1.30	-18.40 ± 1.72	-18.19 ± 2.27	-16.24 ± 2.05	-15.36 ± 2.71	-16.90 ± 3.01
	-15.81 ± 2.20	**-15.62 ± 2.23**	**-14.36 ± 1.74**	**-15.87 ± 1.89**	**-15.77 ± 1.66**	**-16.58 ± 3.28**	**-16.72 ± 3.20**
α_{rc} (deg)							
BASE	-0.95 ± 1.94	0.78 ± 2.68	-3.84 ± 4.23	0.73 ± 3.84	2.79 ± 2.53	-1.02 ± 4.02	-5.83 ± 2.72
MID	3.20 ± 1.43	7.28 ± 1.61	-2.35 ± 4.60	8.17 ± 4.51	1.92 ± 2.31	5.75 ± 1.72	-1.80 ± 3.31
APEX	5.18 ± 1.46	12.71 ± 4.17	1.53 ± 4.68	6.05 ± 3.33	1.67 ± 4.54	7.37 ± 0.89	0.18 ± 4.83
	1.19 ± 1.11	**4.71 ± 1.62**	**-2.57 ± 4.09**	**4.02 ± 3.10**	**2.36 ± 2.21**	**2.20 ± 2.65**	**-3.92 ± 1.20**
α_{rl} (deg)							
BASE	0.75 ± 1.55	2.09 ± 4.46	-0.82 ± 2.30	-5.36 ± 1.76	0.28 ± 2.80	5.84 ± 4.51	3.05 ± 3.19
MID	1.24 ± 1.85	0.73 ± 3.66	-3.12 ± 2.73	-1.91 ± 4.43	5.36 ± 3.25	4.84 ± 4.20	2.85 ± 3.48
APEX	-0.11 ± 2.84	-0.39 ± 3.19	-4.12 ± 4.31	-2.22 ± 7.38	2.54 ± 6.33	4.78 ± 3.31	2.56 ± 3.04
	0.82 ± 1.41	**1.29 ± 3.34**	**-2.23 ± 1.85**	**-3.91 ± 2.00**	**2.18 ± 2.36**	**5.41 ± 4.04**	**2.94 ± 3.01**
α_{cl} (deg)							
BASE	6.14 ± 1.18	5.14 ± 1.79	3.50 ± 3.82	4.91 ± 2.74	8.32 ± 2.44	7.32 ± 1.32	6.83 ± 1.38
MID	5.93 ± 0.69	7.05 ± 0.79	6.49 ± 2.60	5.69 ± 1.72	5.48 ± 2.46	5.09 ± 2.15	5.50 ± 0.87
APEX	6.27 ± 0.99	6.15 ± 4.39	6.88 ± 5.18	6.86 ± 1.74	4.99 ± 4.19	5.50 ± 5.47	4.62 ± 2.09
	6.07 ± 0.92	**5.98 ± 1.14**	**5.06 ± 2.56**	**5.41 ± 2.05**	**7.21 ± 1.96**	**6.30 ± 1.31**	**6.14 ± 1.08**

Table 3-2 LV myocardial strain at time of aortic valve closure (T_{avc}).

The second column (Mean) includes the mean strain at the basal, mid and apical slices before subdivision in the six circumferential segments. In this column, the values in bold represent the mean of the myocardial strain components for the entire LV, without subdivision in slices and segments. The remaining columns of the table represent the mean strain values for each circumferential segment and longitudinal level. The bold values in these columns represent the mean strain value in each circumferential segment, without subdivision in slices. ε_r – radial thickening; ε_c – circumferential shortening; ε_l – longitudinal shortening; α_{rc} – radial-circumferential shear; α_{rl} – radial-longitudinal shear; α_{cl} –circumferential-longitudinal shear. IS - infero-septal; AS - antero-septal; ANT - anterior; AL - antero-lateral; IL - infero-lateral; INF - inferior.

A graphical representation of the mean strain values for each longitudinal slice is given in Figure 3-19.

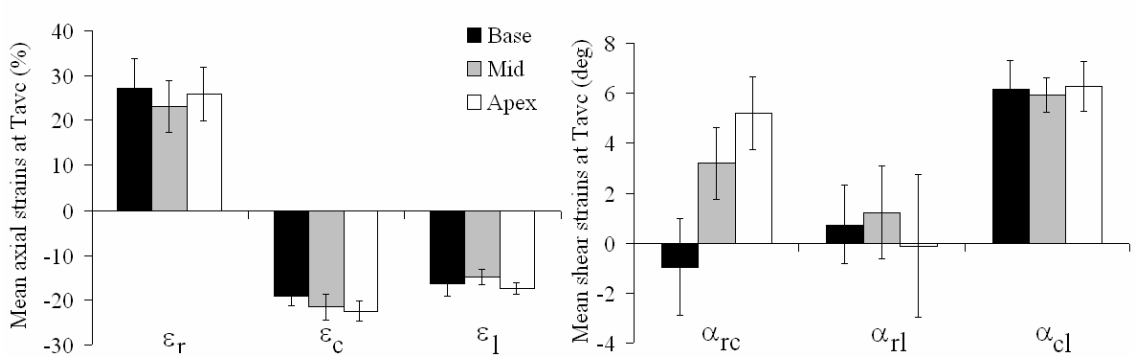

Figure 3-19 3D myocardial strain averaged for each slice at time of aortic valve closure (T_{avc}). Each colour represents a slice, as shown by the legend in the figure. Error bars represent SD. ε_r – radial thickening; ε_c – circumferential shortening; ε_l – longitudinal shortening; α_{rc} – radial-circumferential shear; α_{rl} – radial-longitudinal shear; α_{cl} –circumferential-longitudinal shear.

ε_r is higher at the basal and apical slices than at the mid slice ($P = 0.007$ and $P = 0.03$ for base vs. mid and apex vs. mid respectively). ε_c increases continuously from base towards the apex ($P < 0.001$ for basal vs. mid slice and for basal vs. apical slice). ε_l is higher at the apical slice than at the basal and mid slices ($P<0.05$ for apex vs. base and $P < 0.0001$ for apex vs. mid) and higher at the basal slice than at the mid slice ($P<0.01$). α_{rc} has a negative mean value only at the basal slice, which means that at this level the subepicardium rotates anticlockwise while the subendocardium rotates clockwise (see Chapter 1). This shear strain component increases continuously from base towards the apex ($P < 0.001$ for basal vs. mid slice and for basal vs. apical slice and $P < 0.01$ for mid vs. apical slice). For α_{rl} and α_{cl} no significant difference was observed between the three longitudinal levels. However, for α_{rl} a high variability was observed between subjects, resulting in large standard deviations spanning the axis of zero strain.

A graphical representation of the mean strain values for each circumferential segment is given in Figure 3-20.

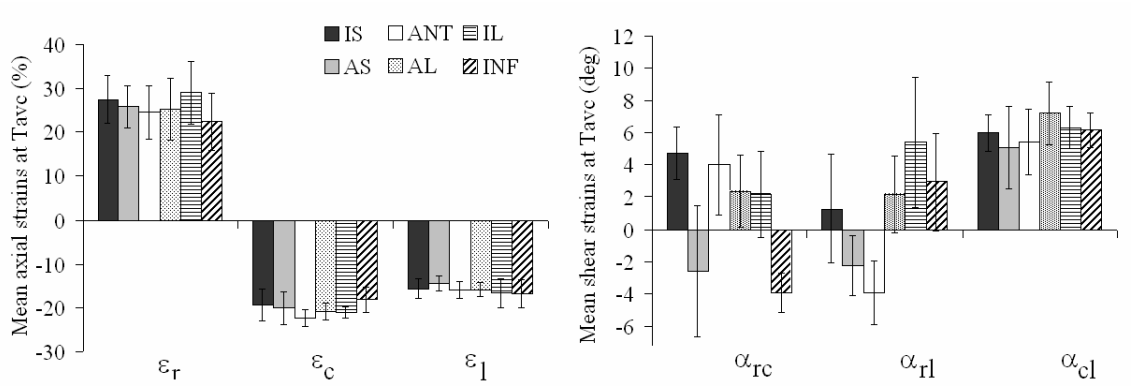

Figure 3-20 3D myocardial strain averaged for each circumferential segment at time of aortic valve closure (T_{avc}).

Each colour or pattern represents a circumferential segment, as shown by the legend in the figure. Error bars represent SD. ε_r – radial thickening; ε_c – circumferential shortening; ε_l – longitudinal shortening; α_{rc} – radial-circumferential shear; α_{rl} – radial-longitudinal shear; α_{cl} –circumferential-longitudinal shear. IS - infero-septal; AS - antero-septal; ANT - anterior; AL - antero-lateral; IL - infero-lateral; INF - inferior.

Most strain components showed significant variations between several circumferential segments. The segments with highest and lowest radial thickening were the IL and INF respectively ($P > 0.05$). Regarding ε_c the largest difference occurred between anterior (ANT) and INF segments ($P < 0.001$), with the circumferential shortening stronger in the anterior region. The largest difference in ε_l was found between INF and AS segments ($P < 0.001$). Regarding shear strain components, a high variability was found for the α_{rc} and α_{rl} between the several circumferential segments, while for torsion (α_{cl}) the results were homogeneous across these segments ($P \geq 0.05$). The largest difference in α_{rc} was observed between IS and INF segments ($P < 0.001$). For α_{rl} the largest difference was observed between IL and ANT segments ($P < 0.001$).

3.3.2. Transmural gradient

The plots for the same two subjects with the mean strain at the three transmural segments are presented in Figure 3-21 and Figure 3-22.

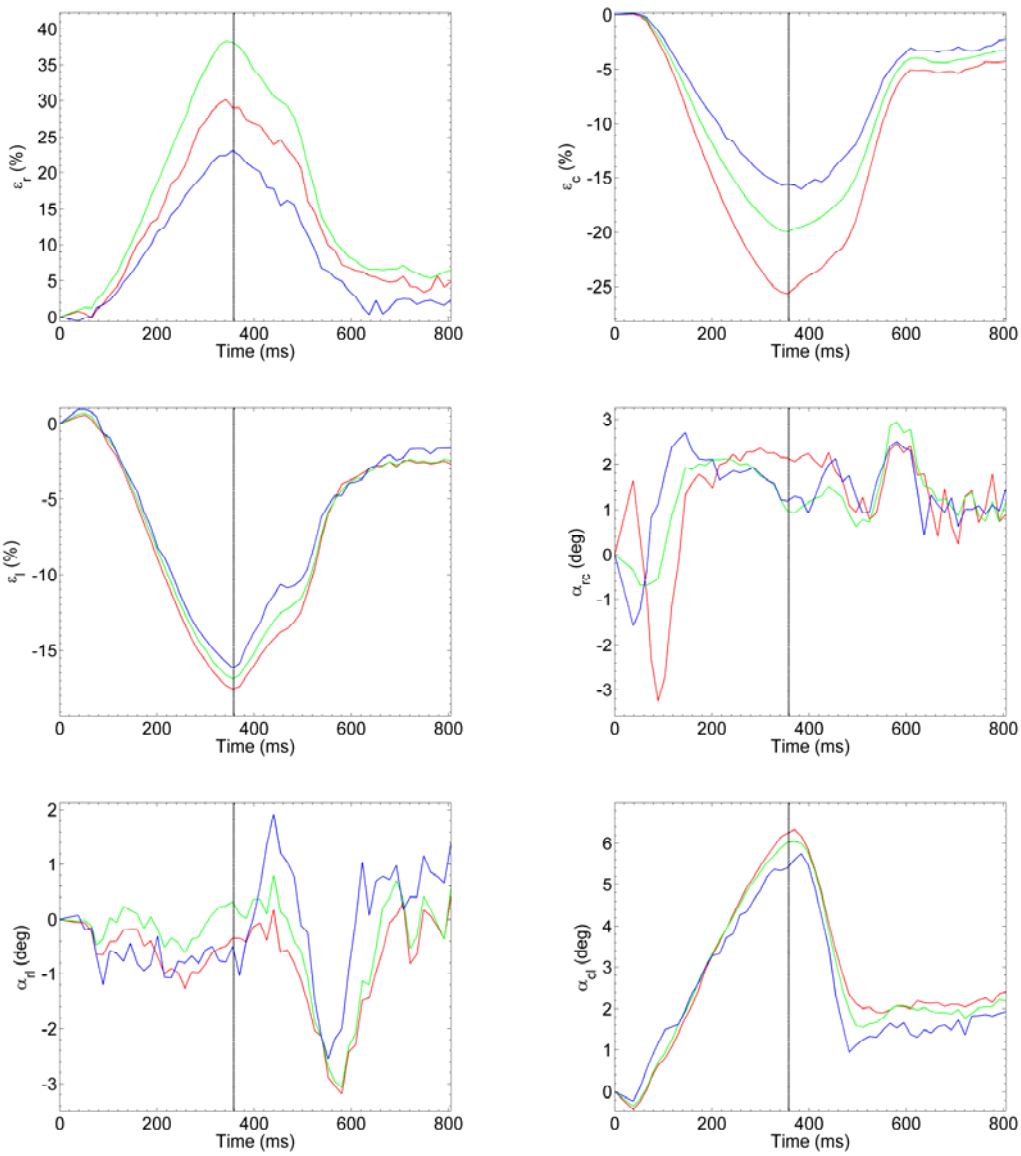

Figure 3-21 Temporal evolution per transmural segment of the LV myocardial strain components during a cardiac cycle (Subject 5). Vertical line denotes the time of aortic valve closure (T_{avc}). Red curve – subendocardium; Green curve – mid wall; Blue curve - subepicardium

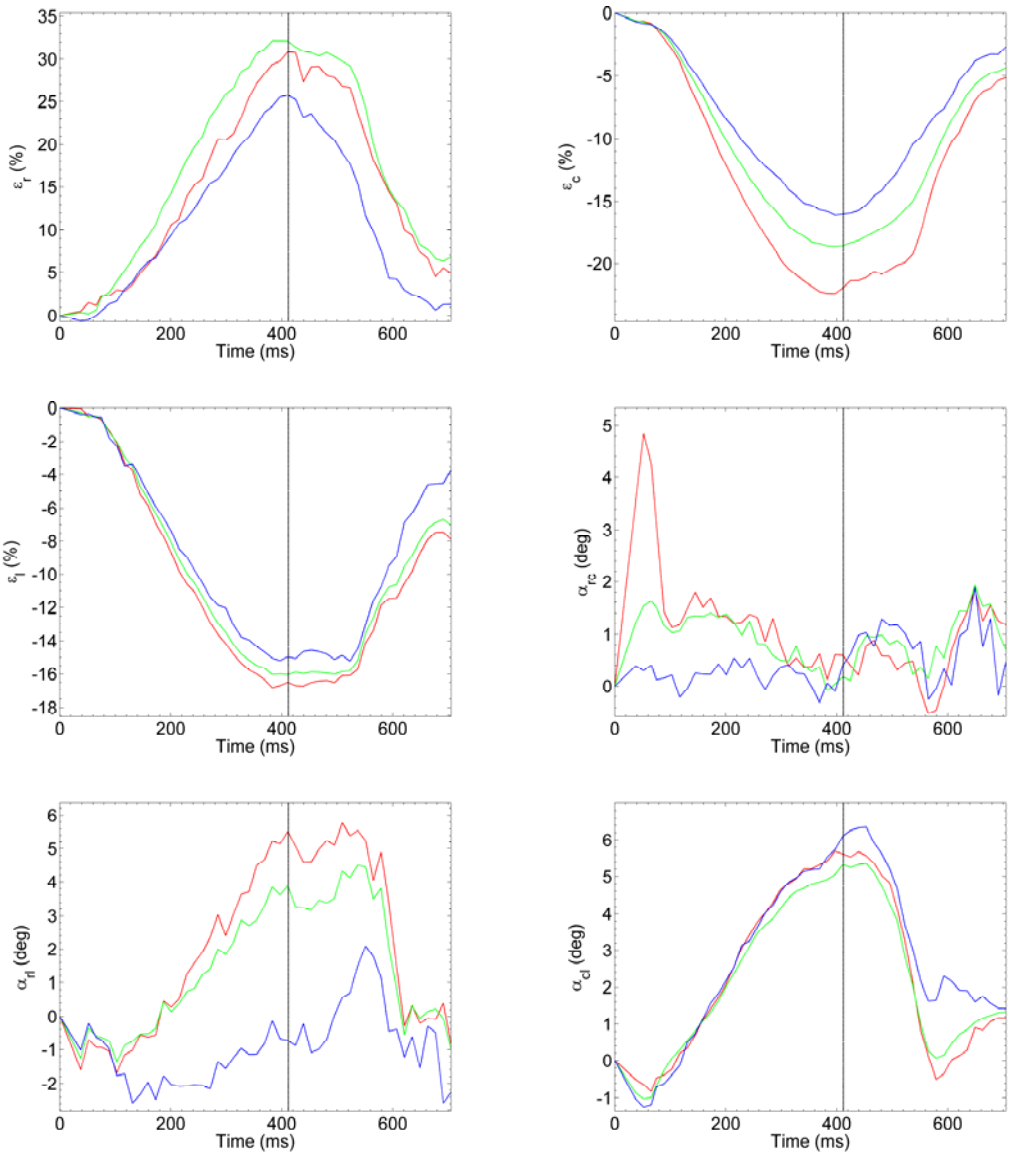

Figure 3-22 Temporal evolution per transmural segment of the LV myocardial strain components during a cardiac cycle (Subject 1). Vertical line denotes the time of aortic valve closure (T_{avc}). Red curve – subendocardium; Green curve – mid wall; Blue curve - subepicardium

The mean strains for each transmural segment at T_{avc} are listed in Table 3-3.

Strain component	Endo	MidWall	Epi
ε_r (%)	24.23 ± 8.76	32.33 ± 6.26	22.21 ± 4.65
ε_c (%)	-24.29 ± 2.71	-19.43 ± 2.22	-14.79 ± 2.24
ε_l (%)	-16.50 ± 2.11	-15.72 ± 2.06	-14.93 ± 2.48
α_{rc} (deg)	1.71 ± 0.79	0.80 ± 0.95	0.35 ± 2.10
α_{rl} (deg)	0.86 ± 2.38	1.14 ± 1.55	0.18 ± 1.18
α_{cl} (deg)	6.31 ± 1.12	6.09 ± 0.89	5.92 ± 0.78

Table 3-3 Mean strain at the subepicardium, midwall, and subendocardium at time of aortic valve closure (T_{avc}).

Endo – subendocardium; Mid – midwall; Epi – subepicardium. ε_r – radial thickening; ε_c – circumferential shortening; ε_l – longitudinal shortening; α_{rc} – radial-circumferential shear; α_{rl} – radial-longitudinal shear; α_{cl} – circumferential-longitudinal shear.

A graphical representation of the mean strain values for each transmural segment is given in Figure 3-23.

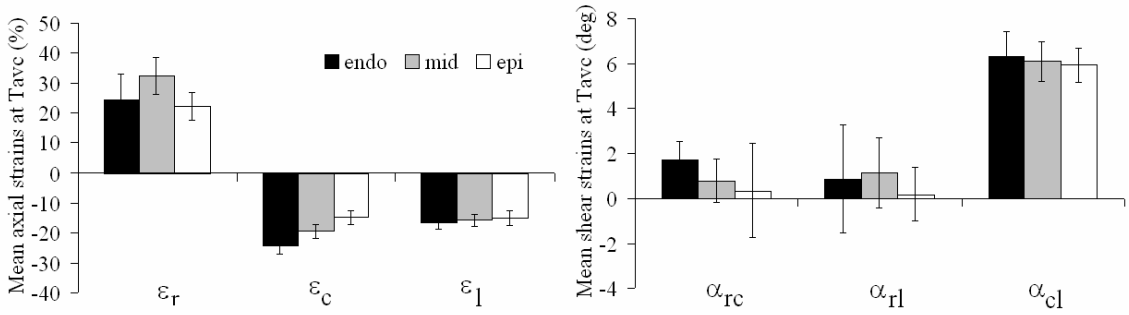

Figure 3-23 3D myocardial strain averaged for each transmural segment at time of aortic valve closure (T_{avc}). Each colour represents a transmural segment, as shown by the legend in the figure. Error bars represent SD. ε_r – radial thickening; ε_c – circumferential shortening; ε_l – longitudinal shortening; α_{rc} – radial-circumferential shear; α_{rl} – radial-longitudinal shear; α_{cl} –circumferential-longitudinal shear. epi – subepicardium; mid – midwall; endo - subendocardium

ε_r is higher at the mid wall ($P < 0.001$). Besides, more radial thickening was found at the subendocardial region than at the subepicardial region ($P = 0.03$). ε_c increases continuously from subepicardium towards subendocardium ($P < 0.001$). ε_l also increases continuously from subepicardium towards subendocardium ($P < 0.001$ for epi vs. endo, $P = 0.006$ for mid vs. endo). Regarding shear strain components, no transmural gradient was found.

3.3.3. Normalised strains

To compare the time evolution of the axial strains and torsion, the strain values were normalised by the peak strain for each of these components. On Figure 3-24 and Figure 3-25 the plots referent to the previous two subjects are presented.

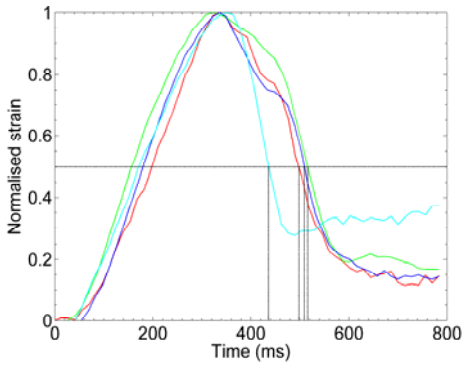

Figure 3-24 Normalised strains of Subject 5.

Vertical lines represent the times at which the strain components have reduced to 50 % of their maximum values. Red curve – normalised radial thickening (ε_r); Green curve – normalised circumferential shortening (ε_c); Blue curve – normalised longitudinal shortening (ε_l); Light blue curve – normalised circumferential-longitudinal shear (α_{cl})

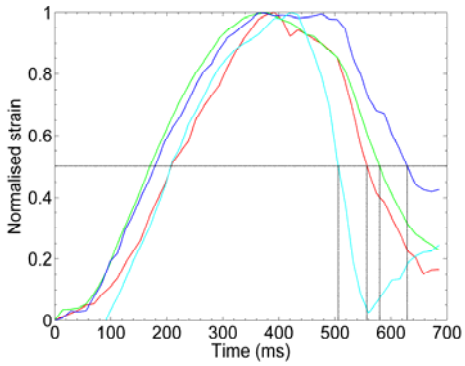

Figure 3-25 Normalised strains of Subject 1.

Vertical lines represent the times at which the strain components have reduced to 50% of their maximum values. Red curve – normalised radial thickening (ε_r); Green curve – normalised circumferential shortening (ε_c); Blue curve – normalised longitudinal shortening (ε_l); Light blue curve – normalised circumferential-longitudinal shear (α_{cl})

From these plots it is observed that the LV first untwist and then relaxes on the radial, longitudinal and circumferential directions. The times required by the axial strain components and torsion to reduce to 50% of their maximum values are listed in Table 3-4. These values show that after the LV untwists, it takes in average 44, 63 and 70 ms until the LV relaxes to

50% of its maximum strain value in the radial, longitudinal and circumferential directions, respectively.

Strain component	T50% (ms) (interpolated)	T50% - T50%(α_{cl}) (ms)
ε_r (%)	503 ± 40	44 ± 12
εc (%)	529 ± 39	70 ± 10
ε_l (%)	522 ± 60	63 ± 33
α_{cl} (deg)	459 ± 33	0 ± 0

Table 3-4 50% relaxation times of diastolic strain.

The second column represents the time at which each strain component has reduced to 50% of its maximum (vertical lines in Figure 3-24 and Figure 3-25). The third column represents the relaxation delay between axial strain components and torsion.

3.3.4. Timing of onset

The healthy LV myocardial strain was further explored by measuring the time to onset of circumferential and longitudinal shortening at the septum and lateral wall of the myocardium.

A graphical representation of the mean time to onset of circumferential and longitudinal shortening at septum and lateral wall is given in Figure 3-26.

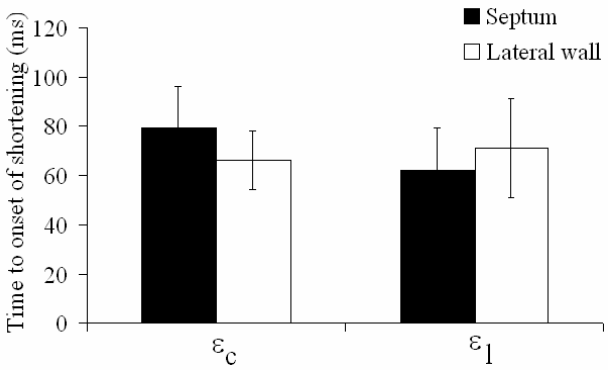

Figure 3-26 Time to onset of shortening averaged for septum and lateral wall.

The septum is represented in black and the lateral wall in white, as shown by the legend in the figure. Error bars represent SD. ε_c – circumferential shortening; ε_l – longitudinal shortening

T_{onset} of ε_c was determined successfully in 97% of the 72 cases of the healthy population (3 slices x 4 segments x 6 subjects). The results show that the mean T_{onset} of ε_c is 79 ± 17 ms for the septum and 66 ± 12 ms for the lateral wall. From multilevel analysis it is verified that, on average, the lateral wall starts to contract 13 ± 3 ms earlier than the septum ($P < 0.0001$) in the circumferential direction.

The T_{onset} of ε_l was determined successfully in 94% of the 72 cases of the healthy population. The mean T_{onset} ε_l at the septum is 62 ± 17 ms and at the lateral wall is 71 ± 20 ms. From multilevel analysis it is verified that in the longitudinal direction the septum starts to contract, on average, 9 ± 4 ms earlier than the lateral wall (P = 0.045).

3.3.5. Previous published results

The global mean obtained for the 3D strain components were compared with previously reported values. The characteristics of these studies are listed in Table 3-5.

	Population	Mean age	Age range	Temporal resolution (ms)	t (ms)
Present study	6	43 ± 13	26-56	14	ES
Kuijer et al [103]	10	46 ± 11	28-61	30	ES
Young et al [89]	12	-	19-37	-	ES
Moore et al [86, 90]	31	37 ± 11	21-62	32.5	Peak strain
Bogaert et al [104]	87	44 ± 15	22-74	8 time points at physiological important phases	ES

Table 3-5 Summary of the characteristics of the studies.
All populations are constituted by healthy volunteers. t - time corresponding to the mean reported strain value.

In the studies of Young et al [89] and Moore et al [86, 90], the strain values were reported as the components of the Lagrangian strain tensor $\vec{E}$. In this thesis and in the remaining reported studies, the axial and shear strain components are reported as percentage change in length and angle respectively. To compare the results obtained in this study with those previously reported, the $\vec{E}$ components were converted to percentage changes in length and angle using Equation 3-11 and Equation 3-12 respectively. The errors were converted assuming linear propagation.

The values reported in these studies are clustered in segments and slices. However, as slice and segment definitions are different for different studies, it is difficult to make an accurate comparison between the studies for different regions of the LV myocardium. Consequently, the range values and global mean values for each strain component are reported for each study in Table 3-6 and Table 3-7.

	ε_r (%)	ε_c (%)	ε_l (%)	α_{rc} (deg)	α_{rl} (deg)	α_{cl} (deg)
Present study	[20,34]	[-24,-17]	[-19,-12]	[-6,13]	[-5,6]	[4,8]
Kuijer et al [103]	[26,42]	[-27,-16]	[-20,-13]	[-4,10]	[-5,6]	[6,10]
Young et al [89]	[2,22]	[-27,-20]	[-23,-15]	[-4,7]	[-4,4]	[2,8]
Moore et al [86, 90]	[30,53]	[-28,-18]	[-21,-15]	[-1,12]	[-5,10]	[2,8]
Bogaert et al [104]	[33,47]	[-32,-23]	[-20,-15]	[-14,11]	[3,17]	[8,11]

Table 3-6 Range of strain values obtained in the studies of Table 3-5.

ε_r – radial thickening; ε_c – circumferential shortening; ε_l – longitudinal shortening; α_{rc} – radial-circumferential shear; α_{rl} – radial-longitudinal shear; α_{cl} –circumferential-longitudinal shear.

	ε_r (%)	ε_c (%)	ε_l (%)	α_{rc} (deg)	α_{rl} (deg)	α_{cl} (deg)
Present study	26 ± 6	-20 ± 2	-16 ± 2	1.2 ± 1.1	0.8 ± 1.4	6.1 ± 0.9
Kuijer et al [103]	31 ± 4	-21 ± 2	-16 ± 2	1.1 ± 1.2	0.6 ± 1.4	7.3 ± 1.5
Young et al [89]	14 ± 7	-23 ± 3	-19 ± 3	2.3 ± 4.0	0.2 ± 4.8	5.7 ± 3.1
Moore et al [86, 90]	38 ± 17	-23 ± 5	-18 ± 4	5.7 ± 9.2	3.9 ± 9.0	5.9 ± 8.3
Bogaert et al [104]	39 ± 9	-26 ± 3	-18 ± 3	-2 ± 5	10.7 ± 6.7	9.8 ± 3

Table 3-7 Global mean strain values obtained in the studies of Table 3-5.

ε_r – radial thickening; ε_c – circumferential shortening; ε_l – longitudinal shortening; α_{rc} – radial-circumferential shear; α_{rl} – radial-longitudinal shear; α_{cl} –circumferential-longitudinal shear.

The mean strain values obtained in each study are represented in Figure 3-27. This plot shows that the strain values obtained with the extended 3D HARP tracking method (denoted in the plot as "Original data") are in agreement with previous published results.

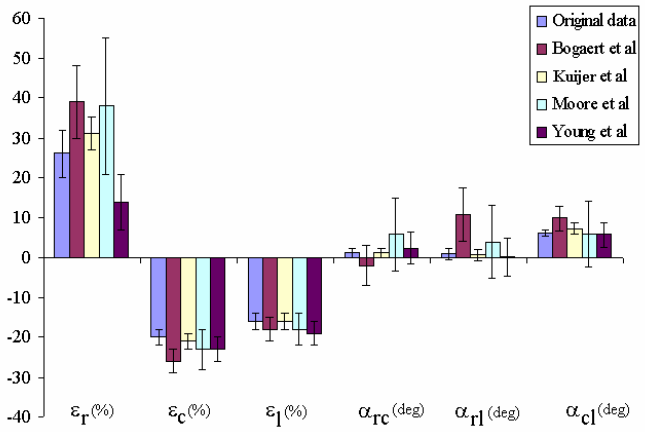

Figure 3-27 Global mean 3D strain components obtained in the studies of Table 3-5.

ε_r – radial thickening; ε_c – circumferential shortening; ε_l – longitudinal shortening; α_{rc} – radial-circumferential shear; α_{rl} – radial-longitudinal shear; α_{cl} –circumferential-longitudinal shear.

3.4. DISCUSSION

In this study a strain map of the healthy LV myocardium was obtained using high temporal resolution myocardial tagging and the extended 3D HARP tracking algorithm. The temporal resolution of 14 ms achieved with the LISA- SSFP sequence allows the study of the entire cardiac cycle (except for the atrial contraction at the very end of the cardiac cycle), contrarily to some previously published studies that could only assess the diastolic or systolic phase ([86, 90, 103]).

In this study the distance between the tag lines was 7 mm. Although the 3D extended HARP tracking is able to track each pixel, the spatial resolution should be considered equal to the tag line distance. Considering that a healthy LV wall has a thickness around 12 mm, the several transmural segments have a thickness smaller than the tracking spatial resolution, which should be taken into account when interpreting the obtained results.

As explained in Chapter 1, the homogeneous strain analysis assumes that the strain is homogeneous inside each tetrahedron. This can be a problem when the aim is to investigate the existence of strain inhomogeneities in the LV wall. However, as the size of the tetrahedrons defined in this study are small (in-plane distance equal to 1.17 mm and an out-of-plane distance ranging between 10 to 15 mm), each region (longitudinal, circumferential or transmural) include many elements of the mesh, which turns possible the detection of strain differences between different myocardial regions.

The mean end-systolic strains obtained in this study are comparable with previous published results (see Figure 3-27). Regarding the radial strain, it is verified that the results obtained are comparable with most of the studies, except the study of Young et al. [89] who reported lower mean radial strains. The radial strain at the base is higher than at the apex, which was already reported by others ([89]). For the transmural segments, the radial strain in the midwall is higher than in the subendocardium and subepicardium. This strain component is the axial strain component with higher variability between subjects, which can be explained by the fact that strain analysis with myocardial tagging is less accurate in the radial direction, as shown in Chapter 2, due to sparse tag lines in this direction. The results obtained for the circumferential and longitudinal strains are in agreement with the previously published results (see Figure 3-27). For both components, the strain at the basal level is lower than at the apical level. Regarding the transmural direction, it is verified that both circumferential and longitudinal strains are higher at the subendocardium than at the subepicardium. These results are in agreement with previous studies [86, 90, 104, 105]. These differences can be explained largely by the geometry of the LV and the architecture of the fibres, which is favourable for more deformation at the subendocardium [104]. Besides, although the trabeculae have been largely excluded during delineation of the LV, some trabeculae could still be included, which contribute to high values

of strain. Relatively to the shear strain components it is verified that for the radial–circumferential and radial–longitudinal shears a high spatial variability is observed intrasubject and intersubject, which has already been reported earlier [90]. However, no transmural gradient was observed and the difference between slices was only significant for the radial-circumferential shear strain, which increases from a negative value at the base to a positive value at the apex. A physiologic meaning for these shear strains is difficult to obtain. However, it should be noted that the highest variability for the shear strain components correspond to the two components that depend on the radial direction. Strain quantification in this direction is less accurate due to the very limited number of tag lines in the transmural direction, which could partially explain the high variability in the shear strain components that depend on the radial direction. However, for a complete interpretation of these results it would be important to use diffusion MRI images to obtain geometric information of the cardiac fibres [106]. The circumferential-longitudinal shear, which represents the LV torsion, is the shear component which presents a well defined pattern between subjects. Contrarily to previous published results, the obtained torsion does not significantly differ between different regions of the LV. Although the torsion is higher in the subendocardium than in the subepicardium, this difference is not statistically significant.

The plots with the normalised strains show that a healthy LV untwists before it fills. This phenomenon has been explained earlier [107] as a mechanism to enhance gradient pressure between the left atrium and the LV during the isovolumetric relaxation [11].

Regarding the time to onset, it is observed that the circumferential shortening starts earlier in the lateral wall than in the septum, with a difference of 13 ms between these two regions. These results are in agreement with previous published results [4] that attributed this difference to the fact that the lateral wall probably stretches more than the septum during atrial contraction, leading to an earlier onset of shortening. However, as this study [4] was performed with a 2D data set, no information regarding the longitudinal time to onset was obtained. In the study presented in this chapter it is found that in this direction, the behaviour is the opposite of that in the circumferential direction, with the longitudinal shortening starting 9 ms earlier in the septum than in the lateral wall ($P < 0.05$). This is an interesting observation, as it has been reported from an early animal study that LV contraction starts with an early longitudinal contraction wave before ongoing circumferential shortening starts [108]. Besides, as electrical activation starts from the endocardium, where the subendocardial fibres run mainly in the longitudinal direction, it may well be that the timing of the longitudinal shortening reflects the electrical activation better than the timing of the circumferential shortening. Nevertheless, it should be considered that the temporal resolution of the extended 3D HARP tracking method is equal to 14 ms, and that this result for the timing of the longitudinal strain should be further explored in a larger population.

3.5. CONCLUSION

In this chapter a 3D strain analysis method based on HARP tracking was presented. The obtained 3D myocardial strains are comparable with previous published results, with the advantage that this technique automatically tracks the myocardial tag pattern, decreasing the time of post-processing considerably and bringing the assessment of myocardial strain analysis with MRI closer to clinical routine. Additionally, the extended 3D HARP tracking method takes into account with the longitudinal displacement of the LV allowing the computation of the true LV deformation.

This study also shows that the 3D strain components obtained with the extended 3D HARP tracking and homogeneous strain analysis are not homogeneous for the entire LV wall, showing significant spatial and timing variability. Consequently, a correct interpretation of abnormal hearts strain implies a regional comparison instead of global. For these comparisons, the healthy LV strain maps should be used as a reference.

Chapter 4.

EXTENDED 3D HARP TRACKING APPLIED TO LBBB PATIENTS

Patients with heart failure (HF) and left bundle branch block (LBBB) are characterized by an asynchronous and inefficient cardiac contraction. Some of these patients can have this situation reversed after cardiac resynchronization therapy (CRT). However, the process presently used to select those patients which will benefit from this intervention is still not optimized. Recently it has been suggested that mechanical dyssynchrony could be a better predictor of improvement than electrical dyssynchrony, usually assessed with QRS duration. In this study, extended 3D HARP tracking and 3D homogeneous strain analysis is applied to a group of LBBB patients and to a group of healthy controls, and the strain parameter that better distinguishes these two populations is investigated. The obtained results show that LBBB patients have a significant lower strain in the septum ($P < 0.001$) while axial strains in the lateral wall are preserved, highlighting the importance of analysing cardiac strain regionally and not globally. Regarding timing of shortening it is verified that for patients both circumferential and longitudinal shortening start earlier in the septum than in the lateral wall. In controls circumferential shortening starts in the lateral wall while longitudinal shortening in the septum. With this study it is shown that the strain parameters that better discriminate LBBB patients from controls is circumferential shortening and time to onset of circumferential shortening in the septum.

4.1. INTRODUCTION

CRT is a new treatment for patients with HF and LBBB. Due to the complexity of this type of intervention and its associated costs, it is important to predict with high accuracy which patients will benefit from it. The current practice to select patients with HF for CRT is to use the QRS duration, since a positive correlation between wider QRS intervals and a positive response to CRT has been observed [109-111]. However, electrical dyssynchrony assessed with QRS duration does not reflect mechanical dyssynchrony [112, 113], and measuring the mechanical dyssynchrony directly appears to be a better predictor of improvement from CRT [19, 111, 114-119]. Usually, mechanical dyssynchrony is assessed with echo-Doppler methods (see Chapter 1 and references [120-122]), however this technique mainly assesses motion. A promising technique to measure mechanical dyssynchrony is tagged MRI [111, 123], as it is able to quantify regional strain with high temporal resolution. The use of MRI to assess candidates for CRT and predict a positive response to this treatment has been hampered by the time consuming post-processing of this technique and the incompatibility with the implanted devices [120]. However, in the near future these limitations will be overcome since promising developments towards pacing in MRI have been made [123, 124] and faster post-processing techniques of tagged MR images are already available [85].

Mechanical dyssynchrony in HF patients is usually a consequence of LBBB [114, 115], which turns the detection of this abnormal interventricular conduction important on the evaluation of this group of patients. The aim of this study is to determine the strain parameter that better distinguishes LBBB patients from healthy controls. For that, tagged MRI with high temporal resolution is used to determine the 3D strain curves. The parameters evaluated in both populations are: 3D strain components at time of aortic valve closure (T_{avc}), time to onset of circumferential and longitudinal shortening and the delay between time to onset of circumferential and longitudinal shortening at the septum and at the lateral wall.

4.2. MATERIALS AND METHODS

4.2.1. Subjects

Six healthy volunteers (6 male; mean age: 43 ± 13), with no history of cardiac disease and 5 patients with LBBB (1 male; mean age: 66 ± 4) were evaluated, after providing informed consent. The New York Heart Association (NYHA) class for these patients varied from I to III.

Healthy	Age	RR (ms)	$N_{time\ frames}$	Gender	NYHA class	T_{avc} (ms)
1	56	1330	49	M	-	412
2	28	1200	63	M	-	345
3	53	1000	49	M	-	347
4	48	1270	49	M	-	375
5	46	1050	56	M	-	358
6	26	800	46	M	-	317
LBBB	**Age**	**RR (ms)**	$N_{time\ frames}$	**Gender**	**NYHA class**	T_{avc} (ms)
1	58	804	41	F	I	386
2	66	969	49	F	II-III	459
3	69	1191	63	F	I	469
4	68	1005	41	M	I	345
5	68	951	56	F	I	400

Table 4-1 Characterization of analysed healthy and LBBB populations.
$N_{time\ frames}$ – Number of tracked time frames. M – male, F - female. T_{avc} – time of aortic valve closure. RR – mean time interval between two R-waves.

4.2.2. Image acquisition

Image acquisition is described in detail in Chapter 3. In summary, subjects were imaged on a 1.5T whole body scanner (Sonata, Siemens Medical Solutions, Erlangen, Germany), using a phased-array receiver coil.

After the electrocardiogram (ECG) R-wave, tissue tagging was applied with two non-selective 45° RF pulses separated by a field gradient in the readout direction, yielding a sinusoidal modulation of the magnetization [66]. The tag line distance was 7 mm and the readout direction perpendicular to the tag lines. Cine imaging was then performed with the steady state free precession (SSFP) sequence using the linearly increasing startup angle approach (LISA) [64], with the parameters described in Chapter 2.

Images were acquired in five short-axis (SA) planes and in three long-axis (LA) planes. SA planes were distributed between base and apex, with an image plane distance of 10 mm to 15 mm. LA planes were uniformly distributed around the left ventricle (LV) and perpendicular to the SA, with an angular spacing equal to 60º [100].

Complementary spatial modulation of magnetization (CSPAMM) was used on the SA and LA image planes to improve the myocardial tagging contrast [92] and to obtain more accurate strain results [93]. Four sets of images were acquired for each SA image plane: vertically and horizontally tagged images with sinusoidal and inverted sinusoidal tagging. Two sets of images were acquired for each LA image plane: tagged images with sinusoidal and inverted sinusoidal tagging with the tagging direction perpendicular to the LA. To avoid

mismatching between the set of images acquired per plane, the multiple brief expiration breath hold scheme described in Chapter 2 was performed.

To determine T_{avc} LA cine images in the 3-chamber view were acquired with SSFP imaging with a temporal resolution of 14 ms and with the image parameters described in Chapter 2.

4.2.3. Post-processing

For each SA and LA image plane, the two SPAMM images with inverted tag patterns were subtracted in order to compute the CSPAMM images, as explained in Chapter 2. To these images it was applied a fast Fourier transform (FFT), high-pass filter and inverse FFT (IFFT), resulting a complex image whose magnitude is designated by harmonic magnitude (HARM) and phase is designated by harmonic phase (HARP) [98]. The HARM images were used to draw the contours that delimit the LV (MASS software package, version 5.1b, MEDIS, Leiden, The Netherlands). The HARP images were used to track the myocardial tissue inside the contours, using the automatic extended 3D HARP tracking method, presented in Chapter 3.

4.2.3.1. Extended 3D HARP Tracking

A detailed description of the method extended 3D HARP tracking is given in Chapter 3. In summary, extended 3D HARP tracking is an automatic method that tracks the myocardial tissue by combining the extended 2D HARP tracking with the 1D HARP tracking. Extended 2D HARP tracking (see Chapter 2 and reference [98]) gives the apparent motion of the tag points in the SA image planes. To determine the complete 3D motion it is necessary to also quantify the tag points displacement on the longitudinal direction. This component of the displacement can be measured by acquiring images on the LA direction, with the tag lines perpendicular to the LA. To track the tag points on these image planes the 1D HARP tracking algorithm was used. This algorithm is based on the same principle as the 2D HARP tracking [85], as is explained in detail in Chapter 3. The 3D displacement of the myocardial points was then obtained by combining the trajectories on the SA image planes with the trajectories on the LA image planes (see Chapter 3 and reference [100]).

4.2.3.2. Strain Analysis

Homogeneous strain analysis was applied to a mesh of tetrahedrons defined with the points tracked in the 5 SA image planes [100]. For each tetrahedron the deformation gradient tensor $\vec{F}$ was computed and the Lagragian strain tensor $\vec{E}$ was then given by:

$$\vec{E} = \frac{1}{2}\left(\vec{F}^T \vec{F} - 1\right) \qquad \text{Equation 4-1}$$

Using the radial-circumferential-longitudinal (rcl) coordinate system, the strain components were given by:

$$\varepsilon_i = \left(\sqrt{1+2E_{ii}} - 1\right) \times 100\% \qquad \text{Equation 4-2}$$

$$sin\,\alpha_{ij} = \frac{2E_{ij}}{\left(\varepsilon_i + 1\right)\left(\varepsilon_j + 1\right)} \quad (i \neq j) \qquad \text{Equation 4-3}$$

where E_{ij} are elements of the strain tensor $\vec{E}$ and i and j are equal to r (radial direction), c (circumferential direction) or l (longitudinal direction). The normal strains ε_i correspond to the percent change in length of a segment initially oriented in the i direction [91]. The shear strain components α_{ij} correspond to the change in angle between segments initially oriented in the perpendicular i and j directions [91].

The results obtained for each strain component at each time frame were averaged in 6 segments for each slice: infero-septal (IS), antero-septal (AS), anterior (ANT), antero-lateral (AL), infero-lateral (IL) and inferior (INF). A schematic representation of these regions is given in Figure 1-51.

4.2.3.3. Healthy vs. LBBB population

To determine which strain parameter better discriminates LBBB patients from healthy controls, the 3D strain components at end-systole (ES) were compared. ES was defined as the T_{avc}.

The time to onset (T_{onset}) of circumferential and longitudinal shortening were also compared. These parameters were computed for each segment in each slice. T_{onset} corresponds to the instant when the down slope of the evaluated strain curve starts [4]. This timing parameter was automatically determined as described before (see Chapter 3 and reference [4]). However, when the observer did not agree with the obtained values, he/she could discard (but not adjust) them.

4.2.4. Statistical Analysis

Results are presented as mean ± SD. P-values < 0.05 are considered statistically significant. To compare 3D strain components and time to onsets of the healthy and LBBB populations a multilevel regression analysis was performed (MLwiN, version 1.02.0002, Centre for Multilevel Modelling, London, United Kingdom [101, 102]). As the data is structured in a hierarchy with three levels (segments are clustered within slices and slices within subjects), the multilevel analysis corrects the regression coefficients between population and the evaluated parameters for dependency in the data due to this hierarchy. The 3D strain components (ε_c, ε_l, ε_r, α_{cl}, α_{rc}, α_{rl},) and time to onsets (T_{onset} ε_c, T_{onset} ε_l) were set as outcome variables and the

population as independent variable (dichotomous variable that takes the value 1 for the healthy population and 0 for the LBBB population). The obtained regression coefficients reflect the differences between the evaluated parameters of both populations. The strain component and time to onset that better distinguishes controls from LBBB patients is determined using the Wald statistic. This parameter corresponds to the squared quotient between the regression coefficient and its standard error [125]. The Wald statistic follows a Chi-square distribution with one degree of freedom. A larger Wald statistic value is indicative of a more significant regression coefficient which in this case reflects a better parameter to distinguish both populations.

To compare the onset of shortening (OS) delay vector of the healthy and LBBB populations an unpaired t-test was performed assuming unequal variances.

4.3. RESULTS

The mean global function parameters obtained for the healthy controls and LBBB patients are listed in Table 4-2.

Global function parameter	Healthy controls	LBBB patients
End-diastolic volume (ml)	178 ± 49	206 ± 67
End-systolic volume (ml)	77 ± 19	130 ± 62
Stroke volume (ml)	100 ± 33	76 ± 22
Ejection fraction (%)	56 ± 6	40 ± 16
Heart Rate (beat/min)	56 ± 11	62 ± 9

Table 4-2 Global function parameters of both populations.
Values are presented as mean ± SD

An example strain curve of a healthy control and a LBBB patient are presented in Figure 4-1 and Figure 4-2. For one healthy control, the strain components and the timing parameter were not determined for the segments IL and INF of the apical slice, as it was impossible to define tetrahedrons in this region.

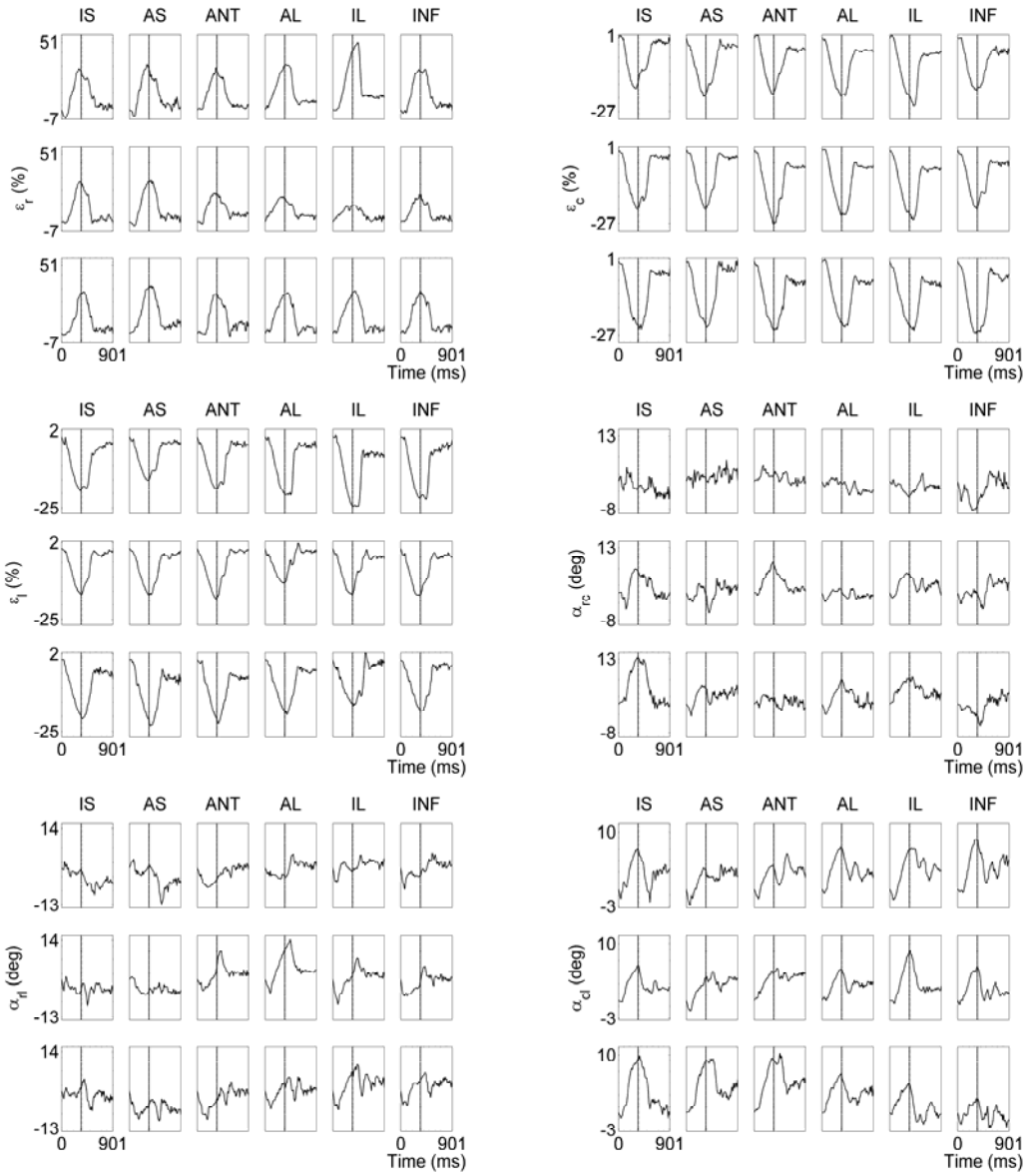

Figure 4-1 Temporal evolution of the LV myocardial strain components of a healthy volunteer in each slice and segment (Subject 2).

Each group of 18 plots represents a component of the strain tensor. Inside each group, the top row corresponds to the basal slice, the mid row to the mid slice and the bottom row to the apical slice. The vertical line denotes the time of aortic valve closure (T_{ave}). ε_r – radial thickening; ε_c – circumferential shortening; ε_l – longitudinal shortening; α_{rc} – radial-circumferential shear; α_{rl} – radial-longitudinal shear; α_{cl} – circumferential-longitudinal shear. IS - infero-septal; AS - antero-septal; ANT - anterior; AL - antero-lateral; IL - infero-lateral; INF - inferior.

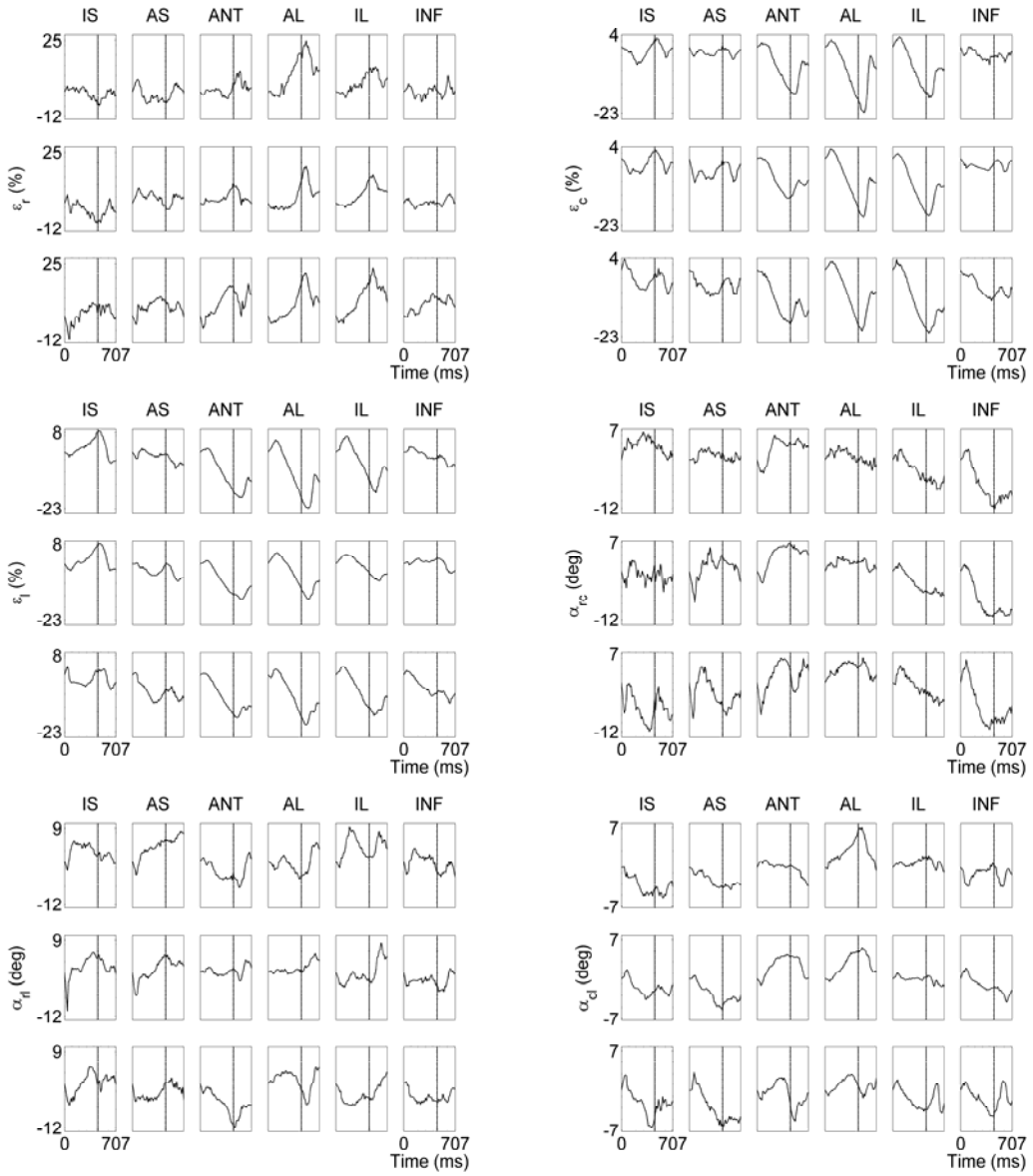

Figure 4-2 Temporal evolution of the LV myocardial strain components of a LBBB patient in each slice and segment (Subject 2).

Each group of 18 plots represents a component of the strain tensor. Inside each group, the top row corresponds to the basal slice, the mid row to the mid slice and the bottom row to the apical slice. The vertical line denotes the time of aortic valve closure (T_{avc}). ε_r – radial thickening; ε_c – circumferential shortening; ε_l – longitudinal shortening; α_{rc} – radial-circumferential shear; α_{rl} – radial-longitudinal shear; α_{cl} – circumferential-longitudinal shear. IS - infero-septal; AS - antero-septal; ANT - anterior; AL - antero-lateral; IL - infero-lateral; INF - inferior.

4.3.1. Strain components

The 3D strain components at T_{avc} were averaged for all slices and segments and the results obtained for both populations are listed in Table 4-3.

Strain parameter	Healthy controls	LBBB patients
ε_r (%)	26 ± 8	16 ± 11
ε_c (%)	-21 ± 3	-15 ± 7
ε_l (%)	-16 ± 3	-11 ± 6
α_{rc} (deg)	2 ± 6	0 ± 6
α_{rl} (deg)	1 ± 5	2 ± 6
α_{cl} (deg)	6 ± 3	1 ± 5

Table 4-3 Global mean strain values of healthy and LBBB populations at T_{avc}.
ε_r – radial thickening; ε_c – circumferential shortening; ε_l – longitudinal shortening; α_{rc} – radial-circumferential shear; α_{rl} – radial-longitudinal shear; α_{cl} –circumferential-longitudinal shear.

A graphical representation of these global mean strains is given in Figure 4-3.

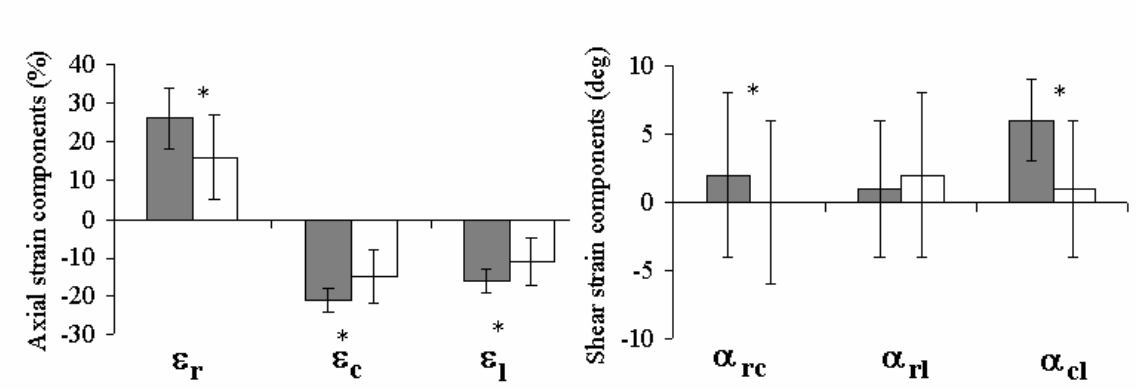

Figure 4-3 Global mean strain values of healthy and LBBB populations at T_{avc}.
ε_r – radial thickening; ε_c – circumferential shortening; ε_l – longitudinal shortening; α_{rc} – radial-circumferential shear; α_{rl} – radial-longitudinal shear; α_{cl} –circumferential-longitudinal shear. Strains of healthy population are represented in grey and strain of LBBB population in white. Error bars represent SD. * $P < 0.001$ obtained with multilevel analysis (see Table 4-4).

These global mean strain components for both populations were compared using multilevel analysis and the obtained regression coefficients are summarized in Table 4-4.

Strain parameter vs. population	regression coefficient	Wald statistics	p-value
ε_r (%)	9.822 ± 1.308	56.39	< 0.001
ε_c (%)	-6.170 ± 0.797	59.93	< 0.001
ε_l (%)	-4.891 ± 0.690	50.25	< 0.001
α_{rc} (deg)	2.799 ± 0.840	11.10	< 0.001
α_{rl} (deg)	-0.678 ± 0.788	0.74	> 0.05
α_{cl} (deg)	4.648 ± 0.561	68.64	< 0.001

Table 4-4 Regression coefficients obtained from multilevel analysis.
The regression coefficients represent the difference between the strain components of the healthy and LBBB populations at the T_{avc}. ε_r – radial thickening; ε_c – circumferential shortening; ε_l – longitudinal shortening; α_{rc} – radial-circumferential shear; α_{rl} – radial-longitudinal shear; α_{cl} –circumferential-longitudinal shear.

LBBB patients show a significant decrease in all three axial strain components. The difference between controls ε_r and LBBB patients ε_r is equal to 10% (see Table 4-4), which represents a decrease relative to the controls of 38% at ES. In the circumferential direction the LBBB patients strain have a relative decrease of 29% and in the longitudinal direction of 30%. Regarding shear strain components, only the α_{rl} is not significant different from controls at T_{avc}.

A ranking of the 3D strain components regarding the efficiency to differentiate LBBB patients from controls is obtained sorting the Wald statistics values in Table 4-4. From this analysis it is verified that torsion (α_{cl}) is the strain component that better differentiates patients from controls, and α_{RC} shear the strain component that worst differentiates them.

Until now both populations are compared using the global average of the strain components. However, as it is shown in Chapter 3, the strain of the healthy LV is not homogeneous and the comparison between controls and patients should be performed regionally. As in patients the septum is expected to be the region more affected, the previous results were analysed separately for the septum (segments IS and AS) and lateral wall (segments AL and IL). The mean 3D strain components for both populations in these two regions at the T_{avc} were computed separately by region, and are presented in Table 4-5.

Strain	Septum		Lateral wall	
parameter	Healthy controls	LBBB patients	Healthy controls	LBBB patients
ε_r (%)	27 ± 6	9 ± 9	26 ± 9	22 ± 9
ε_c (%)	-20 ± 4	-8 ± 6	-21 ± 2	-21 ± 3
ε_l (%)	-16 ± 3	-7 ± 7	-16 ± 3	-14 ± 4
α_{rc} (deg)	3 ± 7	0 ± 4	3 ± 4	0 ± 4
α_{rl} (deg)	-1 ± 4	4 ± 5	4 ± 4	2 ± 5
α_{cl} (deg)	6 ± 3	-2 ± 4	6 ± 3	3 ± 5

Table 4-5 Mean values of 3D strain components in septum and lateral wall of both populations at T_{avc}. Septum includes segments IS and AS and lateral wall segments AL and IL. ε_r – radial thickening; ε_c – circumferential shortening; ε_l – longitudinal shortening; α_{rc} – radial-circumferential shear; α_{rl} – radial-longitudinal shear; α_{cl} –circumferential-longitudinal shear.

A graphical representation of these mean strain values is given in Figure 4-4.

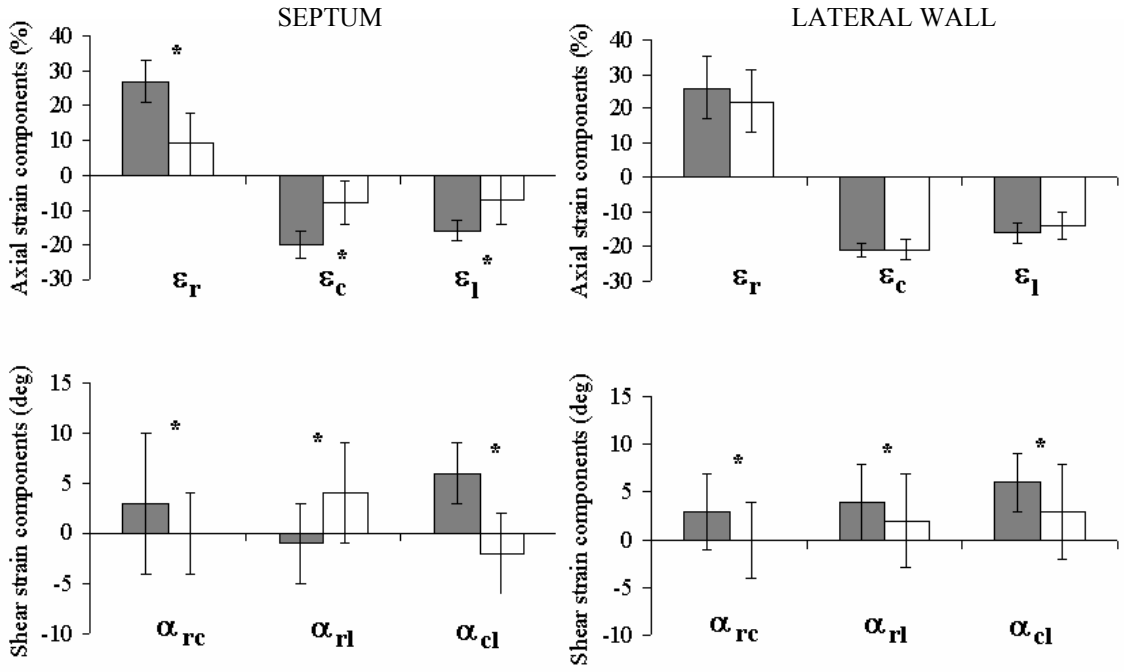

Figure 4-4 Mean values of 3D strain components of both populations in septum (left column) and lateral wall (right column) at T_{avc}.

Septum includes segments IS and AS and lateral wall segments AL and IL. ε_r – radial thickening; ε_c – circumferential shortening; ε_l – longitudinal shortening; α_{rc} – radial-circumferential shear; α_{rl} – radial-longitudinal shear; α_{cl} –circumferential-longitudinal shear; * $P < 0.05$ obtained with multilevel analysis (see Table 4-6)

The regression coefficients obtained with multilevel analysis are given in Table 4-6.

Strain parameter vs. population	Septum			Lateral Wall		
	regression coefficient	Wald statistics	p-value	regression coefficient	Wald statistics	p-value
ε_r (%)	17.473 ± 1.783	96.04	< 0.001	4.106 ± 2.280	3.24	0.07
ε_c (%)	-12.432 ± 1.199	107.51	< 0.001	-0.902 ± 0.671	1.81	0.18
ε_l (%)	-8.552 ± 1.304	43.01	< 0.001	-1.518 ± 0.854	3.16	0.08
α_{rc} (deg)	3.051 ± 1.386	4.85	0.03	3.163 ± 0.931	11.54	< 0.001
α_{rl} (deg)	-4.723 ± 1.067	19.59	< 0.001	2.367 ± 1.196	3.92	< 0.05
α_{cl} (deg)	8.109 ± 0.866	87.68	< 0.001	3.134 ± 1.004	9.74	0.002

Table 4-6 Regression coefficients obtained from multilevel analysis for the septum and lateral wall. The regression coefficients represent the difference between the strain components of the healthy and LBBB populations in these regions at the T_{avc}. ε_r – radial thickening; ε_c – circumferential shortening; ε_l – longitudinal shortening; α_{rc} – radial-circumferential shear; α_{rl} – radial-longitudinal shear; α_{cl} –circumferential-longitudinal shear.

The axial strain components of the patients are significantly lower at the septum, with 66%, 54% and 62% less shortening in the radial, circumferential and longitudinal direction relatively to the controls. At the lateral wall, the axial strain components of the LBBB patients are not significantly affected. Regarding the shear strain components, the difference between both populations is significant for all three components in both regions. However, these strain components present a high variability between subjects, as observed by the large error bars in Figure 4-4. In the septum, the Wald statistic shows that ε_c is the 3D strain component that better differentiates patients from controls, and α_{rc} shear the worst.

4.3.2. Timing of circumferential and longitudinal strain

Additionally to end systolic 3D strain components, the T_{onset} of circumferential and longitudinal shortening were measured for both populations. On the global analysis T_{onset} ε_C was determined successfully in 97% of the 108 cases of the healthy population (3 slices x 6 segments x 6 subjects) and in 79% of the 90 cases of the LBBB population (3 slices x 6 segments x 5 subjects). T_{onset} ε_l was determined successfully in 94% of the 108 cases of the healthy population and in 69% of the 90 cases of the LBBB population. The mean timing parameters obtained for each population are listed in Table 4-7.

Timing parameter	Healthy controls	LBBB patients
$T_{onset}\,\varepsilon_c$ (ms)	73 ± 15	67 ± 41
$T_{onset}\,\varepsilon_l$ (ms)	68 ± 20	83 ± 42

Table 4-7 Mean values of the timing parameters of both populations.
$T_{onset}\,\varepsilon_c$ – time to onset of circumferential shortening; $T_{onset}\,\varepsilon_l$ – time to onset of longitudinal shortening.

These results are graphically represented in Figure 4-5.

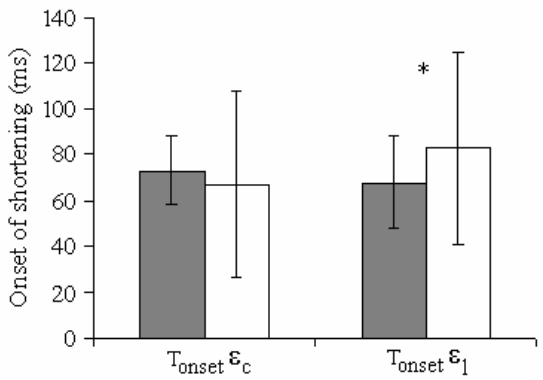

Figure 4-5 Global mean time to onset of circumferential and longitudinal shortening.
Error bars represent SD. The healthy population is represented in grey and the LBBB population in white. * - $P < 0.01$ obtained with multilevel analysis (see Table 4-8). $T_{onset}\,\varepsilon_c$ – time to onset of circumferential shortening; $T_{onset}\,\varepsilon_l$ – time to onset of longitudinal shortening.

The regression coefficients obtained with multilevel analysis for the time to onset of circumferential and longitudinal shortening are presented in Table 4-8

Timing parameter vs. population	regression coefficient	Wald statistics	p-value
$T_{onset}\,\varepsilon_c$ (ms)	5.954 ± 4.354	1.87	> 0.05
$T_{onset}\,\varepsilon_l$ (ms)	-14.605 ± 4.846	9.08	< 0.01

Table 4-8 Regression coefficients obtained with multilevel analysis.
The regression coefficients represent the difference between the time to onset of shortening of healthy and LBBB populations. $T_{onset}\,\varepsilon_c$ – time to onset of circumferential shortening; $T_{onset}\,\varepsilon_l$ – time to onset of longitudinal shortening. Positive difference: onset of shortening in the controls occurs later than in the patients. Negative difference: onset of shortening in the controls occurs earlier than in the patients.

A significant difference was obtained for the $T_{onset}\,\varepsilon_l$ between both populations, with the longitudinal shortening starting 15 ms later on the LBBB patients than on the controls (see Table 4-8). For the regional analysis the timing parameters obtained for the septum and lateral wall are summarized in Table 4-9.

Timing parameter	Septum		Lateral wall	
	Healthy controls	LBBB patients	Healthy controls	LBBB patients
$T_{onset}\,\varepsilon_C$ (ms)	79 ± 17	24 ± 13	66 ± 12	98 ± 21
$T_{onset}\,\varepsilon_L$ (ms)	62 ± 17	32 ± 13	71 ± 20	111 ± 29

Table 4-9 Mean values of the timing parameters of both populations in septum and lateral wall. The septum includes segments IS and AS and lateral wall segments AL and IL. $T_{onset}\,\varepsilon_c$ – time to onset of circumferential shortening; $T_{onset}\,\varepsilon_l$ – time to onset of longitudinal shortening.

The graphical representation of these results is presented in Figure 4-6.

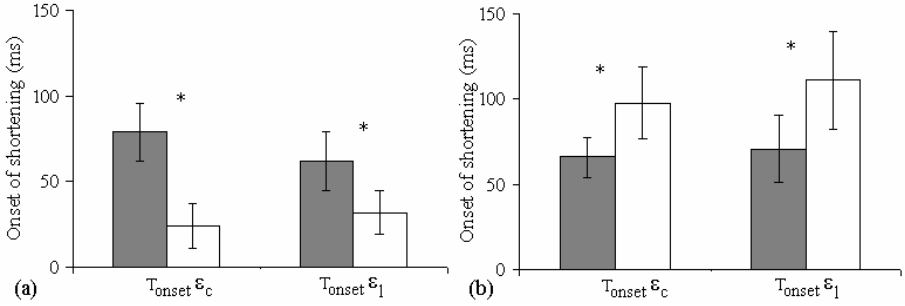

Figure 4-6 Mean time to onset of shortening in septum (a) and lateral wall (b). Error bars represent SD. The healthy population is represented in grey and the LBBB population in white. * - $P < 0.001$ obtained with multilevel analysis (see Table 4-11). $T_{onset}\,\varepsilon_c$ – time to onset of circumferential shortening; $T_{onset}\,\varepsilon_l$ – time to onset of longitudinal shortening.

In this analysis, the percentage of cases which were successfully determined for the $T_{onset}\,\varepsilon_c$ and for the $T_{onset}\,\varepsilon_l$ from the 36 cases for the septum and lateral wall of the healthy population (3 slices x 2 segments x 6 subjects) and from the 30 cases for the septum and lateral wall of the LBBB population (3 slices x 2 segments x 5 subjects) are summarized in Table 4-10.

	Percentage of successful determined cases (%)			
Timing parameter	Septum		Lateral wall	
	Healthy controls	LBBB patients	Healthy controls	LBBB patients
$T_{onset}\,\varepsilon_c$ (ms)	100	73	94	100
$T_{onset}\,\varepsilon_l$ (ms)	97	50	92	90

Table 4-10 Percentage of successful determined cases of time of onset of circumferential and longitudinal shortening for each region for both populations.

$T_{onset}\,\varepsilon_c$ – time to onset of circumferential shortening; $T_{onset}\,\varepsilon_l$ – time to onset of longitudinal shortening.

By comparing the timing parameters separately for the septum and lateral wall, it is observed that the difference is significant for both timing of shortening in both regions (see Table 4-11). Additionally, it is verified that the onset times of circumferential and longitudinal shortening in the septum occur earlier in the patients than in the healthy controls while in the lateral wall these onset times are later. From the Wald statistics it is observed that the timing parameter that better discriminates both populations is the T_{onset} ε_C at the septum (see Table 4-11).

Timing parameter vs. population	Septum			Lateral Wall		
	regression coefficient	Wald statistics	p-value	regression coefficient	Wald statistics	p-value
T_{onset} ε_c (ms)	55.215 ± 4.055	185.41	< 0.001	-32.212 ± 4.216	58.38	< 0.001
T_{onset} ε_l (ms)	30.229 ± 4.782	39.96	< 0.001	-40.054 ± 6.193	42.83	< 0.001

Table 4-11 Regression coefficients obtained from multilevel analysis for septum and lateral wall. The regression coefficients represent the difference between the timing parameters of the healthy and LBBB populations in these regions. Positive difference: onset of shortening in the healthy population occurs later than in the LBBB. Negative difference: onset of shortening in the healthy population occurs earlier than in the LBBB. T_{onset} ε_c – time to onset of circumferential shortening; T_{onset} ε_l – time to onset of longitudinal shortening.

These differences in the time to onset of shortening in circumferential and longitudinal directions were further explored. As the time to onset depends on the moment of triggering (R-wave) and the patients have a wider QRS complex, the triggering in patients occurs later which can decrease the time to onset. To verify if these differences between time to onset of patients and controls are really a consequence of the disease and not of the different moments of triggering, the OS delay-vector was computed for both populations, as this parameter is in principle independent of the trigger time. As asynchrony in LBBB patients occurs mainly between the septum and lateral wall [126], it was only studied the component that is a measure of the temporal asynchrony between septum and lateral wall. As in some segments it is not possible to measure the T_{onset}, to compute the OS delay-vector these missing values are replaced using bilinear interpolation from the neighbouring segments. The magnitude of the reported vector component represents the time difference between lateral wall and septum, with positive values representing an earlier contraction of the septum (T_{onset} of the septum smaller than of the lateral wall). This vector points from the earliest segment to the latest segment. The obtained results are summarized in Table 4-12.

OS delay-vector	Healthy controls	LBBB patients
ε_c (ms)	-15 ± 11	84 ± 21
ε_l (ms)	10 ± 14	78 ± 38

Table 4-12 Septal to lateral delay component of the circumferential and longitudinal shortening delay vectors for both populations.
ε_c – Circumferential shortening. ε_l – Longitudinal shortening

A graphical representation of these results is given in Figure 4-7.

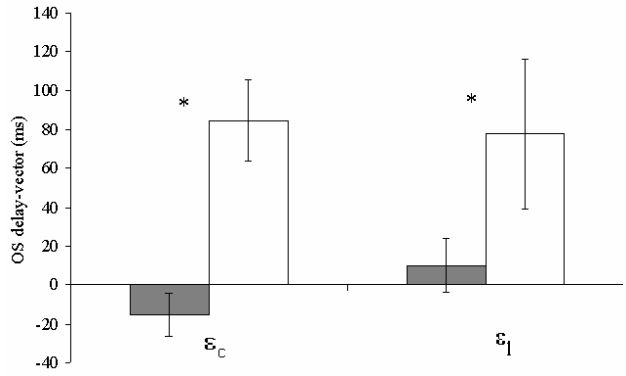

Figure 4-7 Onset of circumferential and longitudinal shortening delay vectors for both populations. Error bars represent SD. Healthy population is represented in grey and LBBB population in white. * - *P*< 0.05 obtained with unpaired t-test (healthy vs. LBBB) assuming unequal variances. ε_c – Circumferential shortening. ε_l – Longitudinal shortening

These results show that the OS delay-vector in the circumferential and longitudinal directions for the LBBB patients are significantly different from the controls. Additionally, in the circumferential direction, the patients show not only a higher asynchrony between septum and lateral wall, but also a change in the direction of the OS delay-vector, which points from the septum to the lateral wall instead of from the lateral wall to the septum as in the healthy subjects. In the longitudinal direction both populations have a delay-vector pointing from septum to lateral wall, with the patients showing a significantly higher asynchrony between these two regions. These results corroborate the differences between both populations for the time to onset of circumferential and longitudinal shortening in the septum and lateral wall, represented in Table 4-9.

4.4. DISCUSSION

In this study, the 3D strain component that better differentiates LBBB patients from healthy controls was evaluated using tagged MRI with high temporal resolution.

The mean age of the healthy and LBBB populations were 43 ± 13 and 66 ± 4 years old respectively, which is significantly different ($p > 0.05$). Nevertheless, previous studies have

shown that there is no aging effect on systolic strain components [103, 127, 128]. As the parameters evaluated in this study were the 3D strain components at the T_{avc} and the T_{onset} of circumferential and longitudinal shortening, it can be assumed that the differences observed between the two groups are mainly a result of the disease and not of their age difference.

Comparing global mean strains of both populations, significant differences are found in all strain components with exception for the radial-longitudinal shear. It is also verified that the strain component that better discriminates LBBB patients from controls is the circumferential-longitudinal shear, also designated by torsion (see Table 4-4), followed by the circumferential shortening, radial thickening, longitudinal shortening and radial-circumferential shear. However, when these differences are analysed regionally (septum vs. lateral wall) the drawn conclusions are different. In this case, all strain components at the septum of the LBBB population are significantly different from all the strain components at the septum of the healthy controls, but at the lateral wall only the shear components are different. In the septal wall, the 3D strain component that better discriminates patients from controls is the circumferential shortening, followed by the radial thickening, torsion, longitudinal shortening, radial-longitudinal shear and radial-circumferential shear. On the lateral wall the ranking of the affected parameters is the following: radial-circumferential shear, torsion and radial-longitudinal shear. These results emphasize the importance of comparing patients and controls strains regionally. Additionally it is also verified that the septum of the patients is affected more than the lateral wall.

Relatively to the global mean onset of circumferential and longitudinal shortening, the T_{onset} ε_l is the only timing parameter affected by the disease, with the onset of longitudinal shortening of patients delayed comparative to controls. However, comparing septum and lateral wall separately, all the timing parameters are significantly different. In the septal wall the onsets of longitudinal and circumferential shortening in patients occur earlier than in controls, while in the lateral wall these onset times are later. Relatively to the OS delay-vector it is verified that both onset of shortening delay vectors of the patients are significantly higher than those of the controls. This means that for both strain components (circumferential and longitudinal) patients show a higher delay between septum and lateral wall indicative of the asynchronous contraction of the LBBB patients LV. It is also interesting to note that in patients the septum starts contraction earlier than the lateral wall in both circumferential and longitudinal directions, while in controls the lateral wall starts earlier than the septum in the circumferential direction. So, in patients mechanical contraction propagates in the same direction as depolarization propagation.

In Chapter 3 it was mentioned that for the healthy subjects the opposed propagations of mechanical contraction in the circumferential direction and depolarization could be explained by the fact that the lateral wall stretches more than the septum during atrial contraction, leading to an earlier onset of shortening, as stated in a previous study [4, 129]. However, for patients

this is apparently not the case which suggests that atrial contraction has limited influence on the high mechanical asynchrony observed in LBBB patients.

Taking into account that most of these patients are asymptomatic (only subject 2 belongs to NYHA class II-III), tagged MRI is able to detect regional differences in strain even before clinical symptoms appear.

4.5. CONCLUSION

In this study the 3D strain components and the timing of onset of circumferential and longitudinal shortening of a healthy and a LBBB population were evaluated.

Regarding the strain components it was verified that the strain component that distinguishes both populations best, is the end-systolic circumferential shortening in the septum. Additionally it was verified that the septum was affected, while the function in the lateral wall was still mainly preserved. These results shows the importance of analysing the septal and lateral wall separately when evaluating LBBB patients, since the regional parameters are more sensitive than the global parameters in detecting the effects of the disease on the LV contraction.

Regarding the timing parameters, the onset time of circumferential shortening in the septum is the best discriminator between patients and healthy subjects, which performs even better (higher Wald statistic) than the end-systolic septal circumferential strain. In the patients, circumferential and longitudinal onset times are earlier in the septum and later in the lateral wall.

In summary, these results show that the septum of the patients contracts less and starts to contract earlier than the septum of the controls in circumferential and longitudinal directions. Additionally the patients show a higher asynchrony between septum and lateral wall.

Chapter 5.

QUANTITATIVE COMPARISON OF 2D AND 3D CIRCUMFERENTIAL STRAIN USING MRI TAGGING IN NORMAL AND LBBB HEARTS

Cardiac resynchronization therapy (CRT) is a new surgical treatment for patients with heart failure (HF) and left bundle branch block (LBBB). The response to this type of therapy can be predicted from the mechanical dyssynchony measured on circumferential strain (ε_c) Circumferential strain can be assessed using either 2D or 3D strain analysis. 3D strain analysis considers the full 3D motion, but is much more complicated to perform than 2D strain analysis, which only quantifies the apparent strain in the 2D image plane. In this study, the difference between 2D and 3D circumferential strain was evaluated using Magnetic Resonance (MR) tagging with high temporal resolution (14 ms). Six healthy volunteers and five patients with LBBB were evaluated. The 2D and 3D circumferential strains were compared by computing the mechanical dyssynchrony, the cross-correlation (r) between 2D and 3D strain curves and by quantifying the differences in peak circumferential shortening, in time to onset of shortening, and in time to peak of shortening. The obtained maximum r^2 was high: 0.97 ± 0.03 and 0.87 ± 16 for the healthy and LBBB population respectively, showing a good similarity between 2D and 3D strain curves. No significant difference was observed between 2D and 3D in time to onset, in time to peak and in peak circumferential shortening. This study shows that there is no significant difference between 2D and 3D circumferential strain. Thus for measuring dyssynchrony, 2D strain analysis will suffice. As 2D analysis is easier to implement than 3D analysis, this finding brings the application of tagged Magnetic Resonance Imaging (MRI) and strain analysis closer to the clinical routine.

Published in:

MRM 2007; 57:485-93

5.1. INTRODUCTION

On the past years, several studies have shown that mechanical dyssynchrony may better predict improvement from CRT [19, 111, 114-119] in patients with HF than electrical dyssynchrony.

Recently, Helm et al [130] showed that dyssynchrony measured on the circumferential direction (predominant orientation of the cardiac fibres in the left ventricle (LV) midwall) is more accurate than the dyssynchrony measured on the longitudinal direction (direction usually assessed with echo Doppler methods). Helm et al [130] used 3D strain analysis to determine the circumferential strain. This parameter can also be assessed using 2D strain analysis. The MR acquisition for a 2D analysis is faster and the image analysis is much more straightforward and easier to implement. However, the 2D strain analysis does not take into account the effect of through-plane rotation on the circumferential strain, and it is still not validated against the 3D strain analysis.

The goal of the study presented in this chapter is therefore to compare 2D and 3D circumferential strain measured with MR tagging. In order to evaluate the difference between both computation methods several parameters regarding circumferential strain are compared, namely: the shape of the curves of circumferential shortening, the timing (time to onset and time to peak of circumferential shortening), the maximum amplitude (peak of circumferential shortening) and the coefficient of variation in circumferential strain as a measure of mechanical dyssynchrony [111].

5.2. MATERIALS AND METHODS

5.2.1. Subjects

Six healthy volunteers (6 male; mean age: 43 ± 13), with no history of cardiac disease were studied (see Table 5.1). To compare both strain computation methods in the presence of abnormal cardiac motion, 5 patients with LBBB (1 male; mean age: 66 ± 4) were also evaluated (see Table 5.1). The New York Heart Association (NYHA) class for these patients varied from I to III. All subjects provided informed consent.

Healthy	Age	RR (ms)	$N_{time\ frames}$	Gender	NYHA class
1	56	1330	49	M	-
2	28	1200	63	M	-
3	53	1000	49	M	-
4	48	1270	49	M	-
5	46	1050	56	M	-
6	26	800	46	M	-
LBBB	**Age**	**RR (ms)**	$N_{time\ frames}$	**Gender**	**NYHA class**
1	58	804	41	F	I
2	66	969	49	F	II-III
3	69	1191	63	F	I
4	68	1005	41	M	I
5	68	951	56	F	I

Table 5-1 Characterization of analysed healthy and LBBB populations.

$N_{time\ frames}$ – Number of tracked time frames. M – male. F - female. RR – mean time interval between two R-waves.

5.2.2. Image Acquisition

Image acquisition is described in detail in Chapter 3. In summary, images were acquired with a 1.5T whole body scanner (Magnetom Sonata, Siemens Medical Solutions, Erlangen, Germany), using a 4 element phased-array receiver coil.

Cine imaging with myocardial tagging was acquired with the steady state free precession (SSFP) sequence using the linearly increasing startup angle (LISA) approach [64], with the parameters described in Chapter 2.

Tissue tagging was applied with two non-selective 45° radio-frequency (RF) pulses separated by a field gradient in the readout direction, yielding a sinusoidal spatial modulation of the magnetization (SPAMM) [66]. The tag line distance was 7 mm, and the readout direction perpendicular to the tag lines.

Five equidistant short-axis (SA) planes were imaged between base and apex, with an image plane distance of 10 mm to 15 mm. Three long-axis (LA) planes uniformly distributed around the LV and perpendicular to the SA were imaged, with an angular spacing equal to 60º [100].

To improve the myocardial tagging contrast, complementary spatial modulation of magnetization (CSPAMM) was used on the SA and LA image planes [92]. Four sets of images were acquired for each SA image plane: vertically and horizontally tagged images with sinusoidal and inverted sinusoidal tagging. Two sets of images were acquired for each LA image plane: tagged images with sinusoidal and inverted sinusoidal tagging with the tagging

direction perpendicular to the LA. A multiple brief expiration breath hold scheme was performed in order to avoid mismatching between the several images per set, as described in Chapter 2.

5.2.3. Post-processing

For the SA and LA image planes, CSPAMM images were computed by subtracting the modulus SPAMM images with inverted tag pattern from the images with non-inverted tag pattern, as explained in Chapter 2. The harmonic magnitude (HARM) and harmonic phase (HARP) images were computed from the CSPAMM images as described in Chapter 2. The HARM images were used to draw the contours that delimit the LV (MASS software package, version 5.1b, MEDIS, Leiden, The Netherlands). The HARP images were used to track the myocardial tissue in between the contours, using for the 2D analysis the automatic method described in Chapter 2 [98] and for the 3D analysis the automatic method described in Chapter 3. As these methods are not limited to tag line intersections, the tracking was applied to each pixel inside the myocardial contours.

5.2.3.1. 2D circumferential strain analysis

The 2D circumferential strain was computed as described in Chapter 2. In summary, for each time frame, a mesh of triangular elements was defined with the points tracked inside the myocardial contours of the basal, mid and apical slices. In the undeformed mesh of triangles the in-plane distance between the tracked points was equal to 1 pixel (1.17 mm). An homogeneous strain analysis was applied [87] and from the deformation of each triangle, the Lagrangian strain tensor $\vec{E}$ was determined, with the circumferential strain defined as the percent change in segment length in the circumferential direction:

$$\varepsilon_c = \left(\sqrt{1+2E_{cc}} - 1\right) \times 100\% \qquad \text{Equation 5-1}$$

with E_{cc} the Lagrangian strain component in this direction.

The results of the 2D circumferential strain were averaged in six segments for each slice: infero-septal (IS), antero-septal (AS), anterior (ANT), antero-lateral (AL), infero-lateral (IL) and inferior (INF). A schematic representation of these regions is given in Figure 1-51.

5.2.3.2. 3D circumferential strain analysis

The 3D circumferential strain was computed as described in Chapter 3. In summary, for each time frame, a mesh of tetrahedrons was defined using the points tracked in the five SA image planes. The mesh in the undeformed state is characterized by an in-plane distance equal to 1.17 mm and an out-of-plane distance ranging between 10 to 15 mm, depending on the distance between the SA image planes. With the knowledge of the 3D motion trajectories of

these myocardial points, the 3D Lagrangian strain tensor was computed for each tetrahedron [100]. The 3D circumferential strain was obtained from the Lagrangian strain tensor using Equation 5-1. The results of the 3D circumferential strain were averaged in the same six segments for the basal, mid and apical slices as in the 2D strain analysis.

This 3D strain analysis did not cover exactly the same myocardium as the 2D strain analysis, for the following reasons: as the tetrahedrons are defined from the points tracked in two neighbouring slices, the 3D slices definition is slightly different from the 2D slices. This is schematically presented in Figure 5-1.

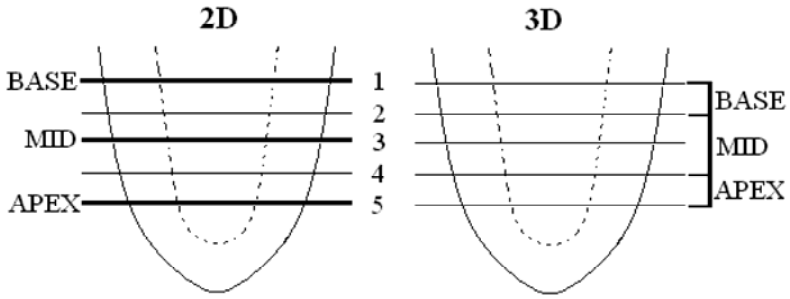

Figure 5-1 Definition of 2D and 3D basal, mid and apical slices.

For the 2D analysis, the mesh of triangles is defined in the image plane. For the 3D analysis the mesh of tetrahedrons is defined between neighbouring image planes. The 3D ε_c at the basal level uses the information of the points tracked in the image planes 1 and 2, at the mid level of the points tracked in the image planes 2, 3 and 4 and at the apical level of the points tracked in the image planes 4 and 5.

Further, the tetrahedrons can only be defined in the intersecting region of the contours of neighbouring image planes, which makes that the 3D strain analysis represents less myocardium than the 2D strain analysis, as illustrated in Figure 5-2.

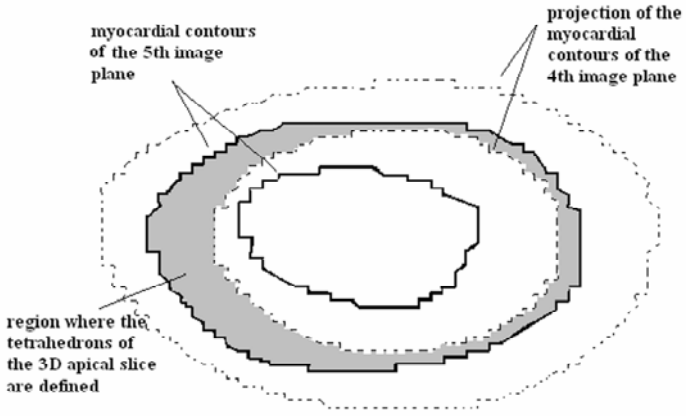

Figure 5-2 Myocardial contours at the apical level (5th image plane) of a healthy volunteer at end-systole (bold lines).

The projection of the myocardial contours of the 4th image plane are represented by the dashed lines. The grey area indicates the overlap between the contours of the 4th and 5th image planes. The 3D ε_c is computed using the tetrahedrons defined in this region. The 2D ε_c is computed using the triangles covering the complete area inside the myocardial contours at the apical level. Note that this situation is the 'worst case' configuration. Between the remaining image planes the overlap between the contours is better.

5.2.3.3. Comparing 2D and 3D circumferential strain

To evaluate the difference between 2D and 3D circumferential strain, several parameters of the strain curves were compared.

Firstly, the cross-correlation, r, between the 2D and 3D strain curves was computed for all segments and slices. The squares of the maximum cross-correlations, r^2, were used in statistical tests, and to report mean values for the healthy subjects and the LBBB patients.

Secondly, the 2D and 3D timing of circumferential shortening was quantified by the time to onset (T_{onset}) and the time to maximum peak ($T_{peak,max}$) of circumferential shortening. These parameters were determined for each segment in each slice. T_{onset} corresponds to the instant when the down slope of the ε_c curve starts and $T_{peak,max}$ to the instant of minimum ε_c [4]. Since patients may present multiple shortening waves, the measurement of the time to the first peak of circumferential shortening ($T_{peak,first}$) can be an important parameter on the evaluation of this group of subjects [126]. 2D and 3D $T_{peak,first}$ were measured on each segment of each slice of the LBBB population. $T_{peak,first}$ is defined as the first zero crossing in the strain rate from a negative strain rate to a positive one [126]. The 2D and 3D maximum peak of circumferential shortening ($\varepsilon_{c,peak,max}$) were also computed, as well as the first peak of circumferential shortening for the LBBB population ($\varepsilon_{c,peak,first}$). All timing parameters and peak amplitudes were automatically determined as described before [4]. When the observer did not agree with the obtained values, he/she could discard them, but not adjust to prevent subjective changes of the results. A typical situation where the peak and time to peak strain could be discarded was in strain curves that had excessive noise in the region of the peak.

Finally, to verify if the mechanical dyssynchrony measured in the circumferential direction by both strain computation methods is equivalent, the coefficient of variation of the 2D and 3D circumferential strains were computed using the formula:

$$CV_{Ecc^*} = 100\% \times \left(\frac{SD_{E_{cc}^*}}{mean\ E_{cc}^*} \right) \qquad \text{Equation 5-2}$$

with E_{cc}* the strain of all segments at the time of maximal circumferential shortening for the complete heart, as described in [111]. The segments for which the time to peak and/or peak circumferential strain were discarded by the observer were not taken into account for the computation of the coefficient of variation.

5.2.3.4. Statistical analysis

Results are presented as mean ± SD. *P*-values < 0.05 are considered statistically significant. To compare the timing of shortening and the peak amplitudes of the 2D and 3D ε_c curves, a multilevel regression analysis was performed (MLwiN, version 1.02.0002, Centre for

Multilevel Modelling, London, United Kingdom) [101, 102]. This analysis was used because the data is structured in a hierarchy with three levels (segments are clustered within slices and slices within subjects). The multilevel analysis corrects the regression coefficients between the strain components and the strain computation method for dependency in the data due to this hierarchy.

The timing of shortening and the peak amplitudes (T_{onset}, $T_{peak,max}$, $\varepsilon_{c,peak,max}$ and also $T_{peak,first}$ and $\varepsilon_{c,peak,first}$ for the patients), were set as outcome variables and the strain computation method as independent variable (dichotomous variable that takes the value 1 for the 2D strain analysis and 0 for the 3D strain analysis). The obtained regression coefficients reflect the differences between the 2D and 3D timing of shortening and peak amplitudes.

The coefficients of variation of the 2D and 3D ε_c were compared using a paired t-test.

5.3. RESULTS

An example of the 2D and 3D circumferential strain curves for a healthy volunteer and a LBBB patient are presented in Figure 5-3.

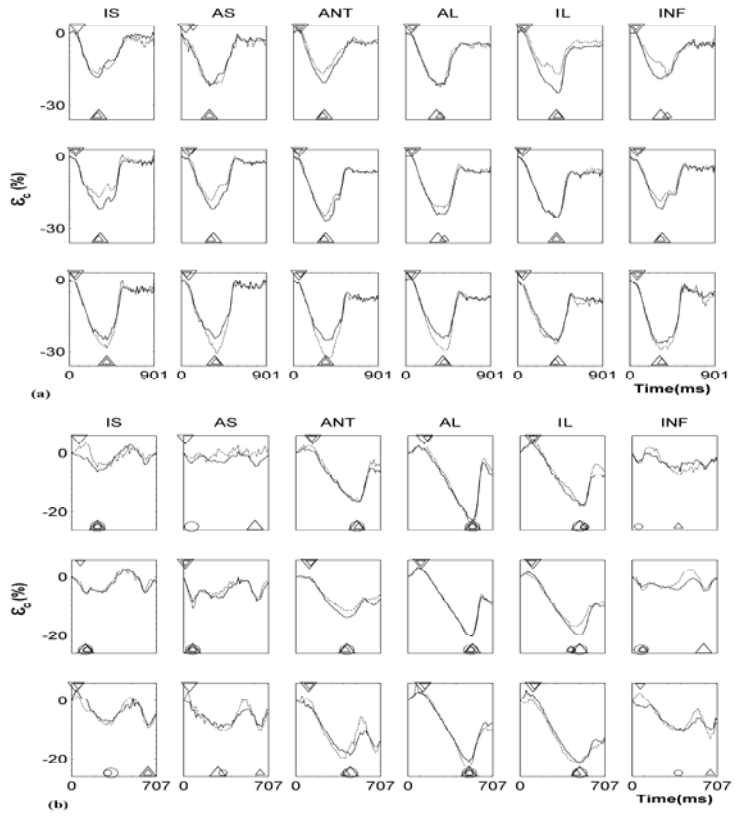

Figure 5-3 Example curve of the 2D (dashed line) and 3D (solid line) ε_c for a healthy volunteer (a) and a LBBB patient (b).

From top to bottom: basal, mid and apical image planes. IS - infero-septal; AS - antero-septal; ANT - anterior; AL - antero-lateral; IL - infero-lateral; INF - inferior. ∇ - 3D T_{onset} , ∇ - 2D T_{onset} , Δ - 3D $T_{peak,max}$, Δ - 2D $T_{peak,max}$, o - 3D $T_{peak,first}$, o - 2D $T_{peak,first}$

For one healthy volunteer it was not possible to define tetrahedrons in the IL and INF segments of the apical slice, since there was no intersection between the contours of the image planes 4 and 5 in those regions.

5.3.1. Cross-correlation

The cross-correlation between the 2D and 3D circumferential strain was computed for each segment and slice of the healthy and LBBB population (see example on Figure 5-4).

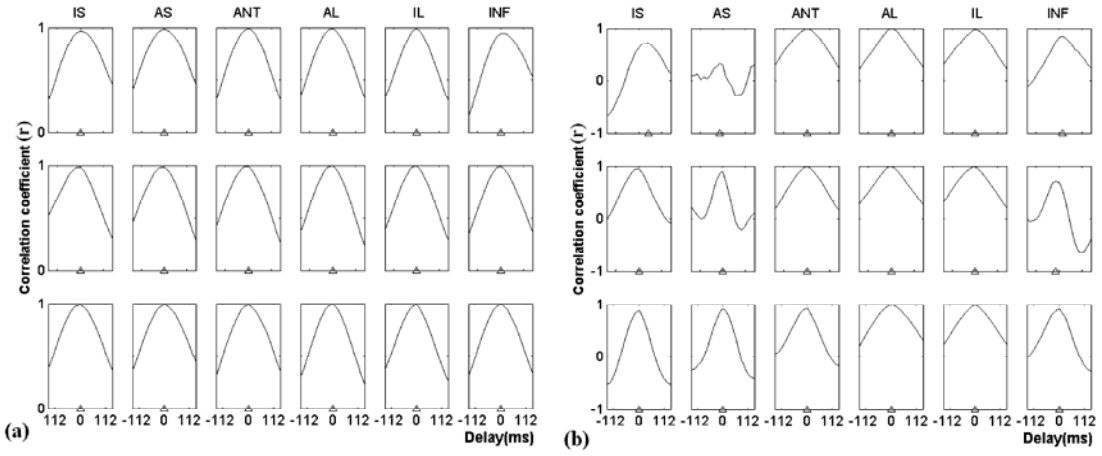

Figure 5-4 Example cross correlation curves between the 2D and 3D ε_c for the healthy volunteer (a) and LBBB patient (b) of Figure 5-3.
From top to bottom: basal, mid and apical image planes IS - infero-septal; AS - antero-septal; ANT - anterior; AL - antero-lateral; IL - infero-lateral; INF - inferior. Δ - maximum correlation coefficient

For both populations the maximum r^2 was high: 0.97 ± 0.03 and 0.87 ± 0.16 for the healthy and LBBB population respectively, which shows a good similarity between the 2D and 3D circumferential strain curves. The maximum r^2 was statistically significant for all 108 cases (3 slices x 6 segments x 6 subjects) of the healthy population ($p < 0.0001$) and for all 90 cases (3 slices x 6 segments x 5 subjects) of the LBBB population ($p < 0.03$).

The mean delay at maximum cross-correlation was 0.5 ± 3.3 ms for the healthy population and -0.2 ± 8.3 ms for the LBBB population, which is clearly insignificant. For the healthy population, 94% of the 108 cases had no delay, 5% had a delay of 14 ms and 1% of –14 ms. For the LBBB population, 84% of the 90 cases had no delay, 3% had a delay of 14 ms, 11% of –14 ms and 2% of 42 ms.

The maximum r^2 and the respective delay were also averaged per segment and slice for both populations (Figure 5-5 and Figure 5-6). From the plots it is clear that the correlation is high for all segments and slices for the healthy and LBBB populations. The delays for both populations are small in all segments and slices.

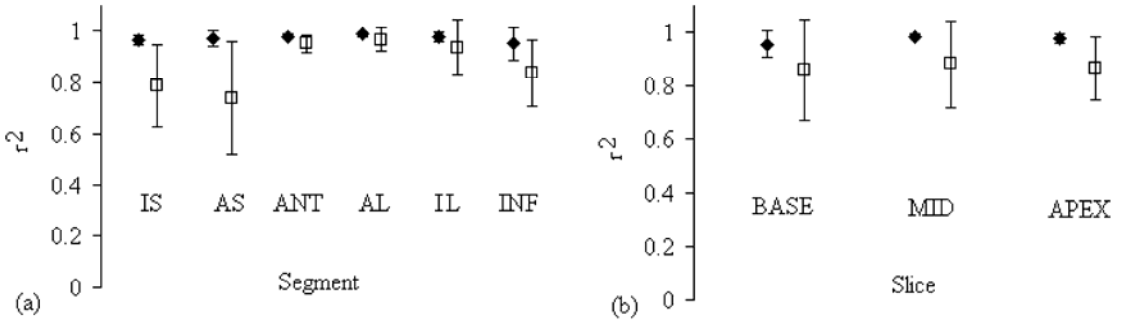

Figure 5-5 Maximum cross-correlation (r^2) between 2D and 3D ε_c curves, averaged per segment (a) and per slice (b).

Error bars correspond to the standard deviation. IS - infero-septal; AS - antero-septal; ANT - anterior; AL - antero-lateral; IL - infero-lateral; INF – inferior. ♦ Healthy population □ LBBB population.

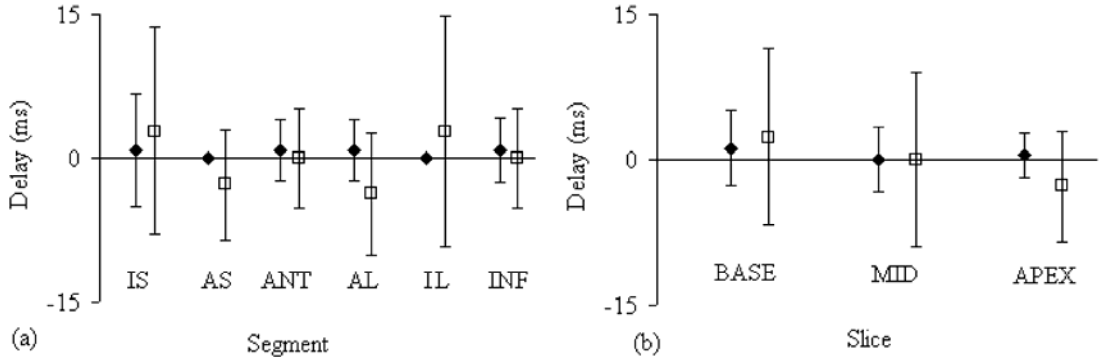

Figure 5-6 Delay at maximum cross-correlation averaged per segment (a) and per slice (b).

Error bars correspond to the standard deviation. IS - infero-septal; AS - antero-septal; ANT - anterior; AL - antero-lateral; IL - infero-lateral; INF – inferior. ♦ Healthy population □ LBBB population.

5.3.2. Timing of shortening

The difference between the 2D and 3D strain computation methods was further explored. The regression coefficients obtained from multilevel analysis between the timing of shortening and the strain computation methods are presented in Table 5-2.

	regression coefficient	p-value
T_{onset} vs. computation method		
Healthy	-0.883 ± 2.034	0.664
LBBB	6.077 ± 6.594	0.357
$T_{peak,max}$ vs. computation method		
Healthy	11.813 ± 6.437	0.066
LBBB	-14.599 ± 15.585	0.349
$T_{peak,first}$ vs. computation method		
LBBB	-3.638 ± 26.085	0.889

Table 5-2 Results from the multilevel regression analysis of the difference between the 2D and 3D timing of circumferential shortening.
The regression coefficient can be interpreted as the difference in timing (in ms) between the 2D and 3D strain computation method.

T_{onset} was determined successfully in 94% of the 216 cases of the healthy population (3 slices x 6 segments x 6 subjects × 2 methods of strain computation) (in 45% with the 2D method and in 49% with the 3D method) and in 78% of the 180 cases of the LBBB population (3 slices x 6 segments x 5 subjects × 2 methods of strain computation) (in 40% with the 2D method and in 38% with the 3D method). For the healthy population, the 2D T_{onset} was 72 ± 18 ms and the 3D T_{onset} was 73 ± 15 ms. From the multilevel analysis, it was observed that the T_{onset} obtained with both computation methods were not statistically different (P = 0.664). For the LBBB population, the 2D T_{onset} did not significantly differ from the 3D T_{onset} (2D T_{onset} = 72 ± 43 ms and 3D T_{onset} = 67 ± 41 ms, P = 0.357).

$T_{peak,max}$ was available in 99% (in 50% with the 2D method and in 49% with the 3D method) and 97% (in 49% with the 2D method and in 48% with the 3D method) of the cases of the healthy and LBBB population, respectively. For the healthy population, the 2D $T_{peak,max}$ was 385 ± 57 ms and the 3D $T_{peak,max}$ was 373 ± 53 ms, which was not statistically different (P = 0.066). For the LBBB population the difference was also not statistically significant (P = 0.349), with the 2D $T_{peak,max}$ equal to 421 ± 128 ms and the 3D $T_{peak,max}$ equal to 435 ± 114 ms.

For the LBBB population the $T_{peak,first}$ was available in 90% of the cases (in 44% with the 2D method and in 46% with the 3D method). The 2D $T_{peak,first}$ was equal to 301 ± 166 ms and the 3D $T_{peak,first}$ was equal to 305 ± 169 ms. The difference between the 2D and 3D $T_{peak,first}$ was not statistically significant (P = 0.889).

5.3.3. Peak of Circumferential Shortening

The regression coefficients obtained from the multilevel analysis between the peak of circumferential shortening and the strain computation methods are presented in Table 5-3.

	regression coefficient	p-value
$\varepsilon_{c,peak,max}$ vs. computation method		
Healthy	0.159 ± 0.474	0.737
LBBB	0.215 ± 0.814	0.792
$\varepsilon_{c,peak,first}$ vs. computation method		
LBBB	0.151 ± 1.198	0.900

Table 5-3 Results from the multilevel regression analysis of the difference between the 2D and 3D peak of circumferential shortening.
The regression coefficient can be interpreted as the difference in peak strain (in %) between the 2D and 3D strain computation method.

$\varepsilon_{c,peak,max}$ was evaluated for the same cases as the $T_{peak,max}$. For the LBBB population, the 2D $\varepsilon_{c,peak,max}$ was equal to –18.1 ± 6.0 % and the 3D $\varepsilon_{c,peak,max}$ was equal to –18.4 ± 6.2 %. The multilevel analysis revealed that this difference was not statistically significant (P = 0.792). The $\varepsilon_{c,peak,first}$ was measured in the same cases as the $T_{peak,first}$ on the LBBB population. The 2D $\varepsilon_{c,peak,first}$ was equal to –16.4 ± 7.8 % and the 3D $\varepsilon_{c,peak,first}$ was equal to –16.5 ± 7.8 %, which is not statistically different (P = 0.900).

For the healthy population, the 2D $\varepsilon_{c,peak,max}$ was equal to –21.7 ± 4.5 % and the 3D $\varepsilon_{c,peak,max}$ was equal to –21.8 ± 3.5%. From the statistical analysis it was verified that the $\varepsilon_{c,peak,max}$ computed with both methods were not statistically different (P = 0.737). However, the obtained regression coefficient (Table 5-3) was dependent on the slice position. This result was further investigated by computing the difference between the 2D $\varepsilon_{c,peak,max}$ and the 3D $\varepsilon_{c,peak,max}$ for the basal, mid and apical slices. The obtained results are summarized in Table 5-4. The 2D $\varepsilon_{c,peak,max}$ tended to be lower than the 3D $\varepsilon_{c,peak,max}$, for the basal and mid slices, and higher for the apical slice. These observations are also clear on the plots of Figure 5-3. To explore whether the disagreement between the definition of the 2D and 3D slices plays a role in this slice-dependent differences in $\varepsilon_{c,peak,max}$, the previous computation was repeated using the image plane 2 as the 2D basal slice and the image plane 4 as the 2D apical slice (Figure 5-1). The obtained results are shown in Table 5-5. Using these slices, the 2D $\varepsilon_{c,peak,max}$ tended to be higher than the 3D $\varepsilon_{c,peak,max}$ for the basal slice and lower for the mid and apical slices, in the healthy population. Hence, using 2D image planes 2 and 4, the trend in the slice-dependent differences tends to be opposite to the trend obtained using the 2D image planes 1 and 5 (compare Table 5-4).

	2D image plane (3D level)		
2D $\varepsilon_{c,peak.max}$ − 3D $\varepsilon_{c,peak.max}$ (%)	**1 (Base)**	**3 (Mid)**	**5 (Apex)**
Healthy	1.22 ± 2.39	1.42 ± 1.72	-2.36 ± 2.57
LBBB	-0.02 ± 2.07	0.35 ±1.82	-0.18 ± 2.21

Table 5-4 Difference between 2D $\varepsilon_{c,peak.max}$ and 3D $\varepsilon_{c,peak.max}$ at basal, mid and apical slices for healthy and LBBB populations.
The 2D basal slice corresponds to image plane 1 and the 2D apical slice to image plane 5 (See Figure 5-1).

	2D image plane (3D level)		
2D $\varepsilon_{c,peak.max}$ − 3D $\varepsilon_{c,peak.max}$ (%)	**2 (Base)**	**3 (Mid)**	**4 (Apex)**
Healthy	-0.21 ± 1.24	1.42 ± 1.72	0.41 ± 2.71
LBBB	-0.87 ± 2.40	0.35 ± 1.82	0.89 ± 2.11

Table 5-5 Difference between 2D $\varepsilon_{c,peak.max}$ and 3D $\varepsilon_{c,peak.max}$ at basal, mid and apical slices for healthy and LBBB populations.
In these calculations, the 2D most basal slice corresponds to image plane 2 and the 2D most apical slice to image plane 4 (See Figure 5-1).

5.3.4. Mechanical dyssynchrony

The 2D and 3D mechanical dyssynchrony was quantified by the coefficient of variation of the circumferential shortening. The results obtained with the 2D and 3D strain analysis methods are presented in Table 5-6. Comparing both computation methods, it was found that the 2D coefficient of variation tends to be higher than the 3D. This difference was only significant within the healthy population ($P < 0.05$).

To study the influence of slice selection on the coefficients of variation, the same analysis was performed using the slices 2, 3, and 4 instead of the slices 1, 3 and 5 for the 2D analysis (see Figure 5-1 and Table 5-6). The obtained results show that the difference between the 2D and 3D coefficients of variation decreases considerably for both populations, with the 2D coefficient of variation still slightly higher than the 3D. The difference between the 2D and 3D coefficients of variation within the healthy population remained statistically significant. The difference between the healthy and LBBB populations in coefficient of variation's was equal to 30 ± 39 ($P > 0.05$) using the 2D analysis with slices 1, 3 and 5, equal to 29 ± 37 ($P > 0.05$) using the 2D analysis with slices 2, 3 and 4 and equal to 28 ± 31 ($P > 0.05$) using the 3D analysis. Clearly the differences between the populations are very similar for the different analysis methods.

2D Analysis (slices 1, 3, 5)		2D Analysis (slices2, 3, 4)		3D Analysis	
Healthy	**LBBB**	**Healthy**	**LBBB**	**Healthy**	**LBBB**
21.3 ± 4.0 *	51.7 ± 35.3	14.1 ± 3.3 *	43.2 ± 33.6	12.7 ± 3.6	40.9 ± 27.0

Table 5-6 Coefficient of variation for the healthy and LBBB populations for each strain analysis

*** 2D coefficient of variation statistically different from 3D coefficient of variation within healthy subjects ($P < 0.05$).**

5.4. DISCUSSION

In this study, the difference between the 2D and 3D circumferential strain was investigated. The strong and positive cross-correlation coefficients obtained between the 2D and 3D circumferential strain, show that there is a high similarity between both computation methods, also for the patient group with strongly abnormal strain patterns. From the multilevel analysis, it was found that the differences between the 2D and 3D timing of circumferential shortening and peaks of circumferential shortening were not statistically significant for both populations.

In the LBBB population the IS and AS segments showed a higher standard deviation (between subjects) in mean r^2 per segment (Figure 5-5a), as compared to the healthy population. This is caused by the poor septal function in some patients, which leads to noisier strain curves and consequently poorer cross-correlations. See for example the AS segment at the base in Figure 5-3b and Figure 5-4b.

From the multilevel analysis, it was found that, for the healthy population, the $\varepsilon_{c,peak,max}$ difference varies with the slice position. For the basal and mid slices, the 2D $\varepsilon_{c,peak,max}$ was slightly lower than the 3D $\varepsilon_{c,peak,max}$, while for the apical slice it was slightly higher. These results can be explained by the differences in slice definition between both computation methods (see Figure 5-1). The 3D tetrahedrons are defined in between the 2D neighbouring image planes, and can only be defined in the intersecting regions inside the contours of these image planes (see Figure 5-2). Being the myocardial wall oblique, in some regions there is a small or (in one case) no intersection between the myocardial contours of neighbouring image planes. For example, at the apical level, the tracked points that are closer to the endocardial contour of the apical image plane (slice 5, Figure 5-1) do not have tracked points on the image plane above (slice 4, Figure 5-1). Consequently, the 3D strain analysis is not able to define tetrahedrons in this region. However, the 2D strain analysis uses all the triangles defined inside the apical slice (slice 5, Figure 5-1), including those that are close to the endocardial contour (see Figure 5-2). As a consequence, the 2D $\varepsilon_{c,peak,max}$ in the apex can be higher than the 3D $\varepsilon_{c,peak,max}$ because it includes more subendocardial tissue, which contributes to higher values of circumferential strain. At the basal level (slice 1, Figure 5-1) the effect is the opposite.

In general, when the image plane used as the 2D slice is on the top of the region used for the 3D slice (see Figure 5-1), the 2D analysis includes more subepicardial tissue than the 3D analysis and consequently the calculated circumferential strain can be lower than in the 3D analysis. When the image plane used as the 2D slice is on the bottom of the region used as the 3D slice, the 2D analysis includes more subendocardial tissue than the 3D analysis, which can lead to values of 2D circumferential strain higher than the 3D. This explanation is corroborated by the inverted results obtained for the differences between the 2D and 3D $\varepsilon_{c,peak,max}$ when the 2D slices 2, 3 and 4 were used instead of the 2D slices 1, 3 and 5 (negative difference at the basal level and positive difference at the apical level, see Table 5-3 and Table 5-4). This finding suggests that the choice of the region of interest that is used to report myocardial function can be of more importance than the used type of strain analysis (2D or 3D).

Regarding the dyssynchrony measured with the coefficient of variance, the values obtained for the patients were small compared with previous reported results [111]. This is probably due to the fact that only one of the 5 evaluated patients was symptomatic (class III). Nevertheless, the asymptomatic patients were also a representative group to study the performance of each strain computation method in abnormal curves, since their strain curves were far from normal. A significant difference was observed between the 2D and 3D coefficient of variation for the healthy population, using either the 2D slices 2, 3 and 4 or the 2D slices 1, 3 and 5. However, to use the dyssynchrony as a parameter to select patients for CRT, one should compare the difference between the coefficient of variation of the healthy population and the coefficient of variation of the LBBB population. It is clear that these differences are very similar for the 2D and 3D computation methods (see Table 5-5). Hence, the 2D and 3D computation methods are also equivalent with respect to assess dyssynchrony.

Over the past years, several methods have been proposed for myocardial tracking [84, 96, 97] and 3D motion reconstruction [94, 131, 132]. In this present study, a 3D extension of the 2D extended HARP tracking method [98] was used to track the myocardial tagging, and the 3D myocardial motion was obtained using a 1D displacement field fitting [100]. The limitation of this 3D analysis method is its restriction to the intersection of the myocardial contours on successive slices. However, this method [100] has the advantage of minimizing the interpolation and smoothing of the data, in comparison with methods based on field fitting [131], since it is only the longitudinal displacement that is interpolated between LA image planes. With this method, the true spatial resolution of the data is preserved within the SA planes.

The circumferential strain assessed with MRI tagging has been reported earlier for healthy subjects and patients using either 2D [4, 129, 133, 134] or 3D [89, 90, 100, 135] strain analysis methods. However, the use of MRI tagging on clinical routine has been hindered by the need for complex and time consuming post-processing. In this study, no difference between 2D

and 3D circumferential strain was found, thereby verifying that 2D circumferential strain values are representative of 3D circumferential strain. Since the 2D strain analysis is faster and much easier to implement, these findings bring the application of MRI tagging and strain analysis in the clinical routine within reach. For example, the quantification of dyssynchrony in circumferential strain to predict improvement from CRT is a promising area for application of MRI tagging in clinical practice. By using the 2D strain analysis instead of the 3D strain analysis, this quantification becomes much less time consuming and the post-processing less complex.

5.5. CONCLUSION

Between 2D and 3D circumferential strain no significant difference was observed in timing parameters and in peak strain. Both computation methods yielded the same differences between the healthy controls and LBBB patients in the coefficient of variation (a measure for mechanical dyssynchrony). Thus for measuring mechanical dyssynchrony in LBBB patients, 2D strain analysis will suffice. As 2D strain analysis is faster to implement than 3D analysis and does not require LA tagging, this finding brings the application of MRI tagging and strain analysis closer to the clinical routine.

Chapter 6.

ERROR SOURCE OF HARP ANGLE COMPUTATION USING HILBERT TRANSFORM

Harmonic Phase (HARP) tracking is a recent tool to automatically compute myocardial displacement from cardiac tagged Magnetic Resonance (MR) images. The Hilbert transform used in this method induces errors in the HARP angle, which results in a low accuracy for the radial strain, while the accuracy for the circumferential strain is high. In Chapter 2 it was hypothesized that there is a contribution of the truncation of the tag signal, the deformation of the tag pattern and/or the filtering in k-space to the observed errors in strain. The aim of this study was to test these hypotheses and to understand the mechanisms by which these contributions result in erroneous strain quantification. Simulations showed that the HARP angle and strain errors were zero when a complex modulation was used, while cosine modulation resulted in errors which were larger in the radial direction than in the circumferential direction. These results led to the conclusion that the main error source in the HARP angle computation is the inability of the method to perfectly isolate the positive tag peak in k-space. Since the complex modulation function has only one peak in k-space no filtering is required and negligible errors are obtained. The error in the radial direction is higher because in this direction, the number of available tag lines is less than in the circumferential direction, leading to wider peaks in k-space and, the radial thickening shifts the tagging peaks towards the centre of k-space, increasing the overlap between the two peaks.

Under submission to MRM

6.1. INTRODUCTION

Myocardial tagging [66, 74, 75] is a promising tool to quantify the mechanical function of the heart wall. This technique allows the tracking of the myocardium by creating patterns of saturation of the magnetization in the heart wall. Several methods have been proposed to analyse the tagged cardiac images [81-84, 94, 96, 97, 131, 132], namely the HARP tissue tracking (see Chapter 1 and reference [85]). The automated nature that characterizes this technique turns its application in clinical routine easier. Nevertheless, the errors in the HARP angle and in the strain obtained with this method are still not well understood. In Chapter 2 [98] it was shown that the strain accuracy obtained from the HARP tracking is low for the radial direction, while for the circumferential direction it is high. Additionally, it was shown that these errors in the strain results are mainly caused by the computation of the HARP angle by the Hilbert transform, leading to the hypothesis that these errors in strain could be a consequence of the truncation of the tag signal, the deformation of the tag pattern and/or the filtering in *k*-space.

A possible explanation for the observed accuracy is peak overlapping in *k*-space and, consequently, the impossibility to perfectly isolate the positive peak with the Hilbert transform. It has been shown that the use of complementary spatial modulation of magnetization (CSPAMM) images instead of spatial modulation of magnetization (SPAMM) images leads to smaller strain errors [93], since the central peak in *k*-space is removed. However, overlap between the two tagging peaks may still occur, due to truncation of the tag signal and deformation of the tag pattern that leads to non-linearity of the tagging frequency over position.

The present study aims to test the hypotheses drawn in Chapter 2 [98] and to understand the mechanisms by which their contributions result in erroneous strain quantification. Simulations with a 1D CSPAMM signal were performed in order to evaluate the effects of truncation of the modulated function (simulation of finite sized objects) and of the variable frequency of the modulation function (simulation of deformation) on the errors in the HARP angle and strain.

6.2. METHODS

6.2.1. HARP angle computation

The detailed explanation of HARP angle computation is given in Chapter 1. Briefly, HARP tracking uses tagged MR images [66] to determine the displacement of the myocardium. The pattern of dark and light stripes of the tagged images is obtained by applying two 45º radio-frequency (RF) tag pulses before the imaging itself. The amplitude of a CSPAMM image [82] with vertical tag lines is given by:

$$I(x,y) = I_0(x,y)\cos(kx + \phi_i) \qquad \text{Equation 6-1}$$

where $I_0(x,y)$ is the amplitude of the underlying image, ϕ_i the initial phase of the tag signal and k its spatial frequency in the x-direction. In k-space this signal is composed by two peaks at $+k$ and $-k$. After applying a high pass filter to isolate the positive frequency peak, the inverse fast Fourier transform (IFFT) is computed and the following complex signal is obtained:

$$g(x,y) = \frac{1}{4} I_0(x,y)\left[\cos(kx + \phi_i) + i\sin(kx + \phi_i)\right] \qquad \text{Equation 6-2}$$

The magnitude of this complex signal is proportional to $I_0(x,y)$ and its phase is given by:

$$\tan a(x) = \frac{Im(g(x,y))}{Re(g(x,y))} \qquad \text{Equation 6-3}$$

$a(x)$, designated by HARP angle, is an estimation of the phase of the tag signal wrapped between $(-\pi,\pi]$, and can be used to track the displacement of the myocardium. The group of steps to compute the HARP angle (fast Fourier transform (FFT), filtering and IFFT), leads to errors in $a(x)$, and consequently in the observed displacement and strain [98].

6.2.2. Simulations

6.2.2.1. Tagging modulation functions

Each simulation in the present study was performed with two types of modulation functions: cosine and complex.

Cosine modulation: The modulation of a 1D object with a cosine function yields a 1D CSPAMM image with amplitude given by:

$$I(x) = I_0 \cos(\phi(x) + \phi_i) \qquad \text{Equation 6-4}$$

where I_0 is the amplitude of the original object and $\phi(x)$ the phase of the modulation function. The spatial frequency of the modulation function, k, is given by $d\phi(x)/dx$, which means that $\phi(x)$ equals $k.x$ only when k is constant. In k-space this modulated object is composed by two peaks at $+k$ and $-k$.

Complex modulation: The modulation of a 1D object with a complex function yields a 1D image which amplitude is given by:

$$I(x) = I_0\left[\cos(\phi(x) + \phi_i) + i\sin(\phi(x) + \phi_i)\right] \qquad \text{Equation 6-5}$$

This modulated object is characterized by having a single peak in k-space, which turns unnecessary the use of filters.

6.2.2.2. Possible sources of error

The possible error sources of the HARP angle evaluated in this study are described in detail hereafter.

Imperfect isolation of the tagging peak in *k*-space: To isolate the positive peak of an object whose amplitude was modulated with a cosine function, it is necessary to apply a filter in *k*-space. This process is not straightforward as, during myocardial deformation, the overlap between the two peaks increases. Depending on the chosen cut-off frequency, some information relative to the negative peak may be included in the filtered signal, while information relative to the positive peak may be removed. In the simulations performed in the present study, two types of filter were evaluated: a high-pass filter with cut-off spatial frequency (ν_c) equal to 20 and a band-pass filter with a width of 32 pixels around the positive peak. ν_c is reported in terms of $\nu_c = k_c / 2\pi.FOV$, with FOV the field-of-view (see Chapter 2). These cut-off values have been used in previous studies [93, 98, 136].

Variability of the tag frequency: During the cardiac cycle, the spatial frequency of the tag lines varies across the myocardial wall due to the tag pattern deformation. During the systolic phase, the myocardial wall becomes thicker, the distance between the tag lines increases in the radial direction, and their spatial frequency decreases. This phenomenon is observed in *k*-space by wider peaks that include the lower frequencies of the deformed tagged image. To simulate this radial thickening of the myocardium the following equation was used for the spatial frequency (k (in rad.pixel^{-1})) of the modulation function:

$$k = k_0 - \frac{1}{2} k_0 \left(\frac{x - 2x_0}{2x_0} \right)^2 \qquad \text{Equation 6-6}$$

with x_0 the middle point of the myocardial wall and k_0 the spatial frequency of the undeformed modulation function. With this formula the frequency of the modulation function remains unchanged near the subepicardium (presented by $x = 2x_0$) and decreases to half at the subendocardium (presented by $x = 0$). Similarly, during the systolic phase the tag lines on the circumferential direction contract, thereby increasing their spatial frequency. This circumferential shortening of the myocardium was simulated using the following formula for the spatial frequency of the modulation function:

$$k = k_0 + \frac{1}{2} k_0 \left(\frac{x - x_0}{x_0} \right)^2 \qquad \text{Equation 6-7}$$

with x_0 the middle point of the myocardial wall and k_0 the spatial frequency of the undeformed modulation function. In this formula, x simulates the circumferential direction. The frequency of

the modulation function remains unchanged in the centre of the wall (presented by $x = x_0$) and increases 50% at the borders (presented by $x = 0$ and $x = 2x_0$).

Truncation of the tag signal: On real images there are discontinuities of the tag pattern at the borders of the tissues inside the FOV. For example, inside the left ventricle (LV) and right ventricle (RV) the tag pattern fades in the first time frames due to blood motion. Inside the lungs there are no tag lines, due to the presence of air. This discontinuity of the tag pattern is also a possible error source of the HARP angle and it was evaluated using the function:

$$I(x) = I_0 \times ModulationFunction \times object \qquad \text{Equation 6-8}$$

with *object* representing the truncation of the tag pattern. *ModulationFunction* is either complex (Equation 6-5) or cosine (Equation 6-4), depending on the simulated case.

In Chapter 2 [98] a high accuracy for the circumferential strain and a low accuracy for the radial strain were reported. It was suggested that these results could be a consequence of the fact that the truncation of the tag signal is more severe in the radial direction than in the circumferential direction. In real images, there are in general 7 to 8 tag cycles in the circumferential direction while in the radial direction there are only 1 to 2 tag cycles. In order to evaluate the effect on the HARP angle error of the number of tag cycles inside the imaged object, simulations with objects of different sizes were performed. The truncation also changes the initial phase of the modulated signal. To verify if this parameter has any influence on the HARP angle error, simulations with different initial phases for the same imaged object were also performed.

6.2.2.3. Simulated cases

The previous hypotheses for the error sources of the HARP angle have complicated interactions. To separate the contribution of each of these error sources as much as possible, different simulations were executed for a simplified 1D FOV of 256 pixels. A list of these simulations and a detailed description of the used naming convention are presented in Table 6-1

Simulations	Error sources present in the simulation			Filter
	imperfect isolation of tagging peak in *k*-space	Variability of the modulation frequency	Truncation of the modulation function	
1XFN	NO	NO	NO	None
1CFN	NO	NO	NO	H
2XVN	NO	YES	NO	None
2CVN	YES	YES	NO	B+H
3XFT*	NO	NO	YES	None
3CFT*	YES	NO	YES	B+H
4XFT§	NO	NO	YES	None
4CFT§	YES	NO	YES	B+H
5XVT*	NO	YES	YES	None
5CVT*	YES	YES	YES	B+H
6XVT§	NO	YES	YES	None
6CVT§	YES	YES	YES	B+H

Table 6-1 List of simulations with the respective error sources.
Simulations names structure:[simulation number]|[ModulationFunction]|[Frequency]|[Truncation]. The modulation function can be complex (X) or cosine (C). The frequency of the modulation function can be fixed (F) or variable (V). The simulation can be with truncation (T) or without truncation (N). Regarding the applied filters None stands for no filter, H for high-pass filter and B for band-pass filter.* Truncation simulated with objects of different sizes and fixed initial phase. § Truncation simulated with a fixed object and different values of initial phase

In simulations 1XFN and 1CFN an ideal case without truncation and with fixed frequency of the modulation function was simulated. The spatial frequency of the complex and cosine modulation functions was equal to $2\pi/6.4$ rad.pixel^{-1}. This value of spatial frequency corresponds to an integer number of cycles inside the FOV (40 cycles), and due to the periodicity of a signal in the discrete Fourier transform, there is no truncation at the borders of the FOV. In simulation 1XFN, no filtering was applied to compute the HARP angle, as the modulation function was complex. In simulation 1CFN, a high-pass filter with cut-off frequency $\nu_c = 20$ was applied. Since the peaks of this modulated function consist of single spikes located at $\nu = \pm 40$ in *k*-space, there is no overlap between them and complete isolation of the positive peak should be achieved.

In simulations 2XVN and 2CVN the effect of the variability of the frequency of the modulation functions on the HARP angle and strain errors was studied. In these simulations two possible scenarios were created: the radial thickening (Equation 6-6) and the circumferential shortening (Equation 6-7) of the myocardium. The frequency of the undeformed modulation functions k_0 was equal to $2\pi/6.4$ rad.pixel^{-1}. In the simulations with cosine modulation (2CVN) a high-pass ($\nu_c = 20$) and a band-pass ($\nu_{c-} = 24$ and $\nu_{c+} = 56$) filter were applied to isolate the positive tagging peak.

Simulations 3 (XFT and CFT) and 4 (XFT and CFT) investigate the effect of the truncation of the modulation functions in the HARP angle and strain errors. Simulations 3 were performed for different objects. The size of these objects ranged between half a tag cycle and 10 tag cycles of the modulation function, in steps of half a tag cycle. The first point of all simulated objects was fixed at $x = 0$. The initial phase of the modulation functions was equal to $\pi/2$, and the tag cycle was 6 pixels. Simulations 4 were performed with different values for the initial phase of the modulation functions in two objects: one with two tag cycles, representing the error in the radial direction, and one with 8 tag cycles, representing the error in the circumferential direction. The first point of both objects was fixed at $x = 0$. The initial phase ranged between 0 and 2π, in steps of 0.01π. The tag cycle of the modulation functions in these simulations was 6 pixels. In the simulations with cosine modulation (3CFT and 4CFT) a high-pass ($\nu_c = 20$) and a band-pass ($\nu_{c-} = 27$ and $\nu_{c+} = 59$) filter were applied to isolate the positive tagging peak.

Simulations 5 (XVT and CVT) and 6 (XVT and CVT) are equivalent to simulations 3 and 4 respectively but with variable frequency of the modulation functions. The frequency of the undeformed modulation functions k_0 was equal to $2\pi/6$ rad.pixel^{-1} in these simulations. For simulations 5 radial thickening (Equation 6-6) and circumferential shortening (Equation 6-7) were simulated for all the objects. For simulations 6 radial thickening was simulated for the object representing the error in the radial direction (2 tag cycles) and circumferential shortening for the object representing the error in the circumferential direction (8 tag cycles). In the simulations with cosine modulation (5CVT and 6CVT) a high-pass ($\nu_c = 20$) and a band-pass ($\nu_{c-} = 27$ and $\nu_{c+} = 59$) filter were applied to isolate the positive tagging peak.

6.2.3. Error of the HARP angle and of the strain

The error of the HARP angle obtained for each simulation was defined as the absolute difference between the analytical HARP, ϕ, and the computed HARP angle, a. The analytical HARP (in radians) was obtained with the formula:

$$\phi = \int_0^x k(x)dx + \phi_i \qquad \text{Equation 6-9}$$

with k the spatial frequency of the modulation function and ϕ_i its initial phase.

Consider the segment X_1X_2 with 1 pixel of length and ϕ_1 and ϕ_2 the analytical HARP at its edges. Due to computational errors, the HARP angles at X_1 and X_2 are not equal to ϕ_1 and ϕ_2. Instead, the analytical HARP values ϕ_1 and ϕ_2 correspond in the HARP angle curve to the edges of a deformed segment $X'_1X'_2$ (Figure 6-1).

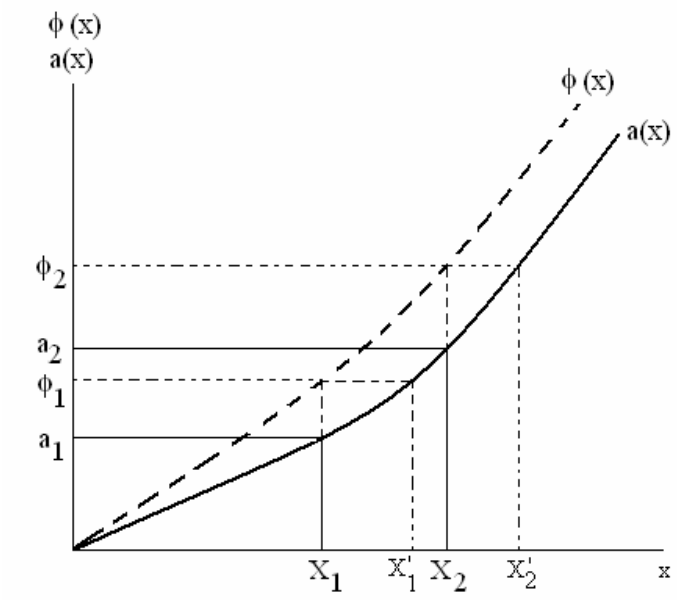

Figure 6-1 Schematic representation of the strain error induced by the HARP angle error. $\phi(x)$ corresponds to the analytical HARP and $a(x)$ to the computed HARP angle. Due to computational errors a_i is different from ϕ_i and, consequently, the segment X_1X_2 is deformed into the segment $X'_1X'_2$, originating a strain error.

This means that the HARP angle error induces a strain error in the analysis of the myocardial deformation. This strain error can be quantified using the formula:

$$\varepsilon_{strain} = \left(\frac{\phi_2 - \phi_1}{a_2 - a_1} - 1 \right) \times 100\% \qquad \text{Equation 6-10}$$

with a_i the computed HARP angle at point i.

The strain error for each simulation was computed using all the points inside the object, with exception for the first point.

6.3. RESULTS

The results obtained for the HARP angle error and for the strain error for each simulation were the following.

6.3.1. Simulations 1XFN and 1CFN

The FFT of the modulated functions are represented in Figure 6-2. In these simulations, none of the error sources evaluated in the present study were present. The error for the HARP angle and strain was zero (within the limits of computer precision), for both modulation functions.

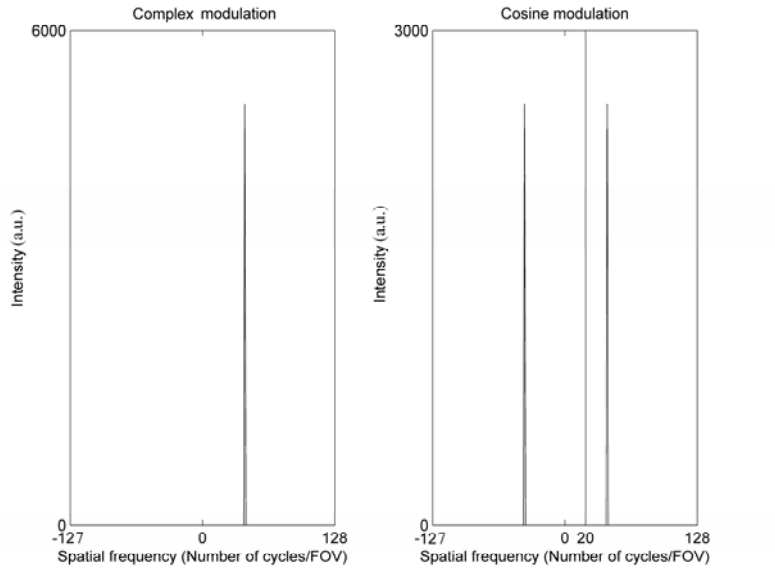

Figure 6-2 Spectra for simulations 1XFN and 1CFN.
In these simulations an ideal situation was created, where none of the error sources evaluated in this study are present. The solid vertical line in the spectrum of the cosine modulation corresponds to the cut-off frequency of the high-pass filter.

6.3.2. Simulations 2XVN and 2CVN

The frequency of the complex and cosine modulation functions and the FFT of the modulated functions are shown in Figure 6-3. In these simulations the present error source was the variability of the frequency of the modulation functions. For the complex modulation (2XVN) the errors of the HARP angle and of the strain were equal to zero for both simulated frequencies (radial thickening and circumferential shortening).

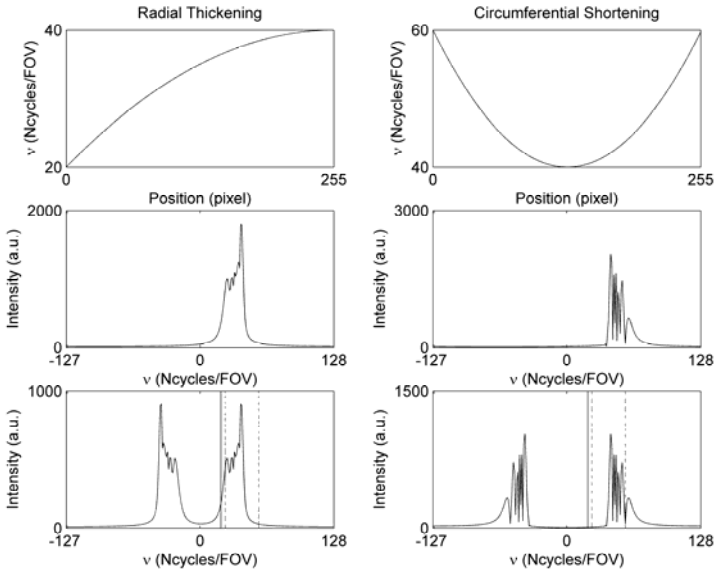

Figure 6-3 From top to bottom row. Frequency of the modulation functions with respect to the position inside the FOV, spectra for the simulations 2XVN and spectra for the simulations 2CVN.
The left column corresponds to the radial thickening and the right column to the circumferential shortening. Radial thickening corresponds to Equation 6-6 and circumferential shortening to Equation 6-7. The solid vertical line in the spectra of the bottom row corresponds to the cut-off frequency of the high-pass filter. The dashed vertical lines correspond to the cut-off frequencies of the band-pass filter. ν - spatial frequency given as $\nu = k/2\pi.FOV$.

For the cosine modulation, the results obtained for the different situations are summarized in Table 6-2. These values show that the high-pass filter led to smaller errors than the band-pass filter and, for the high-pass filter, the circumferential shortening led to smaller errors than the radial thickening.

Filter	HARP angle error (rad)		Strain error (%)	
	Radial thickening	Circumferential shortening	Radial thickening	Circumferential shortening
High-pass	0.07 ± 0.18	0.01 ± 0.05	-0.66 ± 12.38	-0.20 ± 3.36
Band-pass	0.15 ± 0.26	0.15 ± 0.31	-0.89 ± 15.99	1.20 ± 3.57

Table 6-2 HARP angle and strain errors for simulations 2CVN.
In these simulations the evaluated error source was the variability of the frequency of the modulation function (see Table 6-1). Radial thickening corresponds to Equation 6-6 and circumferential shortening to Equation 6-7

6.3.3. Simulations 3XFT and 3CFT

In simulations 3, the effect of the truncation of the modulation functions was analyzed.

For simulation 3XFT where a complex modulation was applied to the signal, the errors in the HARP angle and in the strain were zero for all object sizes.

For simulation 3CFT, the results obtained for each object size are represented in Figure 6-4.

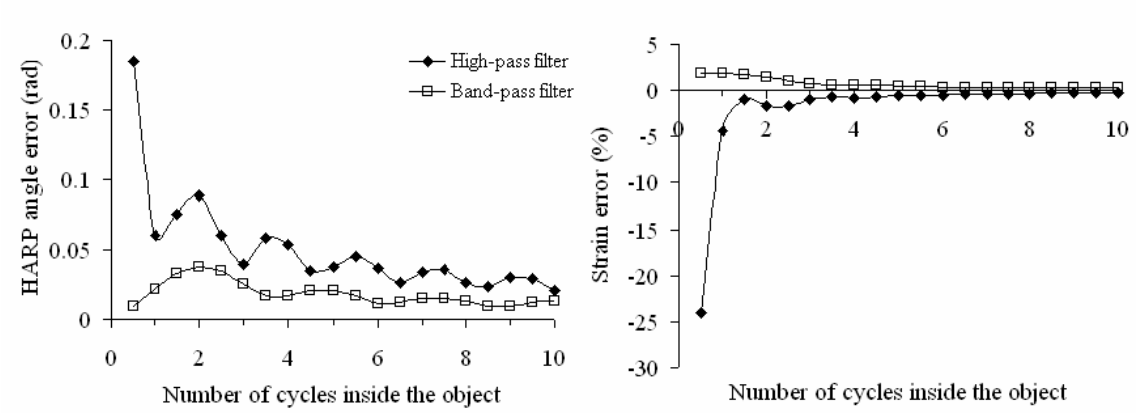

Figure 6-4 HARP angle and strain errors obtained in simulation 3CFT.
In this simulation the present error source was the truncation of the modulation function. The simulation was performed for different object sizes with the initial phase of the modulation function equal to $\pi/2$.

From these plots it is clear that the HARP angle error and the strain error are smaller for larger objects and when the band-pass filter is used. The values of the HARP angle error and of the strain error for the radial direction (2 tag cycles inside the object) and for the circumferential direction (8 tag cycles inside the object) are presented in Table 6-3.

Filter	HARP angle error (rad)		Strain error (%)	
	Radial direction	Circumferential direction	Radial direction	Circumferential direction
High-pass	0.09 ± 0.06	0.03 ± 0.03	-1.64 ± 11.05	-0.41 ± 4.59
Band-pass	0.04 ± 0.02	0.01 ± 0.02	1.47 ± 0.26	0.28 ± 0.49

Table 6-3 HARP angle and strain errors for simulations 3CFT.
In these simulations the evaluated error source was the truncation of the modulation function (see Table 6-1). The HARP angle and strain errors for the radial direction correspond to an object with a length of 2 tag cycles. The HARP angle and strain errors for the circumferential direction correspond to an object with a length of 8 tag cycles.

For both types of filter the errors of the HARP angle and the errors of the strain were higher for the radial direction than for the circumferential direction, which is in agreement with the inverse relation between error and object size. The spectra in *k*-space obtained for these objects are presented in Figure 6-5. For the radial direction, the peak in *k*-space is wider than for the circumferential direction.

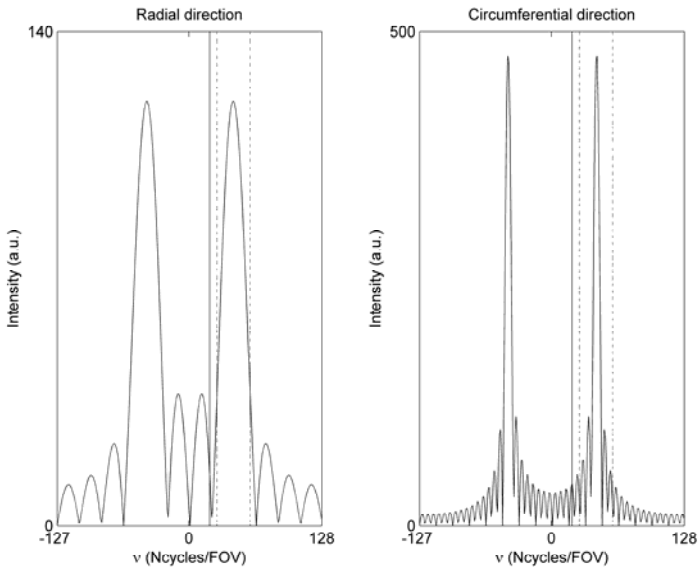

Figure 6-5 Spectrum in *k*-space for the objects of simulation 3CFT representing the error on radial and circumferential direction.
The error in radial direction corresponds to 2 tag cycles inside the object, and in the circumferential direction to 8 tag cycles inside the object. The solid vertical line represents the cut-off frequency of the high-pass filter and the dashed vertical lines the cut-off frequencies of the band-pass filter.

The profiles of the HARP angle error and of the strain error inside these two objects are presented in Figure 6-6. It is observed that the error increases closer to the object border.

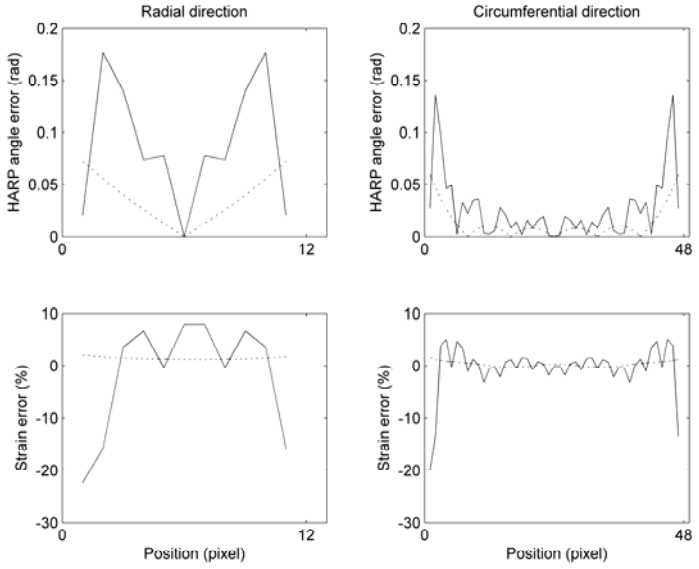

Figure 6-6 Error of the HARP angle and of the strain for simulation 3CFT as a function of the position inside the object.
The error for the radial direction is simulated with an object with 2 tag cycles and the error for the circumferential direction with an object with 8 tag cycles. (A tag cycle is 6 pixels). The solid lines are the results obtained with the high-pass filter and the dashed lines with the band-pass filter.

6.3.4. Simulations 4XFT and 4CFT

In simulations 4 the effect of the truncation of the modulation function is analyzed from a different point of view. In this case, the HARP angle error and the strain error are computed for different values of initial phase in a fixed object.

For simulation 4XFT, the HARP angle error and the strain error were zero for all values of initial phase and for the two analyzed objects (2 cycles and 8 cycles).

For simulations 4CFT the obtained results for the radial (2 cycles) and circumferential (8 cycles) directions are presented in Figure 6-7. In these plots the dependency of the HARP angle error and strain error on the initial phase is clear, showing well defined patterns. It is also verified that, independently of the initial phase, the error in the radial direction is always higher than in the circumferential direction.

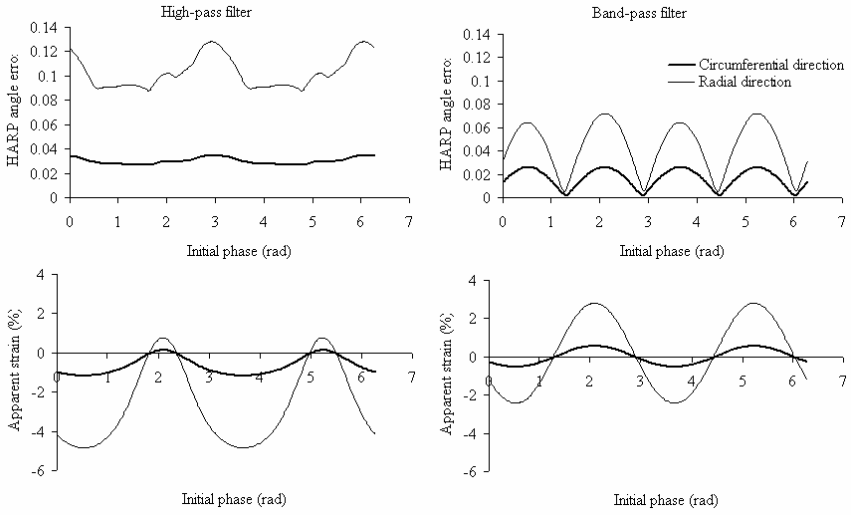

Figure 6-7 HARP angle and strain errors obtained in simulation 4CFT.

In this simulation the present error source was the truncation of the modulation function. The simulation was performed for different values of the initial phase of the modulation function. Two situations were created: the error in the radial direction (object with 2 cycles) and the error in the circumferential direction (object with 8 cycles). Left: a high-pass filter was used to isolate the positive tagging peak. Right: a band-pass filter was used to isolate the positive tagging peak.

6.3.5. Simulations 5XVT and 5CVT

These simulations are equivalent to simulations 3 but with a variable frequency of the modulation function. Two scenarios were simulated: radial thickening and circumferential shortening.

As in simulation 3XFT, the simulation with complex modulation led to zero HARP angle and strains errors, independently of the object size.

The results obtained for simulations 5CVT are presented in Figure 6-8. These plots show that, for most of the objects, the HARP angle and strain errors are smaller when the high-pass filter is applied. Additionally, with the high-pass filter, the HARP angle and strain errors are smaller for the circumferential shortening than for the radial thickening.

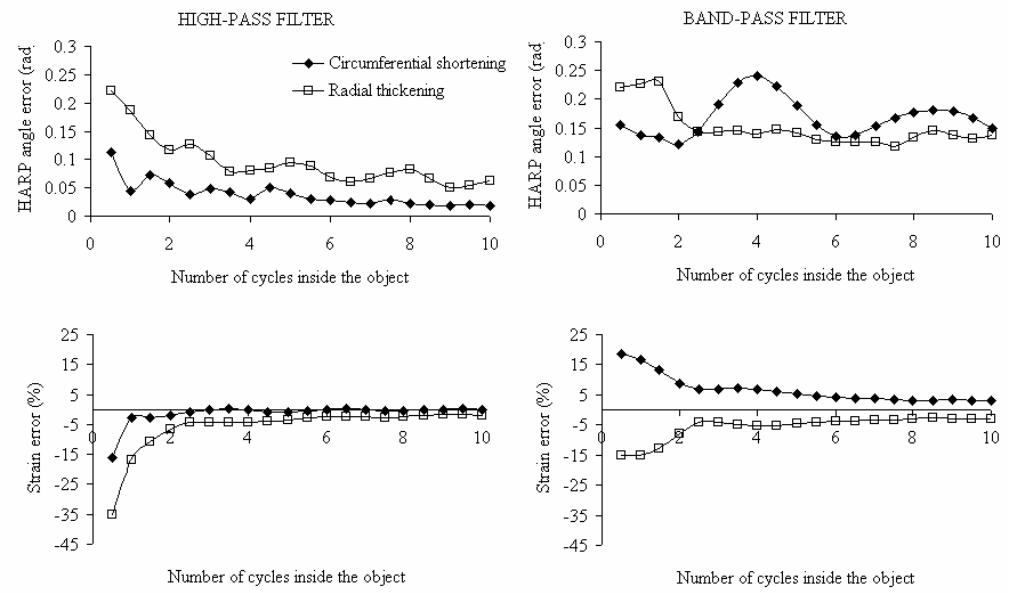

Figure 6-8 HARP angle error and strain error obtained in simulation 5CVT.

In this simulation the present error sources were the truncation of the modulation function combined with the variability of its frequency. The simulation was performed for different object sizes. The initial phase of the modulation function was $\pi/2$ and its frequency was equal to the frequency simulating the radial thickening Equation 6-6 and to the frequency simulating the circumferential shortening Equation 6-7. Left: a high-pass filter was used to isolate the positive tagging peak. Right: a band-pass filter was used to isolate the positive tagging peak.

In Table 6-4 and Table 6-5 the HARP angle errors and strain errors obtained for the objects simulating the errors in the radial and circumferential directions are summarized.

	High-pass filter		Band-pass filter	
	Radial direction	**Circumferential direction**	**Radial direction**	**Circumferential direction**
Radial thickening	0.12 ± 0.07	0.08 ± 0.08	0.17 ± 0.14	0.13 ± 0.16
Circumferential shortening	0.06 ± 0.08	0.02 ± 0.05	0.12 ± 0.14	0.18 ± 0.16

Table 6-4 HARP angle error (rad) for simulations 5CVT.

In these simulations the present error sources were the variability of the frequency of the modulation function and the truncation of the modulated signal (see Table 6-1). The HARP angle errors for the radial direction correspond to an object with a length of 2 cycles. The HARP angle errors for the circumferential direction correspond to an object with a length of 8 cycles. Radial thickening corresponds to Equation 6-6 and circumferential shortening to Equation 6-7.

	High-pass filter		Band-pass filter	
	Radial direction	Circumferential direction	Radial direction	Circumferential direction
Radial thickening	-6.54 ± 17.63	-2.39 ± 9.55	-8.00 ± 14.39	-2.88 ± 8.99
Circumferential shortening	-2.07 ± 6.24	-0.50 ± 3.28	8.84 ± 12.88	3.16 ± 8.34

Table 6-5 Strain error (%) for simulations 5CVT.

In these simulations the present error sources were the variability of the frequency of the modulation function and the truncation of the modulated signal (see Table 6-1). The strain errors for the radial direction correspond to an object with a length of 2 cycles. The strain errors for the circumferential direction correspond to an object with a length of 8 cycles. Radial thickening corresponds to Equation 6-6 and circumferential shortening to Equation 6-7

The spectrum obtained in *k*-space for these objects are presented in Figure 6-9. The profiles of the HARP angle error and of the strain error for these two objects are presented in Figure 6-10. As in the simulation 3CFT, the error increases closer to the object border.

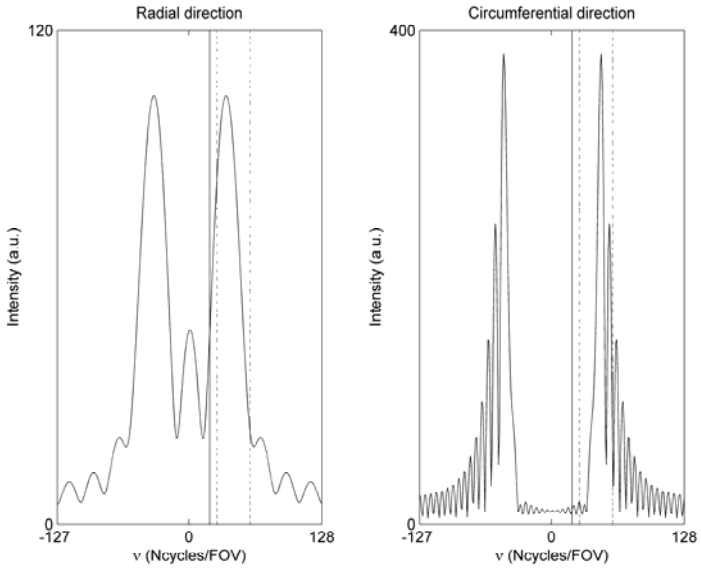

Figure 6-9 Spectra in *k*-space for the objects of simulation 5CVT simulating the error in radial and circumferential directions.

The error in radial direction corresponds to 2 tag cycles inside the object, and in the circumferential direction to 8 tag cycles inside the object. The solid line represents the cut-off frequency of the high-pass filter and the dashed lines the cut-off frequencies of the band-pass filter. For the error in the radial direction the frequency of the modulation function corresponds to the radial thickening (Equation 6-6) and for the error in the circumferential direction corresponds to the circumferential shortening (Equation 6-7)

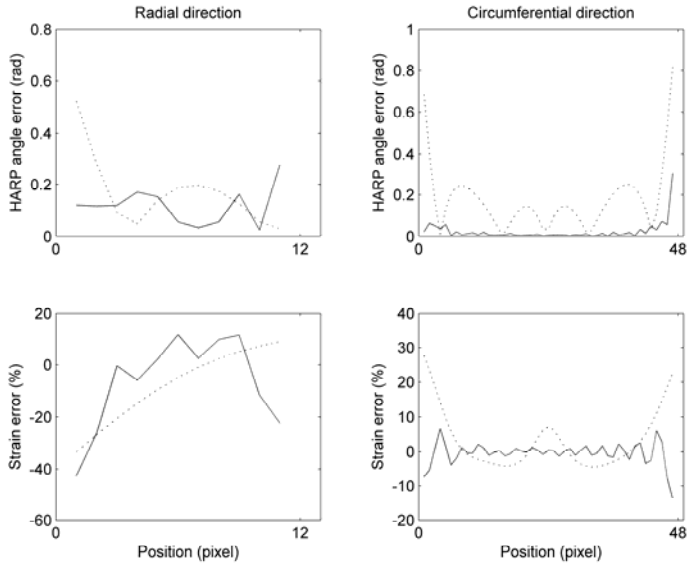

Figure 6-10 Error of the HARP angle and strain as a function of the position inside the object for simulation 5CVT.

The error in the radial direction is simulated with an object with 2 tag cycles and the error in the circumferential direction with an object with 8 tag cycles. For the radial direction, the frequency of the modulation function corresponds to the radial thickening (Equation 6-6), and for the circumferential direction corresponds to the circumferential shortening (Equation 6-7). The solid lines are the results obtained with the high-pass filter and the dashed lines with the band-pass filter.

6.3.6. Simulations 6XVT and 6CVT

These simulations are equivalent to simulations 4 but with a variable frequency of the modulation function.

For the complex modulation (simulation 6XVT), the HARP angle errors and the strain errors are equal to zero, for all initial phases and for both simulated scenarios (radial direction with radial thickening and circumferential direction with circumferential shortening).

For simulation 6CVT, the pattern obtained for the errors are similar to those obtained in simulation 4CFT, with higher amplitudes (Figure 6-11).

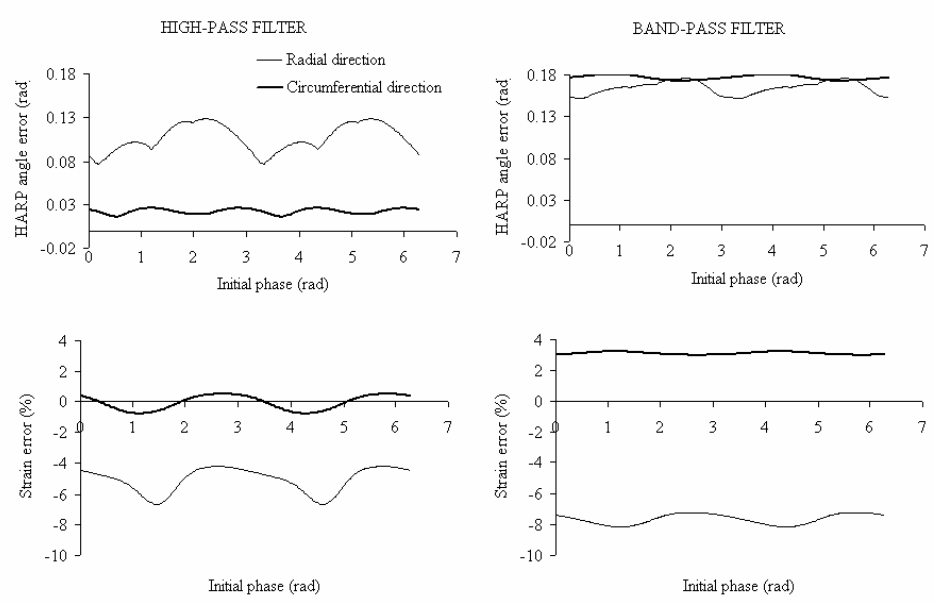

Figure 6-11 HARP angle and strain errors obtained in simulation 6CVT.
In these simulations the present error sources were the truncation of the modulation function and the variability of its frequency. The simulation was performed for different values of the initial phase of the modulation function. Two situations were created: the error in the radial direction (object with 2 cycles) with radial thickening (Equation 6-6) and the error in the circumferential direction (object with 8 cycles) with circumferential shortening (Equation 6-7). Left: a high-pass filter was used to isolate the positive tagging peak. Right: a band-pass filter was used to isolate the positive tagging peak.

Once more, with the high-pass filter the errors in the radial direction with radial thickening are higher than in the circumferential direction with circumferential shortening. Again, with a variable tag modulation frequency, the errors obtained with the band-pass filter are higher than with the high-pass filter.

6.4. DISCUSSION

In this study the error sources of the HARP angle computation with the Hilbert transform were investigated.

For the ideal case (simulation 1), the HARP angle and strain errors were zero for both modulation functions. This result shows that the accuracy of the HARP angle and strain computation can be mainly explained by the error sources evaluated in this study.

On the following simulations (simulations 2 to 6), when the amplitude of the object was modulated with a complex function, the HARP angle and strain errors were always zero, independently of the present error sources (truncation and/or variability of the frequency of the modulation function). This result corroborates the hypothesis of the importance of a perfect isolation of the positive tagging peak in *k*-space to increase the accuracy of the HARP angle and strain, because the complex modulation has one single peak in *k*-space, yielding perfect

isolation of the peak without filtering. On the other hand, the errors obtained for simulations 2 to 6 with cosine modulation are always different from zero. From these simulations several conclusions can be drawn.

Firstly, when the frequency of the modulation function is fixed, the band-pass filter leads to smaller errors than the high-pass filter. This can be due to the fact that for this case the band-pass filter is symmetric around the positive tagging peak, which does not happen when the frequency of the modulation function is variable (compare Figure 6-5 with Figure 6-3 and Figure 6-9). For variable frequency, the high-pass filter behaves better than the band-pass filter since it is able to isolate the positive tagging peak without cutting the higher frequencies and cutting less lower frequencies than the band-pass filter (see Figure 6-3 and Figure 6-9). As the deformation of the myocardium during systole leads to changes in the frequency of the tag lines, these simulations indicate that the high-pass filter is more adequate to compute the HARP angle from real-life CSPAMM images than the band-pass filter.

Secondly, the HARP angle and strain errors obtained for the radial direction (objects with only a few number of tag cycles) with the high-pass filter were always higher than for the circumferential direction (objects with more tag cycles), which is in agreement with the accuracies previously observed (see Chapter2 and reference [98]). Additionally, these errors were also higher for the radial thickening than for the circumferential shortening. These results show that the radial direction is less accurate since in this direction the number of available tag lines is considerably reduced (1 to 2 tag cycles), which results in broader peaks in *k*-space (see Figure 6-5 and Figure 6-9). Additionally, radial thickening is also responsible for more overlapping of the peaks since the tagging peaks are shifted to lower frequencies. The combination of these two factors turns the perfect isolation of the positive tagging peak more difficult in the radial direction. On the other hand, on the circumferential direction the number of available tag lines is higher (7 to 8 tag cycles), which results in narrower peaks (see Figure 6-5 and Figure 6-9), and the circumferential shortening shifts the tagging peaks to higher frequencies in *k*-space, simplifying their isolation. In this case, the combination of these two factors leads to a higher accuracy in the circumferential direction.

Another important result is that the errors in the radial direction and in the circumferential direction decrease when the object size increases. These results also corroborate the hypothesis that the HARP angle error and the strain error result from the imperfect isolation of the positive tagging peak, as larger objects generally have narrower peaks in *k*-space than smaller objects.

Additionally, the error on the radial direction for the simulation with cosine modulation, truncation and variable frequency (simulation closer to the reality) is negative, which means that the HARP tracking method underestimates the strain on the radial direction. This is in agreement with the results obtained in Chapter 2, where the simulations showed that, at

maximum deformation the radial strain was 26% smaller than the analytical value and the radial-circumferential shear 75% (see Figure 2-8).

All these results show that the main error source in the HARP angle computation by the Hilbert transform is the fact that the method does not perfectly isolate the positive tagging peak in *k*-space. For the cosine modulation function this can be explained by the overlap of the tagging peaks that occurs due to the variable frequency and to the truncation of the modulation function (compare Figure 6-2, Figure 6-3, Figure 6-5 and Figure 6-9).

A possible solution to decrease the error in the HARP angle computation could be the extraction of the positive peak in *k*-space by modulating the image with a complex function. As it was shown in the simulations, when this modulation function is used the errors are negligible. This solution has already been proposed by Epstein et al [137] and it is designated by the CANSEL (cosine and sine modulation to eliminate) method. In practice, this method requires the acquisition of four sets of images for each tag direction: two images whose amplitudes are cosine modulated and have inverted tag patterns, and two images whose amplitudes are modulated with a sine function and have inverted tag patterns. The subtraction of the two images with inverted tag patterns for each modulation leads to the elimination of the central peak in *k*-space (CSPAMM images). These two CSPAMM images are then combined in an appropriate way to obtain a single peak in *k*-space. However this method has two main disadvantages that turn its application in the clinical routine difficult. First, the acquisition time is too long for real studies. Secondly, image subtractions always lead to errors. Acquiring the images with inverted tag patterns in the same breath hold decreases the mismatch between the images. However, to obtain a single peak in *k*-space it is assumed that the amplitudes of the underlying images with inverted tag patterns are constant, which in general is not true. In a patient scan the CSPAMM computation may not completely eliminate the central peak in *k*-space e.g. in case of patient movement between scans. This means that even if the CANSEL method is applied, it will be necessary to apply a filtering in *k*-space to eliminate the remaining information of the other peaks, which induces error in the HARP angle and strain.

A more straightforward solution to decrease the HARP angle and strain errors could be the restriction of the HARP angle computation to the middle of the myocardium, since the error increases near its borders.

6.5. CONCLUSION

The error in the HARP angle and in the strain can be explained by the inability of the filtering to perfectly isolate the positive tagging peak in *k*-space from the negative peak. In general, strain errors in the radial direction are at least 5 times larger than strain errors in the circumferential direction. These higher errors in the radial direction are a consequence of the

reduced number of tag lines in this direction, which leads to wider tagging peaks in *k*-space, and of the radial thickening that shifts the tagging peaks towards the center of *k*-space, increasing the overlap between the two peaks. The lower errors in the circumferential direction are a result of the larger number of tag lines in this direction, and the fact that circumferential shortening shifts the tagging peaks towards higher spatial frequencies, which simplifies the isolation of the positive peak in *k*-space. When all error sources are included (variable frequency of the tag modulation, and truncation of the object) the high-pass filter yields smaller errors than the band-pass filter.

Chapter 7.

GENERAL DISCUSSION AND CONCLUSIONS

7.1. SUMMARY

The measurement of myocardial deformation provides information regarding regional cardiac function which can not be obtained with the traditional global parameters like stroke volume and ejection fraction. Presently, tagged MRI is the imaging technique of choice to measure the complete 3D strain tensor of the myocardium. However, its introduction into the clinical practice and its use in scientific patient studies with large patient groups has been hindered by the excessive amount of image post-processing that is required by this technique. Up to now, tagged cine MR images are usually evaluated by visual inspection, with tags in affected regions deforming less than those in normal regions. Semi-automatic methods to track the tag pattern and compute the strain of the myocardium have also been developed. However, the time required to do this analysis is still too long for widespread application.

The primary aim of the research project described in this thesis was to develop a method able to automatically track the 3D motion of the tag pattern and to compute the 3D myocardial strains. In a second stage, this method was applied to healthy subjects and patients with left bundle branch block (LBBB) to obtain strain maps of healthy and LBBB left ventricle (LV) myocardium. Besides measurements and simulations were performed to assess the accuracy of the computed strain components, and to identify the factors that limit the accuracy of the radial strain component.

Harmonic phase (HARP) tracking is a technique that automatically tracks the tag pattern applied to the myocardium in MR images. This technique is based on the fact that the phase of the myocardial points remains constant during all cardiac cycle with their motion reflecting the motion of the underlying cardiac muscle. However, it has been verified that this technique is not able to track the new myocardium that appears in the image plane resultant from the longitudinal motion and conical shape of the heart. To overcome this limitation, the extended 2D HARP tracking method, described in **Chapter 2** was developed. The tracking and strain accuracy of this new method was assessed using simulated tagged images. A tracking accuracy of 0.15 pixels was obtained, which is comparable to the accuracy of previously published methods. The strain accuracy obtained in the circumferential direction was excellent, with a maximum relative error of 0.5%, which shows the efficiency of this method to quantify myocardial deformation in this direction. In the radial direction (radial strain and radial-circumferential shear), the strain accuracy was poor, which is also in line with findings of previously published methods. The advantages of the extended 2D HARP tracking relative to the original version were assessed by applying both methods to a group of six healthy volunteers. It was verified that the new method presented here was able to track all the myocardial points during all the cardiac cycle, leading to a significant decrease of the

circumferential shortening in the mid and apical slices. However, this technique is only able to quantify the apparent motion of the myocardium. To quantify its 3D motion and true myocardial deformation, it is necessary to develop a method that tracks the longitudinal cardiac motion. The extended 3D HARP tracking method, presented in **Chapter 3**, fulfils these conditions and is able to automatically track the true motion of the cardiac muscle by combining the 2D displacement of the tag pattern assessed from the short-axis (SA) tagged images with its longitudinal displacement assessed from the long-axis (LA) tagged images. This method was applied to six healthy volunteers and a 3D strain map of the healthy LV was obtained. The results corroborate the existence of inhomogeneity in normal LV strain, highlighting the importance of comparing the dysfunctional myocardium with the controls regionally and not globally. From the myocardial strain maps the time to onset of circumferential and longitudinal shortening of the healthy LV were measured. The results obtained showed that the circumferential shortening starts earlier in the lateral wall than in the septum, as reported in previous studies. However, in the longitudinal direction the shortening starts earlier in the septum than in the lateral wall, reflecting the direction of propagation of the action potential. This result suggests that electrical activation is better reflected by longitudinal shortening, as the fibres in the subendocardium are mainly oriented in this direction. Extended 3D HARP tracking was also applied to five LBBB patients in order to explore which strain parameter better discriminates these patients from healthy controls. The results, presented in **Chapter 4**, show that the strain parameter most affected by the disease is the end-systolic circumferential shortening in the septum and the time to onset of the circumferential shortening in the septum. It is also verified that the cardiac function is preserved in the lateral wall in this group of patients, while the septum contracts less and starts to contract earlier than in healthy controls, for both the circumferential and longitudinal directions. As the cardiac fibres in the midwall of the LV are mainly oriented in the circumferential direction, the strain component in this direction is usually assessed to evaluate LV deformation. This parameter can be quantified using 2D or 3D strain analysis methods. Although the 3D analysis takes into account the longitudinal motion, it is not known if this motion affects the circumferential strain assessed with 2D strain analysis. In order to evaluate the difference between 2D and 3D circumferential strain, in **Chapter 5** the extended 2D and 3D HARP tracking methods were applied to a group of healthy controls and LBBB patients. This comparative study leads to the conclusions that there are no significant differences in the timing parameters between 2D and 3D circumferential shortening, in the peak circumferential shortening, or in the dyssynchrony of the circumferential shortening. This result opens the prospect of using tagged MRI in clinical routine to quantify circumferential myocardial strain, as 2D strain analysis is much more straightforward and much less time consuming than 3D strain analysis. The limited accuracy of the extended HARP tracking in the radial direction was further explored in **Chapter 6**. To investigate what the error sources are in

HARP tracking and strain computation, several simulations were performed using a 1D model. The obtained results led to the conclusion that the main error source in the HARP angle computation is the inability of the method to perfectly isolate the positive tag peak in *k*-space. The error in the radial direction is higher because of two reasons. Firstly, in this direction, the number of available tag lines is less than in the circumferential direction, leading to wider peaks in *k*-space. Secondly, the radial strain is positive (stretching), which leads to a decrease of the spatial frequency of the tag lines, and hence to a decreased distance in *k*-space of the corresponding peaks. Both effects make the peaks less well separable.

7.2. GENERAL DISCUSSION

7.2.1. HARP tracking

HARP tracking is a unique technique to automatically measure regional myocardial deformation using tagged MRI. Contrarily to previously published semi-automatic methods, HARP tracking is more automatic and not limited to tag line intersections and is thus able to track any pixel of the LV cardiac wall, resulting in many more tracked points. This increment of tracked points is crucial in 3D strain analysis, in which a high volume of data is required.

In this thesis HARP tracking is applied to vertically and horizontally tagged images separately. Acquiring images with perpendicular tag lines could decreases the acquisition time by (at most) a factor of 2. However, the resultant grid tag pattern corresponds in the frequency domain to two symmetric peaks in the vertical and horizontal directions. In order to obtain the HARP images corresponding to the vertical and horizontal tag patterns, the corresponding positive frequency peaks have to be removed using band-pass filters. As it was shown in this thesis, tracking errors and resultant strain errors are mainly a consequence of the inability of the Hilbert transform to perfectly remove the positive tag peak. If images with a tagging grid were acquired, the overlap between the different tag peaks in *k*-space would be higher, leading to higher tracking and strain errors.

The main limitation of HARP tracking is its limited accuracy in the radial direction. However, this characteristic is not exclusive of the HARP tracking but of all methods that quantify strain using tagged MR images, due to a limited number of tag lines in this direction.

Although the tracking and strain computation of the myocardium are performed automatically, both extended 2D and 3D HARP tracking algorithms depend on the contours of the LV. These myocardial contours were drawn manually for all time frames, which is still a very time consuming process, since a data set acquired with high temporal resolution (14 ms in this thesis) has around 50 time frames for each slice. In order to use this technique in clinical routine, this time consuming step of user interaction has to be suppressed by automated

segmentation of the LV myocardium using the HARM images, or by registration of standard anatomical cines, which can be segmented more easily, with the HARP images.

Another approach to study 3D LV deformation is to use 3D tagged images [138]. In this case, possible matching problems that appear when combining SA tagged images with LA tagged images would be overcome. However, at present the acquisition of these 3D tagged images is still too time consuming and requires sophisticated breath-holding techniques [138].

7.2.2. Strain analysis

In this thesis a homogeneous strain analysis approach was used to compute myocardial strain. In 2D analysis, a mesh of triangles was defined, using the tag points tracked in the SA image planes, and in 3D strain analysis a mesh of tetrahedrons was defined using the tag points tracked in neighbouring SA image planes. This method has the limitation of assuming that myocardial strain is homogeneous inside each element, while the LV strain is inhomogeneous, as shown in previous studies and corroborated in this thesis. However, as tagged images were analysed using the HARP tracking method, each pixel of the LV was tracked resulting in relatively small elements. Consequently, strain differences between these small elements can still be quantified with this approach. Another approach could be to perform field fitting in all directions, instead of only in the longitudinal direction. However, this would result in additional smoothing of the strain and the true spatial resolution would not be preserved.

7.2.3. 3D strain of the LV

With extended 2D and 3D HARP tracking 2D and 3D LV myocardial strain were quantified. The obtained strain results were in agreement with those previously published, with the advantage that, in this analysis, myocardial strain was computed automatically.

Relatively to the radial-circumferential and radial-longitudinal shear, a high intra- and inter- subject variability was obtained. These curves were noisier and it is not possible to define a pattern between subjects. Additionally, the physiological meaning of these strain components is still not clear. To overcome this latter point, tagged MRI should be combined with diffusion MRI, which provides myocardial fibre architecture, allowing to investigate the relation between the fibre architecture and shear strains.

The method was also applied to patients with LBBB and it was verified that, in this group of patients, the septal strains are more affected than the strains in the lateral wall and that the onset of shortening propagates from septum to lateral wall, which is roughly the same direction as the propagation of the action potential. However, in healthy subjects, it is known that contraction is not only governed by the action potential, as circumferential shortening propagates from lateral wall towards septum. To understand the remaining factors that influence

the asynchrony of ventricular contraction it would be important to study atrial contraction. This could be done using the automatic method presented in this thesis, when retrospective triggered data (covering the full cardiac cycle including the atrial kick) would be acquired.

7.3. CONCLUSIONS

HARP tracking is a unique method to analyse tagged MR images automatically. With this method regional strain maps of the cardiac wall are obtained non-invasively, with a high spatial and temporal resolution. The study of the LV deformation is an important parameter in the evaluation of the cardiac function as, contrarily to other parameters, it can be assessed regionally and it is independent of rigid body translations and rotations of the heart. This method, being automatic and non-invasive opens the prospect of the application of MRI myocardial tagging in clinical routine to assess cardiac function.

APPENDIX I

EXTENDED 2D HARP TRACKING

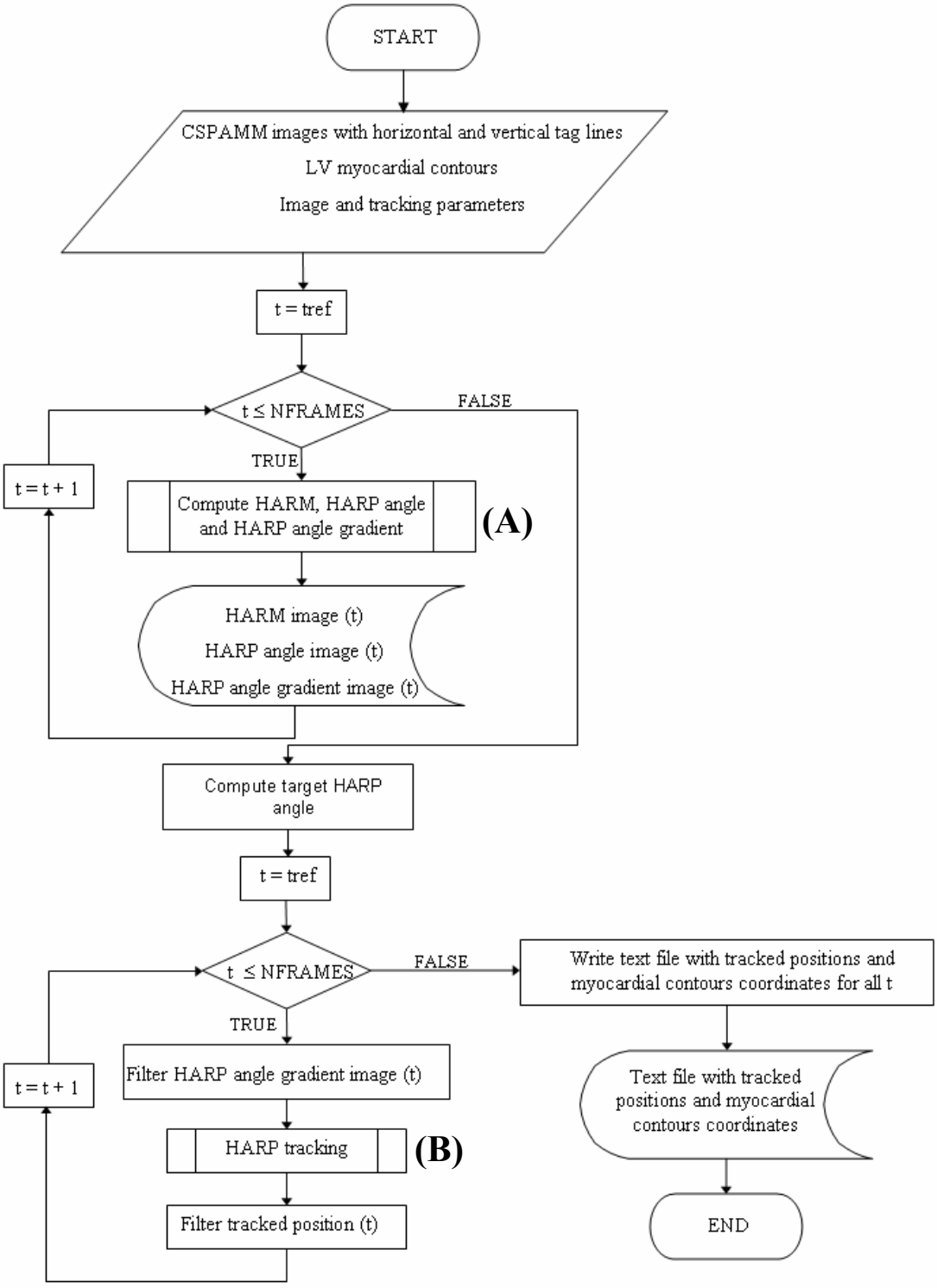

FUNCTION (A)

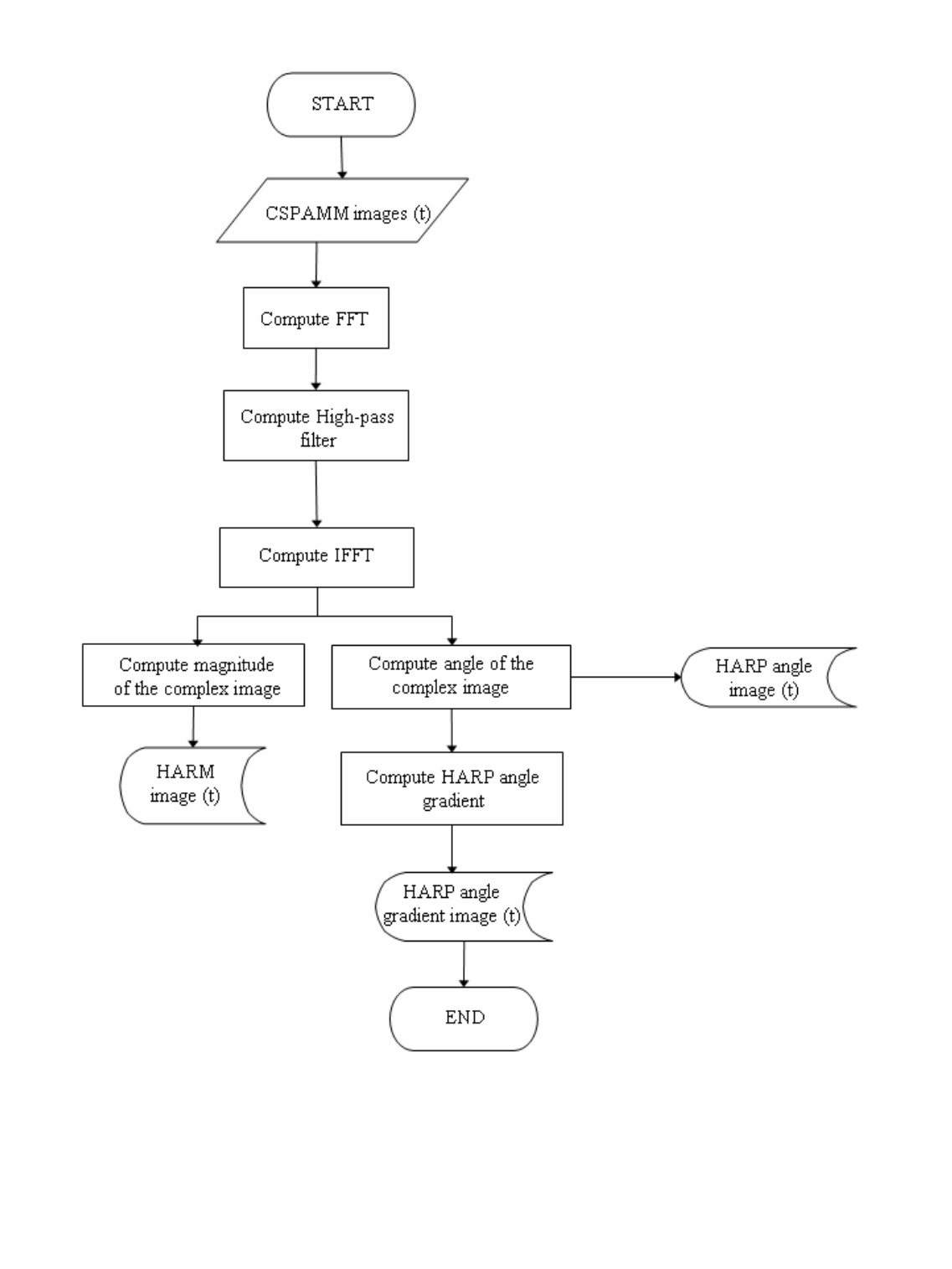
START
CSPAMM images (t)
Compute FFT
Compute High-pass filter
Compute IFFT
Compute magnitude of the complex image
Compute angle of the complex image
HARP angle image (t)
HARM image (t)
Compute HARP angle gradient
HARP angle gradient image (t)
END

FUNCTION (B)

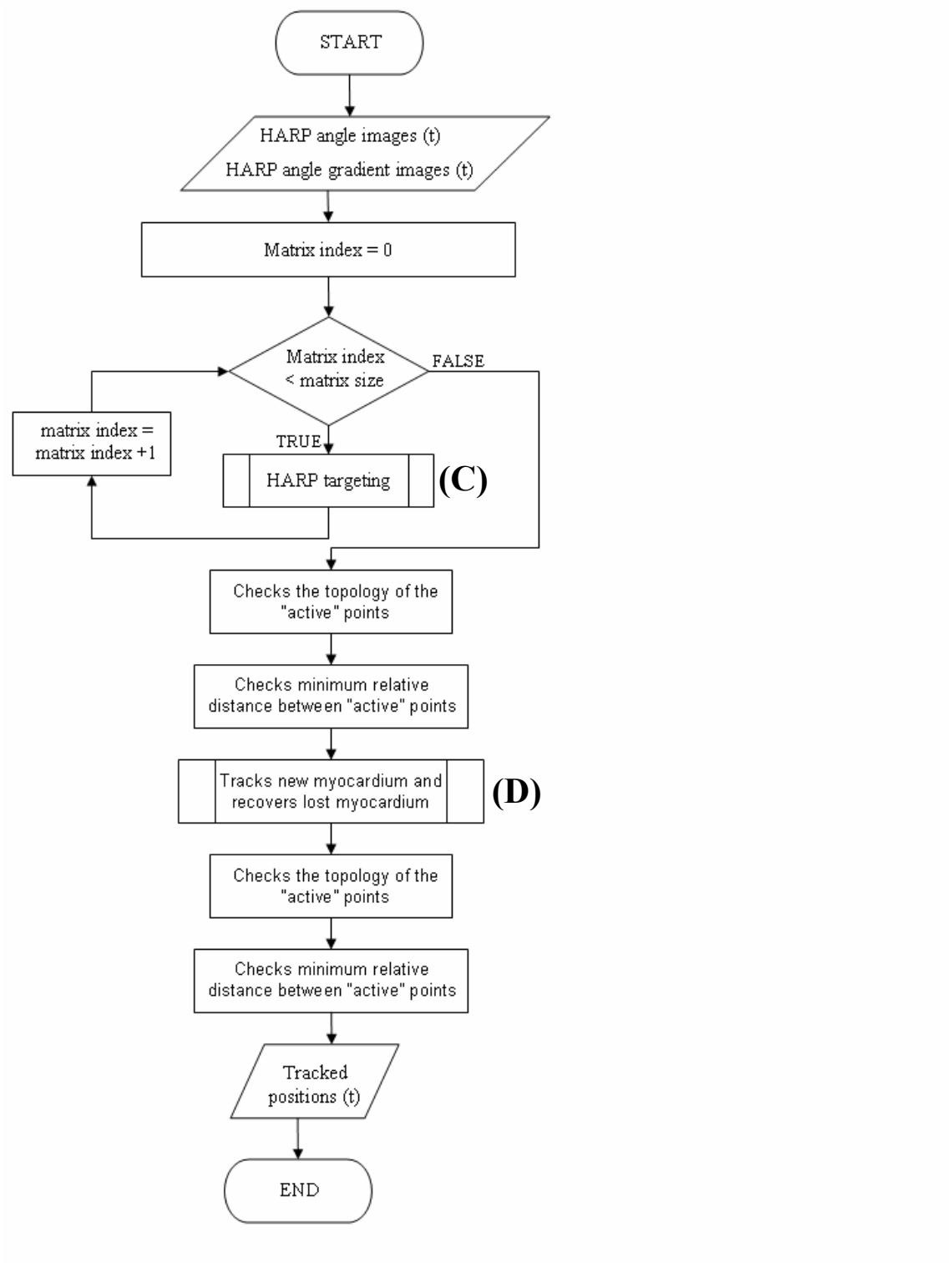
START
HARP angle images (t)
HARP angle gradient images (t)
Matrix index = 0
Matrix index < matrix size
FALSE
TRUE
matrix index = matrix index +1
HARP targeting
(C)
Checks the topology of the "active" points
Checks minimum relative distance between "active" points
Tracks new myocardium and recovers lost myocardium
(D)
Checks the topology of the "active" points
Checks minimum relative distance between "active" points
Tracked positions (t)
END

FUNCTION (C)

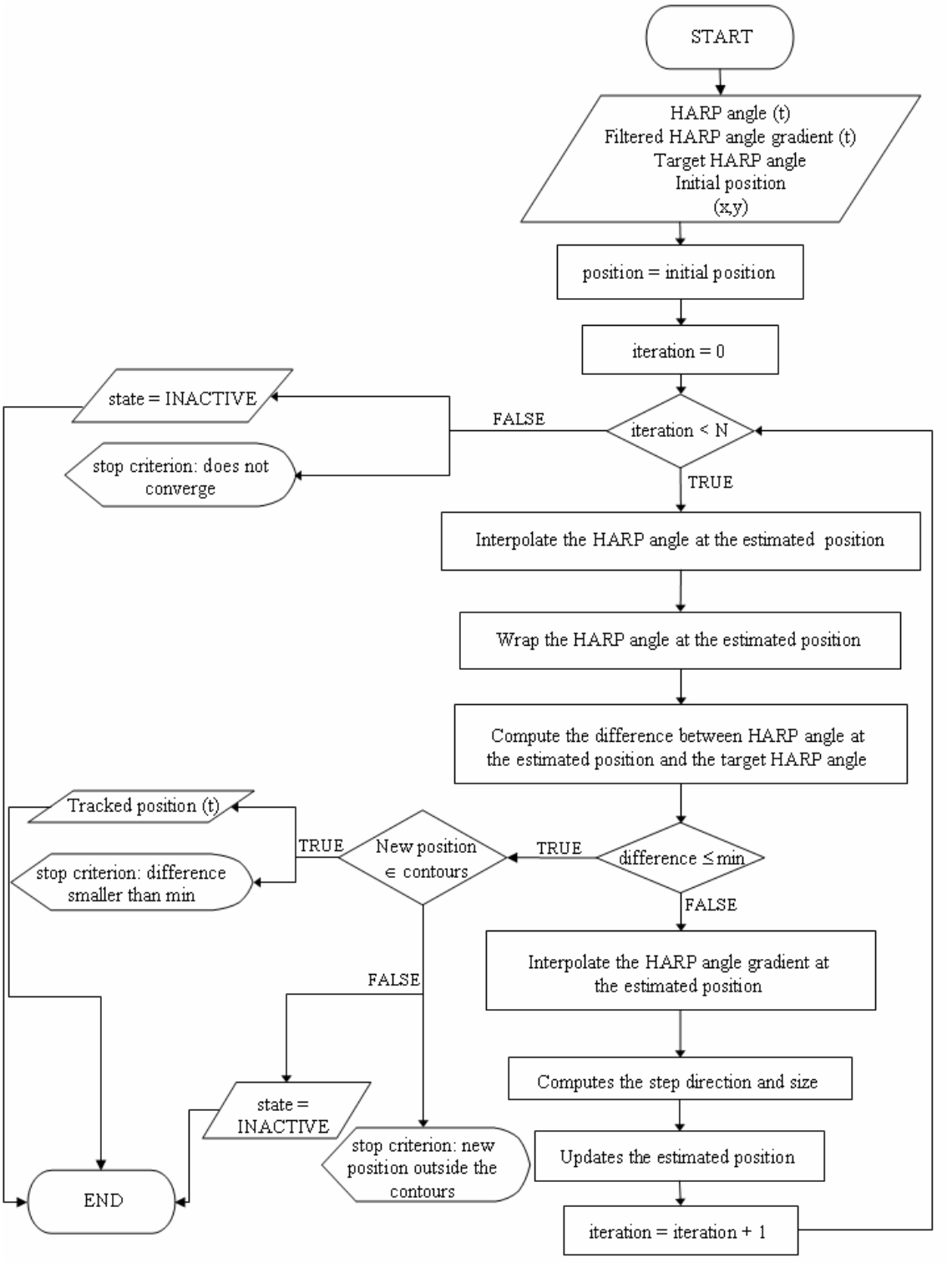
START
HARP angle (t)
Filtered HARP angle gradient (t)
Target HARP angle
Initial position
(x,y)
position = initial position
iteration = 0
state = INACTIVE
FALSE
iteration < N
stop criterion: does not converge
TRUE
Interpolate the HARP angle at the estimated position
Wrap the HARP angle at the estimated position
Compute the difference between HARP angle at the estimated position and the target HARP angle
Tracked position (t)
TRUE
New position ∈ contours
TRUE
difference ≤ min
stop criterion: difference smaller than min
FALSE
Interpolate the HARP angle gradient at the estimated position
FALSE
Computes the step direction and size
state = INACTIVE
stop criterion: new position outside the contours
Updates the estimated position
END
iteration = iteration + 1

FUNCTION (D)

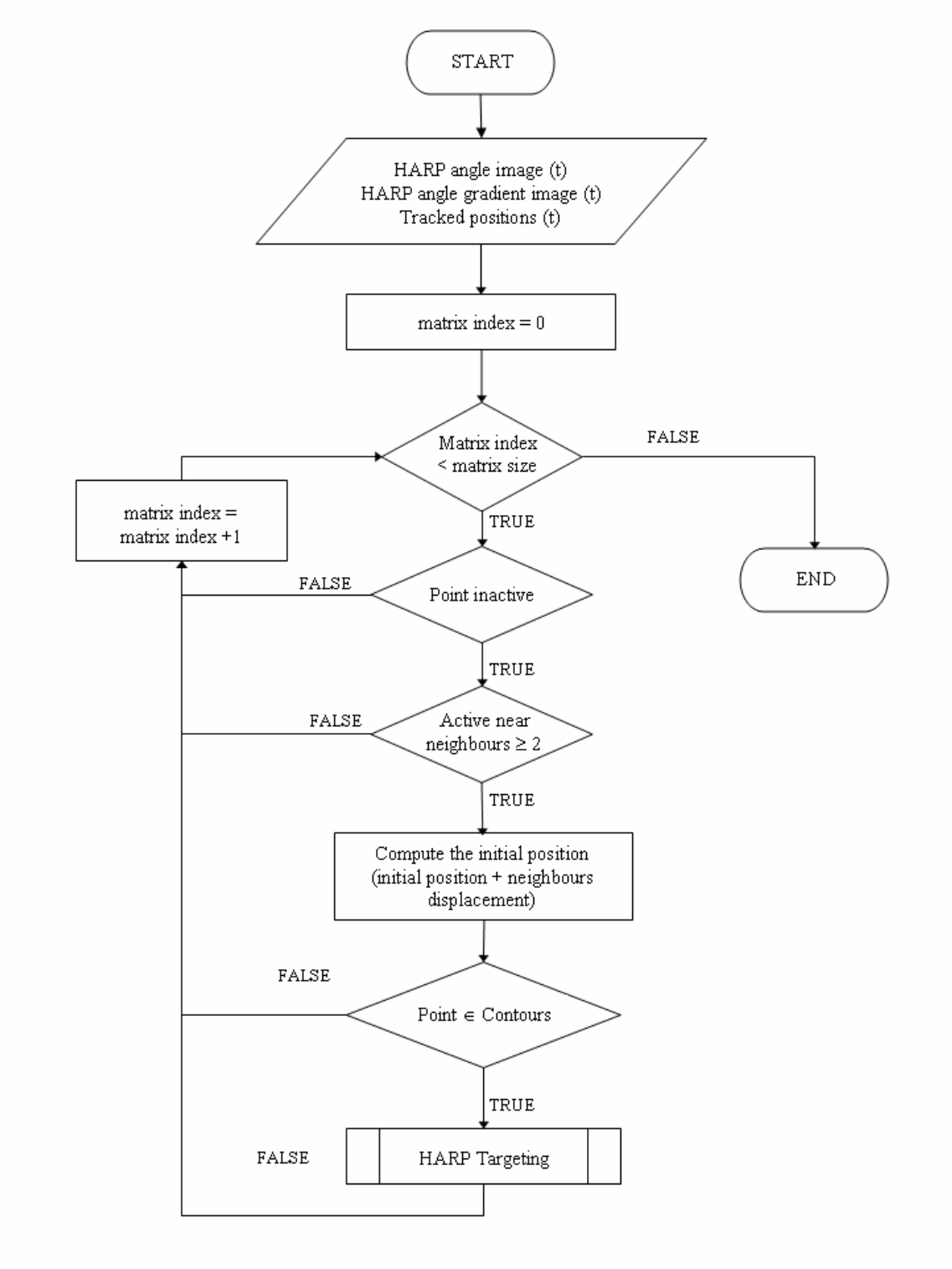
START
HARP angle image (t)
HARP angle gradient image (t)
Tracked positions (t)
matrix index = 0
Matrix index
< matrix size
FALSE
TRUE
END
matrix index =
matrix index +1
FALSE
Point inactive
TRUE
FALSE
Active near
neighbours ≥ 2
TRUE
Compute the initial position
(initial position + neighbours
displacement)
FALSE
Point ∈ Contours
TRUE
FALSE
HARP Targeting

APPENDIX II

1D HARP TRACKING

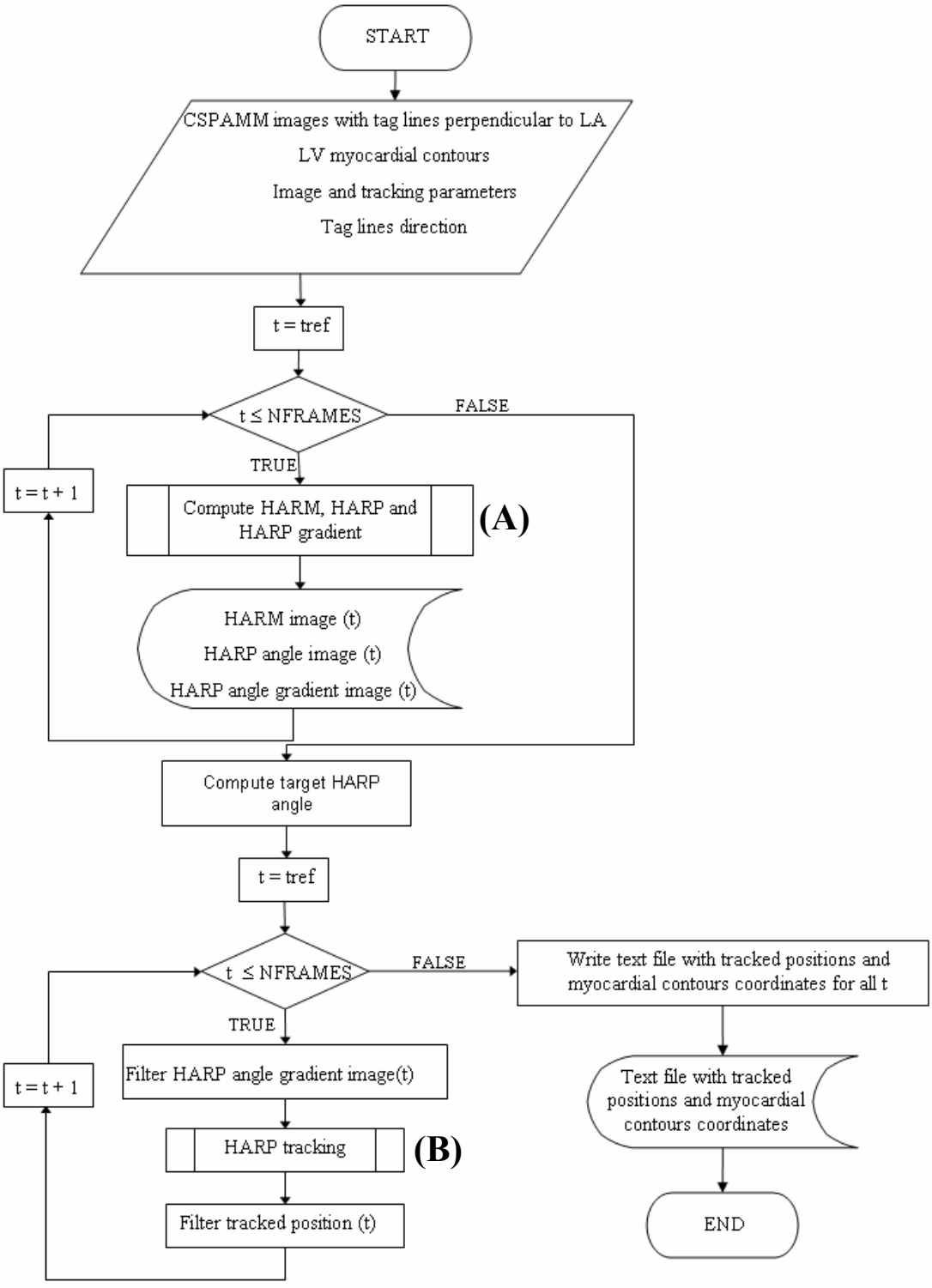

FUNCTION (A)

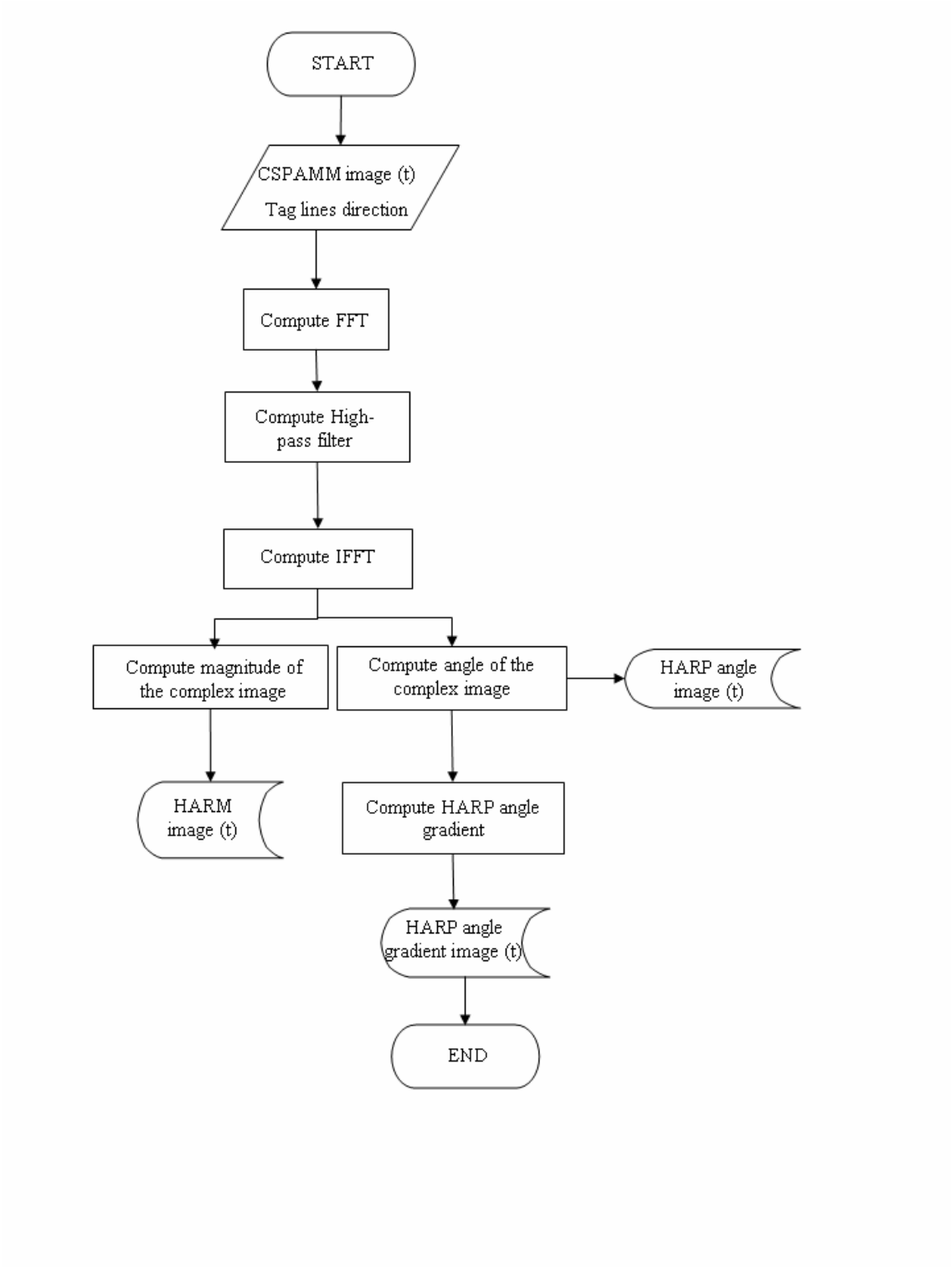
START
CSPAMM image (t)
Tag lines direction
Compute FFT
Compute High-pass filter
Compute IFFT
Compute magnitude of the complex image
Compute angle of the complex image
HARP angle image (t)
HARM image (t)
Compute HARP angle gradient
HARP angle gradient image (t)
END

FUNCTION (B)

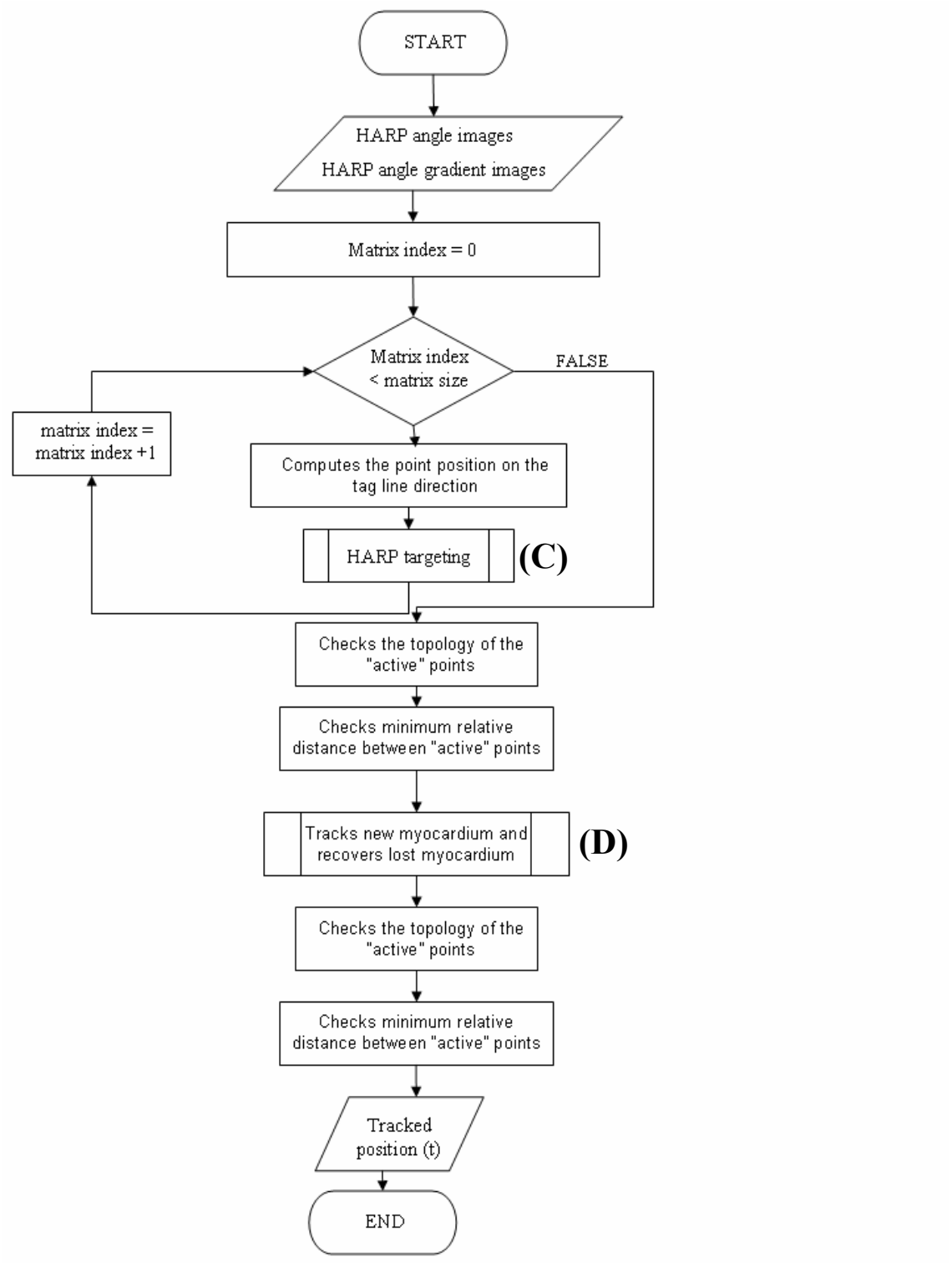
START
HARP angle images
HARP angle gradient images
Matrix index = 0
Matrix index < matrix size
FALSE
matrix index = matrix index +1
Computes the point position on the tag line direction
HARP targeting
(C)
Checks the topology of the "active" points
Checks minimum relative distance between "active" points
Tracks new myocardium and recovers lost myocardium
(D)
Checks the topology of the "active" points
Checks minimum relative distance between "active" points
Tracked position (t)
END

FUNCTION (C)

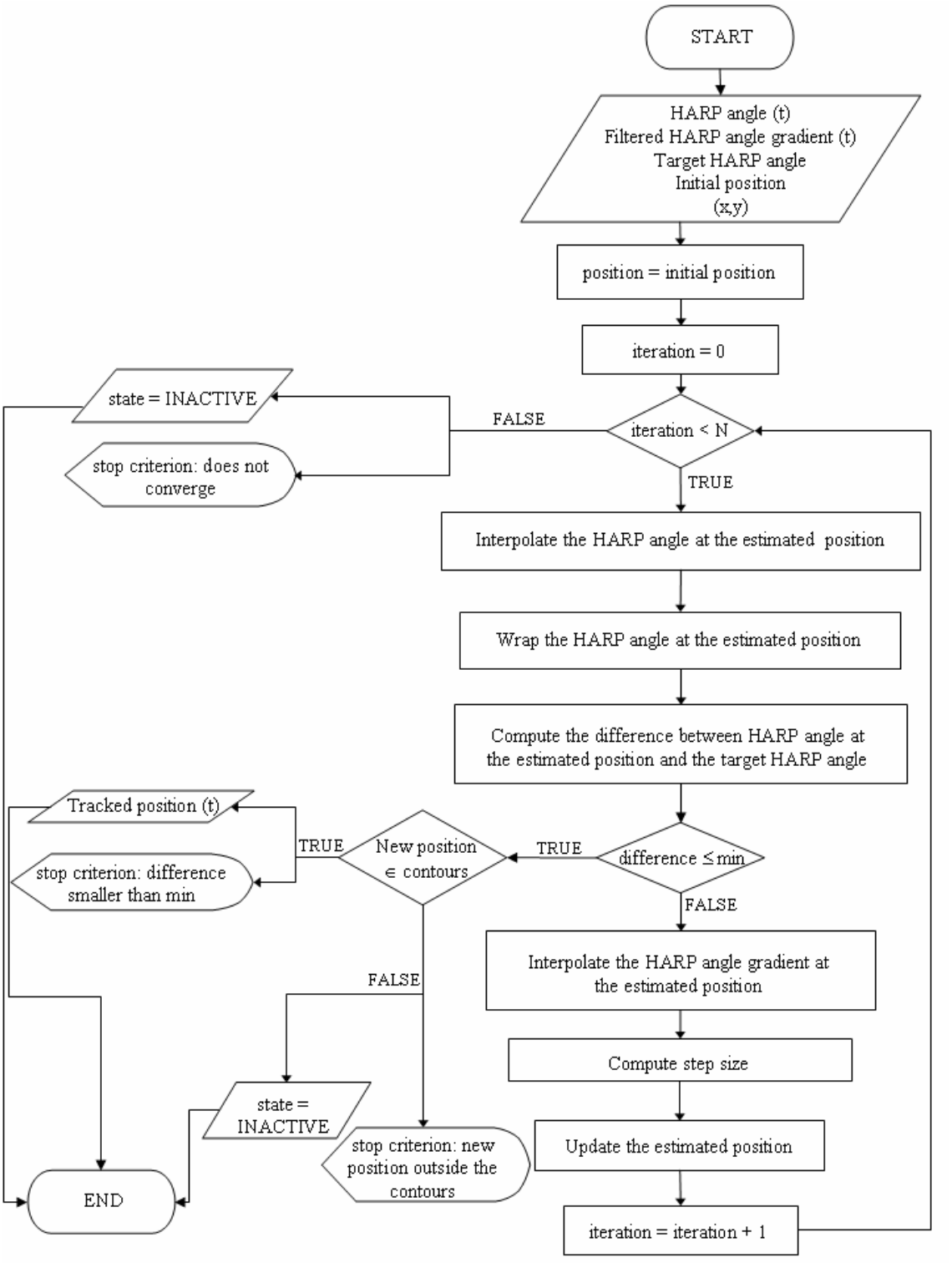
START
HARP angle (t)
Filtered HARP angle gradient (t)
Target HARP angle
Initial position
(x,y)
position = initial position
iteration = 0
state = INACTIVE
FALSE
iteration < N
stop criterion: does not converge
TRUE
Interpolate the HARP angle at the estimated position
Wrap the HARP angle at the estimated position
Compute the difference between HARP angle at the estimated position and the target HARP angle
Tracked position (t)
TRUE
New position ∈ contours
TRUE
difference ≤ min
stop criterion: difference smaller than min
FALSE
Interpolate the HARP angle gradient at the estimated position
FALSE
Compute step size
state = INACTIVE
stop criterion: new position outside the contours
Update the estimated position
END
iteration = iteration + 1

FUNCTION (D)

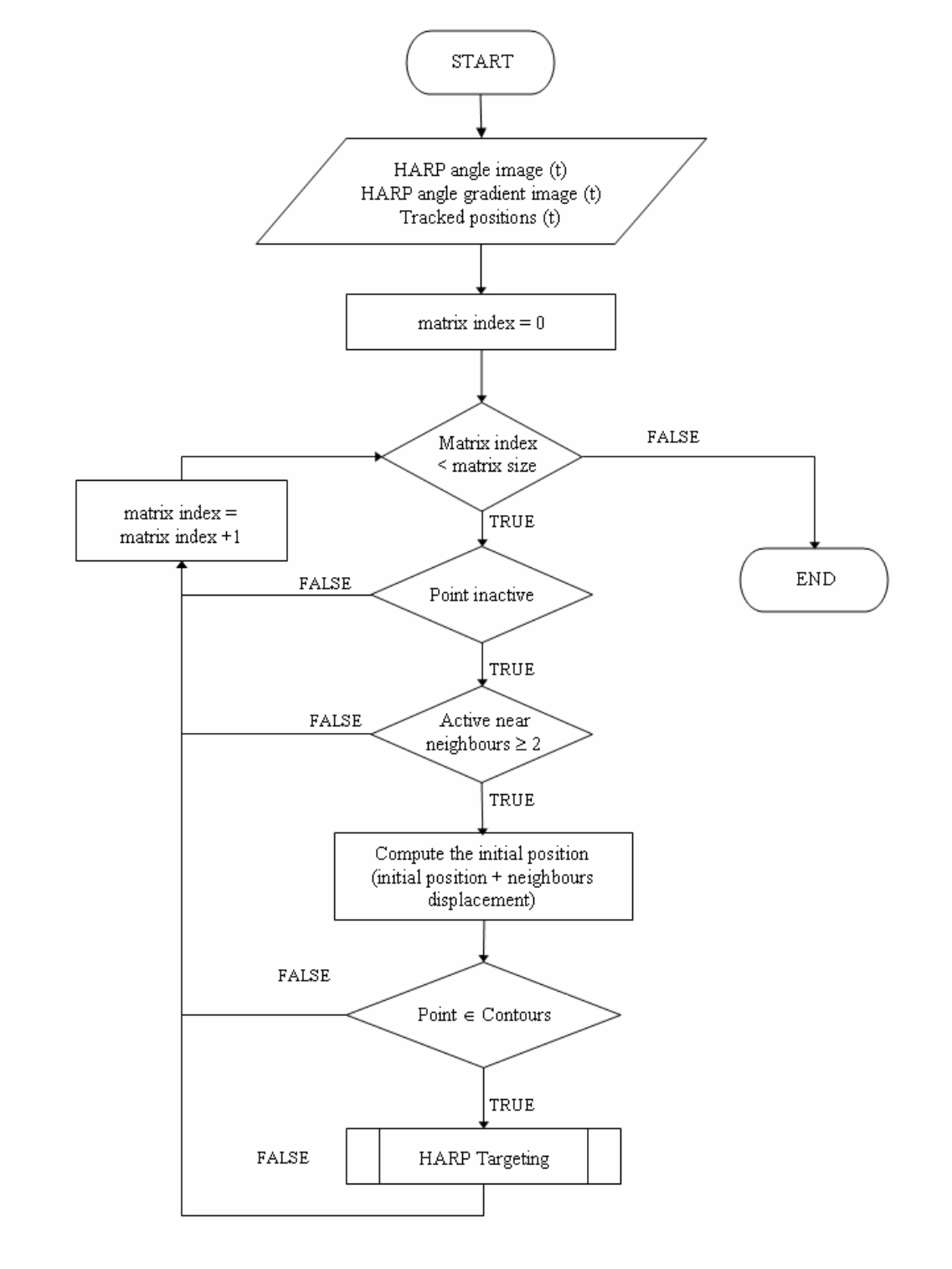
START
HARP angle image (t)
HARP angle gradient image (t)
Tracked positions (t)
matrix index = 0
Matrix index
< matrix size
FALSE
TRUE
END
matrix index =
matrix index +1
FALSE
Point inactive
TRUE
FALSE
Active near
neighbours ≥ 2
TRUE
Compute the initial position
(initial position + neighbours
displacement)
FALSE
Point ∈ Contours
TRUE
FALSE
HARP Targeting

LIST OF FIGURES

LIST OF TABLES

REFERENCES

1. Tortora, G.J. and S.R. Grabowski, *Principles of Anatomy and Physiology*. 8th ed. 1996, New York: HarperCollins College Publishers.
2. Petersen, S., et al., *European cardiovascular disease statistics.* British Heart Foundation, 2005.
3. *http://www.spc.pt/*. 2007.
4. Zwanenburg, J.J., et al., *Timing of cardiac contraction in humans mapped by high-temporal-resolution MRI tagging: early onset and late peak of shortening in lateral wall.* Am J Physiol Heart Circ Physiol, 2004. **286**(5): p. H1872-80.
5. Guyton, A.C. and J.E. Hall, *Textbook of medical physiology*. 10th ed. 2000: W. B. Saunders.
6. Sedmera, D., *Form follows function: developmental and physiological view on ventricular myocardial architecture.* Eur J Cardiothorac Surg, 2005. **28**(4): p. 526-8.
7. Buckberg, G.D., *Architecture must document functional evidence to explain the living rhythm.* Eur J Cardiothorac Surg, 2005. **27**(2): p. 202-9.
8. Sengupta, P.P., et al., *Left ventricular structure and function: basic science for cardiac imaging.* J Am Coll Cardiol, 2006. **48**(10): p. 1988-2001.
9. Kocica, M.J., et al., *The helical ventricular myocardial band: global, three-dimensional, functional architecture of the ventricular myocardium.* Eur J Cardiothorac Surg, 2006. **29 Suppl 1**: p. S21-40.
10. Anderson, R.H., et al., *The anatomical arrangement of the myocardial cells making up the ventricular mass.* Eur J Cardiothorac Surg, 2005. **28**(4): p. 517-25.
11. Kuijer, J.P., *Myocardial deformation measured with magnetic resonance tagging: tactics for two- and three-dimensional analysis in the human heart*. 2000, Vrije Universiteit: Amsterdam.
12. *http://en.wikipedia.org/*. 2007.
13. Bushberg, J.T., et al., *The essential physics of medical imaging*. 2nd ed. 2002, Philadelphia: Lippincott Williams & Wilkins.
14. Thomas, J.D. and Z.B. Popovic, *Assessment of left ventricular function by cardiac ultrasound.* J Am Coll Cardiol, 2006. **48**(10): p. 2012-25.
15. van der Vleuten, P.A., et al., *Quantification of global left ventricular function: comparison of multidetector computed tomography and magnetic resonance imaging. a meta-analysis and review of the current literature.* Acta Radiol, 2006. **47**(10): p. 1049-57.

16. http://folk.ntnu.no/stoylen/. 2007.
17. D'Hooge, J., et al., *Regional strain and strain rate measurements by cardiac ultrasound: principles, implementation and limitations.* Eur J Echocardiogr, 2000. **1**(3): p. 154-70.
18. Bleeker, G.B., et al., *Relative merits of M-mode echocardiography and tissue Doppler imaging for prediction of response to cardiac resynchronization therapy in patients with heart failure secondary to ischemic or idiopathic dilated cardiomyopathy.* Am J Cardiol, 2007. **99**(1): p. 68-74.
19. Pitzalis, M.V., et al., *Cardiac resynchronization therapy tailored by echocardiographic evaluation of ventricular asynchrony.* J Am Coll Cardiol, 2002. **40**(9): p. 1615-22.
20. D'Hooge, J., et al., *Echocardiographic strain and strain-rate imaging: a new tool to study regional myocardial function.* IEEE Trans Med Imaging, 2002. **21**(9): p. 1022-30.
21. Edvardsen, T., et al., *Quantification of left ventricular systolic function by tissue Doppler echocardiography: added value of measuring pre- and postejection velocities in ischemic myocardium.* Circulation, 2002. **105**(17): p. 2071-7.
22. http://www.medical.siemens.com. 2007.
23. Mundigler, G. and M. Zehetgruber, *Tissue Doppler imaging: myocardial velocities and strain - Are there clinical applications?* J Clin Basic Cardiol, 2002. **5**: p. 125-132.
24. Ho, C.Y. and S.D. Solomon, *A clinician's guide to tissue Doppler imaging.* Circulation, 2006. **113**(10): p. e396-8.
25. Abraham, T.P., et al., *Strain rate imaging for assessment of regional myocardial function: results from a clinical model of septal ablation.* Circulation, 2002. **105**(12): p. 1403-6.
26. Sutherland, G.R., et al., *Strain and strain rate imaging: a new clinical approach to quantifying regional myocardial function.* J Am Soc Echocardiogr, 2004. **17**(7): p. 788-802.
27. Gilman, G., et al., *Strain rate and strain: a step-by-step approach to image and data acquisition.* J Am Soc Echocardiogr, 2004. **17**(9): p. 1011-20.
28. Amundsen, B.H., et al., *Noninvasive myocardial strain measurement by speckle tracking echocardiography: validation against sonomicrometry and tagged magnetic resonance imaging.* J Am Coll Cardiol, 2006. **47**(4): p. 789-93.
29. Perk, G., P.A. Tunick, and I. Kronzon, *Non-Doppler two-dimensional strain imaging by echocardiography--from technical considerations to clinical applications.* J Am Soc Echocardiogr, 2007. **20**(3): p. 234-43.
30. Hung, J., et al., *3D echocardiography: a review of the current status and future directions.* J Am Soc Echocardiogr, 2007. **20**(3): p. 213-33.

31. Lang, R.M., et al., *Three-dimensional echocardiography: the benefits of the additional dimension.* J Am Coll Cardiol, 2006. **48**(10): p. 2053-69.
32. Schoenhagen, P., et al., *Noninvasive imaging of coronary arteries: current and future role of multi-detector row CT.* Radiology, 2004. **232**(1): p. 7-17.
33. Kalender, W.A., *X-ray computed tomography.* Phys Med Biol, 2006. **51**(13): p. R29-43.
34. Berman, D.S., et al., *Roles of nuclear cardiology, cardiac computed tomography, and cardiac magnetic resonance: assessment of patients with suspected coronary artery disease.* J Nucl Med, 2006. **47**(1): p. 74-82.
35. Schoepf, U.J., et al., *CT of coronary artery disease.* Radiology, 2004. **232**(1): p. 18-37.
36. Cury, R.C., et al., *Comprehensive cardiac CT study: evaluation of coronary arteries, left ventricular function, and myocardial perfusion--is it possible?* J Nucl Cardiol, 2007. **14**(2): p. 229-43.
37. Gibbons, R.J., P.A. Araoz, and E.E. Williamson, *The year in cardiac imaging.* J Am Coll Cardiol, 2006. **48**(11): p. 2324-39.
38. Belge, B., et al., *Accurate estimation of global and regional cardiac function by retrospectively gated multidetector row computed tomography: comparison with cine magnetic resonance imaging.* Eur Radiol, 2006. **16**(7): p. 1424-33.
39. Salm, L.P., et al., *Global and regional left ventricular function assessment with 16-detector row CT: comparison with echocardiography and cardiovascular magnetic resonance.* Eur J Echocardiogr, 2006. **7**(4): p. 308-14.
40. Juergens, K.U. and R. Fischbach, *Left ventricular function studied with MDCT.* Eur Radiol, 2006. **16**(2): p. 342-57.
41. Mahnken, A.H., et al., *Assessment of myocardial viability in reperfused acute myocardial infarction using 16-slice computed tomography in comparison to magnetic resonance imaging.* J Am Coll Cardiol, 2005. **45**(12): p. 2042-7.
42. Paul, A.K. and H.A. Nabi, *Gated myocardial perfusion SPECT: basic principles, technical aspects, and clinical applications.* J Nucl Med Technol, 2004. **32**(4): p. 179-87; quiz 188-9.
43. Russell, R.R., 3rd and B.L. Zaret, *Nuclear cardiology: present and future.* Curr Probl Cardiol, 2006. **31**(9): p. 557-629.
44. Cuocolo, A., et al., *The many ways to myocardial perfusion imaging.* Q J Nucl Med Mol Imaging, 2005. **49**(1): p. 4-18.
45. Jadvar, H., H.W. Strauss, and G.M. Segall, *SPECT and PET in the evaluation of coronary artery disease.* Radiographics, 1999. **19**(4): p. 915-26.
46. Sciagra, R. and M. Leoncini, *Gated single-photon emission computed tomography. The present-day "one-stop-shop" for cardiac imaging.* Q J Nucl Med Mol Imaging, 2005. **49**(1): p. 19-29.

47. Slart, R.H., et al., *Imaging techniques in nuclear cardiology for the assessment of myocardial viability.* Int J Cardiovasc Imaging, 2006. **22**(1): p. 63-80.
48. Clark, A.N. and G.A. Beller, *The present role of nuclear cardiology in clinical practice.* Q J Nucl Med Mol Imaging, 2005. **49**(1): p. 43-58.
49. Machac, J., *Cardiac positron emission tomography imaging.* Semin Nucl Med, 2005. **35**(1): p. 17-36.
50. Cacciabaudo, J.M. and M. Szulc, *Gated cardiac SPECT: has the addition of function to perfusion strengthened the value of myocardial perfusion imaging?* J Nucl Med, 2001. **42**(7): p. 1050-2.
51. Haacke, E., et al., *Magnetic Resonance Imaging: Physical principles and sequence design*. 1999, New York: John Wiley & Sons.
52. Hornak, J., *The basics of MRI*. 2007.
53. Huettel, S., A. Song, and G. McCarthy, *Functional magnetic resonance imaging*. 2004.
54. Paschal, C.B. and H.D. Morris, *K-space in the clinic.* J Magn Reson Imaging, 2004. **19**(2): p. 145-59.
55. Nitz, W.R., *MR imaging: acronyms and clinical applications.* Eur Radiol, 1999. **9**(5): p. 979-97.
56. Hoa, D., A. Micheau, and G. Gahide, *http://www.e-mri.org/*.
57. Hashemi, R. and W. Bradley, *MRI the basics*. 1997: Williams & Wilkins.
58. Bitar, R., et al., *MR pulse sequences: what every radiologist wants to know but is afraid to ask.* Radiographics, 2006. **26**(2): p. 513-37.
59. Nitz, W.R., *Fast and ultrafast non-echo-planar MR imaging techniques.* Eur Radiol, 2002. **12**(12): p. 2866-82.
60. Scheffler, K. and S. Lehnhardt, *Principles and applications of balanced SSFP techniques.* Eur Radiol, 2003. **13**(11): p. 2409-18.
61. Fuchs, F., G. Laub, and K. Othomo, *TrueFISP--technical considerations and cardiovascular applications.* Eur J Radiol, 2003. **46**(1): p. 28-32.
62. Glockner, J.F., et al., *Parallel MR imaging: a user's guide.* Radiographics, 2005. **25**(5): p. 1279-97.
63. Heidemann, R.M., et al., *A brief review of parallel magnetic resonance imaging.* Eur Radiol, 2003. **13**(10): p. 2323-37.
64. Zwanenburg, J.J., et al., *Steady-state free precession with myocardial tagging: CSPAMM in a single breathhold.* Magn Reson Med, 2003. **49**(4): p. 722-30.
65. Scheffler, K., O. Heid, and J. Hennig, *Magnetization preparation during the steady state: fat-saturated 3D TrueFISP.* Magn Reson Med, 2001. **45**(6): p. 1075-80.
66. Axel, L. and L. Dougherty, *MR imaging of motion with spatial modulation of magnetization.* Radiology, 1989. **171**(3): p. 841-5.

67. Zwanenburg, J.J., *Mapping asynchrony of circumferential shortening in the human heart with high temporal resolution MRI tagging*. 2005, VU: Amsterdam.
68. Reeder, S.B., et al., *Advanced cardiac MR imaging of ischemic heart disease.* Radiographics, 2001. **21**(4): p. 1047-74.
69. *http://www.scmr.org*. 2007.
70. Constantine, G., et al., *Role of MRI in clinical cardiology.* Lancet, 2004. **363**(9427): p. 2162-71.
71. Pujadas, S., et al., *MR imaging assessment of cardiac function.* J Magn Reson Imaging, 2004. **19**(6): p. 789-99.
72. Marcu, C.B., A.M. Beek, and A.C. van Rossum, *Clinical applications of cardiovascular magnetic resonance imaging.* Cmaj, 2006. **175**(8): p. 911-7.
73. Castillo, E., J.A. Lima, and D.A. Bluemke, *Regional myocardial function: advances in MR imaging and analysis.* Radiographics, 2003. **23 Spec No**: p. S127-40.
74. Zerhouni, E.A., et al., *Human heart: tagging with MR imaging--a method for noninvasive assessment of myocardial motion.* Radiology, 1988. **169**(1): p. 59-63.
75. Axel, L., A. Montillo, and D. Kim, *Tagged magnetic resonance imaging of the heart: a survey.* Med Image Anal, 2005. **9**(4): p. 376-93.
76. Axel, L. and L. Dougherty, *Heart wall motion: improved method of spatial modulation of magnetization for MR imaging.* Radiology, 1989. **172**(2): p. 349-50.
77. Schwitter, J., *Myocardial perfusion.* J Magn Reson Imaging, 2006. **24**(5): p. 953-63.
78. Schwitter, J., *Myocardial perfusion imaging by cardiac magnetic resonance.* J Nucl Cardiol, 2006. **13**(6): p. 841-54.
79. Forder, J.R. and G.M. Pohost, *Cardiovascular nuclear magnetic resonance: basic and clinical applications.* J Clin Invest, 2003. **111**(11): p. 1630-9.
80. Sandstede, J.J., *Assessment of myocardial viability by MR imaging.* Eur Radiol, 2003. **13**(1): p. 52-61.
81. Kass, M., A. Witkin, and D. Terzopoulos, *Snakes: active contour models.* Int J Comp Vision, 1988. **1**: p. 321-331.
82. Prince, J.L. and E.R. McVeigh, *Motion estimation from tagged MR image sequences.* Medical Imaging, IEEE Transactions on, 1992. **11**(2): p. 238-249.
83. Gupta, S.N. and J.L. Prince. *On variable brightness optical flow for tagged MRI*. in *Information Processing in Medical Imaging: 14th International Conference*. 1995. Dordrecht.
84. Guttman, M.A., J.L. Prince, and E.R. McVeigh, *Tag and contour detection in tagged MR images of the left ventricle.* Medical Imaging, IEEE Transactions on, 1994. **13**(1): p. 74-88.

85. Osman, N.F., et al., *Cardiac motion tracking using CINE harmonic phase (HARP) magnetic resonance imaging.* Magn Reson Med, 1999. **42**(6): p. 1048-60.
86. Moore, C.C., E.R. McVeigh, and E.A. Zerhouni, *Quantitative tagged magnetic resonance imaging of the normal human left ventricle.* Top Magn Reson Imaging, 2000. **11**(6): p. 359-71.
87. Axel, L., R.C. Goncalves, and D. Bloomgarden, *Regional heart wall motion: two-dimensional analysis and functional imaging with MR imaging.* Radiology, 1992. **183**(3): p. 745-50.
88. Spencer, A., *Continuum mechanics*. 2004, New York: Dover publications, inc.
89. Young, A.A., et al., *Three-dimensional left ventricular deformation in hypertrophic cardiomyopathy.* Circulation, 1994. **90**(2): p. 854-67.
90. Moore, C.C., et al., *Three-dimensional systolic strain patterns in the normal human left ventricle: characterization with tagged MR imaging.* Radiology, 2000. **214**(2): p. 453-66.
91. Fung, Y., *A first course in continuum mechanics: for physical and biological scientists and engineers*. 1994: Englewood Cliffs:Prentice-Hall.
92. Fischer, S.E., et al., *Improved myocardial tagging contrast.* Magn Reson Med, 1993. **30**(2): p. 191-200.
93. Kuijer, J.P., et al., *Improved harmonic phase myocardial strain maps.* Magn Reson Med, 2001. **46**(5): p. 993-9.
94. Young, A.A. and L. Axel, *Three-dimensional motion and deformation of the heart wall: estimation with spatial modulation of magnetization--a model-based approach.* Radiology, 1992. **185**(1): p. 241-7.
95. Marcus, J.T., et al., *Myocardial function in infarcted and remote regions early after infarction in man: assessment by magnetic resonance tagging and strain analysis.* Magn Reson Med, 1997. **38**(5): p. 803-10.
96. Pan, L., et al., *Fast tracking of cardiac motion using 3D-HARP.* IEEE Trans Biomed Eng, 2005. **52**(8): p. 1425-35.
97. Denney, T.S., Jr., *Estimation and detection of myocardial tags in MR image without user-defined myocardial contours.* IEEE Trans Med Imaging, 1999. **18**(4): p. 330-44.
98. Tecelao, S.R., et al., *Extended harmonic phase tracking of myocardial motion: improved coverage of myocardium and its effect on strain results.* J Magn Reson Imaging, 2006. **23**(5): p. 682-90.
99. Li, J. and T.S. Denney, Jr., *Left ventricular motion reconstruction with a prolate spheroidal B-spline model.* Phys Med Biol, 2006. **51**(3): p. 517-37.

100. Kuijer, J.P., et al., *Three-dimensional myocardial strain analysis based on short- and long-axis magnetic resonance tagged images using a 1D displacement field.* Magn Reson Imaging, 2000. **18**(5): p. 553-64.
101. Goldstein, H., *Multilevel analysis Models*. 1995, London: Adward Arnold.
102. Goldstein, H., et al., *A user's guide to MLWin.* 1998, London: University of London.
103. Kuijer, J.P., et al., *Three-dimensional myocardial strains at end-systole and during diastole in the left ventricle of normal humans.* J Cardiovasc Magn Reson, 2002. **4**(3): p. 341-51.
104. Bogaert, J. and F.E. Rademakers, *Regional nonuniformity of normal adult human left ventricle.* Am J Physiol Heart Circ Physiol, 2001. **280**(2): p. H610-20.
105. Palmon, L.C., et al., *Intramural myocardial shortening in hypertensive left ventricular hypertrophy with normal pump function.* Circulation, 1994. **89**(1): p. 122-31.
106. Dou, J., et al., *Cardiac diffusion MRI without motion effects.* Magn Reson Med, 2002. **48**(1): p. 105-14.
107. Rademakers, F.E., et al., *Dissociation between left ventricular untwisting and filling. Accentuation by catecholamines.* Circulation, 1992. **85**(4): p. 1572-81.
108. Rushmer, R.F., *Initial phase of ventricular systole: asynchronous contraction.* Am J Physiol, 1956. **184**(1): p. 188-94.
109. Kass, D.A., et al., *Improved left ventricular mechanics from acute VDD pacing in patients with dilated cardiomyopathy and ventricular conduction delay.* Circulation, 1999. **99**(12): p. 1567-73.
110. Auricchio, A., et al., *Effect of pacing chamber and atrioventricular delay on acute systolic function of paced patients with congestive heart failure. The Pacing Therapies for Congestive Heart Failure Study Group. The Guidant Congestive Heart Failure Research Group.* Circulation, 1999. **99**(23): p. 2993-3001.
111. Nelson, G.S., et al., *Predictors of systolic augmentation from left ventricular preexcitation in patients with dilated cardiomyopathy and intraventricular conduction delay.* Circulation, 2000. **101**(23): p. 2703-9.
112. Yu, C.M., et al., *High prevalence of left ventricular systolic and diastolic asynchrony in patients with congestive heart failure and normal QRS duration.* Heart, 2003. **89**(1): p. 54-60.
113. Ghio, S., et al., *Interventricular and intraventricular dyssynchrony are common in heart failure patients, regardless of QRS duration.* Eur Heart J, 2004. **25**(7): p. 571-8.
114. Leclercq, C. and D.A. Kass, *Retiming the failing heart: principles and current clinical status of cardiac resynchronization.* J Am Coll Cardiol, 2002. **39**(2): p. 194-201.
115. Leclercq, C. and J.M. Hare, *Ventricular resynchronization: current state of the art.* Circulation, 2004. **109**(3): p. 296-9.

116. Bax, J.J., et al., *Echocardiographic evaluation of cardiac resynchronization therapy: ready for routine clinical use? A critical appraisal.* J Am Coll Cardiol, 2004. **44**(1): p. 1-9.

117. Lecoq, G., et al., *Clinical and electrocardiographic predictors of a positive response to cardiac resynchronization therapy in advanced heart failure.* Eur Heart J, 2005. **26**(11): p. 1094-100.

118. Breithardt, O.A., et al., *Echocardiographic quantification of left ventricular asynchrony predicts an acute hemodynamic benefit of cardiac resynchronization therapy.* J Am Coll Cardiol, 2002. **40**(3): p. 536-45.

119. Leclercq, C., et al., *Systolic improvement and mechanical resynchronization does not require electrical synchrony in the dilated failing heart with left bundle-branch block.* Circulation, 2002. **106**(14): p. 1760-3.

120. Yu, C.M., et al., *Tissue Doppler echocardiographic evidence of reverse remodeling and improved synchronicity by simultaneously delaying regional contraction after biventricular pacing therapy in heart failure.* Circulation, 2002. **105**(4): p. 438-45.

121. Bax, J.J., et al., *Left ventricular dyssynchrony predicts response and prognosis after cardiac resynchronization therapy.* J Am Coll Cardiol, 2004. **44**(9): p. 1834-40.

122. Bax, J.J., et al., *Usefulness of myocardial tissue Doppler echocardiography to evaluate left ventricular dyssynchrony before and after biventricular pacing in patients with idiopathic dilated cardiomyopathy.* Am J Cardiol, 2003. **91**(1): p. 94-7.

123. Lardo, A.C., T.P. Abraham, and D.A. Kass, *Magnetic resonance imaging assessment of ventricular dyssynchrony: current and emerging concepts.* J Am Coll Cardiol, 2005. **46**(12): p. 2223-8.

124. Roguin, A., et al., *Modern pacemaker and implantable cardioverter/defibrillator systems can be magnetic resonance imaging safe: in vitro and in vivo assessment of safety and function at 1.5 T.* Circulation, 2004. **110**(5): p. 475-82.

125. Altman, D., *Pratical statistics for medical research*. 1999: Chapman and Hill.

126. Zwanenburg, J.J., et al., *Propagation of onset and peak time of myocardial shortening in time of myocardial shortening in ischemic versus nonischemic cardiomyopathy: assessment by magnetic resonance imaging myocardial tagging.* J Am Coll Cardiol, 2005. **46**(12): p. 2215-22.

127. Fonseca, C.G., et al., *Aging alters patterns of regional nonuniformity in LV strain relaxation: a 3-D MR tissue tagging study.* Am J Physiol Heart Circ Physiol, 2003. **285**(2): p. H621-30.

128. Oxenham, H.C., et al., *Age-related changes in myocardial relaxation using three-dimensional tagged magnetic resonance imaging.* J Cardiovasc Magn Reson, 2003. **5**(3): p. 421-30.

129. Zwanenburg, J.J., et al., *Regional timing of myocardial shortening is related to prestretch from atrial contraction: assessment by high temporal resolution MRI tagging in humans.* Am J Physiol Heart Circ Physiol, 2005. **288**(2): p. H787-94.

130. Helm, R.H., et al., *Cardiac dyssynchrony analysis using circumferential versus longitudinal strain: implications for assessing cardiac resynchronization.* Circulation, 2005. **111**(21): p. 2760-7.

131. O'Dell, W.G., et al., *Three-dimensional myocardial deformations: calculation with displacement field fitting to tagged MR images.* Radiology, 1995. **195**(3): p. 829-35.

132. Deng, X. and T.S. Denney, Jr., *Three-dimensional myocardial strain reconstruction from tagged MRI using a cylindrical B-spline model.* IEEE Trans Med Imaging, 2004. **23**(7): p. 861-7.

133. Garot, J., et al., *Fast determination of regional myocardial strain fields from tagged cardiac images using harmonic phase MRI.* Circulation, 2000. **101**(9): p. 981-8.

134. Geskin, G., et al., *Quantitative assessment of myocardial viability after infarction by dobutamine magnetic resonance tagging.* Circulation, 1998. **98**(3): p. 217-23.

135. Ennis, D.B., et al., *Assessment of regional systolic and diastolic dysfunction in familial hypertrophic cardiomyopathy using MR tagging.* Magn Reson Med, 2003. **50**(3): p. 638-42.

136. Kraitchman, D.L., et al., *Quantitative ischemia detection during cardiac magnetic resonance stress testing by use of FastHARP.* Circulation, 2003. **107**(15): p. 2025-30.

137. Epstein, F.H. and W.D. Gilson, *Displacement-encoded cardiac MRI using cosine and sine modulation to eliminate (CANSEL) artifact-generating echoes.* Magn Reson Med, 2004. **52**(4): p. 774-81.

138. Ryf, S., et al., *Myocardial tagging with 3D-CSPAMM.* J Magn Reson Imaging, 2002. **16**(3): p. 320-5.